while including the effects of friction and bearing stresses (from dowel misalignment); see Figure 4.56(b). For all specimens, slip occurred after the pullout force per dowel increased above 1124 lbs -1574 lbs, which corresponds to average bond shear stress (τ_b) of 30.0 psi to 43.0 psi.

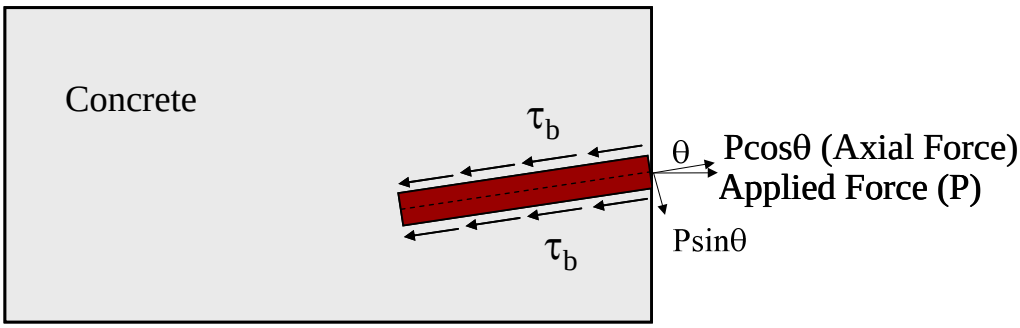

(a) Before Initial Slip

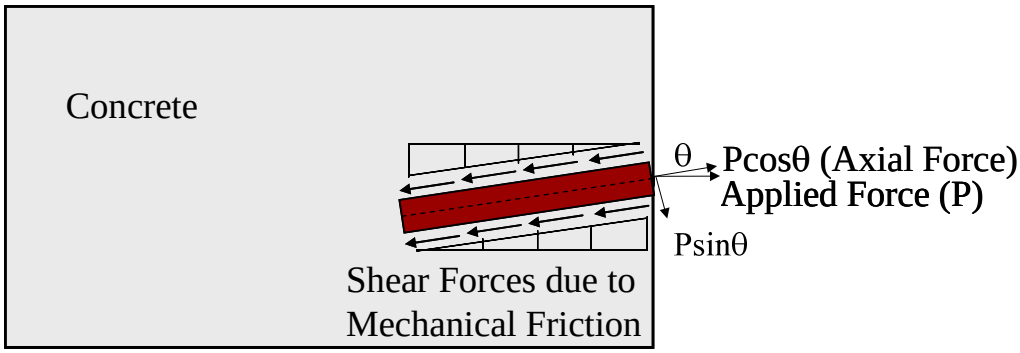

(b) Post-slip

Figure 4.56: Forces on a misaligned dowel and surrounding concrete

In chapter 5, the assumptions made and the results from the three dimensional finite element models are presented.

CHAPTER 5

DEVELOPMENT OF 3D FINITE ELEMENT MODELS

5.1 INTRODUCTION

This chapter presents the development of the three dimensional (3D) nonlinear finite element models for the concrete pavement specimens. The input parameters for the steel dowel and concrete material model are presented. The development and calibration of the 3D finite element model for the pullout behavior of single and multiple misaligned dowel bars are also presented in this chapter.

5.2 NEED FOR A 3D FINITE ELEMENT MODEL

The experimental results presented in chapter 4 provide basic information regarding the overall joint opening behavior of concrete pavements with aligned or misaligned dowel bars. The experimental results indicate that the force-joint opening behavior consists of two regions: (i) the initial fully bonded region, and (ii) the post-slip debonded region. Initial slip occurs when the load applied across the joint increases beyond the threshold limit corresponding to the average bond stress (τ_b). The post-slip (debonded) region includes hardening and softening behavior corresponding to increase or decrease in the load applied across the joint depending on the misalignment type, magnitude and distribution of dowel bars. The experimental results indicate that larger misalignment results in larger pullout forces, which can potentially lead to spalling or cracking type distress around the dowel bars in some cases.

A major limitation of the experimental investigations is that they cannot provide detailed information or insight regarding the interaction between the dowel bar and the surrounding concrete. The experimental results and observations do not provide direct knowledge regarding: (a) the longitudinal bond and transverse (bearing) interaction between the dowel and the concrete slabs; (b) the complex 3D stress states in the concrete and (c) the structural distresses produced by stress concentrations and excessive stresses in the concrete surrounding the dowel bars. In light of these limitations analytical models and results will provide a better understanding of the mechanics of dowel concrete interaction, the 3D stresses and the distress (damage) produced due to misaligned dowels in the pavement slabs.

5.3 THE 3D FINITE ELEMENT MODEL – ELEMENT SELECTION

The concrete pavement specimens are modeled as two concrete slabs connected at the joint using 1.25 in. diameter steel dowel bars. The dowel bar is placed in the center of the joint at mid depth. In case of multiple dowel bar specimens, the dowel bars are placed at a distance of 12 in. on center. Three dimensional (3D) first order reduced integration continuum elements (C3D8R - Bricks) are used to model the concrete slab and the steel dowel bars. These elements are versatile and can be used in models for simple linear analysis or for complex nonlinear analyses involving contact, plasticity and large deformations. The typical solid elements in Abaqus are shown in figure 5.1. A typical mesh discretization of the concrete and dowel bar is shown in figure 5.2.

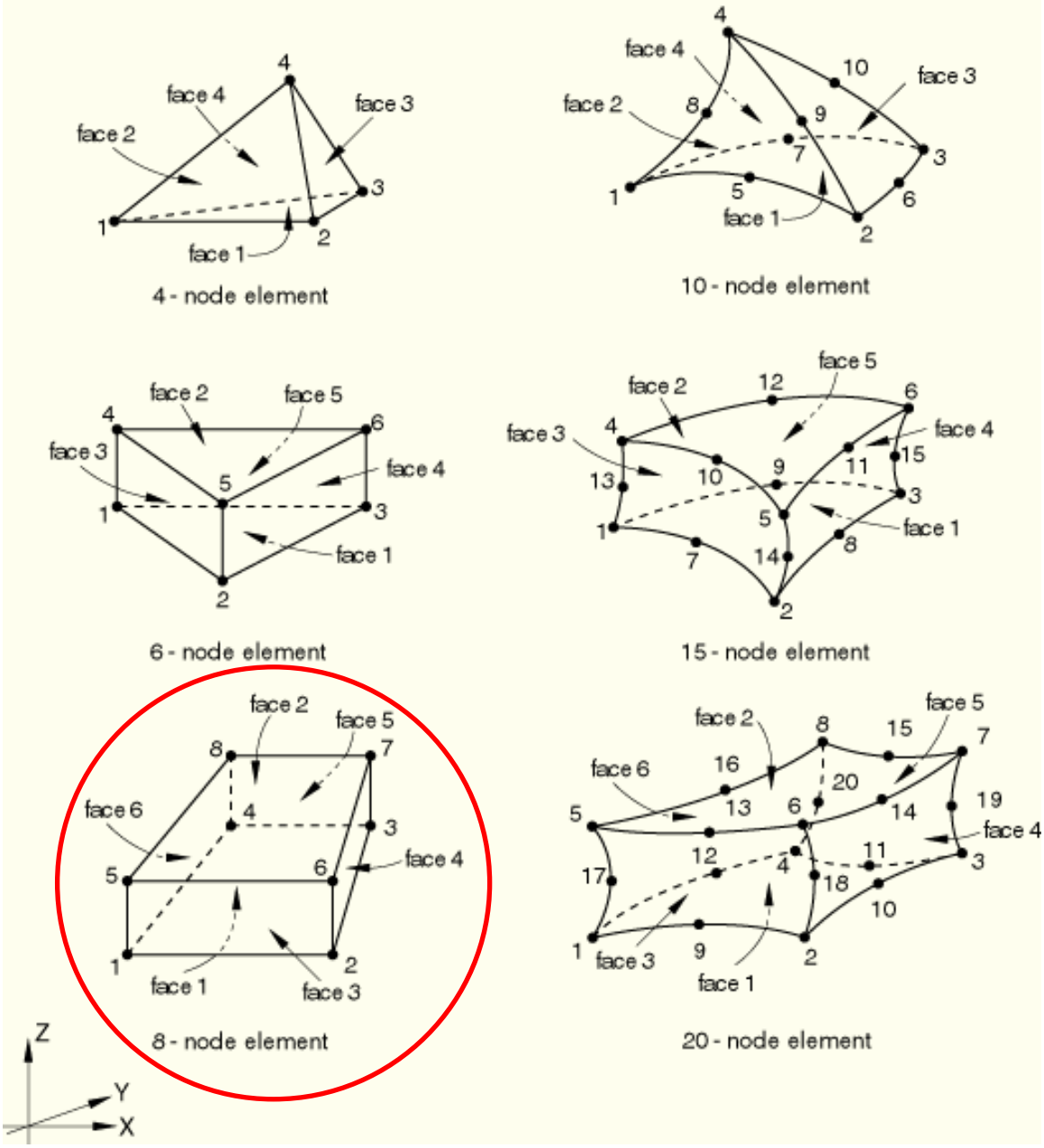

Figure 5.1: Abaqus Solid element Library (Abaqus User Manual 2004)

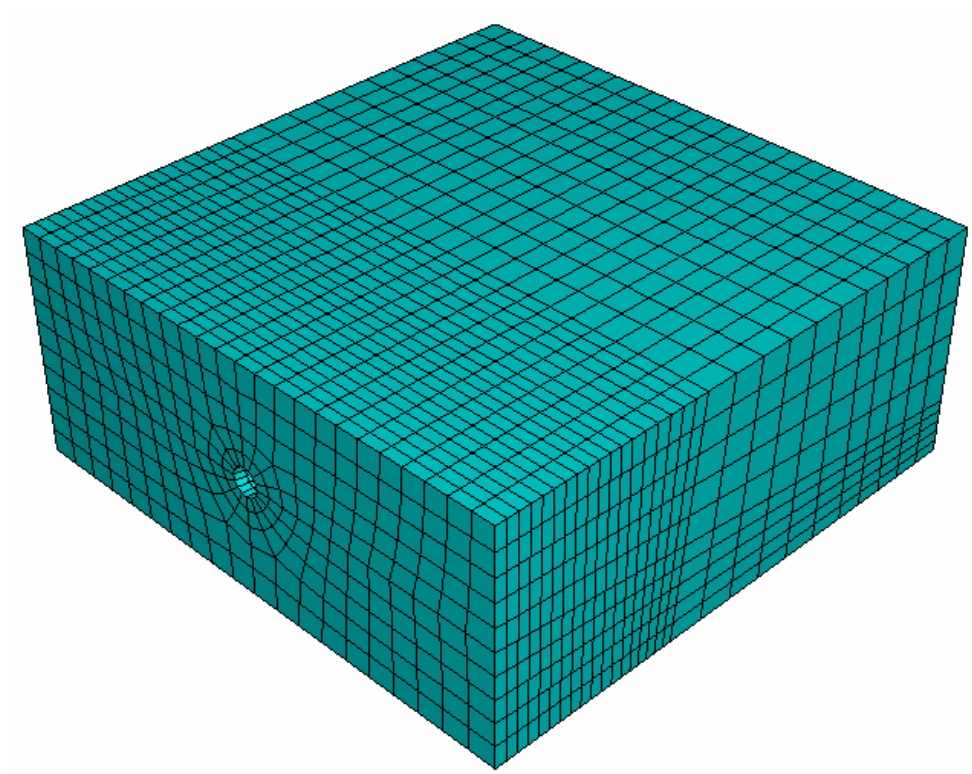

(a) Concrete Slab discretized using brick elements for a single dowel bar

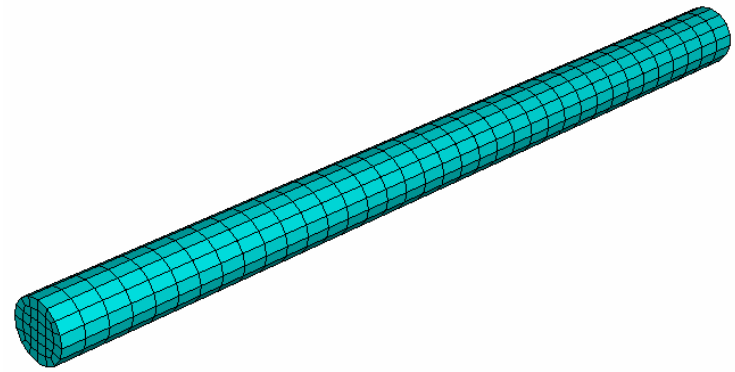

(b) Dowel bar (Dia 1.25in. and 18 in. length) discretized using brick elements

Figure 5.2: Finite Element Model discretization of the concrete slab and dowel bar.

5.4 MATERIAL MODEL – BEHAVIOR AND CALIBRATION

The three dimensional (3D) finite element models were developed using Abaqus because it includes a robust concrete damage plasticity and cracking model that is needed for this research. The concrete elements were modeled with the nonlinear concrete damaged plasticity material model. The steel elements were provided with isotropic multiaxial elastic material model.

5.4.1 TYPES OF CONCRETE MATERIAL MODELS

There are currently three concrete models to model plain and reinforced concrete in Abaqus (2004). These include the smeared cracking model, the concrete damage plasticity model and the cracking model for concrete.

5.4.1.1 The Smeared Cracking Model

This model is appropriate for modeling the behavior of concrete structures subjected to *monotonic loading* under fairly low confining pressures (less than four to five times the uniaxial compressive stress). This model assumes cracking as the main failure mechanism. Cracking is assumed to occur when the stresses reach the failure surface defined in the *p-q plane* also called the crack detection surface and *p*- is the first stress invariant and *q*- is the second stress invariant of the deviatoric stress. This model assumes a smeared cracking approach, which does not track the individual micro cracks at each numerical integration point. The presence of a crack affects the stresses and material stiffness associated with that integration point. The model uses a multi-axial plasticity model when the stresses are compressive. This model uses a two parameter

Drucker-Prager yield surface, associated flow rule and isotropic hardening. As the model assumes an associative flow rule, it simplifies the actual behavior and over predicts the inelastic strain when concrete is strained beyond the ultimate stress point.

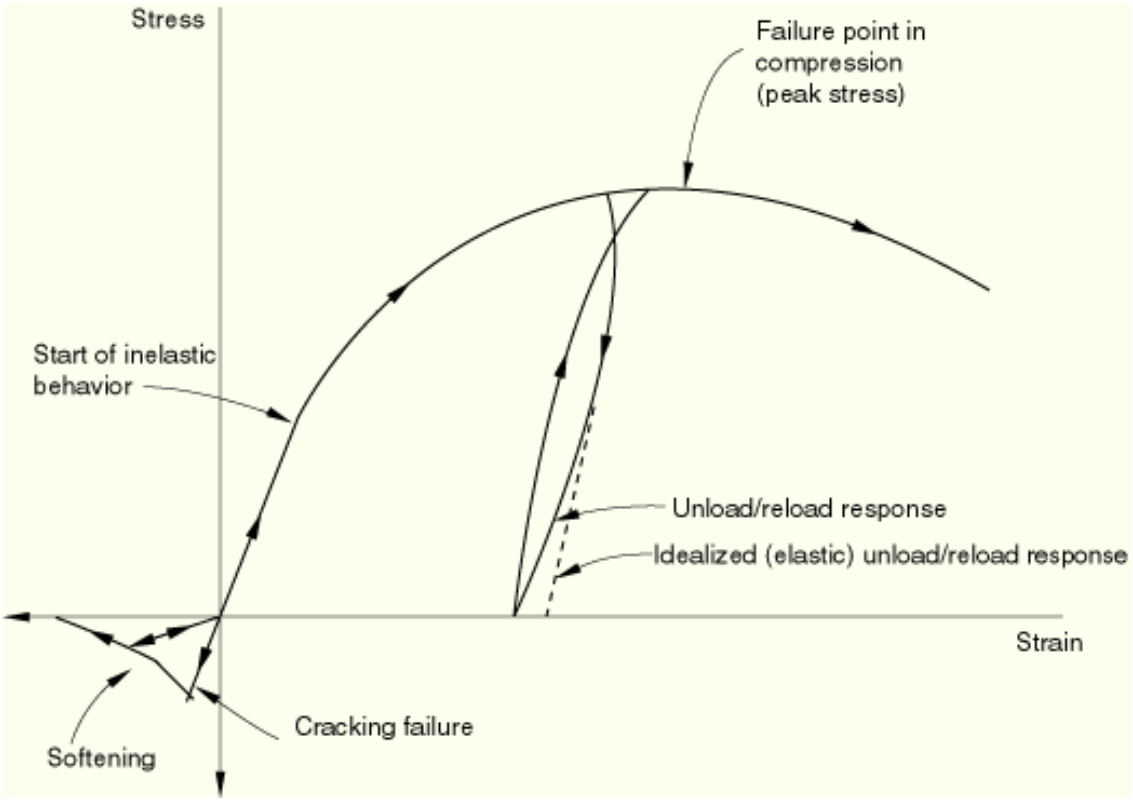

Figure 5.3: Uniaxial behavior of plain concrete (Abaqus User Manual 2004)

As shown in figure 5.3, as the compression stresses increases, the material undergoes inelastic straining in the form of hardening followed by eventual softening. Upon unloading the model assumes an idealized elastic unloading and re-loading response. In reality the unloading response of the material is slightly softer than the initial elastic response. This model makes no attempt to predict the cyclic or dynamic response as it was developed primarily for applications related to monotonically applied loading.

5.4.1.2 The Cracking Model for Concrete

This model is used for modeling concrete structures subjected to dynamic loading only. The primary failure mechanism is dominated by tensile cracking of concrete. In compression, the model behaves linear elastic. The specialty of this model is that it allows removal of elements after failure. Failure is defined similar to the smeared cracking model in terms of crack to determine the discontinuous behavior of concrete. The model uses a simple Rankine criterion which states that crack forms when the maximum tensile stress exceeds the tensile strength of the material.

5.4.1.3 The Concrete Damage Plasticity Model

This concrete model is very versatile and capable of predicting the behavior of concrete structures subjected to monotonic, cyclic and / or dynamic loading. It assumes two main failure mechanisms, i.e., tensile cracking and compressive crushing of the concrete material. In compression, the model uses a multi-axial plasticity model with non-associated flow and an isotropic scalar hardening. The model in tension uses a multi-axial damage elasticity model. The equivalent tensile and compressive strains, PEEQT and PEEQ, as the hardening variables control the evolution of the yield surface. The model behavior in uniaxial tension and compression is shown in figure 5.4. The input parameters for the material model are explained in detail in the latter sections of this chapter.

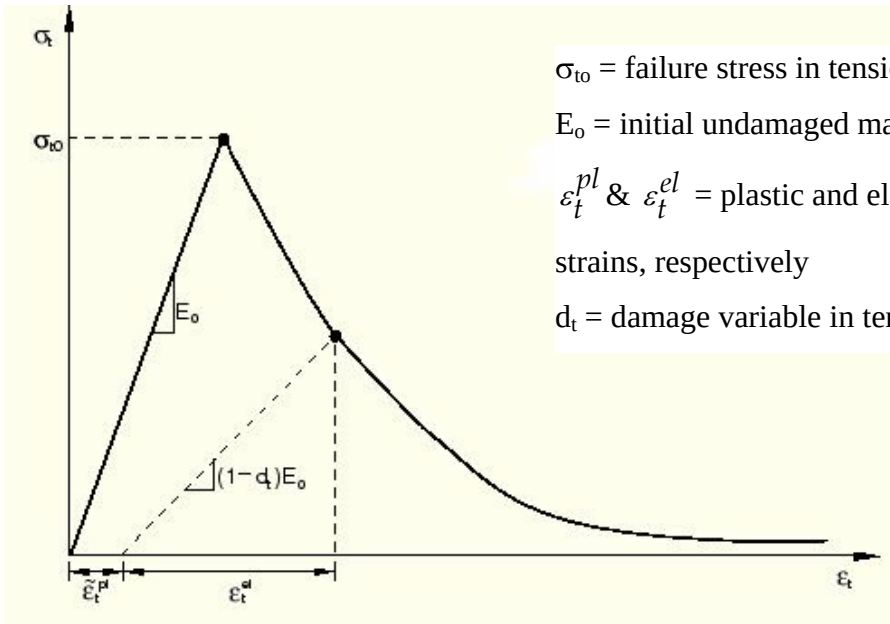

σ_{to} = failure stress in tension

E_o = initial undamaged material modulus

ε_t^{pl} & ε_t^{el} = plastic and elastic tensile strains, respectively

d_t = damage variable in tension

(a) Uniaxial Tensile Loading

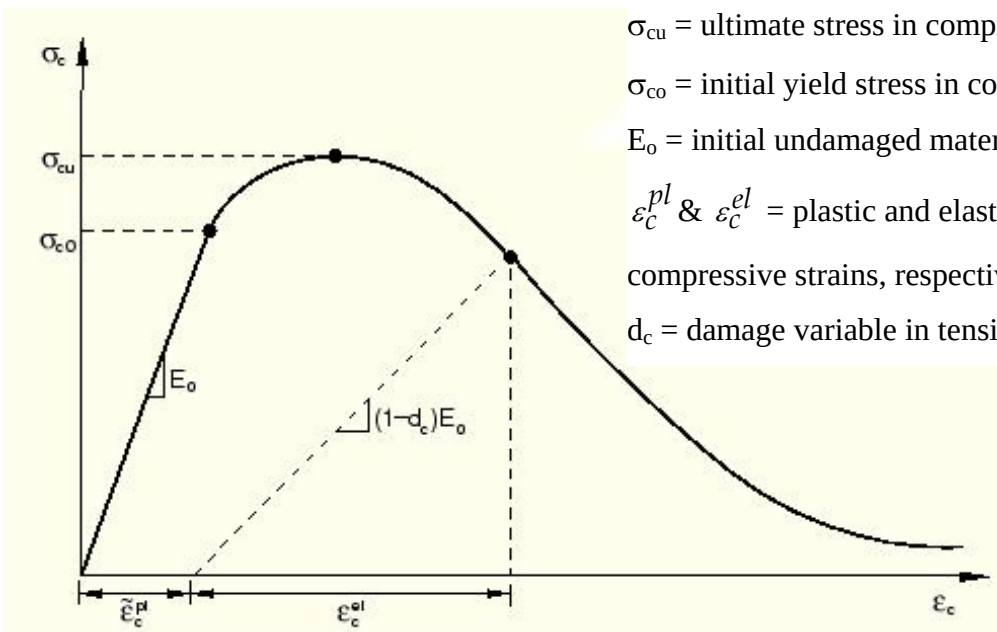

σ_{cu} = ultimate stress in compression

σ_{co} = initial yield stress in compression

E_o = initial undamaged material modulus

ε_c^{pl} & ε_c^{el} = plastic and elastic compressive strains, respectively

d_c = damage variable in tension

(b) Uniaxial compressive loading

Figure 5.4: Typical concrete uniaxial stress –strain curve in tension and compression (Abaqus User Manual 2004)

5.4.2 FEATURES OF CONCRETE BEHAVIOR

Concrete is a composite material that consists of coarse aggregates and a continuous cement paste and fine aggregate particles. Its mechanical behavior is complex due to the structure of the composite material. The stress-strain behavior is influenced by the development of micro- and macro-cracking of the material. The constitutive behavior of concrete under various loading conditions has been well documented in the published literature. A variety of constitutive models have been proposed for concrete, the Mohr-Coulomb model, the Drucker-Prager model, William-Warnke model, Ottosen model, etc. The aim of these models is to mathematically reproduce the stress-strain behavior of concrete.

Concrete exhibits a nonlinear stress-strain behavior during loading and has a significant irreversible strain upon loading. Under confining pressures and compressive loading, concrete shows ductile behavior. These irreversible deformations in concrete are modeled using the theory of plasticity. There are three basic assumptions in any plasticity model (Chen and Han, 1995):

(i) An initial yield surface in the stress space that defines the stress levels at which plastic deformation begins.

(ii) A flow rule which is related to a plastic potential function and gives an incremental plastic stress-strain relation.

(iii) A hardening rule that defines the change of loading surface as well as the change of the hardening properties of the material during the course of plastic flow.

The concrete models typically differ from each other in the shape of the failure and loading surfaces, the hardening rule, and the flow rule. As shown in figure 5.5, in the hydrostatic plane (details about this can be found in Chen & Han 1995), the failure surface encloses all the loading surfaces and serves as a bounding surface which is assumed to remain unchanged during loading. The initial yield surface has a closed shape. During hardening, the loading surface expands and changes its shape from the initial yield surface to the final shape that matches with the failure surface.

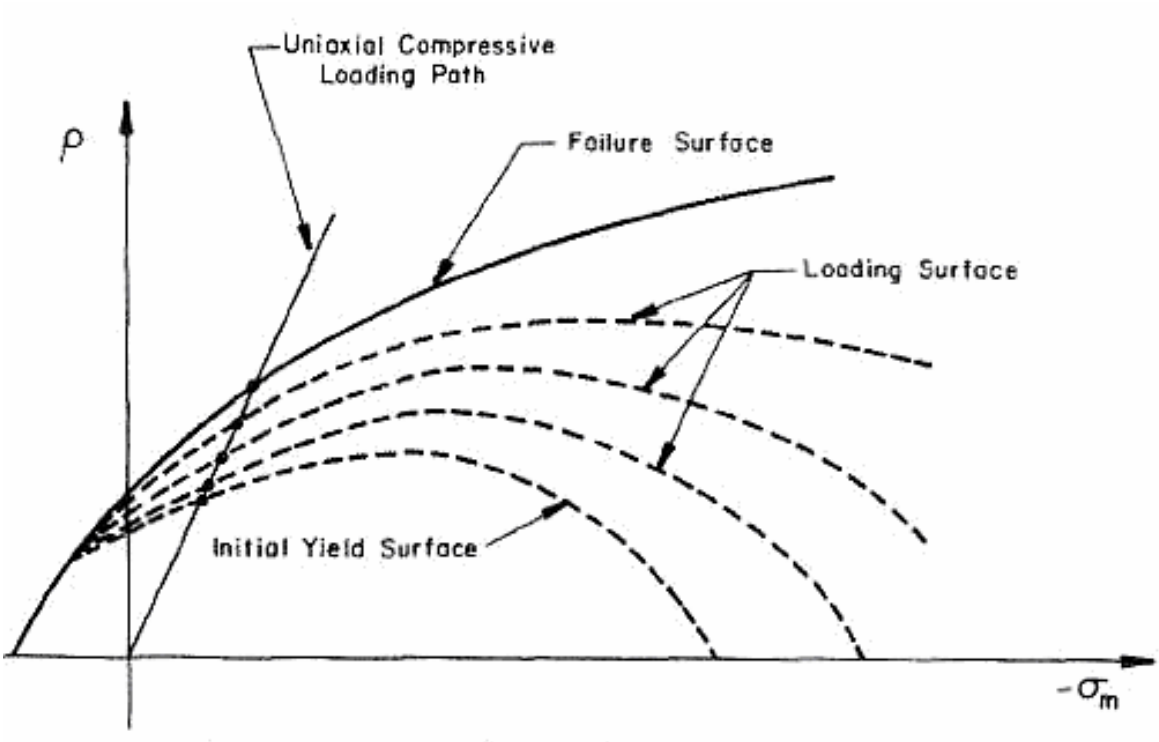

Figure 5.5: A plasticity hardening model for concrete (Chen and Han, 1995)

Concrete exhibits nonlinear volume change during hardening. Experimental results have indicated that under compressive loadings, inelastic volume contraction occurs at the beginning of yielding and volume dilation occurs at 75 to 90% of ultimate

(f'_c) stress. This basically violates the associated flow rule and a plastic potential function other than the yield surface is used for the flow rule.

A schematic of hardening and flow for the linear Drucker Prager model in the deviatoric plane (details about this can be found in Chen & Han 1995) is shown in figure 5.6. The associated flow rule assumes that the the material friction angle β to be equal to the material dilation angle ψ. For granular materials and concrete, the non-associative flow rule is assumed in the *p-q plane*, in the sense that the flow is assumed to be normal to the yield surface in the Π plane but at an angle ψ to the *q-axis* in the *p-q plane*, where $\psi < \beta$. If $\psi > 0$, the material dilates, hence ψ is referred to as the dilation angle. This flow potential is continuous and smooth and it ensures that the flow direction is defined uniquely.

ψ = material dilation angle

β = material friction angle

$d\varepsilon^{pl}$ = incremental plastic strain

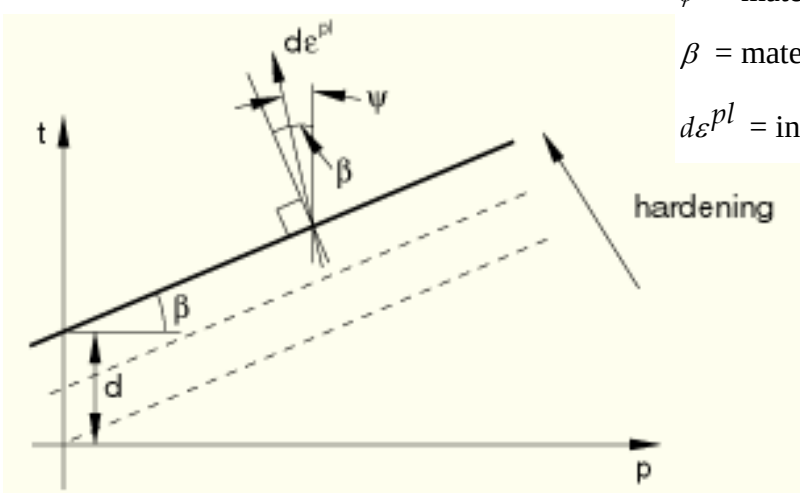

Figure 5.6: Schematic of yield surface and flow in the meridinal plane. (Abaqus User Manual 2004)

The concrete damage plasticity model was used in this research study. It uses the following definitions for the yield surface and the flow potential.

Yield Surface: The plastic damage concrete model uses a yield condition based on the yield function proposed by Lubliner et al (1989) and incorporates the modifications

proposed by Lee and Fenves (1998) to account for the different evolution of strength under tension and compression. In terms of effective stresses, the yield function takes the form:

$$F\left(\bar{\sigma},\tilde{\varepsilon}^{pl}\right)=\frac{1}{1-\alpha}\left(\bar{q}-3\alpha\bar{p}+\beta\left(\tilde{\varepsilon}^{pl}\right)\left\langle\hat{\bar{\sigma}}_{\max}\right\rangle-\gamma\left\langle-\hat{\bar{\sigma}}_{\max}\right\rangle\right)-\bar{\sigma}_c\left(\tilde{\varepsilon}_c^{pl}\right)=0$$

……..…Equation 5.1

where,

$\bar{p}=\frac{1}{3}\bar{\sigma}:I$ is the effective hydrostatic pressure;

$q=\sqrt{\frac{3}{2}\bar{S}:\bar{S}}$ is the Mises equivalent stress, where $\bar{S}=\bar{p}I+\bar{\sigma}$ is the deviatoric part of the effective stress tensor $\bar{\sigma}$;

$$\alpha=\frac{\left(\frac{\sigma_{bo}}{\sigma_{co}}\right)-1}{2\left(\frac{\sigma_{bo}}{\sigma_{co}}\right)-1};0\le\alpha\le0.5\ ;\ \gamma=\frac{3\left(1-K_c\right)}{2K_c-1};\ \beta=\frac{\bar{\sigma}_c\left(\tilde{\varepsilon}_c^{pl}\right)}{\bar{\sigma}_t\left(\tilde{\varepsilon}_t^{pl}\right)}\left(1-\alpha\right)-\left(1+\alpha\right)$$

where α and γ are material constants.

σ_{bo}/σ_{co} = ratio of the initial equibiaxial compressive yield stress to initial uniaxial compressive yield stress (experimental values range from 1.10 to 1.16 from Lubliner et al (1998);

K_c = ratio of the second stress invariant on the tensile meridian to that on the compressive meridian at initial yield for any given value of pressure invariant p. Note that the value of K_c (default 2/3) should vary $0.5<K_c<1$

$\hat{\bar{\sigma}}_{\max}$ = max principal effective stress

The evolution of the yield surface is controlled by two hardening variables, $\tilde{\varepsilon}_t^{pl}$ and $\tilde{\varepsilon}_c^{pl}$ which are defined as the equivalent tensile (PEEQT) and compressive strains (PEEQ) that are linked to the failure mechanisms in tension and compression respectively.

Flow Rule and Potential: The concrete damaged plasticity model assumes non-associated potential plastic flow. This flow potential, which is continuous and smooth, ensures that the flow direction is always uniquely defined. The flow potential *G* used for this model is the Drucker-Prager hyperbolic function:

$$G = \sqrt{\left(\varepsilon\ \sigma_{to} \tan\psi\right)^2 + \bar{q}^2} - \bar{p}\tan\psi \quad \text{……..Equation 5.2}$$

where,

ψ = the dilation angle measure in the $p - q$ plane at high confining pressure (measured in degrees)

σ_{to} = the uniaxial tensile stress at failure

ε = eccentricity parameter, defining the rate at which the function approaches the asymptote, default is 0.1.

The flow rule is given as, $d\varepsilon_{ij}^{pl} = d\lambda \dfrac{\partial G}{\partial \sigma_{ij}}$ …..…….Equation 5.3

The input parameters that were considered for the nonlinear concrete damage plasticity material and isotropic elastic material model for steel is presented in the next section

5.4.3 INPUT PARAMETERS FOR THE CONCRETE MATERIAL MODEL

The input parameters required for the defining concrete material model are: (i) the uniaxial compression stress- strain curve; (ii) the uniaxial tension stiffening stress–strain curve, (iii) the volumetric dilation angle ψ, (iv) the biaxial compression strength ratio

σ_{bc}, and (v) the ratio of tensile-to-compressive meridian K. These input parameters for the model are defined as follows:

The uniaxial compression stress-strain curve was defined using the experimentally measured properties such as; elastic modulus E_c and compressive strength f'_c and the modified Popovic's empirical stress-strain model recommended by Collins et al. (1992). A typical uniaxial compressive stress-strain curve for 3500 psi concrete is shown in figure 5.8.

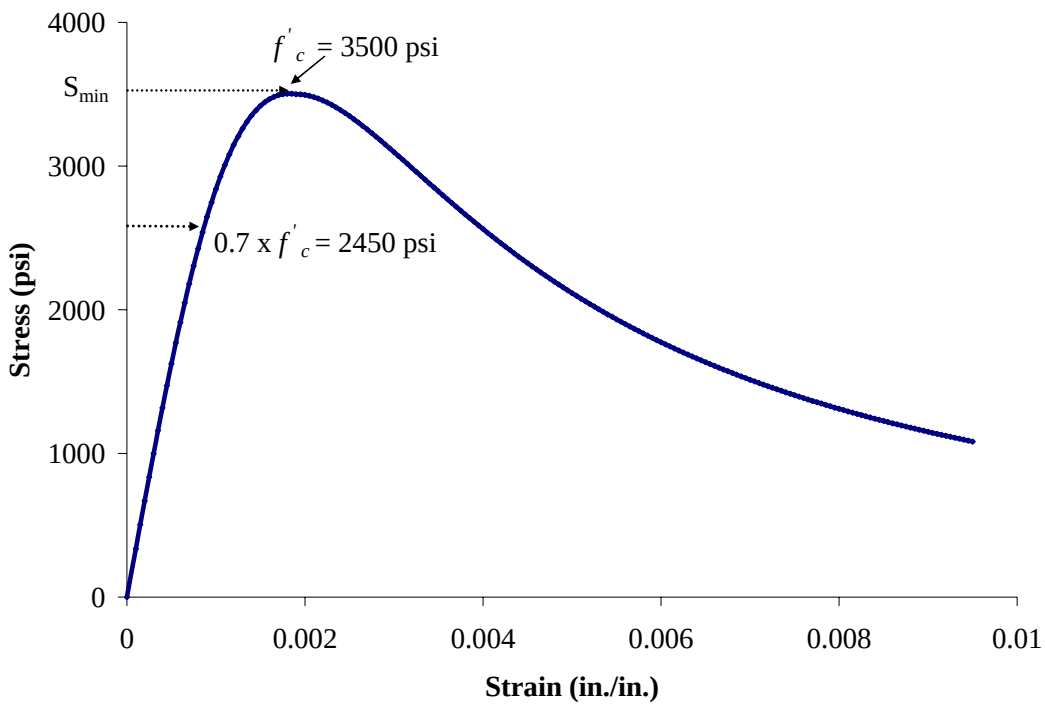

Figure 5.8: Typical uniaxial compressive strength of concrete, Collins et al (1992)

The tension stiffening stress-strain curve was developed using the fracture energy criterion, Abaqus (2004). The post failure response of concrete in the model can be defined using a stress-strain response. The post failure stress-strain response usually causes mesh sensitivity and is not recommended when there is no steel reinforcement to

arrest cracking of the concrete material. Instead, the Hillerborg (1976) approach of using fracture energy criterion to model the post failure response is used. Hillerborg defines the energy required to open a unit area of crack, G_f as a material parameter, using brittle fracture concepts. In this approach the model uses the stress-displacement response, shown in figure 5.9, instead of the stress-strain response to predict the cracking behavior of concrete. Using this concept, fracture energy, G_f, and the failure stress, σ_{t0} are defined in a tabular form. The model assumes a linear loss of strength after cracking.

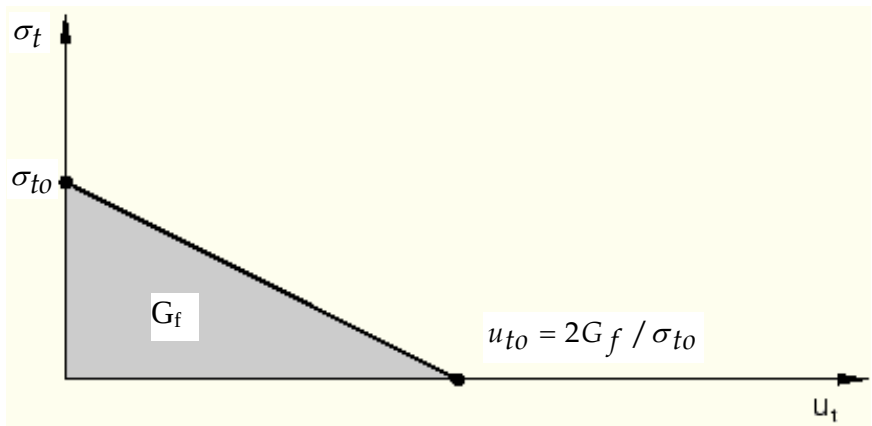

Figure 5.9: Typical Post failure Stress – Displacement curve using fracture energy criterion

Typical values of G_f range from 0.22 lb/in for normal concrete (compressive strength = 2850 psi) to 0.67 lb/in for high strength concrete (compressive strength = 5700 psi). The model calculates the strain in the element by using the elemental characteristic length. Abaqus calculates the cracking displacement at which complete loss of strength takes place using the equation, $u_{t0} = 2G_f / \sigma_{t0}$. The model then automatically converts these cracking displacement values to equivalent plastic displacement and then equivalent plastic strains using the characteristic element length. A simple analysis of the typical values obtained from laboratory split cylinder tensile tests and the G_f calculated using the respective cylinder compressive strength is shown in figure 5.10. G_f is the area under the

stress-displacement curve and its sensitivity depends on both the tensile failure stress and the uniaxial compressive strength of concrete.

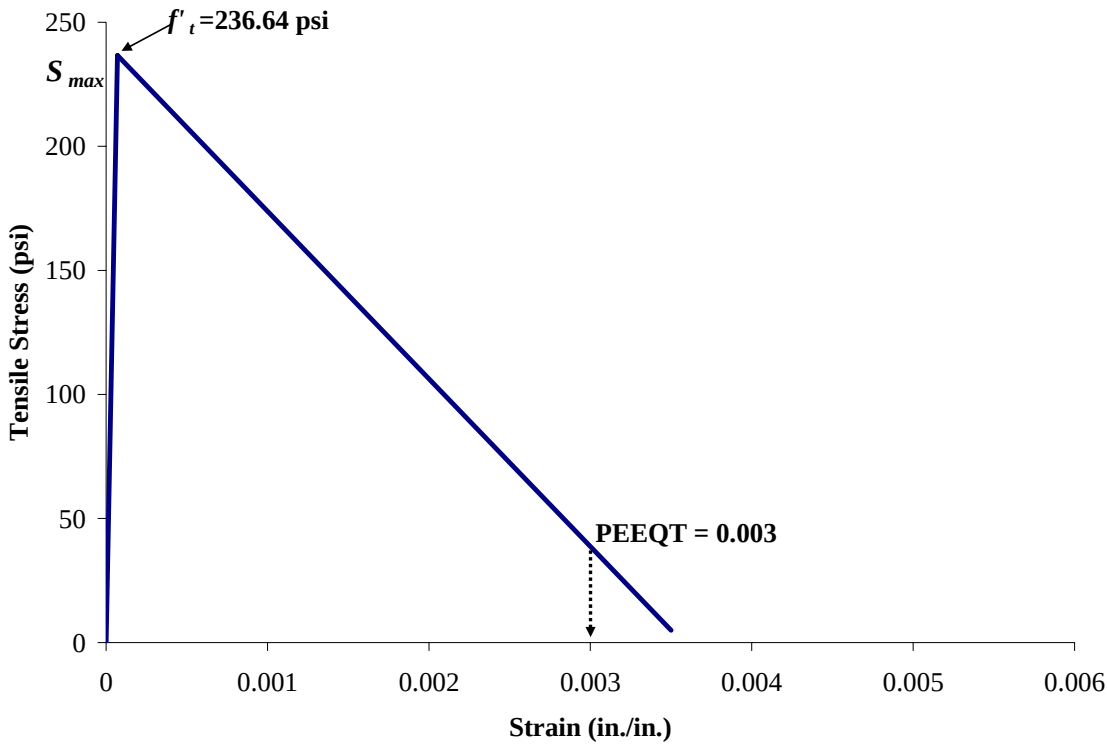

Figure 5.10: Typical tensile post failure stress-strain curves using the fracture energy criterion

The calculations for the dilation angle involved complex mathematical derivations and assumptions using the yield surface of the concrete damage plasticity model. From the data for axial and lateral stress-strain in multiaxial state given by Palaniswamy et al (1974) and Chadappa et al (1999, 2001), the dilation angle for unconfined concrete was assumed to be 15 degrees (15°). The biaxial stress ratio and the tensile-to-compressive meridian ratio were assumed to be equal to 1.16, and 0.667, respectively based on recommendations of Kupfer and Gerstle (1976) and Chen and Han (1995).

5.4.4 STEEL DOWEL BAR MATERIAL MODEL

The steel dowel bars were modeled using an isotropic elastic multiaxial material model. The elastic modulus, Es, was based on results of standard ASTM (A370-97a) uniaxial tension tests on coupons fabricated from the billet steel grade M60 dowel bars. The measured elastic modulus was equal to 29,000 ksi, the yield stress and ultimate stress were equal to 68 ksi and 94.56 ksi, respectively. The yield and ultimate stresses were not required because the results of preliminary finite element analysis indicated that the dowel bar remained elastic throughout the experimental investigation.

5.5 DEVELOPMENT OF THE DOWEL – CONCRETE INTERACTION BOND MODEL

The longitudinal and transverse interactions between the dowel bars and the concrete slabs were modeled using two models: the first model focused on the longitudinal bond between the steel and concrete due to irregularities on the dowel surface and static friction. The second model focused on the transverse interaction between the steel dowel and surrounding concrete resulting in large contact or bearing stresses and additional friction bond in the longitudinal direction due to the normal (bearing) stresses and coulomb friction coefficients. The behavior of the spring elements and contact interactions, how it was calibrated to the pullout vs. joint opening behavior is presented in the next section.

5.5.1 THE LONGITUDINAL BOND BEHAVIOR

The behavior of the pavement specimens with aligned dowels is dominated by the longitudinal bond between the dowel bars and the concrete. The transverse interaction

between the dowel bar and concrete does not participate in the behavior of the joint with aligned dowel bars. Hence the longitudinal bond behavior was calibrated using the experimental results (pullout force – joint opening data) from aligned dowel bar tests (1A, 2A and 5A) as follows. Spring elements with nonlinear force-deformation relations in the longitudinal direction were used to model the longitudinal bond between the dowel bar and surrounding concrete nodes of the finite element model. The relative displacement (joint opening) across the spring element is the change in length of the spring between the initial and current position. The pullout load vs. joint opening behavior from the experiment is converted to the average bond stress over half length (9 in.) of the dowel bar using the relation, average bond stress = pullout force / circumferential area along (π x 1.25 x 9 in^2) length. The average bond stress is then converted to the force in the spring by assuming a tributary area at the point of connectivity. The springs elements are assigned between the coinciding nodes of the dowel bar and concrete. These coinciding nodes are oriented along four diametrically opposite lines, as shown in figure 5.11 and 5.12. In the model, the force vs. the relative spring displacement is applied on both sides of the doweled joint. Typical forces in the spring elements are shown in figure 5.13.

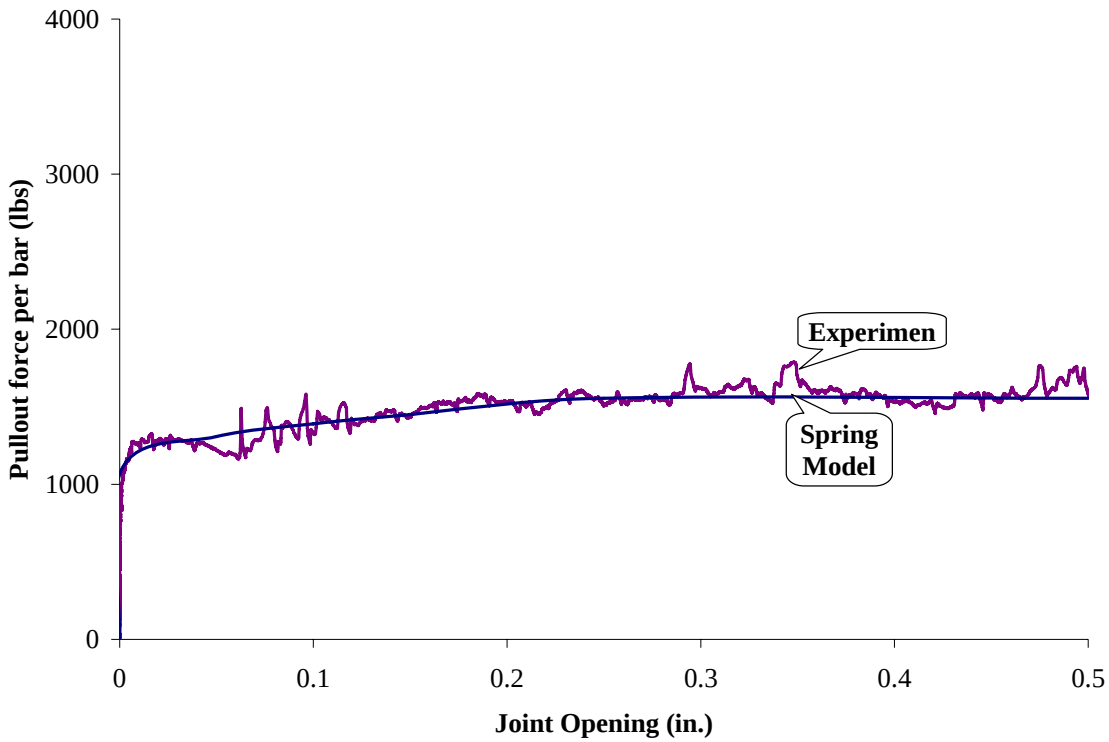

Figure 5.11: Spring model derived from the control test specimen (aligned single dowel bar).

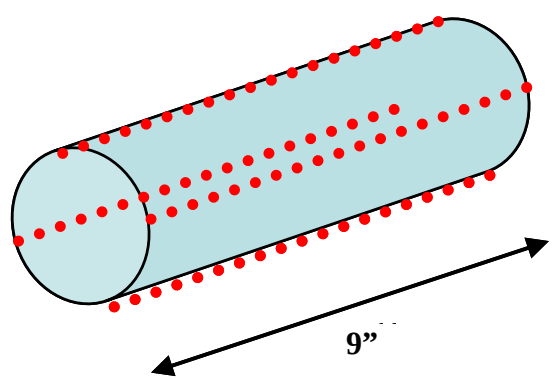

Figure 5.12: Distribution of spring forces along half length of the dowel bar

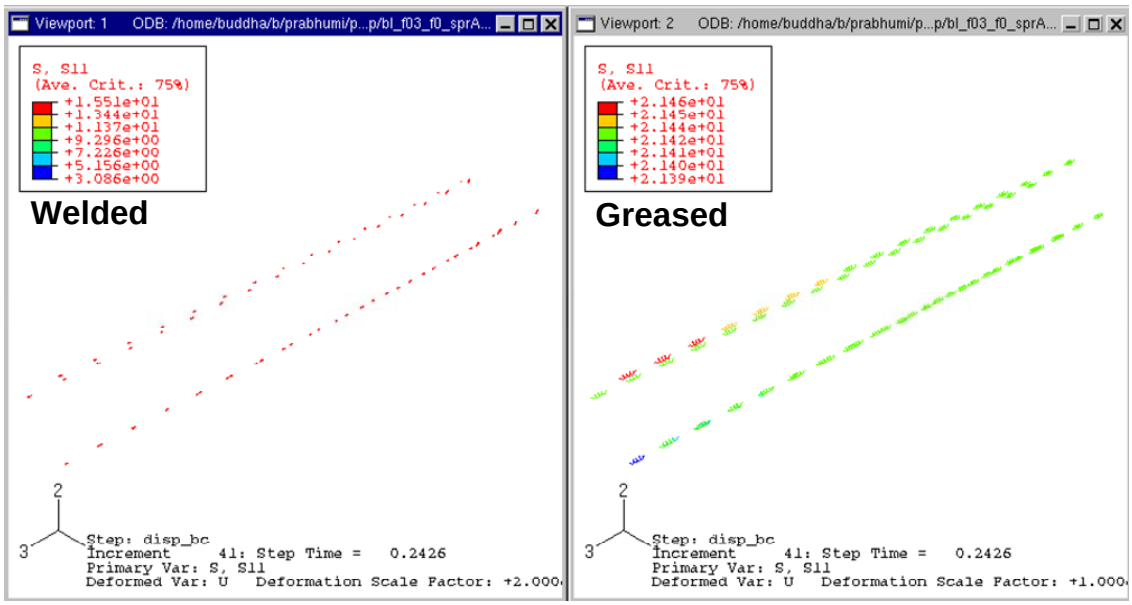

Figure 5.13: Typical spring forces (lbs) at ¼ in joint opening in the 1V18 model

5.5.2 THE TRANSVERSE INTERACTION BEHAVIOR

The second model focuses on the transverse interactions between the steel dowel, the concrete slab and the resulting frictional bond. The transverse interaction was modeled using special surface-to-surface contact elements. These elements model hard contact behavior with coulomb friction. The hard surface contact results in large bearing (normal) stresses at contact locations, and the coulomb friction model permits slip only if the applied shear is greater than the normal stress multiplied by the friction coefficient. Thus, the transverse interaction model includes additional longitudinal bond resulting from coulomb friction and large localized bearing stresses.

Two cases of coefficient of friction were considered for the greased and uncoated side of the dowel bar. In each misalignment model study, two cases with different input parameters were considered. Case I correspond to the use of idealized friction coefficients (0.0 and 0.3 on the greased and uncoated sides, respectively) and idealized

material properties (uniaxial compressive strength (f'_c) of 3500 psi & tensile strength (f'_t) of 236 psi. Case II corresponds to the use of friction coefficients measured by Shoukry *(2003)* (0.076 and 0.384 for greased and ungreased sides, respectively) and measured material properties of the hardened concrete specimens collected during actual laboratory tests. The idealized (Case I) and measured (Case II) compressive and tensile strengths and frictional coefficients for the various cases is shown in Table 5.1

Table 5.1: Case I and Case II input parameters for the various models

	Case I	Case II
• Uniaxial Compressive Strength (f'_c)	3500 psi	Data obtained from cylinder tests (Appendix A)
• Tensile Strength (f'_t)	236.64 psi	
• Friction coefficient on greased side	0.0	0.076
• Friction coefficient on welded side	0.30	0.384

5.6 LIMITATIONS AND SHORT COMINGS OF THE FE MODEL

The pullout force per dowel-joint opening behavior of all specimens consisted of two regions: an initial fully bonded region and a post-slip debonded region. The initial bond (corresponding to the debond stress τ_b) is caused by a variety of reasons including chemical adhesion, mechanical interlock between the dowel surface and concrete, shrinkage of concrete around the dowel bars, etc. This initial bond behavior can be highly variable depending on the concrete mix design, water content, surface finish of the dowel bar, friction between dowel surface and surrounding concrete, and various other parameters. Figure 5.14 shows the variation of the initial debond stress (τ_b) for various pavement specimens. This variability in the initial debond stress is typical for longitudinal bond between steel (embedded) and concrete. It is difficult to model

deterministically due to the variable nature of the problem. Probabilistic or stochastic modeling was beyond of the scope of the research.

The analytical approach consisted of using the experimental results for pavement specimens (1A, 2A, and 5A) with fully aligned dowel bars to define the spring model for the longitudinal bond between the dowel surface and the concrete. The underlying assumption is that specimens with no misalignment have only longitudinal bond behavior. There is no transverse (bearing) interaction and corresponding friction addition to the longitudinal bond of these specimens.

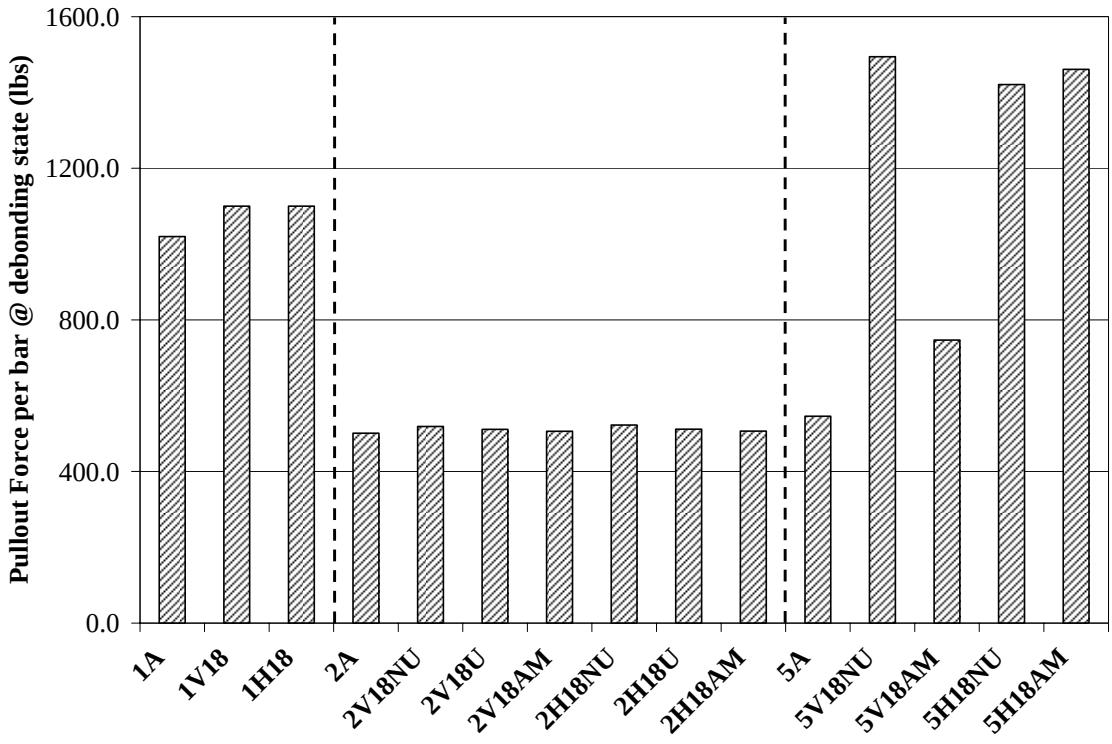

(a) Pullout force per bar just at debonding

Figure 5.14: Summary of the Pullout force per bar at debonding limit state (A) and the debonding stress for the aligned and misaligned test cases

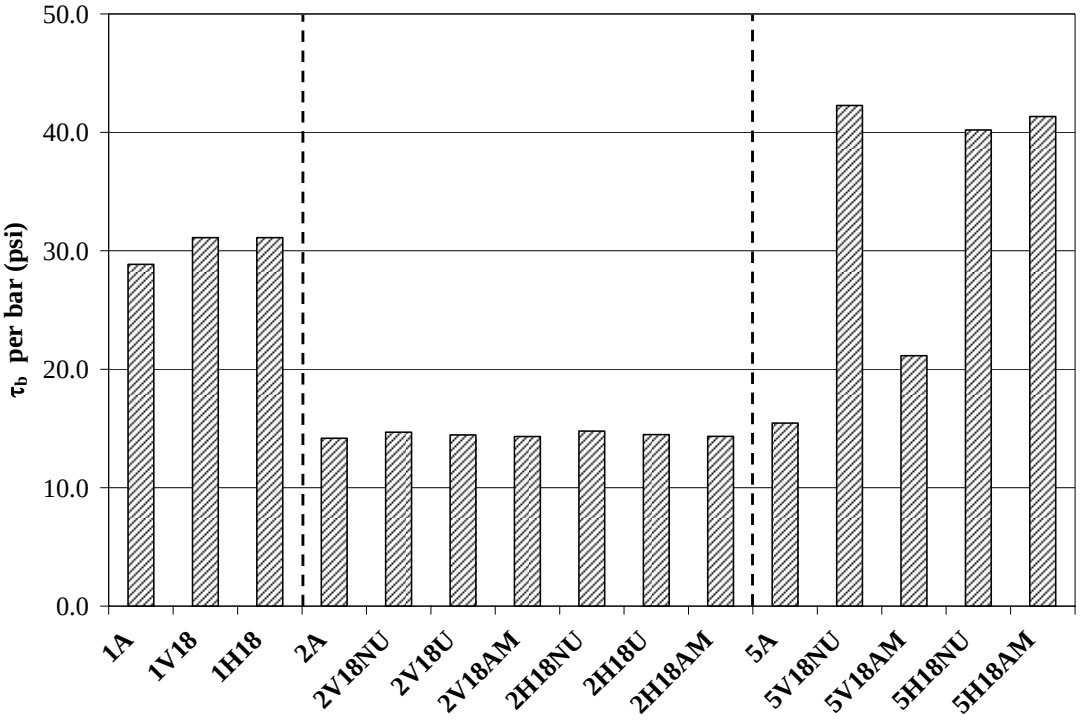

(b) Debonding Stress in the dowel bar

Figure 5.14 (cont'd).

The 3D finite element models were developed using ABAQUS, a commercially available FEA software. The experimental results were used to define the model input parameters, for example, (i) the longitudinal bond was defined using the results for specimens with aligned bars, (ii) the steel and concrete material properties were defined based on material test results, and (iii) the friction coefficient between the dowel surface and surrounding concrete were defined using the experimental results of Shoukry et al (2003). These models were used to predict the joint opening behavior of the specimens with misaligned dowel bars with different misalignment type, magnitude, and distribution. The joint opening behavior results predicted for these specimens were compared directly with the experimental results, without any additional modification or calibration.

The comparisons focused on the overall pullout force per dowel-joint opening behavior predicted by the models and measured experimentally. The localized multiaxial stresses and strains computed by the models at the sites of stress concentration could not be verified because the corresponding measurements were not performed during the experiments. These stress concentration sites are located inside the concrete specimens at the interface of dowel and concrete. The sensors required to measure such local stresses and strains were not embedded in the specimens. Additionally, non-destructive techniques were not used to monitor the formation of distresses within the concrete specimens at the dowel-concrete interfaces. These are major limitations of the experimental approach used in this research, and should be addressed by future research.

It is important to note that pavement joint opening occurs due to thermal movements induced by changes in ambient conditions. It is a cyclic, time-varying phenomenon that depends completely on the weather (ambient) conditions. This research does not consider the effects of: (i) joint locking due to thermal gradients, (ii) friction at the base of the pavement specimens from the underlying base layers, or (iii) cyclic joint opening behavior. This is a major limitation of the research project.

Since joint opening is a cyclic, time-varying phenomenon, the problem becomes one of cyclic material fatigue at the distress (stress concentration) locations. This was not the focus of the research. The fatigue stress or strain – life relationships for pavements with misaligned dowel bars have not been addressed or developed. This is a major limitation that needs future research.

5.7 LOADING AND BOUNDARY CONDITIONS

The loading and boundary conditions are designed to simulate the experimental behavior of the tested specimens. They are applied in two steps. The first step applies loads due to the dead load (gravity load / self weight) of the two sides of the concrete slab and the dowel are applied as body force and the concrete base is assumed to be fixed from translation, as shown in figure 5.15. This step is used to generate the appropriate contact forces between the dowel and concrete interfaces and activate the Coulomb friction model. The second step uses a displacement control approach to pull each side of the pavement specimen in the opposite direction by 0.25 in., thereby giving a total joint opening of 0.5 in. In this step, the model is supported and restrained from out of plane movements, using support (roller) lines, as shown in figure 5.16.

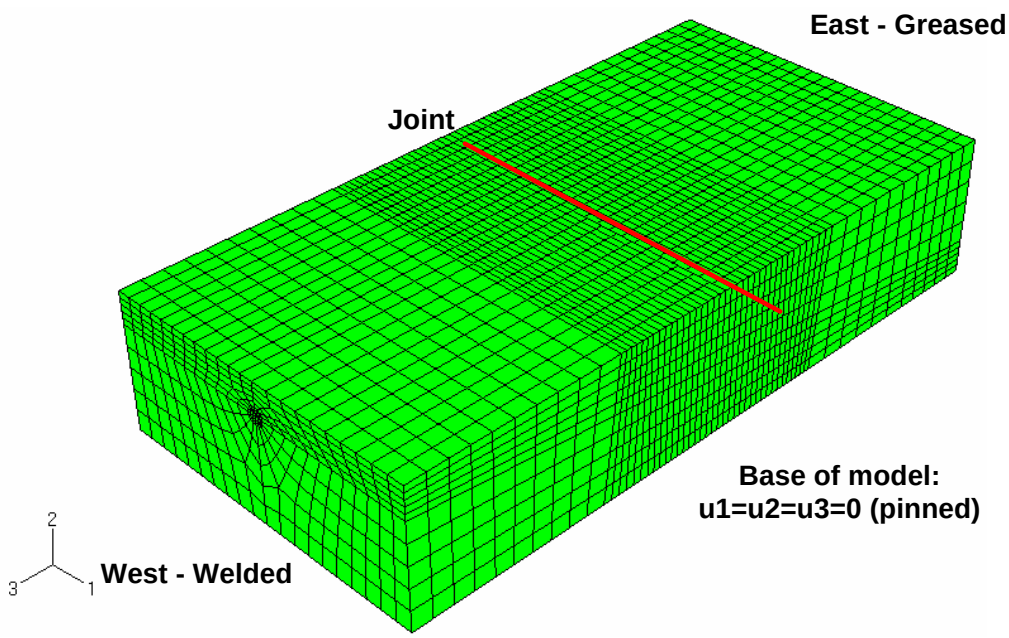

Figure 5.15: Step I – Dead (gravity / self weight) Load due to the concrete and dowel

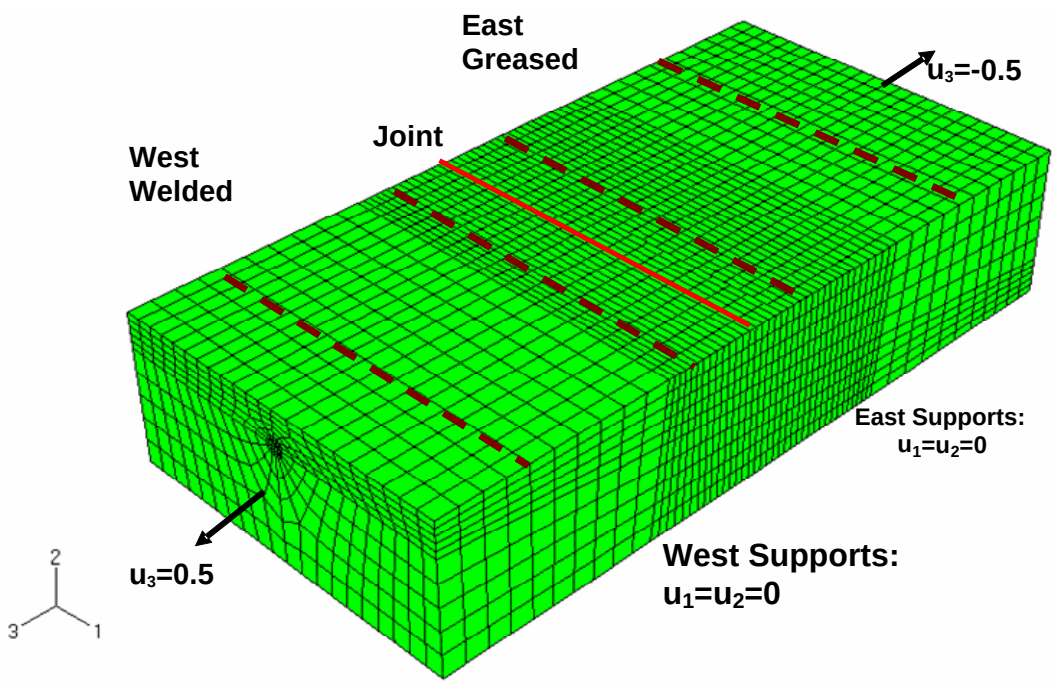

Figure 5.16: Step II – Displacement Control step simulating joint opening

5.8 THE 3D FINITE ELEMENT MODEL RESULTS

The results from the 3D finite element analyses include the pullout force-joint opening behavior of the concrete specimens and the complex state of multiaxial (3D) stresses and strains in the model. Figure 5.17 compares the experimental and analytical pullout force-joint opening behavior for the single dowel specimens. These specimens are listed in table 4.1 (a). Figures 5.18 and 5.19 compare the experimental and analytical pullout force-joint opening behavior for specimens with two dowels misaligned vertically or horizontally, respectively. Similarly, figures 5.20 and 5.21 compare the experimental and analytical pullout force-joint opening behavior for specimens with five dowels misaligned vertically or horizontally, respectively. In Figures 5.17 through 5.21, Cases I and II correspond to the use of idealized and experimentally established static friction coefficients and material properties as explained earlier. In several cases, the post slip

behavior of the pullout force obtained from the analyses using case I and II parameters bound the dowel pullout force obtained from the experiments.

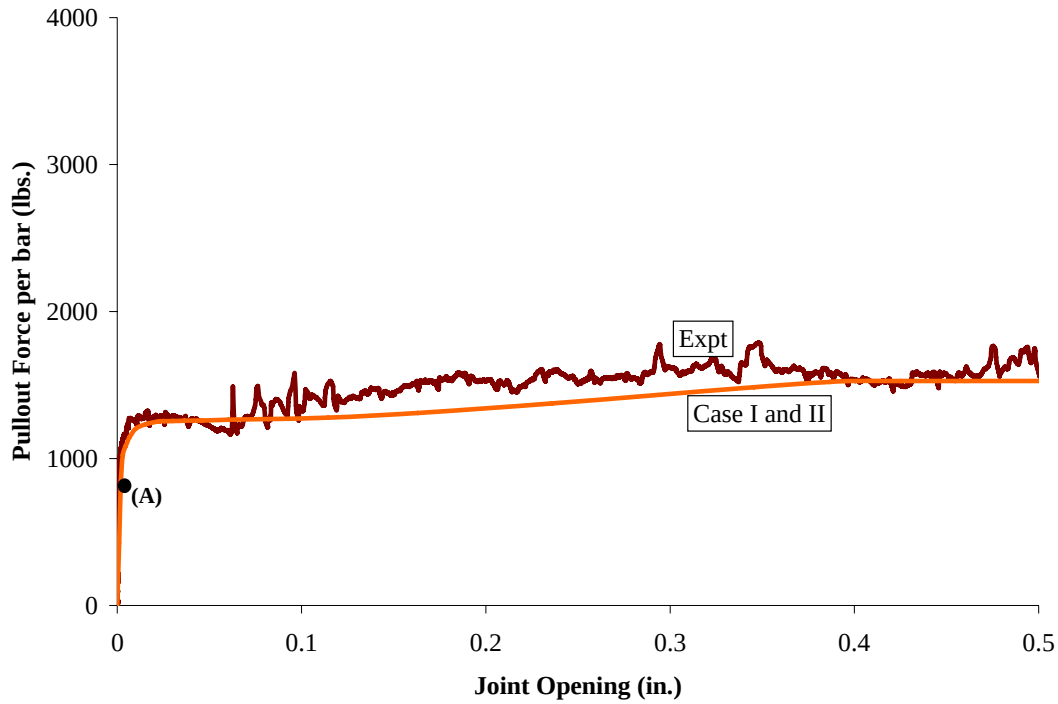

(a) Comparison of 1A model

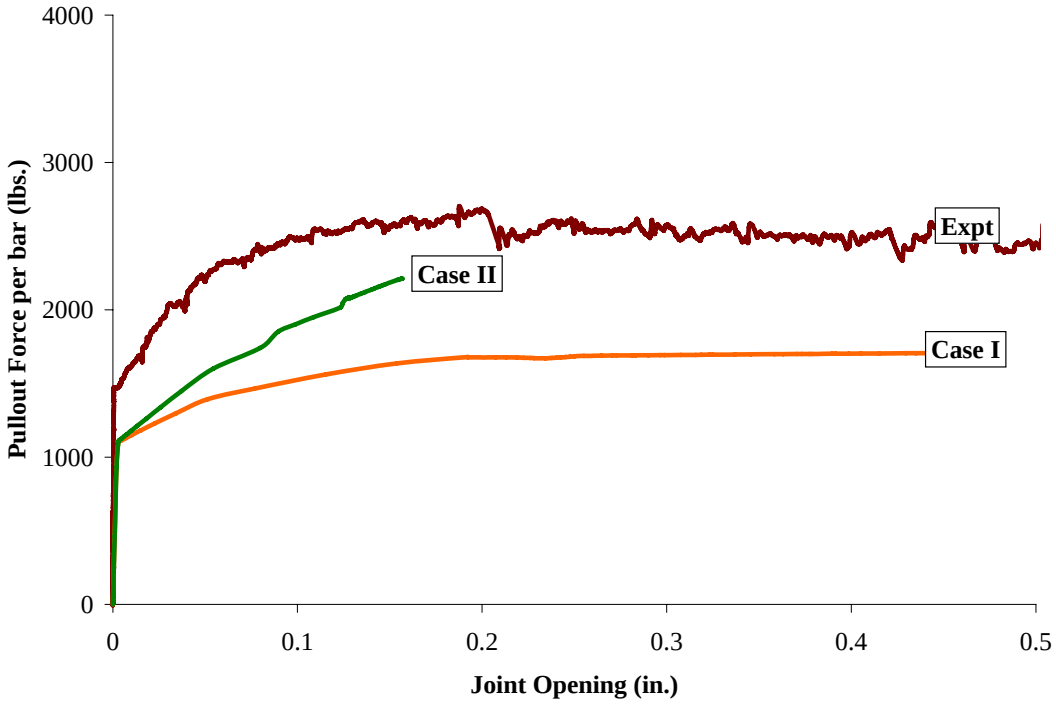

(b) Comparison of 1V18 model

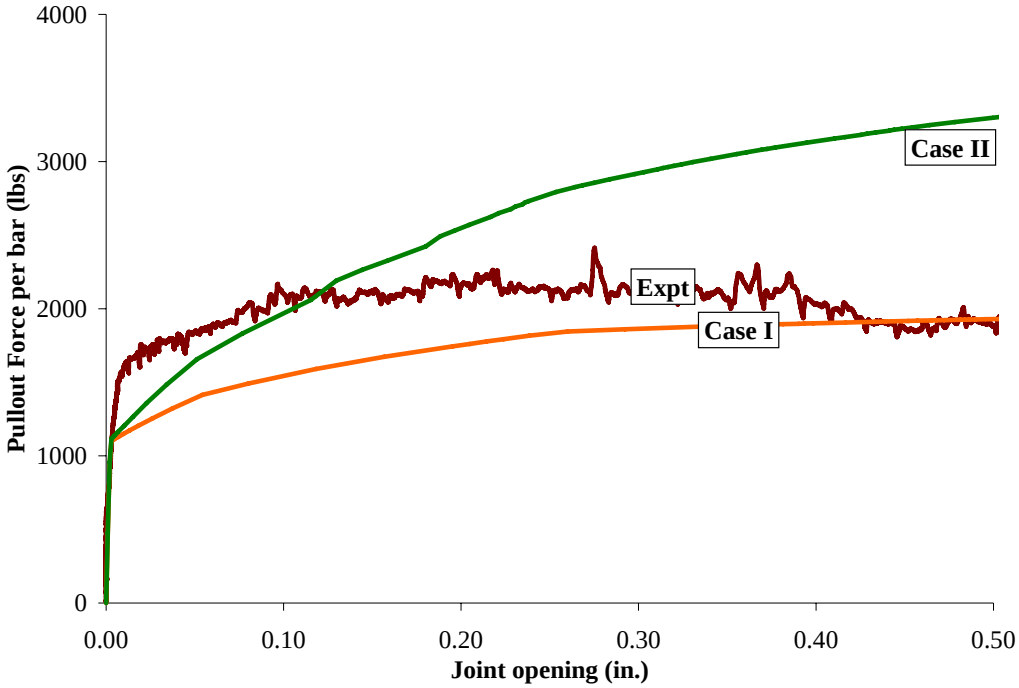

(c) Comparison of 1H18 model

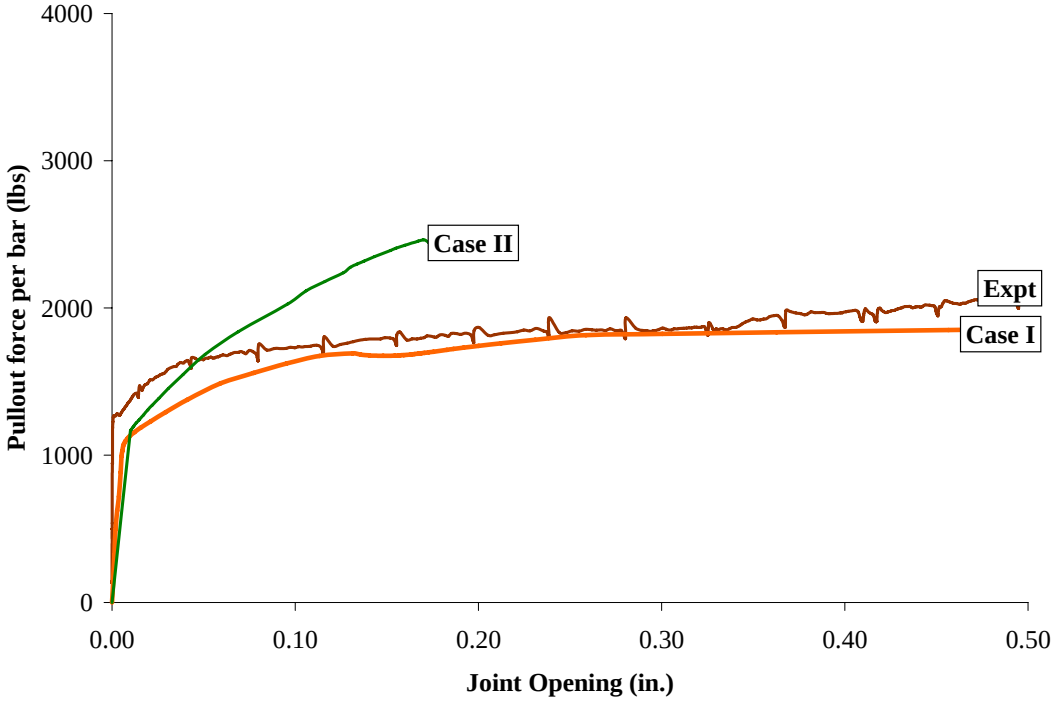

(d) Comparison of 1C18 model

Figure 5.17: Comparison of finite element results and experimental data for a single misaligned 1/18 radians dowel bar.

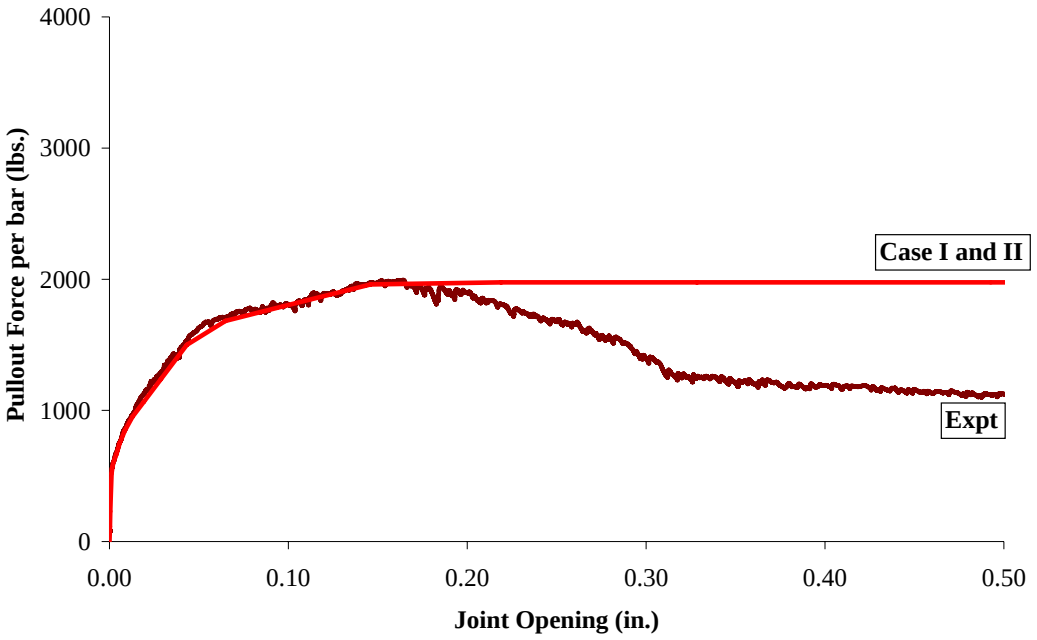

(a) Comparison of 2A model

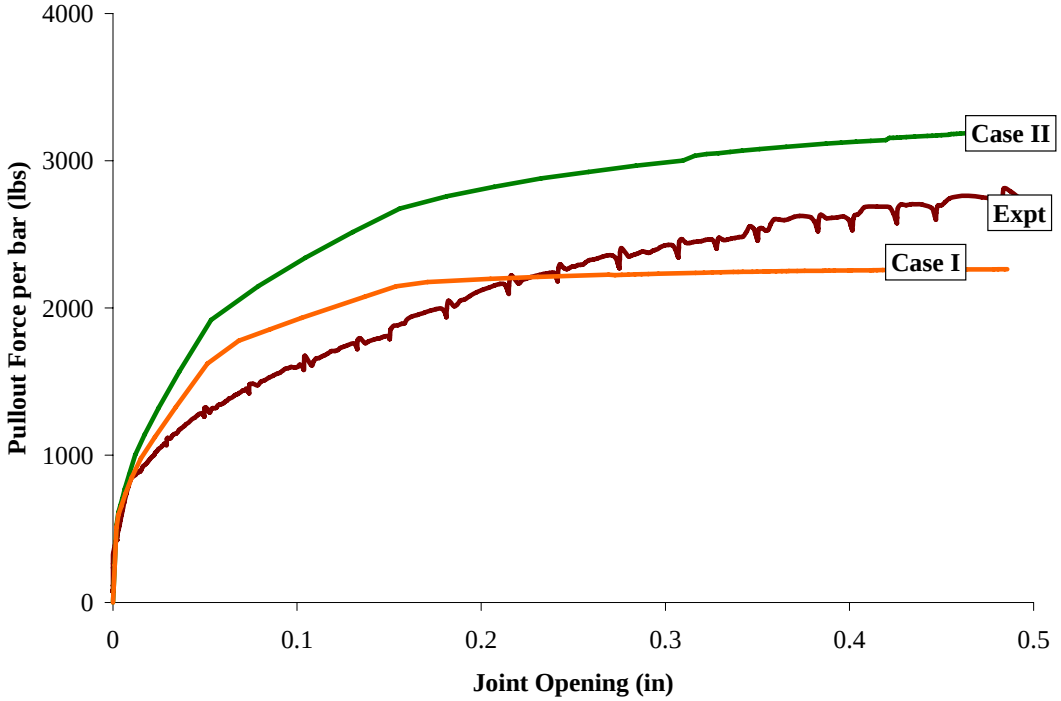

(b) Comparison of 2V18NU model

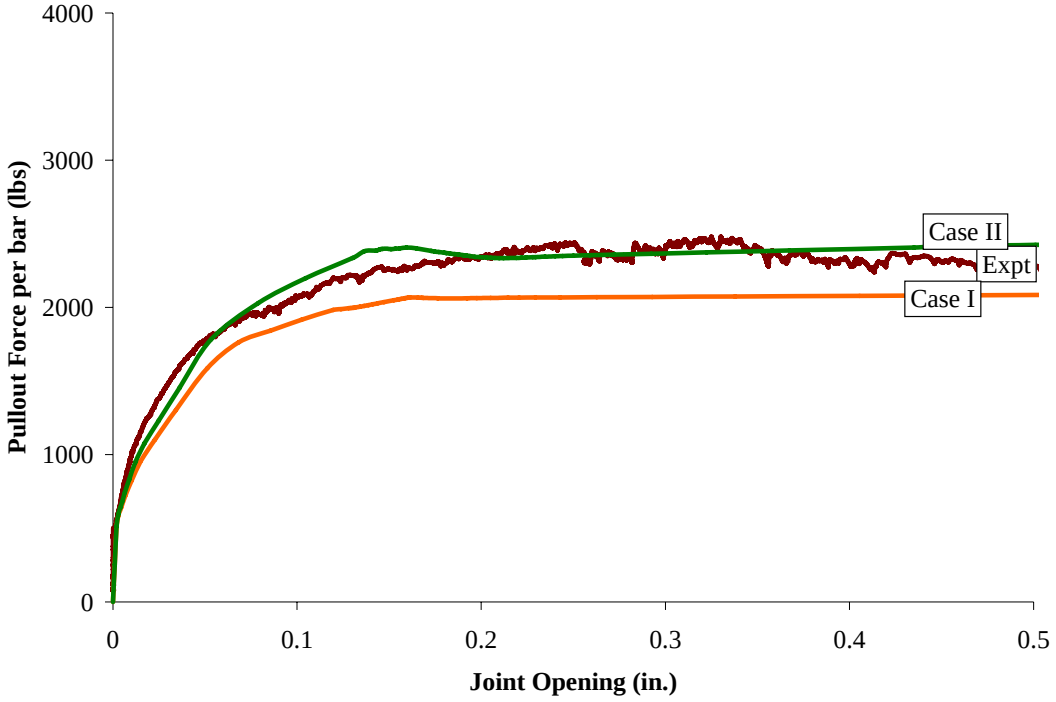

(c) Comparison of 2V18U model

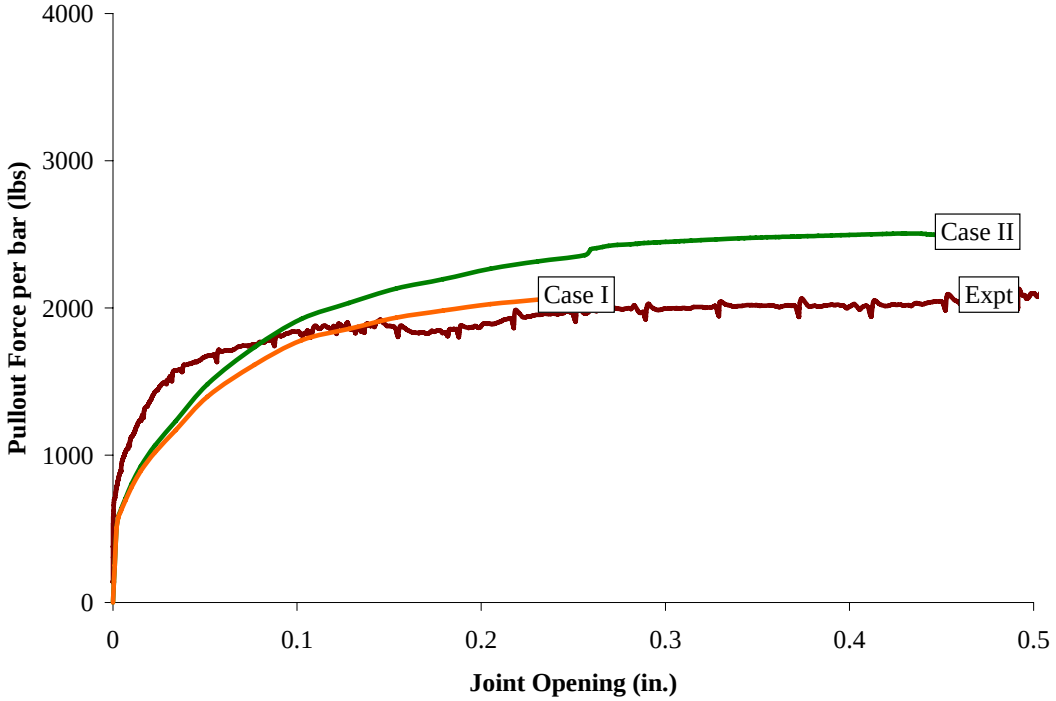

(d) Comparison of 2V18AM model

Figure 5.18: Comparison of finite element results and experimental data for two vertically misaligned 1/18 radians dowel bar.

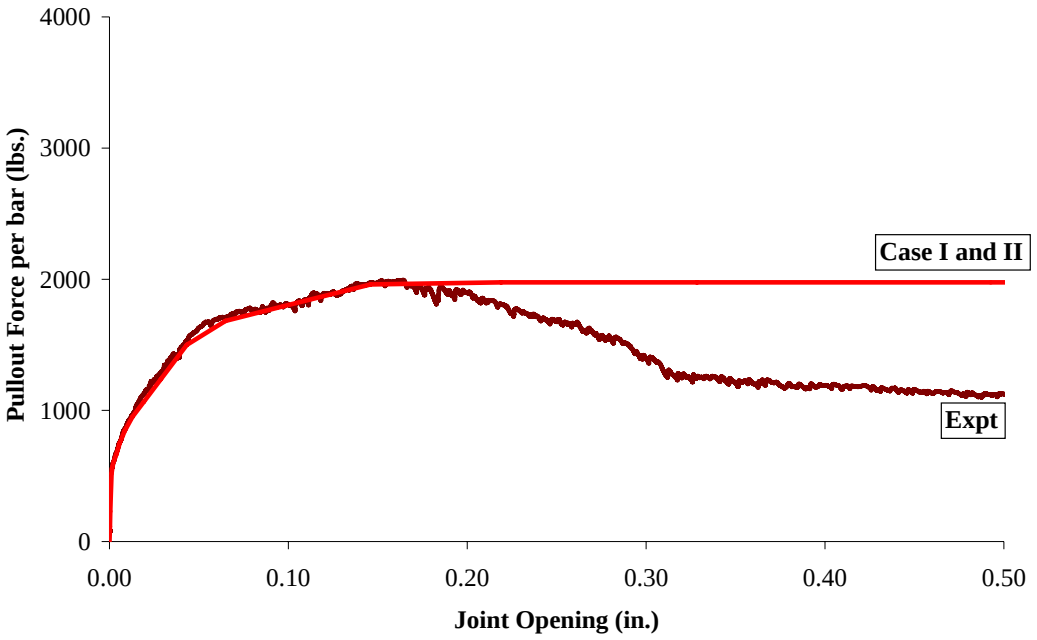

(a) Comparison of 2A model

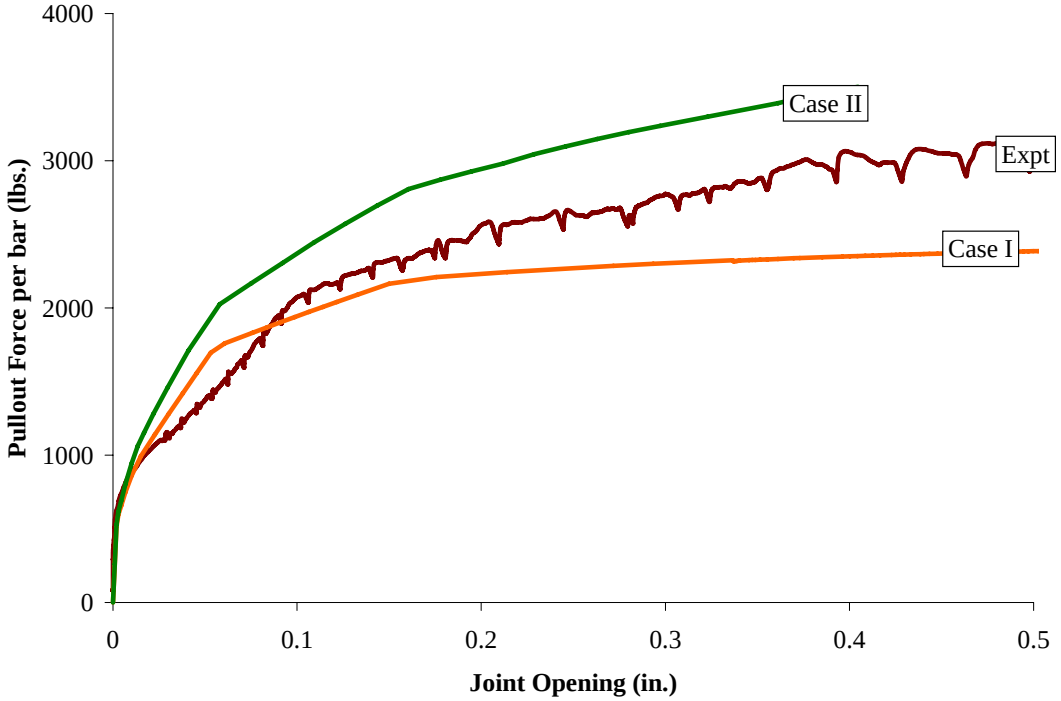

(b) Comparison of 2H18NU model

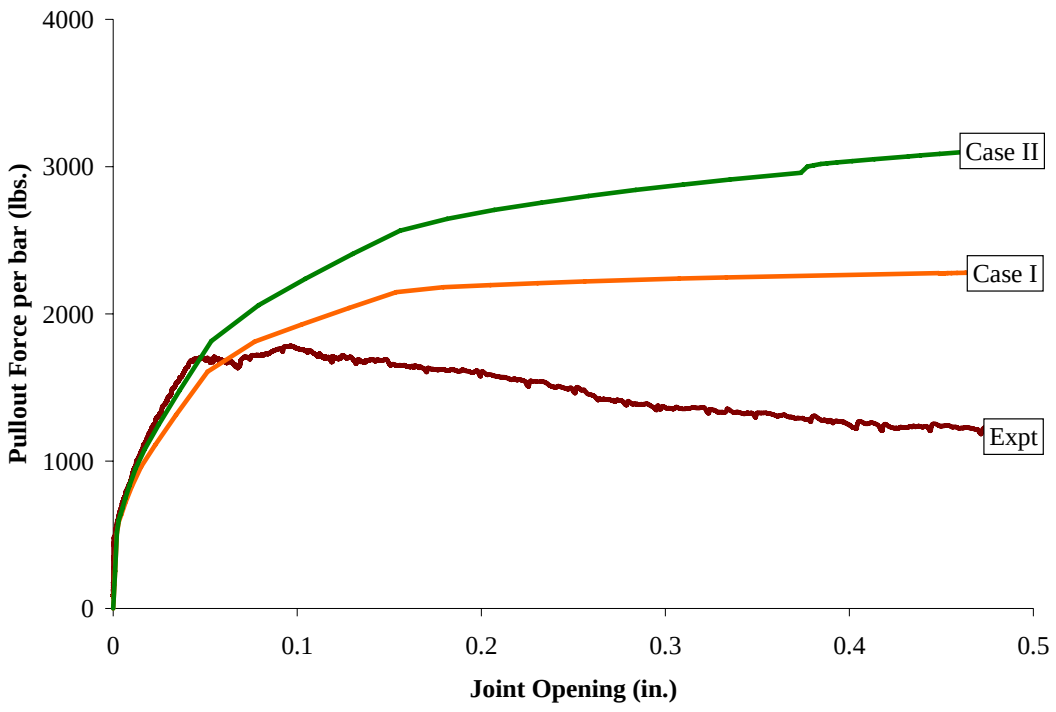

(c) Comparison of 2H18U model

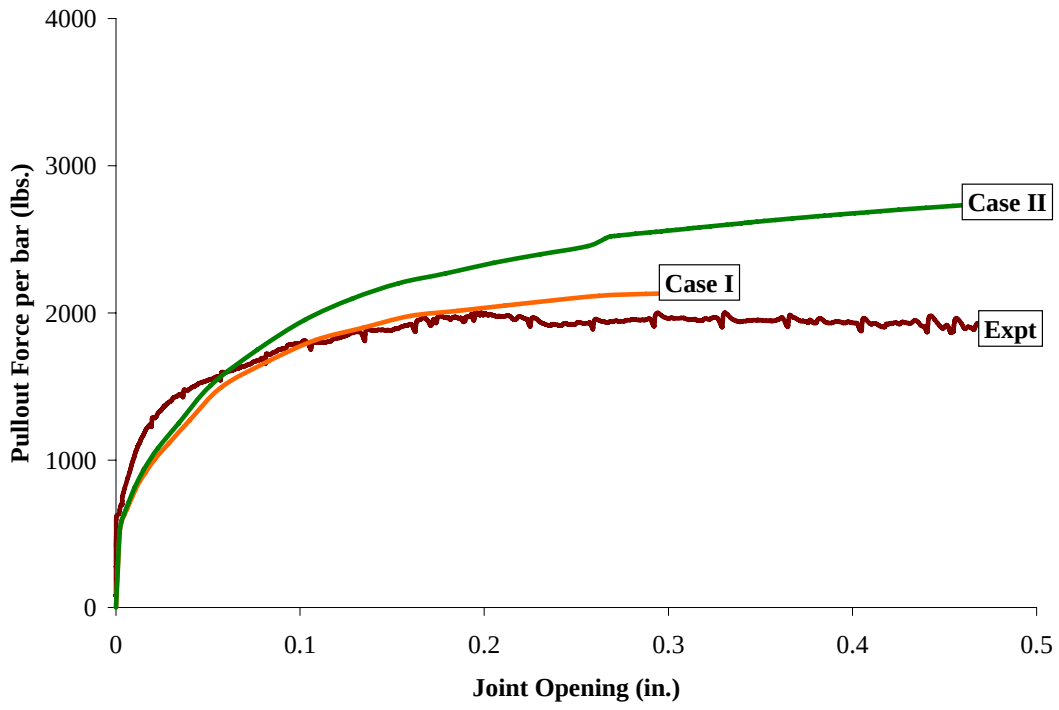

(d) Comparison of 2H18AM model

Figure 5.19: Comparison of finite element results and experimental data for two horizontally misaligned 1/18 radians dowel bar.

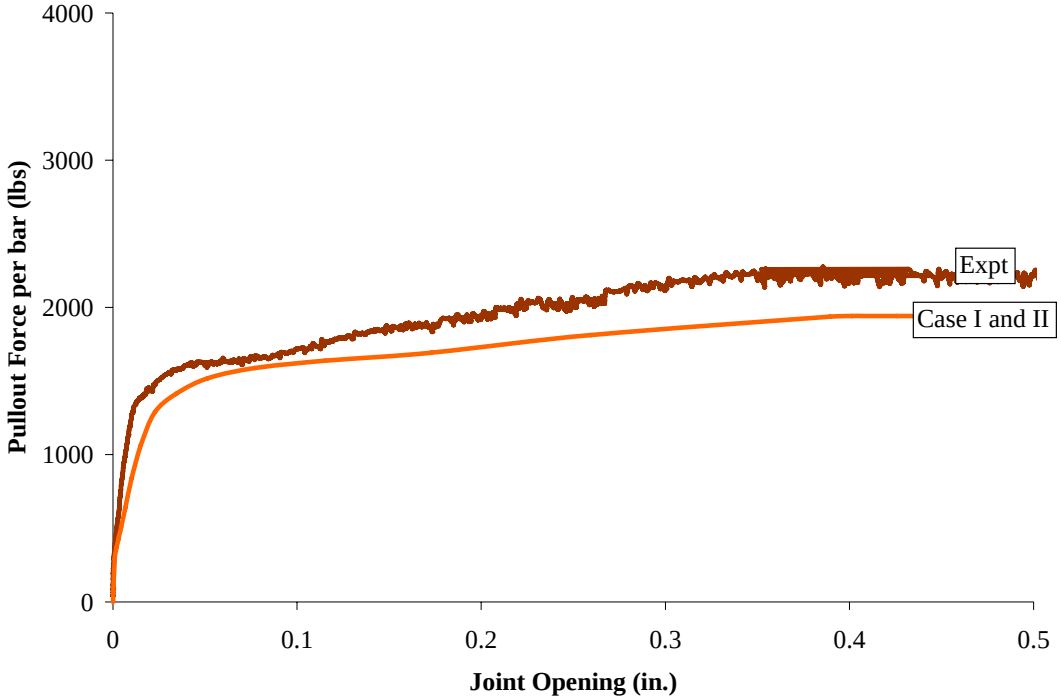

(a) Comparison of 5A model

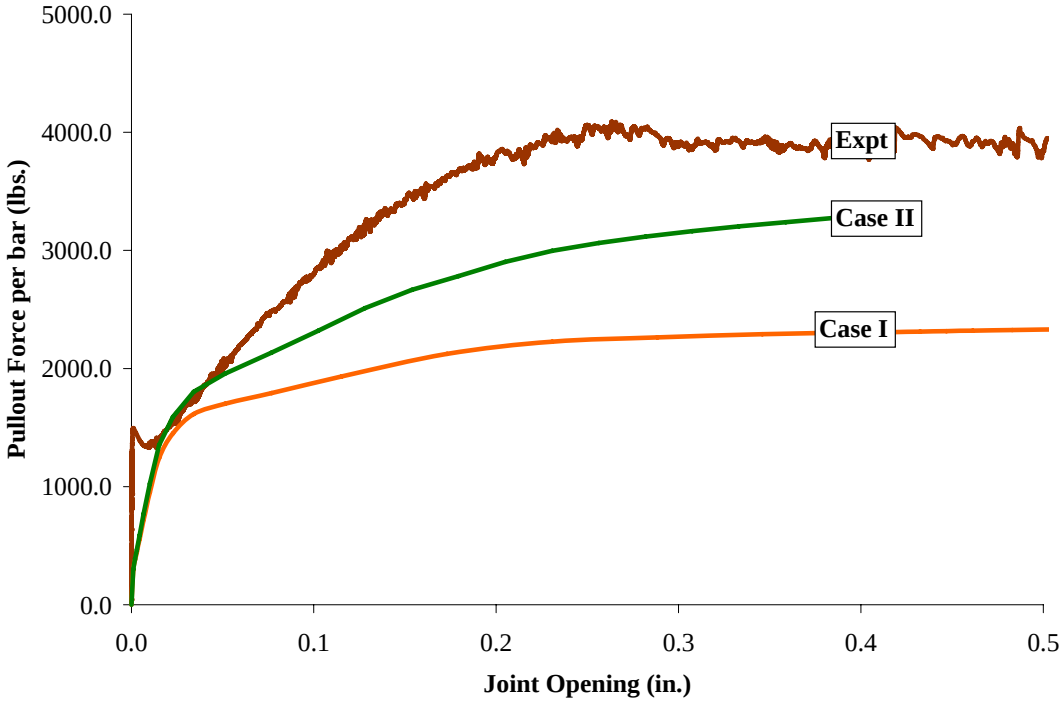

(b) Comparison of 5V18NU model

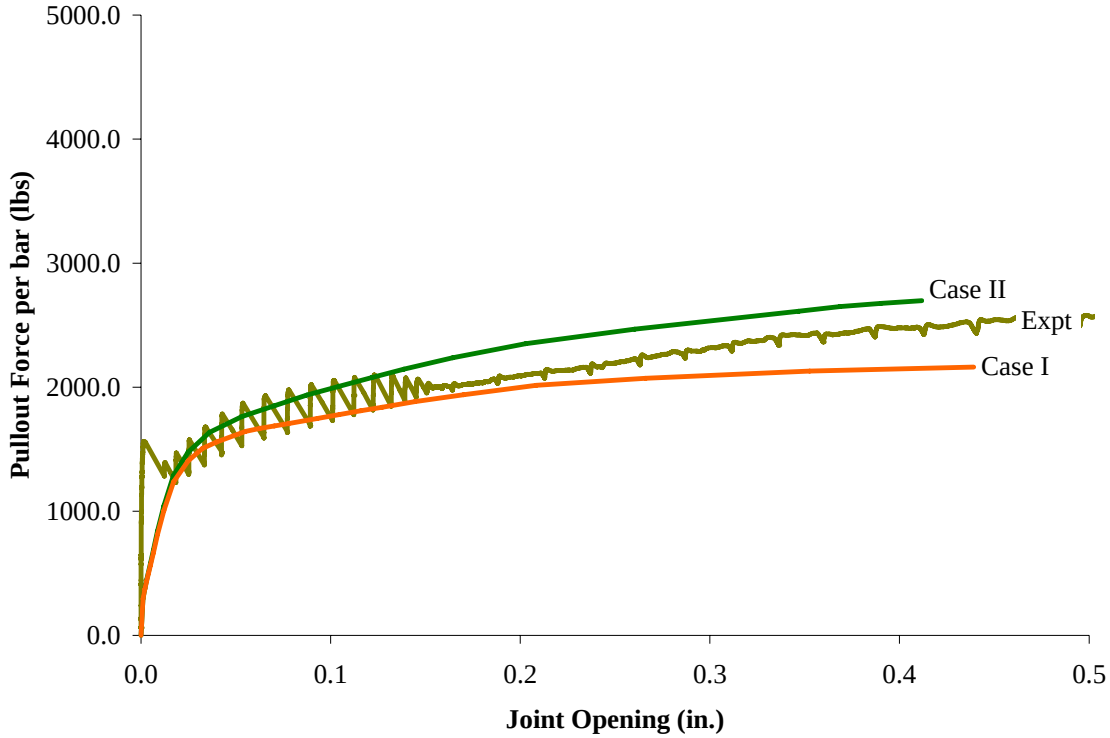

(c) Comparison of 5V18AM model

Figure 5.20: Comparison of finite element results and experimental data for five vertically misaligned 1/18 radians dowel bar.

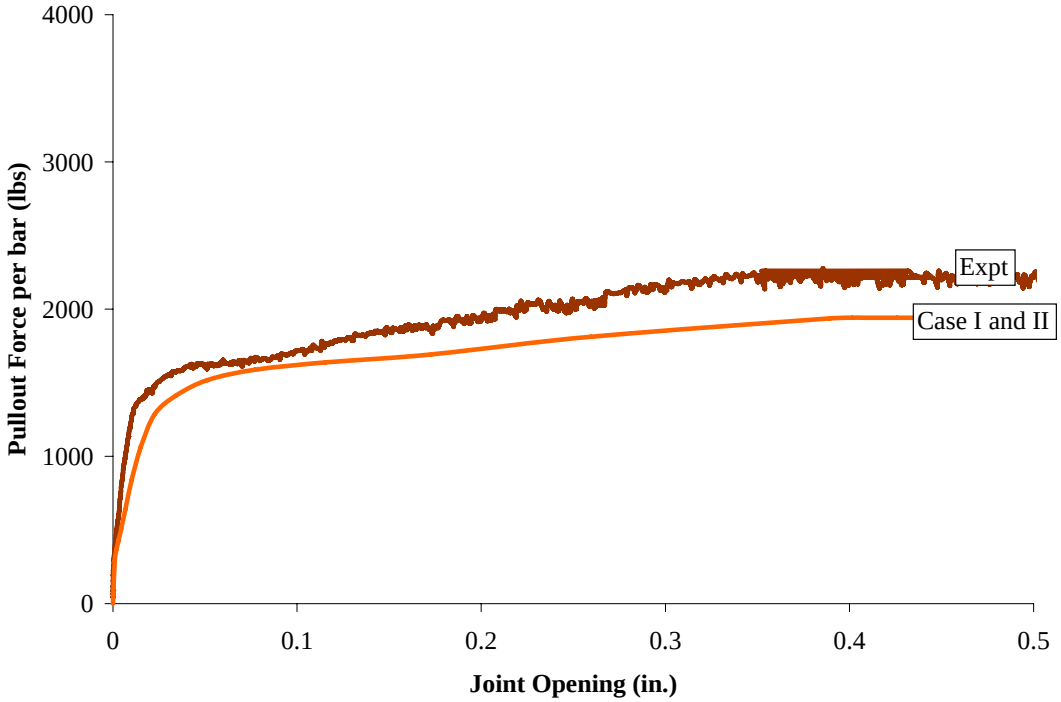

(a) Comparison of 5A model

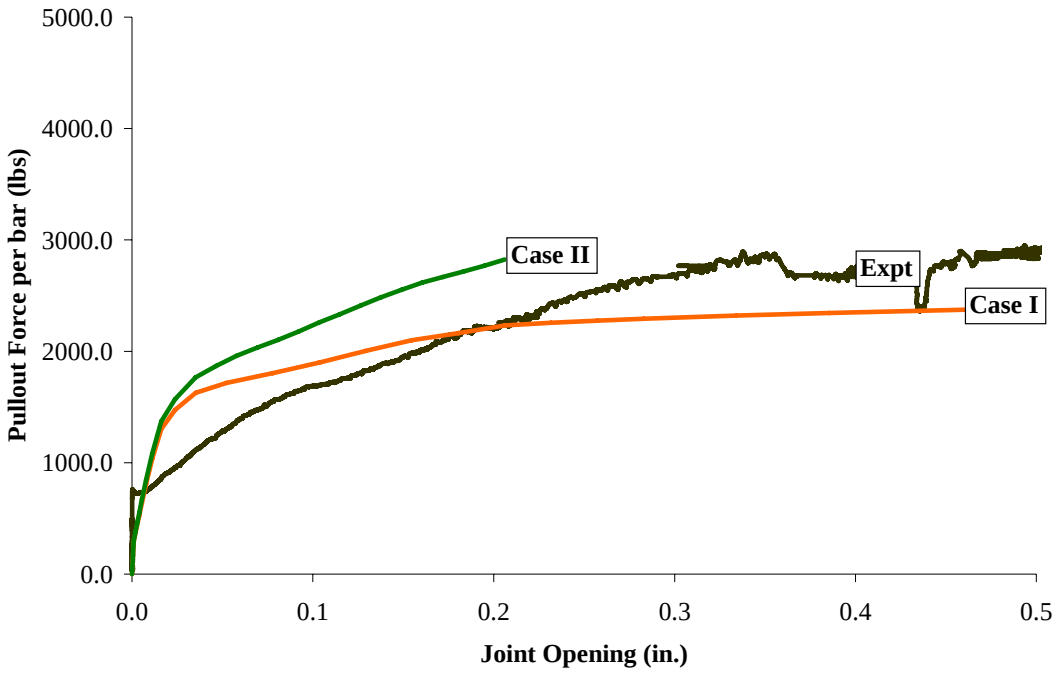

(b) Comparison of 5H18NU model

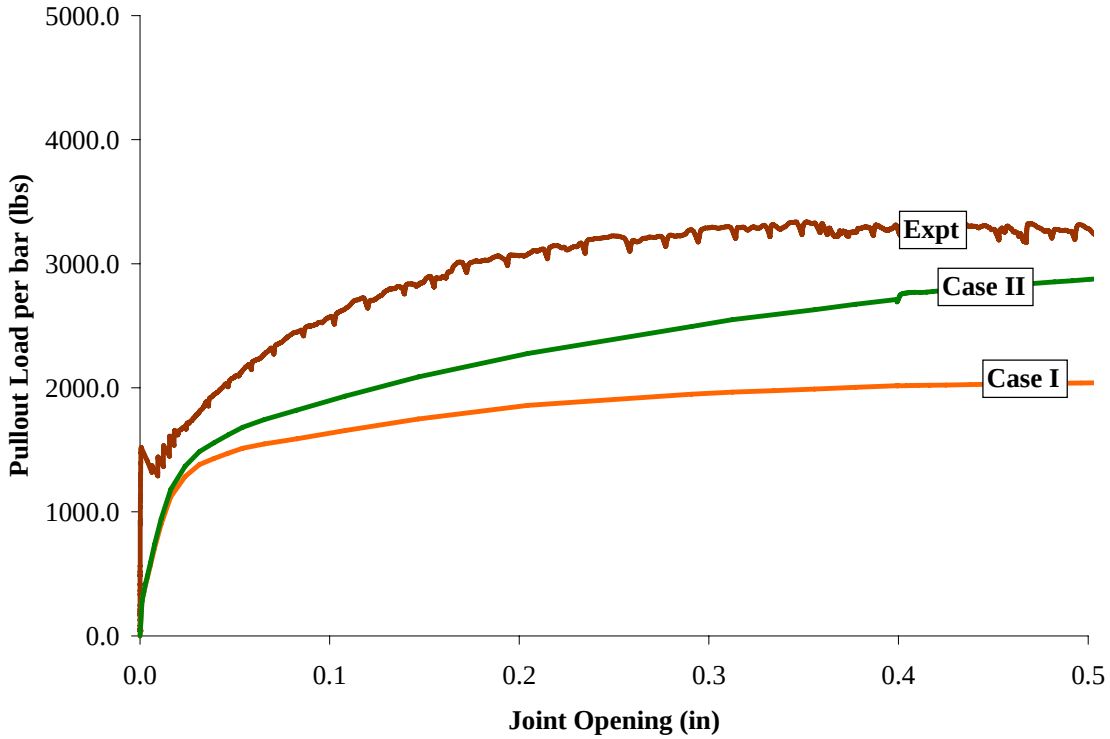

(c) Comparison of 5H18AM model

Figure 5.21: Comparison of finite element results and experimental data for five horizontally misaligned 1/18 radians dowel bar.

In all the finite element models, stress concentration zones occurred in the concrete at the joint face around misaligned dowel bars. For example, Figure 5.22(a) shows the stress concentrations in the test specimen, 2V18NU with non-uniformly misaligned dowel bars. Figure 5.22(b) shows the stress concentrations around test specimen, 2V18AM with alternate misaligned dowel bars. The joint opening in both cases is 0.05 in with case I input parameters.

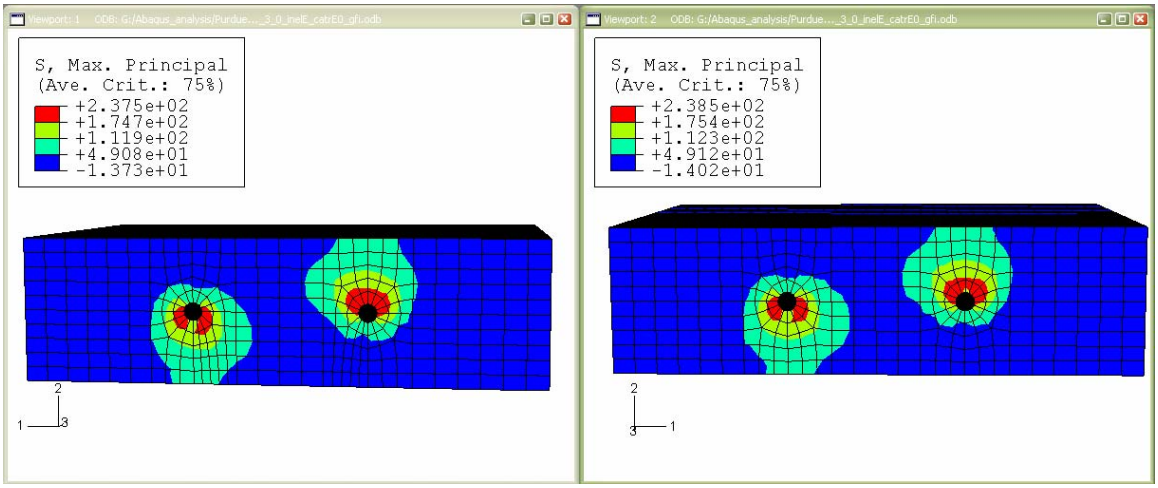

(a) S_{max} Stress contours at the face of the joint for the 2V18NU model

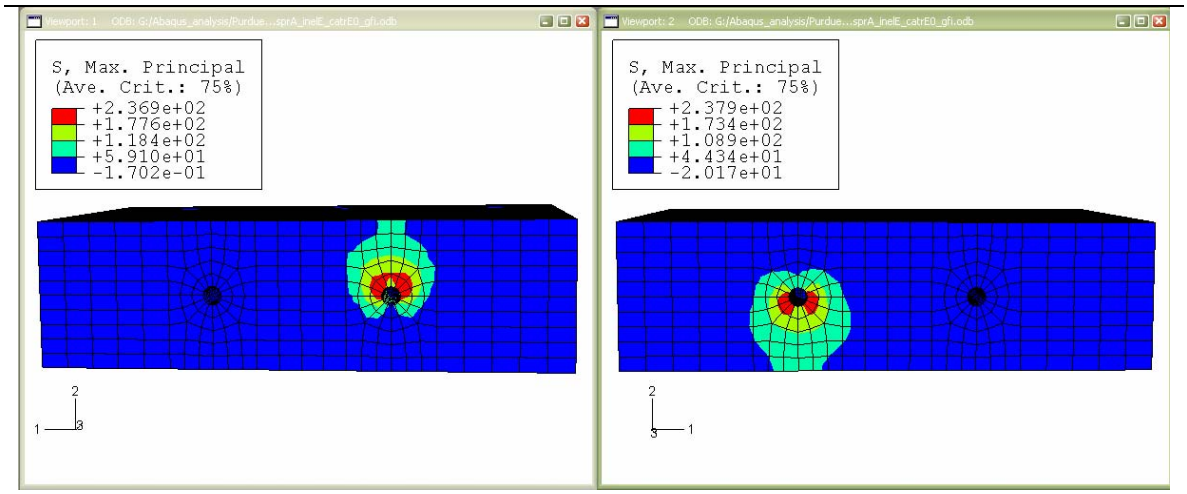

(b) S_{max} Stress contours at the face of the joint for the 2V18AM model

Figure 5.22: Typical stress contours at material damage / limit state (C) in the FE model for Case I input parameters at 0.05 in. joint opening

5.9 CONCLUDING REMARKS

The comparisons in figures 5.17- 5.21 indicate that the analytical results compare favorably with the experimental results. Cases I and II generally bound the experimental results. However, neither the experimental nor the analytical pullout force-opening curves provide insight or knowledge regarding the 3D stress states and limit states or distress in the concrete pavement specimens. Hence, the analytical results (3D stresses and strains) from the finite element analyses were evaluated further to identify significant limit states and distresses in the concrete pavement joints. The protocol for defining the material failure / limit states is further explained in chapter 6.

CHAPTER 6

THREE DIMENSIONAL FINITE ELEMENT ANALYSIS RESULTS

6.1 INTRODUCTION

This chapter identifies the various events, i.e., the material damage limit states that occur in the pavement specimen models during the analysis. These events are identified using the analytical results and indicated on the predicted force-joint opening responses to help understand evolution of behavior. This chapter also presents the results from the analytical parametric studies including the overall force-joint opening responses and the events that occur at the dowel-joint interface. All the analytical results and experimental results from chapter 3 were used to establish limits for dowel misalignment.

6.2 MATERIAL EVENTS OR DAMAGE LIMIT STATES

The analytical results (3D stresses and strains) from the finite element analyses were used to identify significant events or damage limit states occurring in the concrete material at the dowel-pavement interface.

The following events or damage limit states were identified based on the material 3D stress state results:

(A) Debonding / initial slip state (τ_b)

(B) Onset of concrete material inelasticity or cracking

(C) Maximum principal stresses (S_{max}) exceeds the concrete tensile (f'_t) strength

(D) Minimum principal stresses (S_{min}) exceeds the concrete compressive (f'_c) strength

(E) Significant crushing (compressive inelastic strains)

(F) Significant cracking (tensile cracking strains).

These events / damage limit states are indicated on the analytically predicted pullout force-joint opening behavior plots and are further explained below.

Event (A) Debonding / Initial slip state (τ_b) - The debonding / initial slip state (τ_b) is defined as the point where debonding occurs between the dowel and the concrete slab and the joint opening begins. The initial joint opening is approximately 0.003 in. This is the only limit state corroborated by experimental measurements and analytical results. It should be noted that the debonding state is a change in longitudinal bond from sticking to slipping or static to kinematic bond, as shown in figure 6.1.

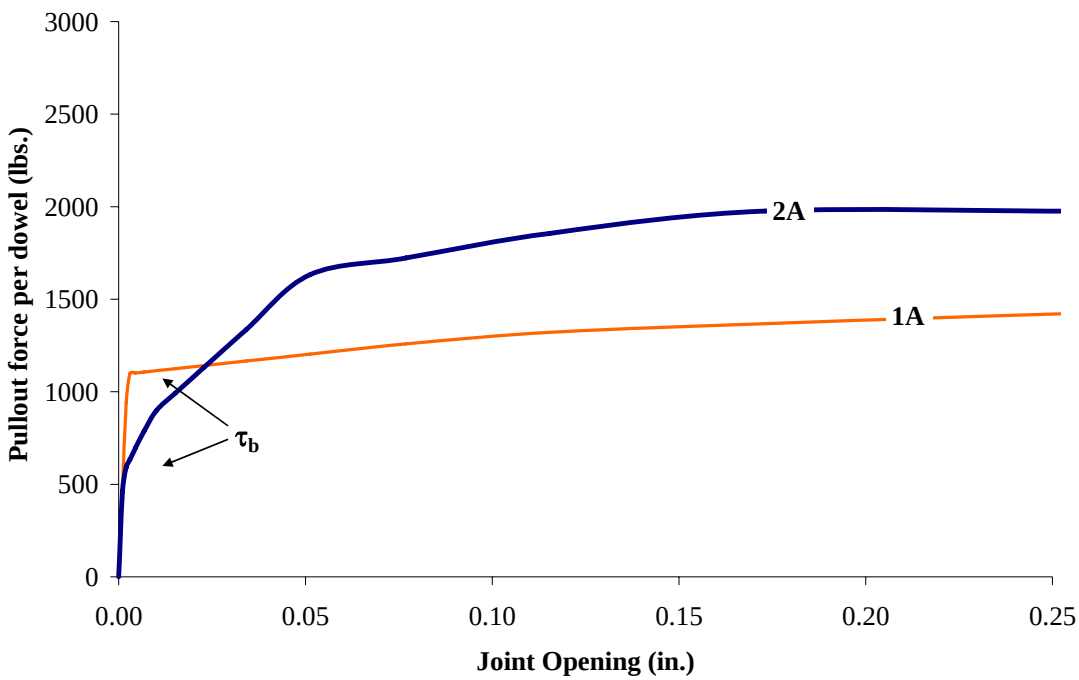

Figure 6.1: Typical location of initial slip state (A) for single and two aligned dowel bars

Event B occurs when the inelastic plastic strain in compression (PEEQ) and tension (PEEQT) values predicted by the finite element analysis became non-zero. PEEQ

and PEEQT are computed from the 3D finite element analysis results and they represent the effective lumped plastic strains in compression and tension, respectively. Concrete inelasticity or cracking initiates when these PEEQ and PEEQT values become non-zero. The initiation of concrete inelasticity (PEEQ > 0) and concrete cracking (PEEQT > 0) were first considered individually. However, they were always found to occur almost instantaneously. Hence, they were combined into one event limit state (B).

Events (C) and (D) pertains to the Principal Stress States (S_{max} and S_{min}) computed from the finite element analysis results. Event C occurs when the maximum principal stress (S_{max}) exceeds the concrete tensile strength (f'_t), see figure 6.2. This does not necessarily indicate cracking in a multiaxial stress state. Event D occurs when the minimum principal stress (S_{min}) exceeds the concrete compressive strength (f'_c), shown in figure 6.2. This does not necessarily mean crushing in a multiaxial stress state.

Event (E) represents significant crushing strain at the material point. It was assumed to occur when the effective plastic strain (PEEQ) exceeds 0.0035. PEEQ represents the total inelastic strain at the material point, which is resolved into the directional plastic strain tensor according to the non-associated flow rule. It is related to the uniaxial inelastic stress-strain behavior of the material. Figure 6.2(b) shows the uniaxial compressive stress-strain curve of concrete. This curve is used to calibrate the multiaxial flow rule in compression. This PEEQ = 0.0035 in the multiaxial strain state corresponds to the same magnitude of inelastic strain in compression. The value of PEEQ = 0.0035 was chosen to represent significant crushing at the material point. This value accounts for the inherent ductility of the material (shaded region in figure 6.2(b)) and the localized nature of the stress state.

Event (F) represents significant cracking strain at a material point was assumed to occur when the effective lumped plastic strain in tension (PEEQT) at a material point exceeded 0.003. PEEQT is similar to PEEQ with the exception that it is in tension. PEEQT is related to the uniaxial tension stress-cracking strain behavior of the material. The multiaxial behavior in tension is calibrated to the uniaxial stress-cracking strain behavior of the material. Thus, PEEQT=0.003 in a multiaxial strain state corresponds to the same magnitude of inelastic cracking strain state in uniaxial tension. The value of PEEQT=0.003, was chosen to represent significant cracking at the material point. This value is approximately ten times the initial cracking strain. It accounts for the material ductility and the highly localized nature of stresses.

6.2.1 ADDITIONAL DISCUSSION AND LIMITATIONS

Verification and Implications of Local Events

The localized multiaxial stresses and strains and events (A – F) predicted by the numerical models could not be validated experimentally. The experimental results focused on the overall force per dowel – joint opening behavior of the pavement specimens. The stresses and strains at the dowel-concrete interfaces were not measured because they were highly localized and deep inside the concrete pavement specimens. The localized material distresses at the dowel-concrete interfaces due to the stress concentrations were also not measured using acoustic-emission or other non-destructive techniques. These are the major limitations of the experimental research, and they should be addressed by future researchers.

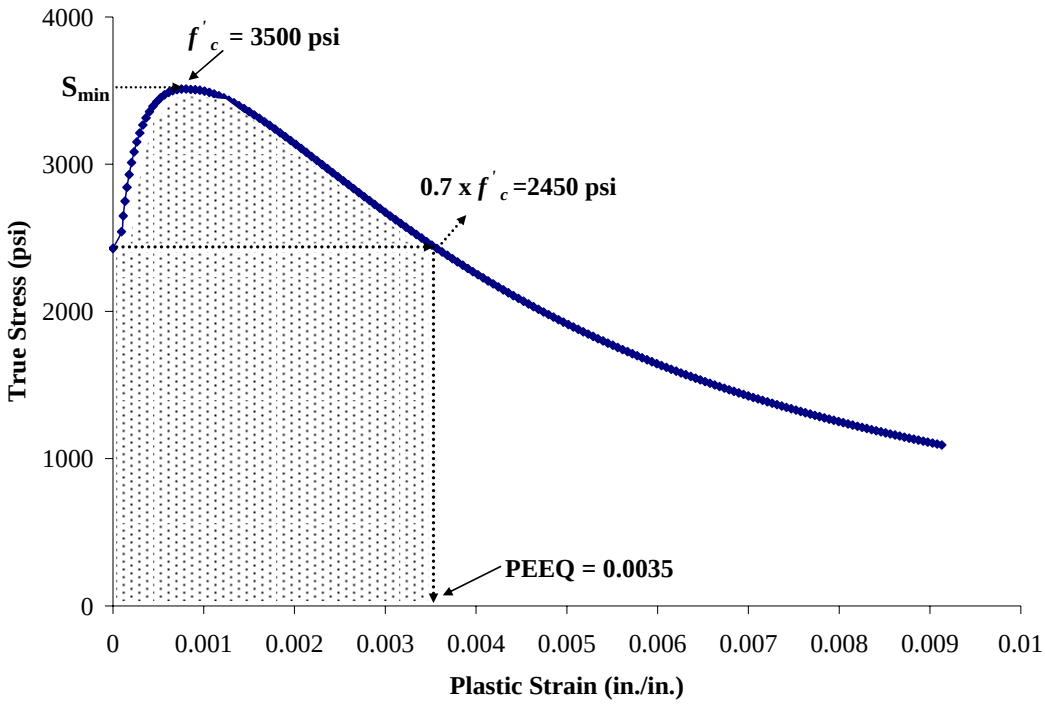

(a) Limit states (B), (D) and (E) on the compressive stress-strain curve

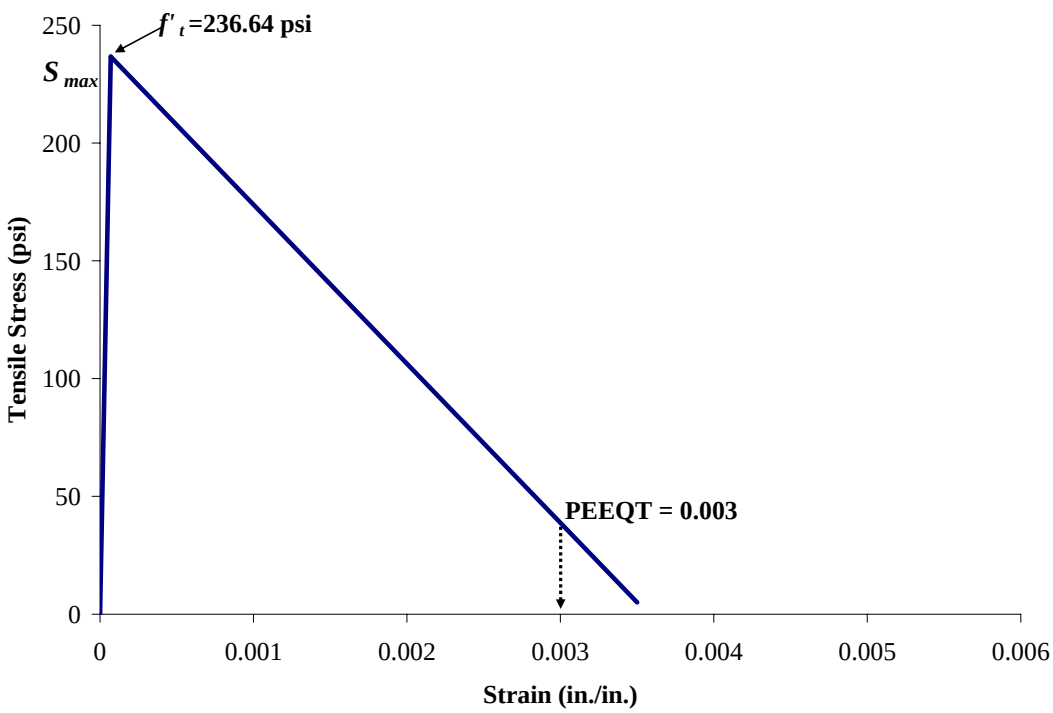

(b) Limit states (B), (C) and (F) on the tensile stress-strain curve

Figure 6.2: Identification of various limit states on the concrete compression – tension stress-strain curves

As shown in later sections 6.3 and so on, the occurrence of events (A – F) helps gain significant insight into the behavior and distresses of pavements with misaligned dowel bars. However, since the localized multiaxial stresses, strain, and events (A – F) could not be validated experimentally, they should be considered cautiously by the readers. The discussion in the following sections (6.3 and so on) implies that the events (A – F) occurred in the numerical finite element models. They do not imply or suggest that the events occur at the same joint opening in real pavement specimens. However, it is logically assumed that these distresses and events (A – F) will occur eventually in the experimental or real pavement specimens. The relative occurrence of these events for pavement specimens with different misaligned dowel bars is probably more important than their absolute joint opening values.

Discussion and Implication of Events (E) and (F)

Events (E) and (F) represent the occurrence of significant crushing and cracking plastic strains, respectively, at a material point in the numerical model. These events were chosen because the stresses and strains at the dowel-concrete interfaces have significant concentration due to dowel misalignment. As mentioned earlier in Section 5.6, joint opening is a cyclic time-varying phenomenon that will lead to fatigue failure (crack initiation) at the material point over several fatigue cycles. According to strain-life fatigue criteria (Bannantine et al. 1992), the occurrence of significant plastic strains at the material points is the major cause leading to low-cycle fatigue failure. Such fatigue strain-life equations have not yet been developed for dowel-concrete interfaces, and are a topic for future research. Without this information, it is difficult to establish a logical quantitative limit for ‘significant’ crushing or cracking plastic strains.

It is important to note that events (E) and (F) do not imply that the corresponding plastic values represent quantitatively ‘significant’ or ‘failure’ or ‘limiting’ strains because that can be established only by developing fatigue strain – life equations. Events E and F represent ‘milestones’ indicating that the material point has reached cumulative plastic strain values equal to 0.0035 and 0.003, respectively. That is the extent of implications from events E and F, nothing more. The values of 0.0035 and 0.003 were chosen arbitrarily as explained earlier. Other milestones can be chosen or used by future researchers.

The selection of events (E) and (F) was based on the cumulative plastic strain at the material point because according to the theory of plasticity, this cumulative plastic strain (PEEQ or PEEQT) has the most direct correlation with the corresponding uniaxial plastic strains in compression or tension (ABAQUS – theory manual). When the multiaxial cumulative plastic strain reaches a certain value, for example, PEEQ=0.0035, it corresponds to the same exact level of plastic strain in the uniaxial case, for example, 0.0035. No other parameter has similar exact correlations in the multiaxial and uniaxial states. The volumetric plastic strain energy was considered (area under plastic stress-strain curve, Figure 6.2 above) but not selected because it has a weaker correlation between the multiaxial and uniaxial cases. Additionally, it would require an inconsistent shift in the post-processing of the results to focus on volumetric strain energy rather than cumulative plastic strains, which is the basis for other events, for example, event B. Additionally, in the absence of a calibrated fatigue strain – life equation, both parameters (cumulative plastic strain and volumetric strain energy) imply qualitative ‘behavior’, i.e., ‘significant’ crushing or cracking, rather than quantitative assessment of fatigue life.

6.3 DISCUSSION OF ANALYTICAL AND EXPERIMENTAL RESULTS

The results from the 3D finite element analyses include the pullout force-joint opening behavior of the concrete specimens and the complex state of multiaxial (3D) stresses and strains in the model. These results can be used to identify events of damage limit states that occur in the material during the force-joint opening behavior. This section presents the results from the finite element analyses of pavement specimen models with one, two or five dowel bars at the joint. The models focuses on specimens with misalignment magnitude equal to 1/18 radians to enable greater understanding and insight. Tables 6.1(a), (b) and (c) show the specimen identification of the typical finite element models that are going to be discussed. The results from the analytical models and experimental data for the tests conducted in this research are presented in Appendix C.

Table 6.1(a) Test Matrix of the single dowel bar

Slab Dimensions	Number of Dowels	ID	Misalignment	Magnitude (in rad.)	Magnitude (in in.)
2 slabs each 24 x 24 x 10 in.	1	1A	Aligned	0	0
		1V18	Vertical	1/18	½ in. over 9 in. length of dowel
		1H18	Horizontal		
		1C18	Combined		

Table 6.1(b) Test Matrix of the two dowel bars

Slab Dimensions	Number of Dowels	ID	Misalignment	Magnitude (in rad.)	Magnitude (in in.)
2 slabs each 36 x 24 x 10 in.	2 Aligned	2A	Aligned	0	0
	2 (Uniform)	2V18U	Vertical	$+1/18$; $+1/18$	+ ½ in; +½ in. over 9 in. length
		2H18U	Horizontal		
		2C18U	Combined		
	2 (Non - Uniform)	2V18NU	Vertical	$+1/18$; $-1/18$	+ ½ in; -½ in. over 9 in. length
		2H18NU	Horizontal		
		2C18NU	Combined		
	2 (One Bar Misaligned)	2V18AM	Vertical	$1/18$; 0	+ ½ in; 0 over 9 in. length
		2H18AM	Horizontal		
		2C18AM	Combined		

Table 6.1(c) Test Matrix of the five dowel bars

Slab Dimensions	Number of Dowels	ID	Misalignment	Magnitude (in rad.)	Magnitude (in in.)
2 slabs each 72 x 36 x 10 in.	5 Aligned	5A	Aligned	0	0
	5 (Non - Uniform)	5V18NU	Vertical	$+1/18$; $-1/18$; $+1/18$; $-1/18$; $+1/18$	+ ½ in; - ½ in; + ½ in; - ½ in; + ½ in over 9 in. length
		5H18NU	Horizontal		
		5C18NU	Combined		
	5 (Alternate Bar Misaligned)	5V18AM	Vertical	$1/18$; 0; $-1/18$; 0; $1/18$	+ ½ in; 0; - ½ in; 0; + ½ in over 9 in. length
		5H18AM	Horizontal		
		5C18AM	Combined		

Figure 6.3 compares the experimentally measured and analytically predicted pullout force-joint opening behavior for single dowel specimens. Figures 6.4 and 6.5 compare the experimentally measured and analytically predicted pullout force-joint opening behavior for specimens with two dowels misaligned vertically or horizontally, respectively. Similarly, figures 6.6 and 6.7 compare the experimentally measured and analytically

predicted pullout force-joint opening behavior for specimens with five dowels misaligned vertically or horizontally, respectively. In figures 6.3 through 6.7, Cases I and II correspond to the use of idealized and experimentally established static friction coefficients and material properties, as explained earlier in section 5.4.3.

6.3.1 SINGLE DOWEL BAR MODELS

Figures 6.3 (a-d) compare the experimental and analytical pullout force-joint opening results for the single dowel bar specimens. These figures include the analytical results for cases I and II and identify the events / damage limit states (A) to (F) on the analytical results. As shown in figure 6.3(a), for specimen 1A, only the debonding event occurs in the analytical models. No other events or material damage limit states were observed, confirming the hypothesis that an aligned dowel bar gives the best performance in a pavement joint.

Table 6.2(a) presents the joint opening and the pullout forces for the various events or damage limit states (B) to (F) as they occur during the force-joint opening behavior of the analysis of specimens 1V18 and 1H18. Both the cases I and II are included in Table 6.2(a). For specimen 1V18, event (E) occurs for case II at joint opening = 0.349 in. and a dowel pullout force = 2675.23 lbs. Event (F) is not reached in the analysis of specimen 1V18. For specimen, 1H18, shown in figure 6.3(c), events or damage limit states (B - F) all occur at nearly the same joint opening for cases I and II. The analytical results indicate that the event (F) occurs prior to (E), which indicates that significant cracking occurs before significant crushing. For specimen, 1C18, shown in figure 6.3(d), events or damage limit states (B-C) and (B-E) occur for cases I and II.

Table 6.2(a) presents the pullout force and joint opening at which these events or damage limit states occur in the FE model.

6.3.2 TWO DOWEL BAR MODELS

Figure 6.4(a-d) compares the experimental and analytical results, i.e., force-joint opening responses for the two dowel bar specimens with vertical misalignment magnitude of 1/18 radians only. These include specimens with aligned dowels (2A), non-uniform (2V18NU), uniform (2V18U) and alternate misalignments (2V18AM).

As shown in figure 6.4(a), both the experimental and analytical results for specimen 2A indicate the occurrence of only the debonding limit state (event A). For specimen 2V18NU, shown in figure 6.4(b), the analytical results indicate that all the events / material damage limit states (A-F) occur for case (I) analysis. Case II analysis results show that event / material damage limit state (E) occurs but the event / material damage limit state (D) ($S_{min} > f'_c$) does not occur. This is because inelasticity occurs due to multiaxial stresses with $S_{min} < f'_c$. Events (B) and (E) occur but event (D) which focused on ($S_{min} > f'_c$) does not occur. This indicates that inelastic strain event or damage limit states (E, F) should be emphasized over the principal stress limit states (C, D) due to the multiaxial nature of the stress state. For specimen 2V18U, for both cases I and II, only events or damage limit states (A)-(C) occur in the finite element models as shown in figure 6.4(c). This means that very little material damage or inelasticity occurs in this specimen. Similar trend in the formation of events / damage limit states are observed in the 2V18AM specimen, as shown in figure 6.4(d).

Figure 6.5(a-d) compares the experimental and analytical force-joint opening results for the two dowel bar specimens with horizontal misalignment magnitude 1/18

radians only. These include specimens with aligned dowels (2A), non-uniform (2H18NU), uniform (2H18U) and alternate misalignments (2H18AM). As shown in figure 6.5(b), for specimen 2H18NU, all events / material damage limit states (A-F) occur for case I and II analysis. For specimen 2H18U, events / material damage limit states (A-E) occur in the analysis of case I whereas all the events / material damage limit states (A-F) occurs in case II, as shown in figure 6.5(c). In specimen 2H18AM, figure 6.5(d), all the events / damage limit states (A-F) occur in case I and II analysis.

Figure 6.6(a-d) compares the experimental and analytical force-joint opening results for the two dowel bar specimens with combined misalignment magnitude of 1/18 radians only. The results shown are for analysis of specimens with aligned dowels (2A), non-uniform (2C18NU), uniform (2C18U) and alternate misalignments (2C18AM). As shown in figure 6.6(b), for specimen 2C18NU, all events / material damage limit states (A-F) occur for case I and II analysis. For specimen 2C18U, events / material damage limit states (A-D) occur in the analysis of case I whereas all the events / material damage limit states (A-F) occurs in case II, as shown in figure 6.6(c). In specimen 2C18AM, figure 6.6(d), all the events / damage limit states (A-F) occur in case I and II analysis.

Table 6.2(b), (c) and (d) present the joint opening and pullout force for the various events / damage limit states (A) to (F) as they occur in the analysis for two dowel bars having vertical, horizontal and combined type of misalignments, respectively.

6.3.3 FIVE DOWEL BAR MODELS

Figure 6.7(a-c) compares the experimental and analytical force-joint opening results for the five dowel bar specimens with vertical misalignment magnitude of 1/18 radians only. These include specimens with aligned dowels (5A), non-uniform (5V18NU) and alternate

misalignments (5V18AM). As shown in figure 6.7(b) and 6.7(c), for specimen 5V18NU and 5V18AM respectively, all events / damage limit states (A-F) occur for case I and II analyses. These results indicate that the specimen will fail significantly in cracking and crushing at the dowel-concrete interfaces.

Figures 6.8(a-c) compares the experimental and analytical force-joint opening results for the five dowel bar specimens with horizontal misalignment magnitude 1/18 radians only. These include specimens with aligned dowels (5A), non-uniform (5H18NU) and alternate misalignments (5H18AM). As shown in figure 6.8(b), for specimen 5H18NU, all events / damage limit states (A-F) occur for case I and for case II analysis, events / damage limit states from A-D occur. For specimen 5H18AM, figure 6.8(c), all the events / damage limit states (A-F) occur in the case I and II analyses.

Figure 6.9(a-c) compares the experimental and analytical force-joint opening results for the five dowel bar specimens with combined misalignment magnitude of 1/18 radians only. These include specimens with aligned dowels (5A), non-uniform (5C18NU) and alternate misalignments (5C18AM). As shown in figure 6.9(b) and (c), for specimen 5C18NU and 5C18AM respectively, all events / damage limit states (A-F) occur for case I and II analyses. These results indicate that the specimen will fail significantly in cracking and crushing at the dowel-concrete interfaces. The joint opening and pullout forces per bar are presented in tables 6.2(e), (f) and (g), for five dowels with vertical, horizontal and combined misalignments respectively.

Table 6.2(a): Summary of the pullout load – joint opening for cases I and II in the 1V18, 1H18 and 1C18 tests

Events	1V18				1H18				1C18			
	Joint Opening (in)		Pullout Load (lbs)		Joint Opening (in)		Pullout Load (lbs)		Joint Opening (in)		Pullout Load (lbs)	
	(I)	(II)	(I)	(II)	(I)	(II)	(I)	(II)	(I)	(II)	(I)	(II)
(B)	0.015	0.038	1180.0	1450	0.018	0.034	1200.0	1480.0	0.012	0.014	1160.0	1240.0
(C)	0.115	-	1560.0	-	0.018	0.051	1200.0	1660.0	0.016	0.014	1190.0	1240.0
(D)	-	0.148	-	2170	0.214	0.228	1780.0	2680.0	-	0.116	-	2180.0
(E)	-	-	-	-	0.535	0.425	1940.0	3180.0	-	0.126	-	2240.0
(F)	-	-	-	-	0.260	0.217	1840.0	2620.0	-	-	-	-

Table 6.2(b): Summary of pullout load-joint opening for case (i) and (ii) in the 2V18NU, 2V18U and 2V18AM test

Events	2V18NU				2V18U				2V18AM			
	Joint Opening (in)		Pullout Load (lbs)		Joint Opening (in)		Pullout Load (lbs)		Joint Opening (in)		Pullout Load (lbs)	
	(I)	(II)	(I)	(II)	(I)	(II)	(I)	(II)	(I)	(II)	(I)	(II)
(B)	0.010	0.021	846.00	1002.53	0.015	0.012	957.78	947.95	0.002	0.002	505.34	507.34
(C)	0.023	0.025	112.82	1321.06	0.034	0.025	1302.88	1229.25	0.015	0.015	893.57	925.84
(D)	0.339	0.552	2244.78	3247.22	-	-	-	-	0.051	0.034	1397.25	1232.84
(E)	0.337	0.335	2244.09	3059.84	-	-	-	-	-	-	-	-
(F)	0.269	0.233	2225.76	2880.03	-	-	-	-	-	-	-	-

Table 6.2(c): Summary of pullout load-joint opening for case (i) and (ii) in the 2H18NU, 2H18U and 2H18AM test

Events	2H18NU				2H18U				2H18AM			
	Joint Opening (in)		Pullout Load (lbs)		Joint Opening (in)		Pullout Load (lbs)		Joint Opening (in)		Pullout Load (lbs)	
	(I)	(II)	(I)	(II)	(I)	(II)	(I)	(II)	(I)	(II)	(I)	(II)
(B)	0.010	0.010	859.91	943.06	0.016	0.012	963.53	949.91	0.013	0.015	852.68	937.34
(C)	0.023	0.022	1141.23	1279.29	0.034	0.0362	1314.26	1481.65	0.040	0.034	1272.77	1251.89
(D)	0.214	0.280	2243.57	3139.88	0.333	0.374	2247.57	2957.96	0.262	0.266	2116.95	2507.60
(E)	0.293	0.297	2299.83	3236.9	0.5452	0.492	2297.17	3128.53	-	0.348	-	2619.57
(F)	0.272	0.246	2285.39	3098.24	0.4101	0.335	2267.68	2912.34	0.288	0.256	2129.46	2454.00

Table 6.2(d): Summary of pullout load-joint opening for case (i) and (ii) in the 2C18NU, 2C18U and 2C18AM test

Events	2C18NU				2C18U				2C18AM			
	Joint Opening (in)		Pullout Load (lbs)		Joint Opening (in)		Pullout Load (lbs)		Joint Opening (in)		Pullout Load (lbs)	
	(I)	(II)	(I)	(II)	(I)	(II)	(I)	(II)	(I)	(II)	(I)	(II)
(B)	0.014	0.014	935.0	1025.0	0.0038	0.0098	530.65	735.0	0.0097	0.009	794.0	805.0
(C)	0.017	0.017	1070.0	1225.0	0.0075	0.015	615.0	980.0	0.018	0.026	980.0	1195.0
(D)	0.154	0.205	2330.0	3225.0	0.534	0.253	1125.0	1165.0	0.179	0.200	2095.0	2455.0
(E)	0.231	0.239	2415.0	3330.0	-	0.126	-	2410.0	-	0.259	-	2605.0
(F)	0.202	0.205	2395.0	3225.0	-	-	-	-	0.227	0.200	2175.0	2455.0

Table 6.2(e): Summary of the pullout load – joint opening for cases I and II in the 5V18NU and 5V18AM tests

Events	5V18NU				5V18AM			
	Joint Opening (in)		Pullout Load (lbs)		Joint Opening (in)		Pullout Load (lbs)	
	(I)	(II)	(I)	(II)	(I)	(II)	(I)	(II)
(B)	0.022	0.015	1451.97	1353.50	0.032	0.017	1510.0	1290.0
(C)	0.051	0.034	1701.96	1802.57	0.047	0.036	1600.0	1640.0
(D)	0.230	0.358	2227.88	3239.90	0.208	0.260	2020.0	2470.0
(E)	0.346	0.358	2289.98	3239.90	0.352	0.368	2130.0	2610.0
(F)	0.404	0.307	2307.90	3163.28	0.439	0.347	2160.0	2650.0

Table 6.2(f): Summary of the pullout load – joint opening for cases I and II in the 5H18NU and 5H18AM tests

Events	5H18NU				5H18AM			
	Joint Opening (in)		Pullout Load (lbs)		Joint Opening (in)		Pullout Load (lbs)	
	(I)	(II)	(I)	(II)	(I)	(II)	(I)	(II)
(B)	0.016	0.0077	1302.90	843.0	0.016	0.016	1120.0	1180.0
(C)	0.052	0.023	1715.65	1570.0	0.046	0.046	1470.0	1620.0
(D)	0.155	0.206	2099.70	2820.0	0.146	0.147	1750.0	2090.0
(E)	0.232	-	2256.34	-	0.290	0.290	1950.0	2490.0
(F)	0.257	-	2275.36	-	0.377	0.355	2000.0	2630.0

Table 6.2(g): Summary of the pullout load – joint opening for cases I and II in the 5C18NU and 5C18AM tests

Events	5C18NU				5C18AM			
	Joint Opening (in)		Pullout Load (lbs)		Joint Opening (in)		Pullout Load (lbs)	
	(I)	(II)	(I)	(II)	(I)	(II)	(I)	(II)
(B)	0.0152	0.012	1340.0	1140.0	0.004	0.004	531.0	1550.0
(C)	0.0158	0.013	1360.0	1240.0	0.006	0.006	759.0	1810.0
(D)	0.137	0.142	2100.0	2670.0	0.012	0.013	1140.0	2270.0
(E)	0.373	0.388	2460.0	3630.0	-	0.254	-	3330.0
(F)	0.170	0.265	2230.0	3280.0	0.154	0.143	2040.0	3090.0

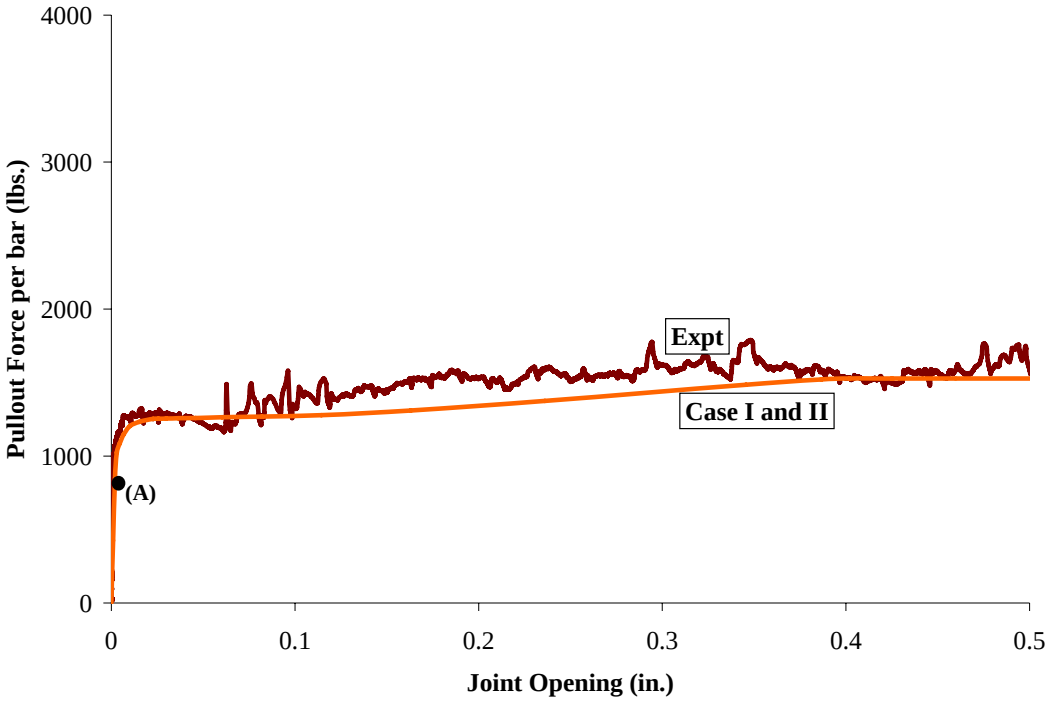

(a) Model for 1A Test

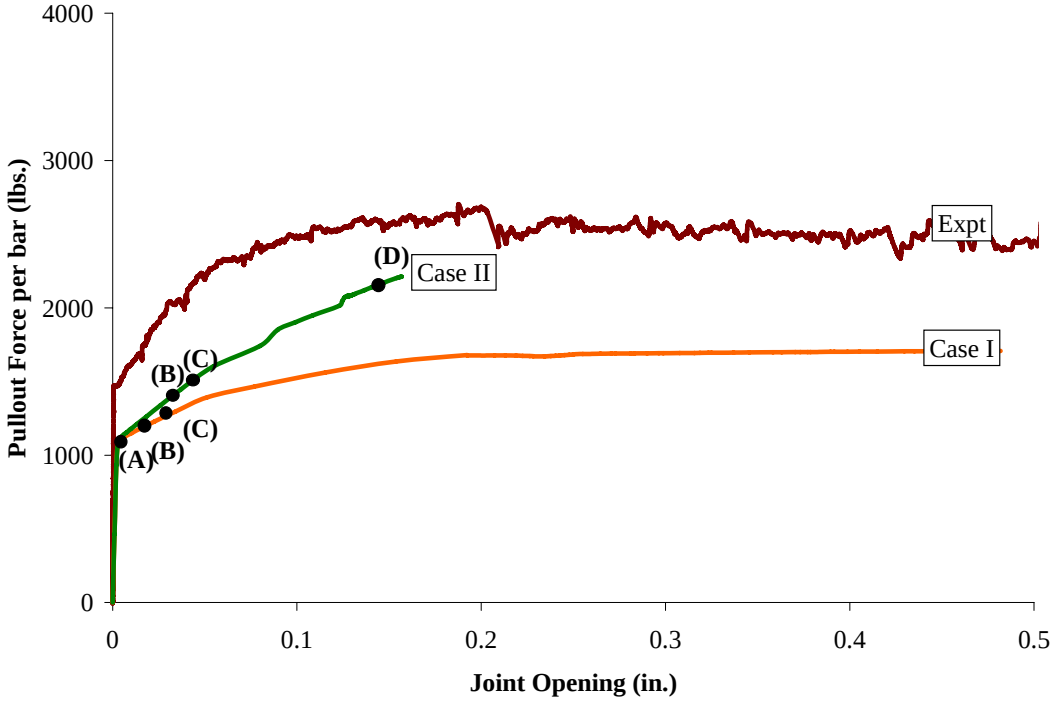

(b) Model for 1V18 Test

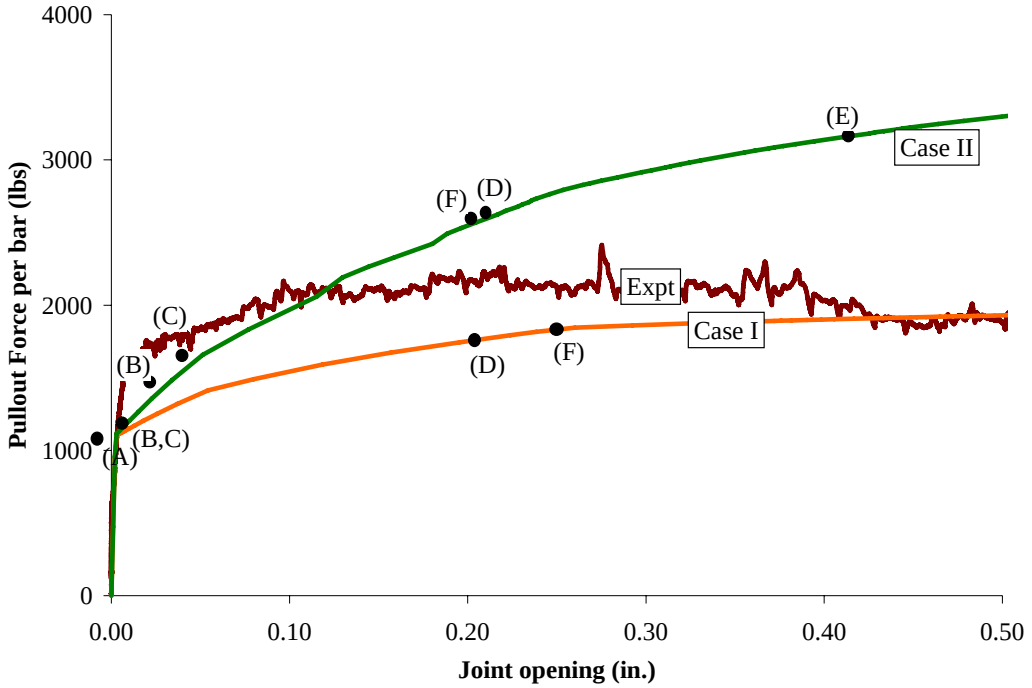

(c) Model for 1H18 Test

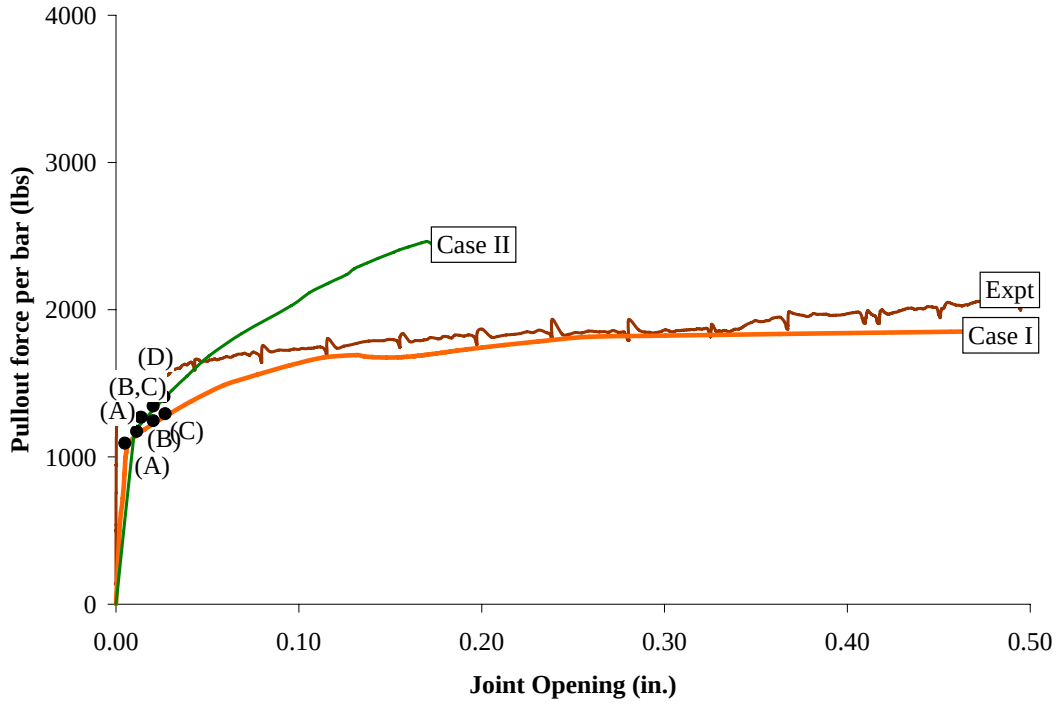

(d) Model for 1C18 Test

Figure 6.3: Comparison of the FEM model with the experimental data for a single dowel bar specimen

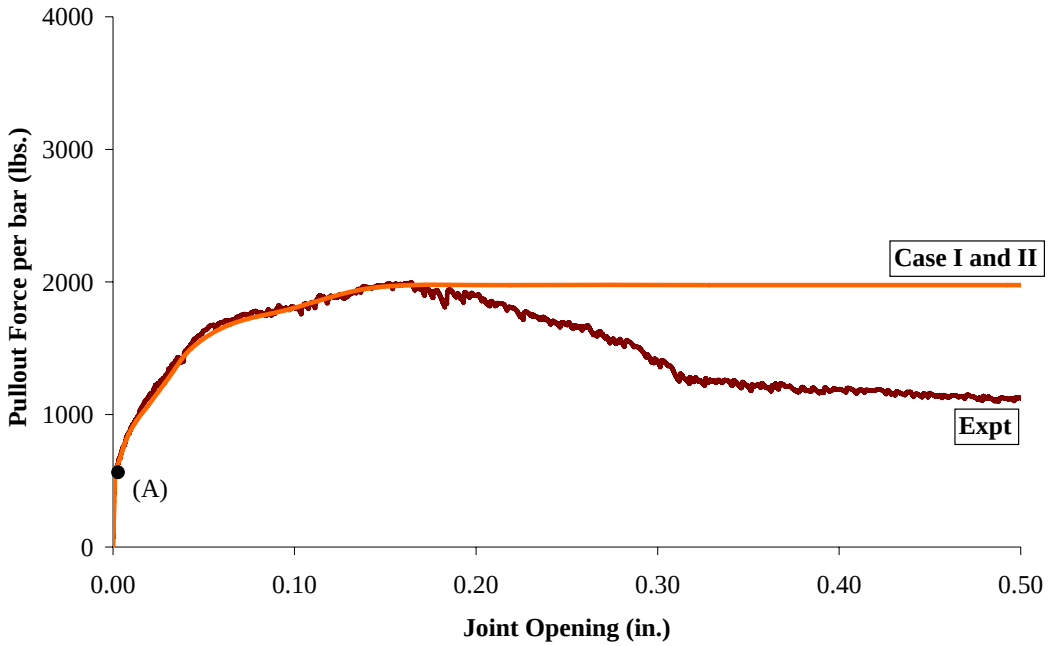

(a) Model for 2A Test

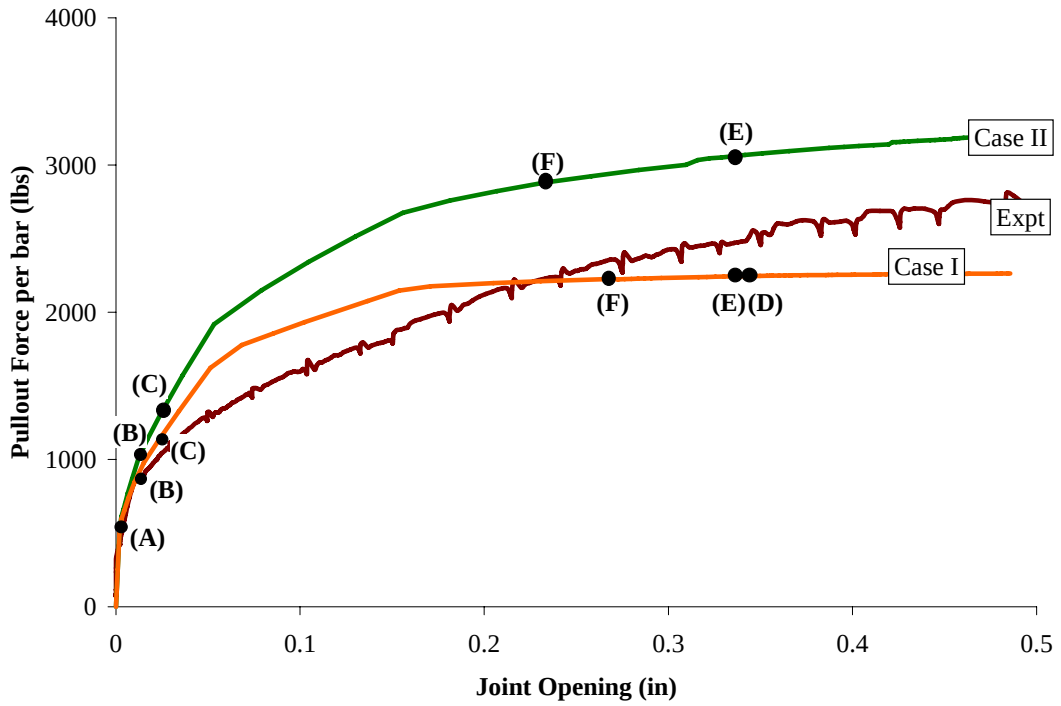

(b) Model for 2V18NU Test

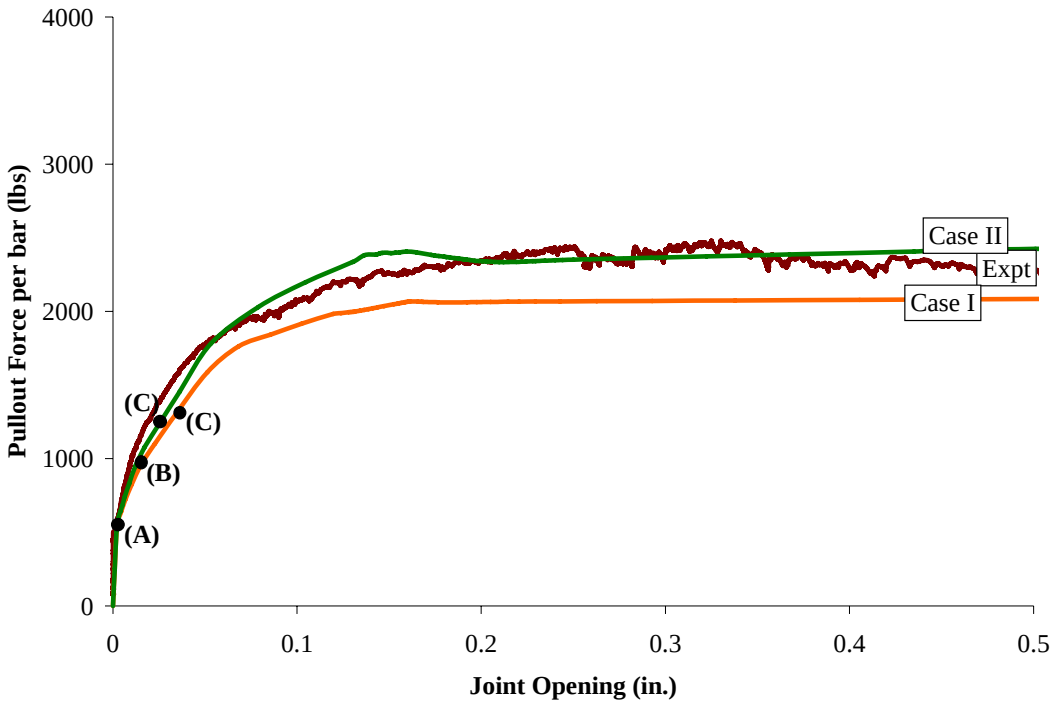

(c) Model for 2V18U Test

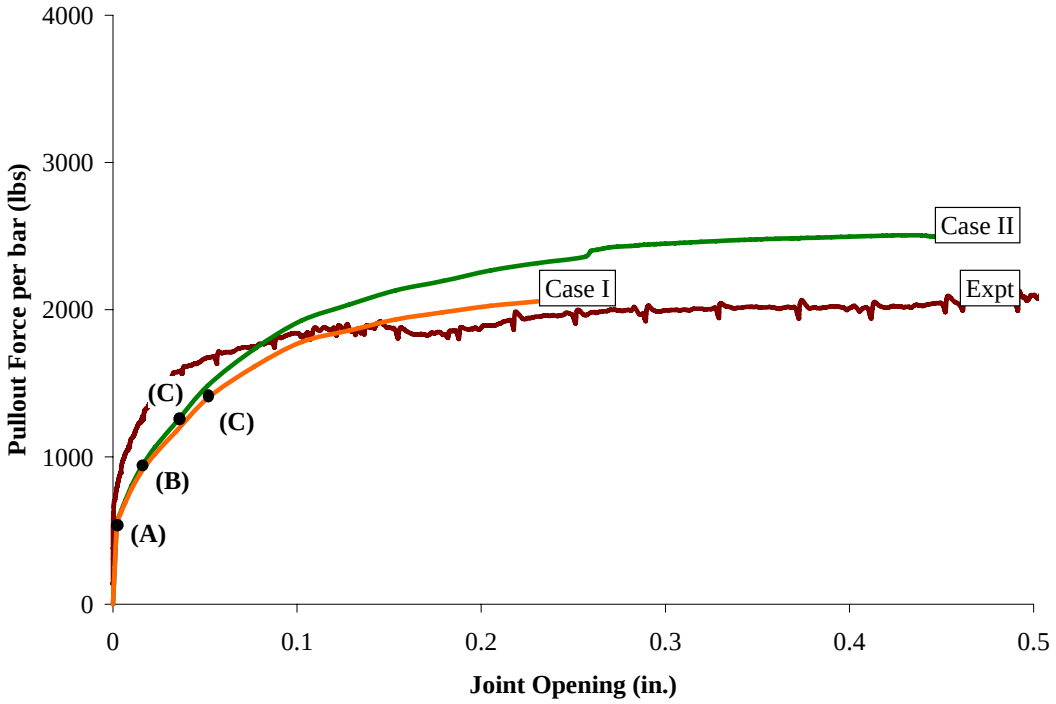

(d) Model for 2V18AM Test

Figure 6.4: Comparison of FEM and experimental data for a two dowel bars with vertical misalignment

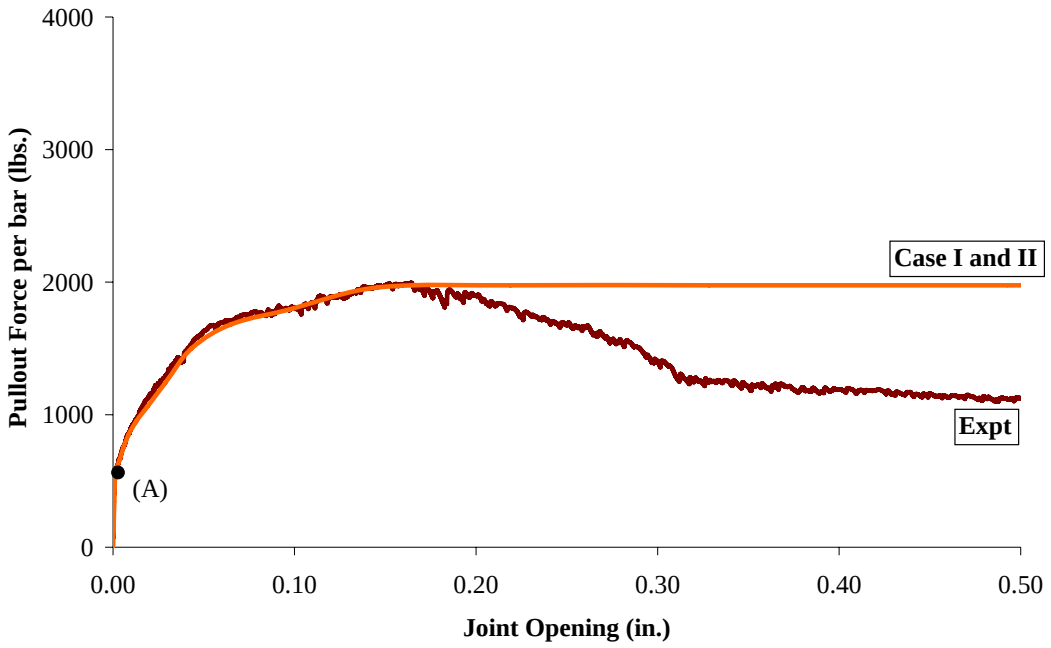

(a) Model for 2A Test

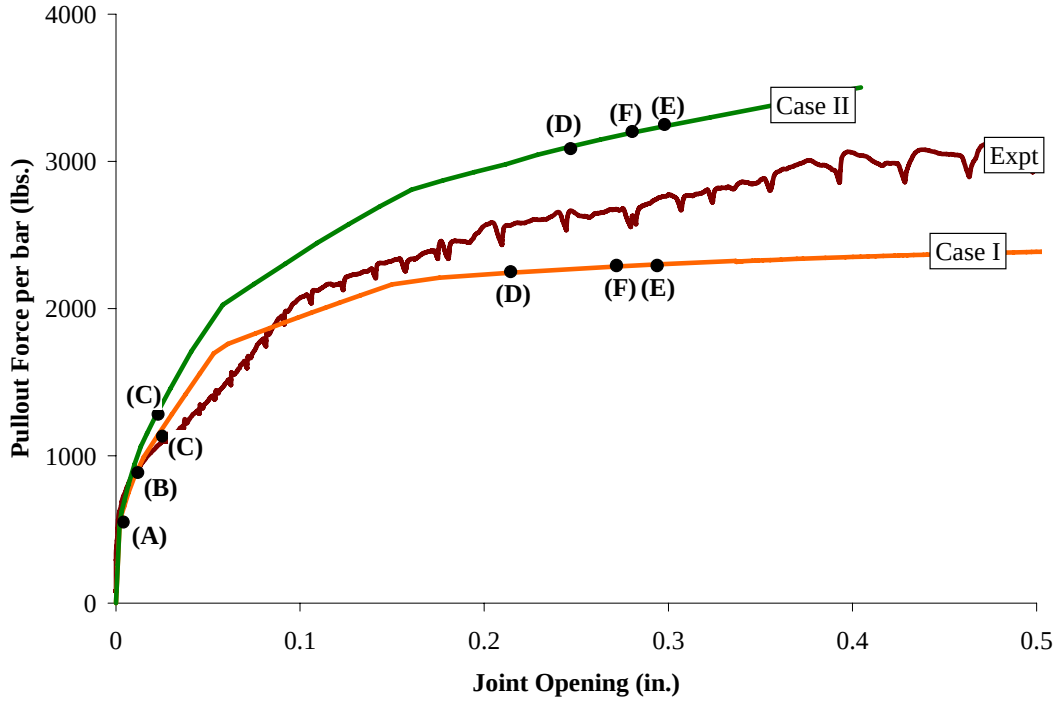

(b) Model for 2H18NU Test

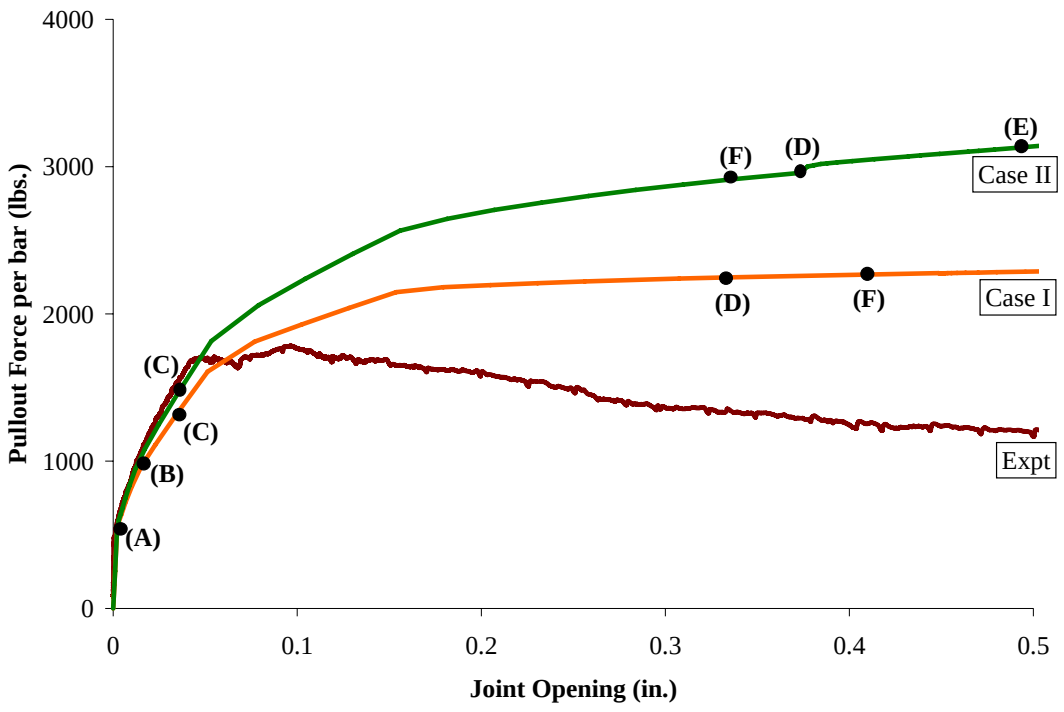

(c) Model for 2H18U Test

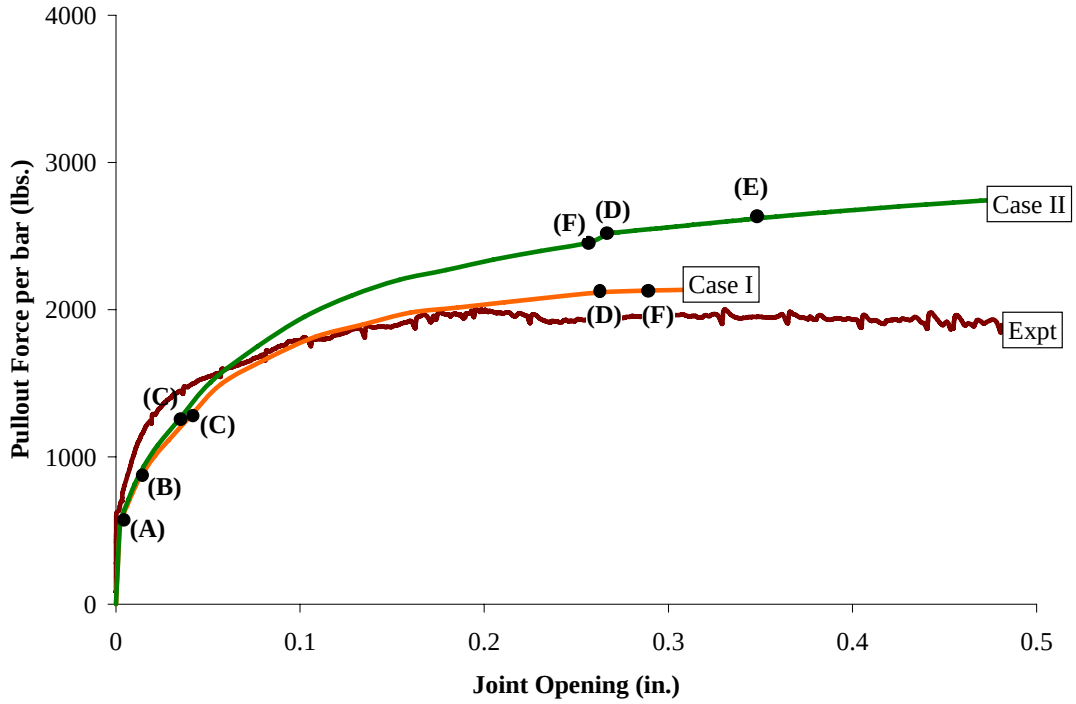

(d) Model for 2H18AM Test

Figure 6.5: Comparison of FEM and experimental data for a two dowel bars with horizontal misalignment

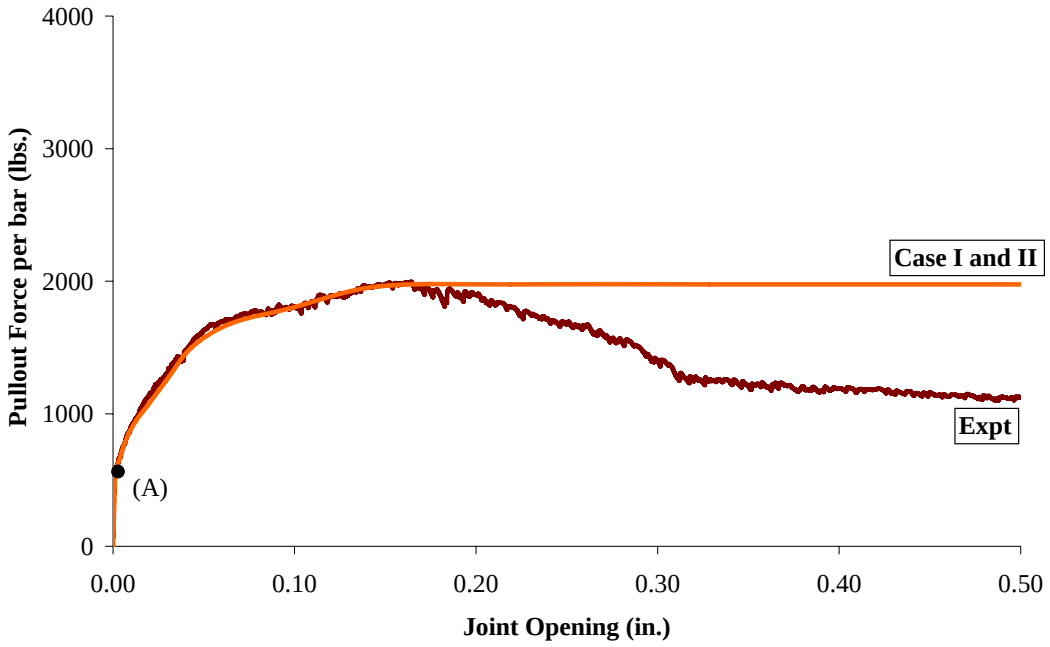

(a) Model for 2A Test

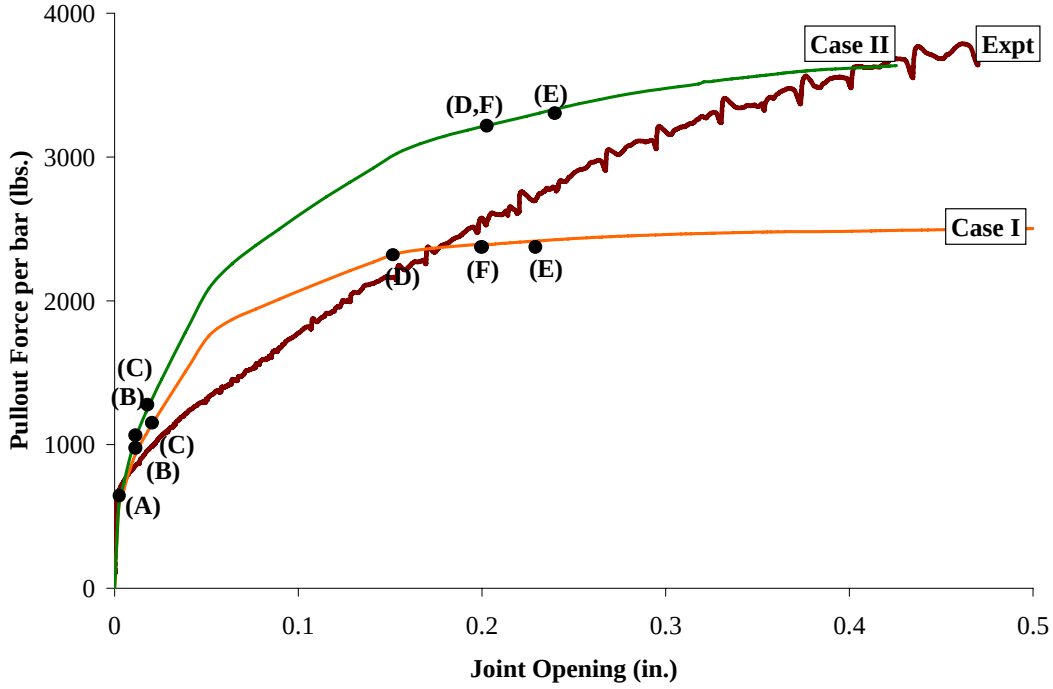

(b) Model for 2C18NU Test

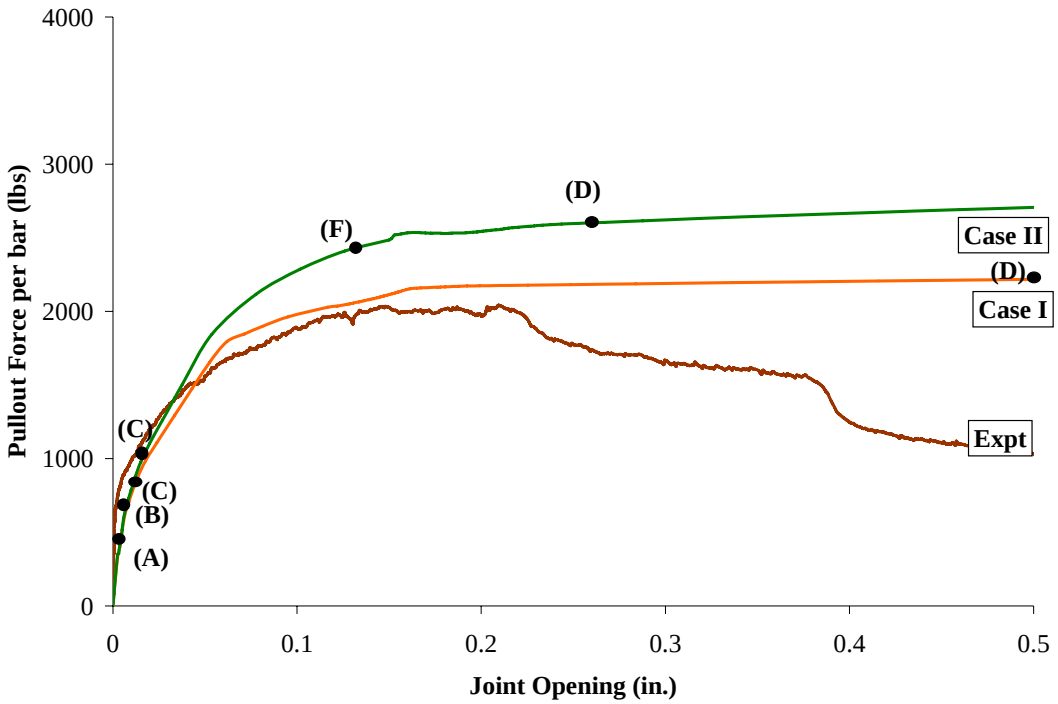

(c) Model for 2C18U Test

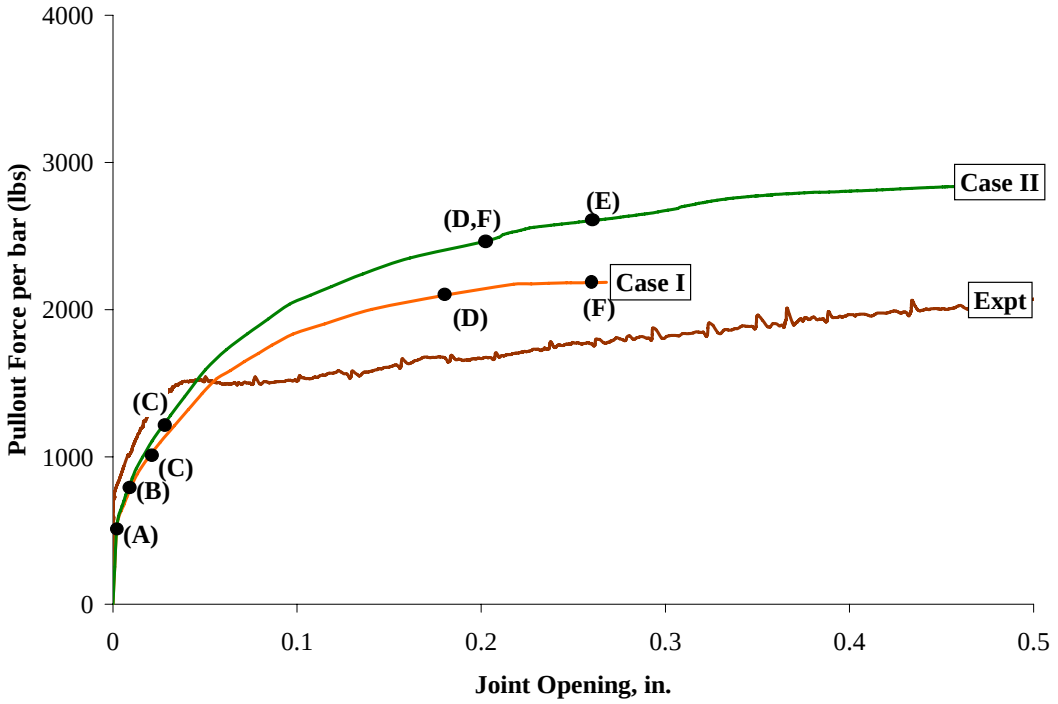

(d) Model for 2C18AM Test

Figure 6.6: Comparison of FEM and experimental data for a two dowel bars with combined misalignment

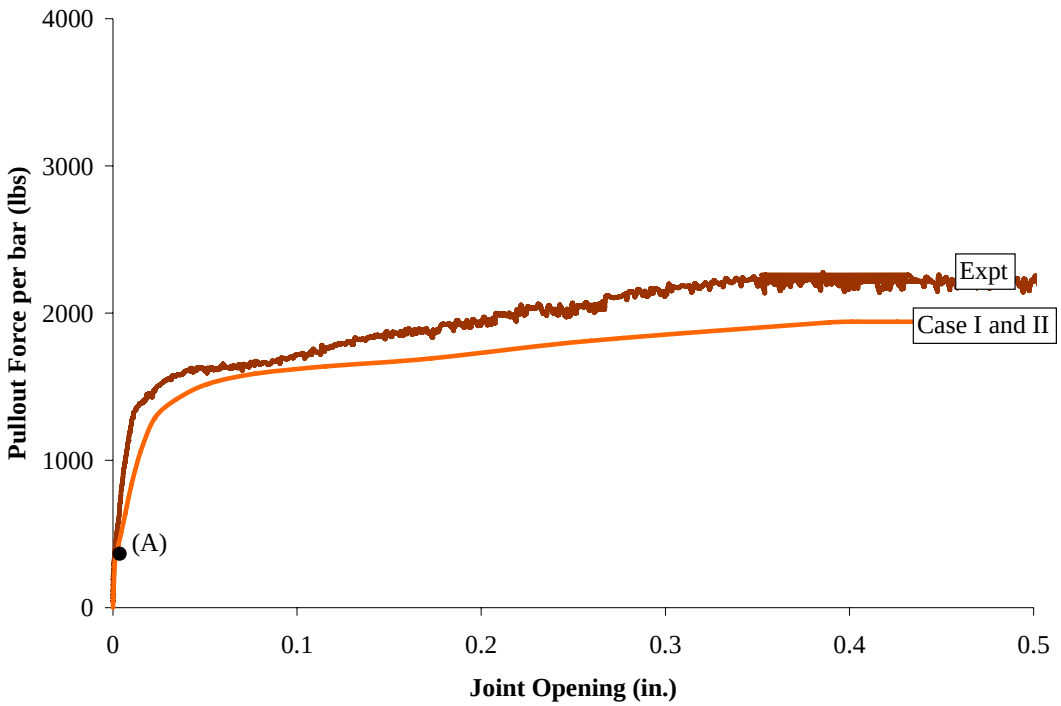

(a) Model for 5A Test

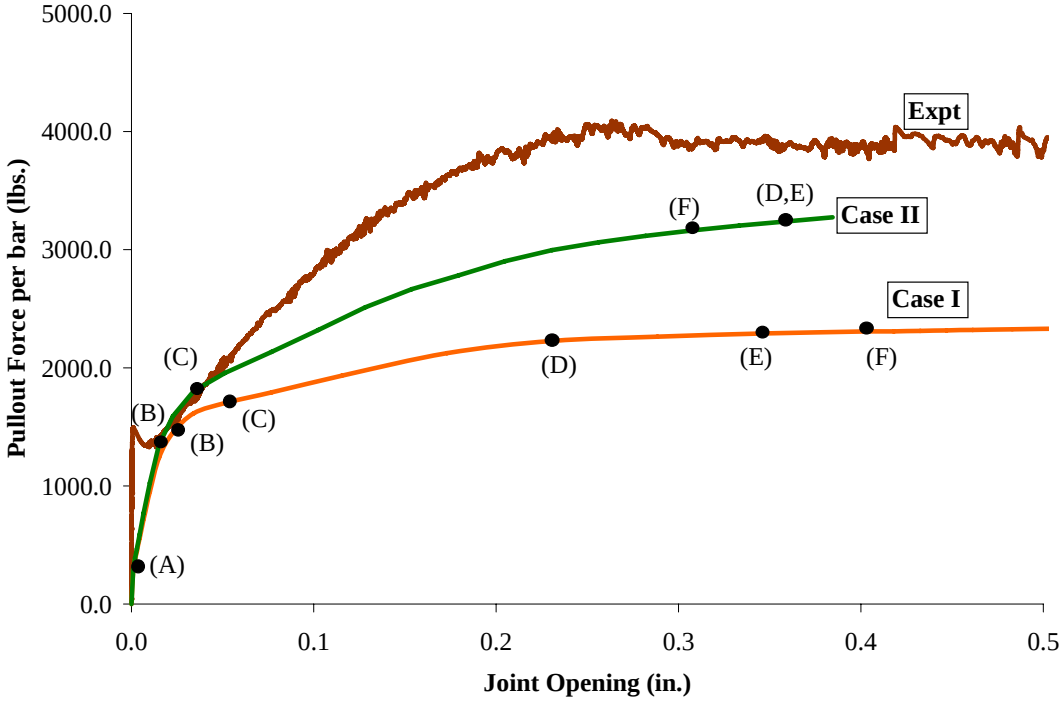

(b) Model for 5V18NU Test

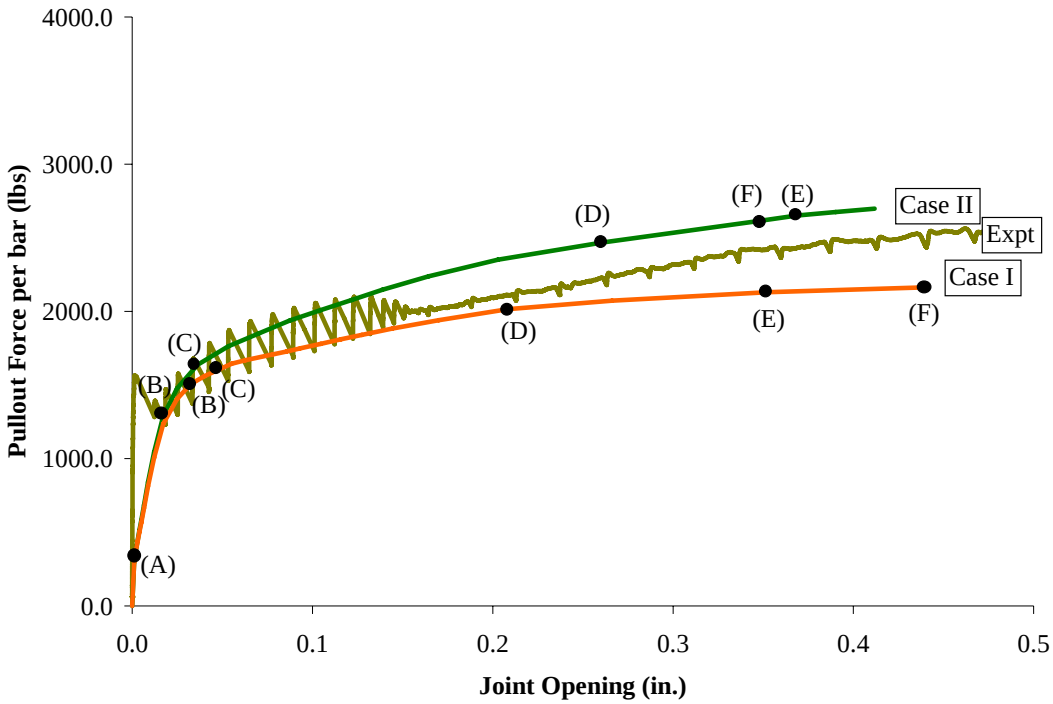

(c) Model for 5V18AM Test

Figure 6.7: Comparison of FEM and experimental data for five dowel bars with vertical misalignment

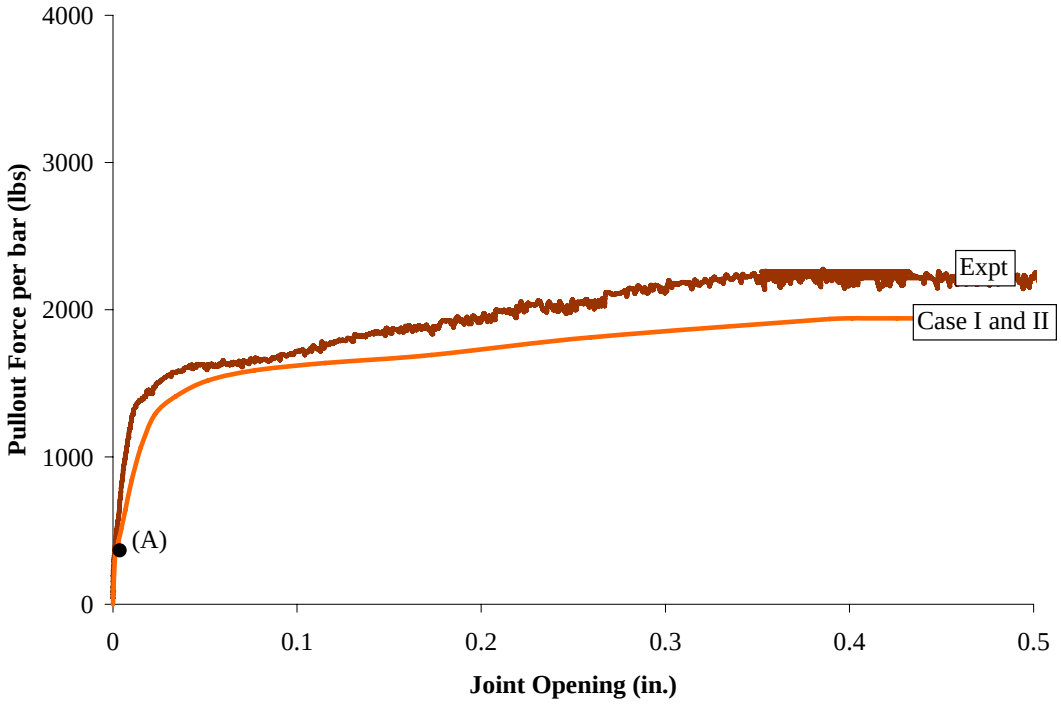

(a) Model for 5A Test

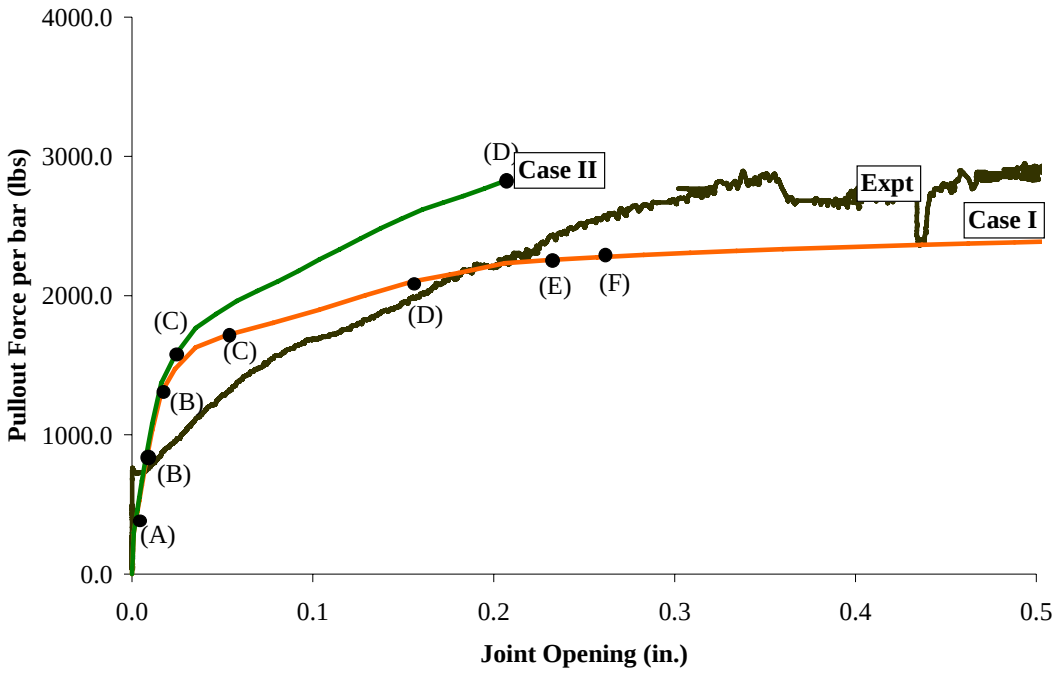

(b) Model for 5H18NU Test

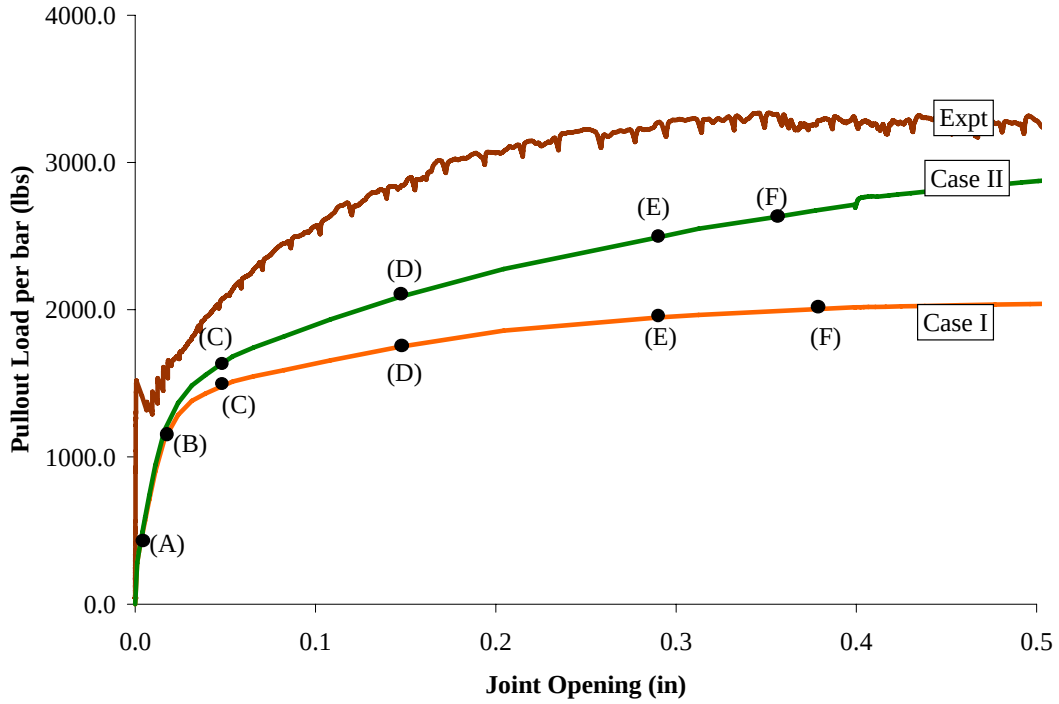

(c) Model for 5H18AM Test

Figure 6.8: Comparison of FEM and experimental data for five dowel bars with horizontal misalignment

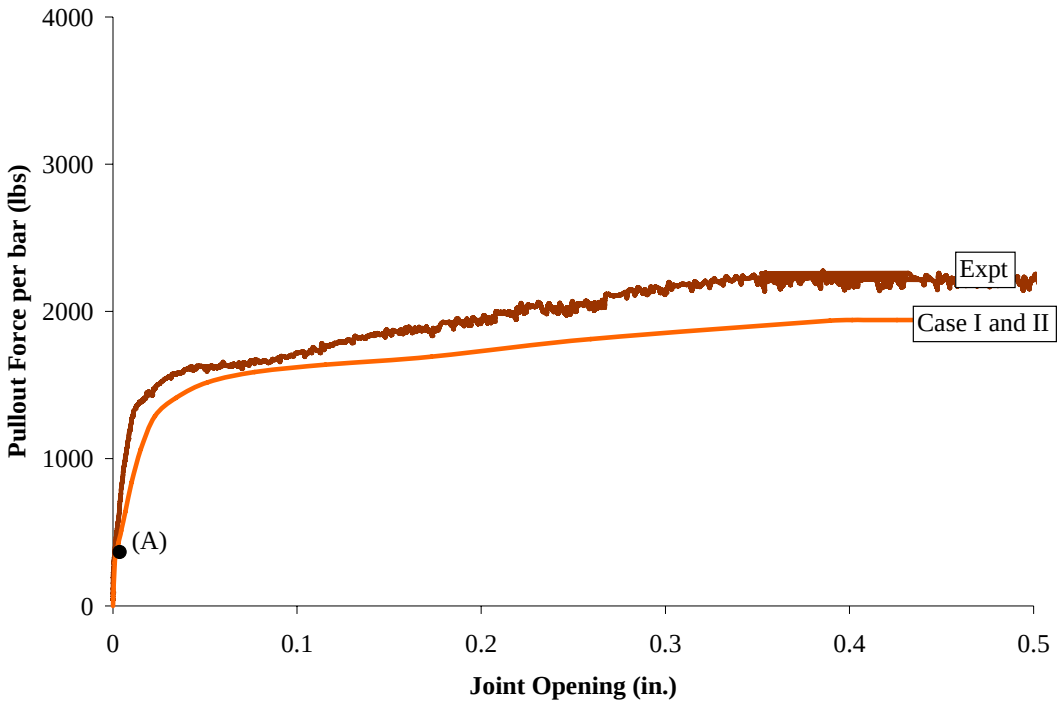

(a) Model for 5A Test

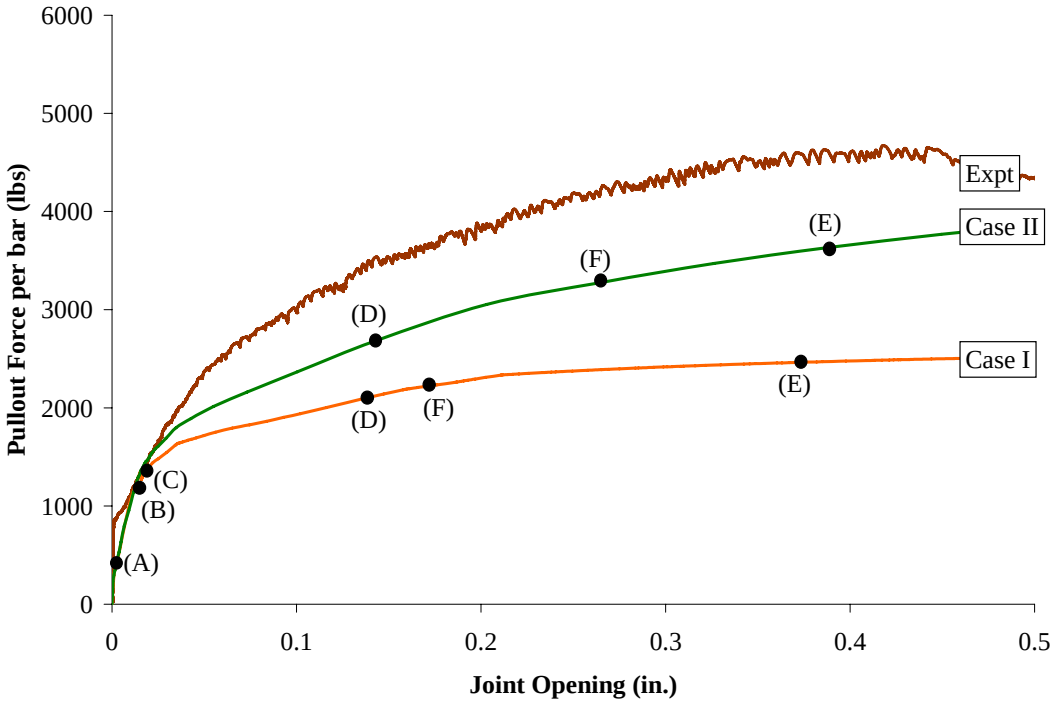

(b) Model for 5C18NU Test

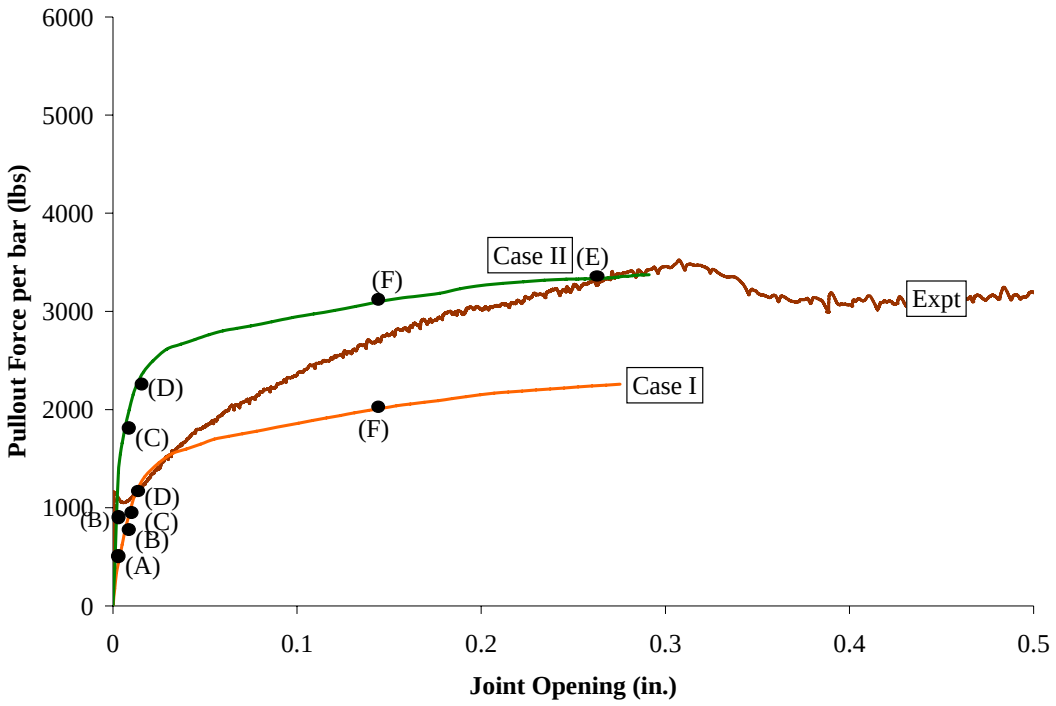

(c) Model for 5C18AM Test

Figure 6.9: Comparison of FEM and experimental data for five dowel bars with combined misalignment

6.3.4 CONCLUDING REMARKS ON THE 3D FINITE ELEMENT ANALYTICAL MODELS WITH EVENTS / MATERIAL DAMAGE LIMIT STATES

In all the finite element analytical models, stress concentration zones occurred in concrete at the joint face around misaligned dowel bars. The results from the 3D finite element models provide significant insight into the 3D stress states and the events or damage limit states in the pullout force-joint opening behavior of concrete pavement with misaligned dowel bars. These validated models, analytical modeling approaches, and events or damage limit states definitions can be used to further investigate the effects of dowel misalignment on the stresses and structural distresses, damage in realistic concrete pavements subjected to combined traffic and thermal loads.

A parametric study on the analytical model was conducted. The parameters that were varied and the results obtained from the analyses are presented in the next section.

6.4 ANALYTICAL PARAMETRIC STUDY

Finite element models were developed for ½", ¼" and ⅛" misaligned magnitudes for one- and two- dowel bars with non-uniform, uniform and alternate orientation of misalignments. Table 6.3 shows the various cases that were considered for the analytical parametric studies. Field investigations, laboratory studies and construction specifications have shown that extremely high misalignment magnitudes are detrimental to the concrete surrounding the dowel bar and cause distresses leading to failure of the pavement slab.

Table 6.3: Summary of the Finite Element Analysis conducted

Orientation	Magnitude		1 bar	2 bars		
	(in in.)	(in rad.)		U	NU	AM
Aligned	0	0	⊙	⊙		
Vertical	1/2	18	⊙	⊙	⊙	⊙
	1/4	36	⊙	⊙	⊙	⊙
	1/8	72	⊙	⊙	⊙	⊙
Horizontal	1/2	18	⊙	⊙	⊙	⊙
	1/4	36	⊙	⊙	⊙	⊙
	1/8	72	⊙	⊙	⊙	⊙
		Total	7	7	6	6

Two cases with different input parameters were considered for each of the finite element model analyses. Case I corresponds to the use of idealized friction coefficients (0.0 and 0.3 on the greased and uncoated sides) and idealized material properties (uniaxial compressive strength (f'_c) of 3500psi & tensile strength (f'_t) of 236 psi. Case II

corresponds to the use of friction coefficients measured by Shoukry (0.076 and 0.384 for greased and ungreased sides, respectively) and measured material properties of the hardened concrete specimens collected during actual laboratory tests. In all the analyses, the uniaxial compressive stress-strain curve was developed using the modified Popovics equations as given in Collins et al (1992). The fracture energy criterion developed by Hillerborg was used to model the tensile post peak failure behavior.

6.5 RESULTS AND DISCUSSION

The results obtained from the various analyses of the 3D finite element models are presented in the following subsections.

6.5.1 ONE MISALIGNED DOWEL BAR

Tables 6.4(a) and (b) present the joint openings corresponding to the occurrence of events or damage limit states for models with a single dowel bar with vertical or horizontal misalignment. Both for cases I and II are included in the tables. Figures 6.10 (a) and (b), summarize the joint opening corresponding to the occurrence of events or damage limit states. These figures illustrate the results from the finite element analyses of the models with one misaligned dowel bar.

The results indicate that for a single misaligned dowel bar, the debonding / initial event (A) occurs at 0.003 in joint opening. The post slip behavior was governed by the magnitude of misalignment. The analytical results using case I (idealized) parameters and case II (measured) parameters indicate the occurrence of events / damage limit states (B), (C) and (D).

As shown in figure 6.10(a), for vertically misaligned dowel bars with Case I input parameters the occurrence of events / damage limit states (B) and (C) gets delayed as the misalignment magnitude is reduced. A similar trend is observed for models with Case II input parameters. As shown in figure 6.10(b) events / damage limit state (D) occurs for model 1V18 at joint opening of 0.15 in. As shown in figures 6.10 (a) and (b), for horizontally misaligned dowel bars with case I and case II input parameters, material events / damage limit states (B), (C) and (D) occur for the 1H18 and 1H36 analytical models. Limit state (D) does not occur in the 1H72 models using cases I and II input parameters.

Table 6.4(a): Summary of the Damage Limit States and Joint Opening (in.) for Case I
Case I: 0.30 and 0.0

	1A	1V18	1V36	1V72	1H18	1H36	1H72
(A)	0.0030	0.0030	0.0030	0.0030	0.0030	0.0030	0.0030
(B)	-	0.0152	0.0260	0.0788	0.0018	0.0258	0.0532
(C)	-	0.0153	0.0372	0.1173	0.0018	0.0372	0.1173
(D)	-	-	-	-	0.214	0.349	-
(E)	-	-	-	-	-	-	-
(F)	-	-	-	-	0.260	-	-

Table 6.4(b): Summary of the Damage Limit States and Joint Opening (in.) for Case II
Case II: 0.384 and 0.076

	1A	1V18	1V36	1V72	1H18	1H36	1H72
(A)	0.003	0.0030	0.0030	0.0030	0.0030	0.0030	0.0030
(B)	-	0.0257	0.0257	0.0557	0.0342	0.0273	0.0532
(C)	-	0.030	0.0372	0.1198	0.051	0.0387	0.1045
(D)	-	0.1476	-	-	0.2281	0.437	-
(E)	-	-	-	-	0.425	-	-
(F)	-	-	-	-	0.217	-	-

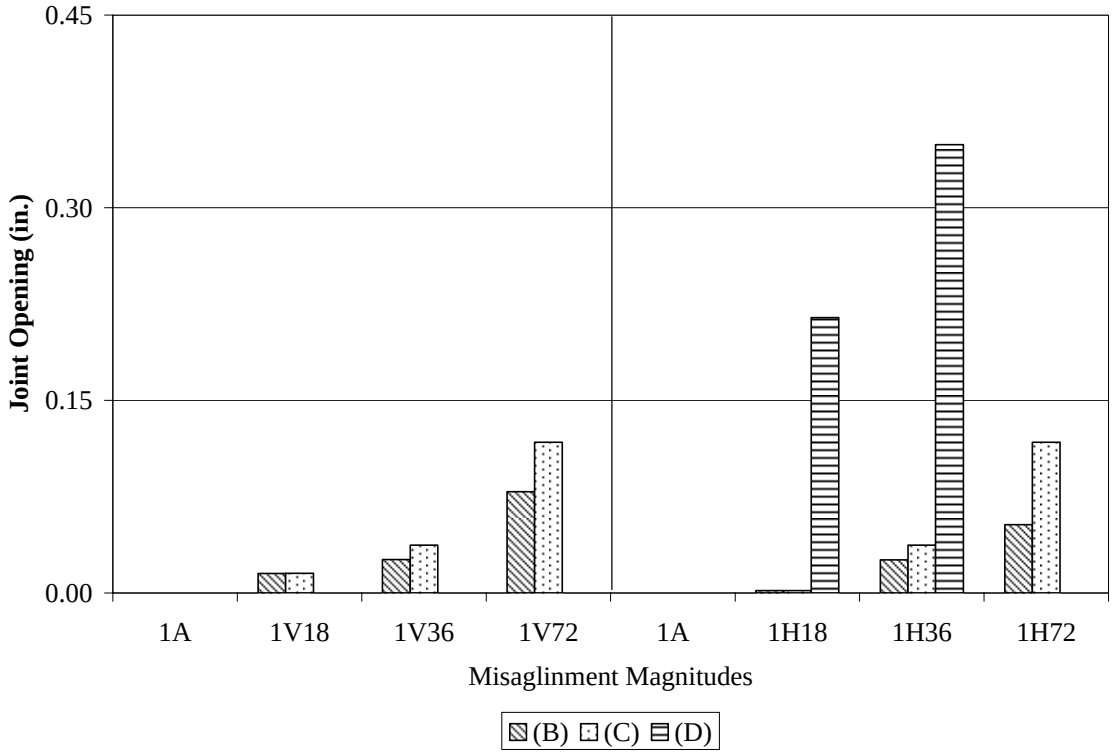

(a) Case I Analysis results

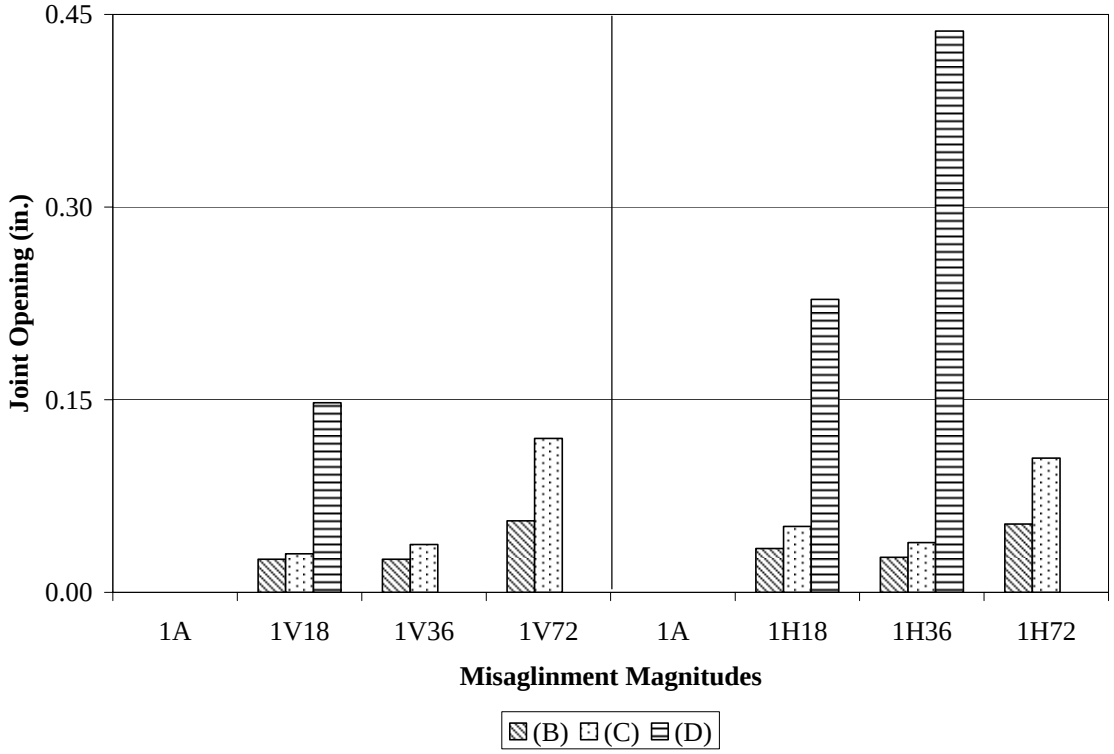

(b) Case II Analysis results

Figure 6.10: Summary of Joint Opening Behavior and Limit States of single misaligned dowel bars

6.5.2 TWO MISALIGNED DOWEL BARS

Tables 6.5(a-b) and 6.6 (a-b), present the joint openings corresponding to the occurrence of events on damage limit states for models with dowel bars with vertical or horizontal misalignment. Both cases I and II input parameters are included in the tables. Figures 6.11 to 6.14 present graphical summaries of the joint opening corresponding to the occurrence of events / damage limit states (B –D) in the analysis.

The analysis results for the models with vertically misaligned dowel bars are shown in figures 6.11 and 6.12 for case I and II input parameters. The results show that as the dowel misalignment increases from 1/72 radians to 1/18 radians, the events (B) and (C) occur for smaller joint openings. This trend is observed for pavements with less than 0.125 in joint opening. Events (D), (E) and (F) did not occur for models with two dowel bars with uniform or alternate misalignments up to 1/18 rad. These events occur for models with two dowel bars with non-uniform misalignment is more detrimental than uniform or alternate misalignment. As shown in figure 6.11(b) and 6.12(b) the event or damage limit state (F) occurs first for smaller joint opening followed by events (D) and (E). Thus for non uniform vertical misalignment significant tensile cracking (F) occurs before significant crushing in compression. This endorses the finding that non-uniform vertical misalignment can be more detrimental.

Table 6.5(a): Summary of the Damage Limit States and Joint Opening (in.) for Case I with Vertically Misaligned dowel bars
Case I: 0.30 and 0.0

	2A	2V18NU	2V36NU	2V72NU	2V18U	2V36U	2V72U	2V18AM	2V36AM	2V72AM
(A)	0.0020	0.0020	0.0020	0.0020	0.0020	0.0020	0.0020	0.0020	0.0020	0.0020
(B)	-	0.0101	0.0227	0.0512	0.0152	0.0227	0.0594	0.0152	0.0237	0.0494
(C)	-	0.0227	0.0342	0.0769	0.0342	0.0512	0.0879	0.0513	0.0351	0.0835
(D)	-	0.3395	0.4987	0.9803	-	-	-	-	-	-
(E)	-	0.3369	0.6230	-	-	-	-	-	-	-
(F)	-	0.2691	0.4987	-	-	-	-	-	-	-

Table 6.5(b): Summary of the Damage Limit States and Joint Opening (in.) for Case II with Vertically Misaligned dowel bars
Case II: 0.384 and 0.076

	2A	2V18NU	2V36NU	2V72NU	2V18U	2V36U	2V72U	2V18AM	2V36AM	2V72AM
(A)	0.0020	0.0020	0.0020	0.0020	0.0020	0.0020	0.0020	0.0020	0.0020	0.0020
(B)	-	0.0012	0.0227	0.0512	0.0121	0.0342	0.0569	0.0152	0.0227	0.0513
(C)	-	0.0248	0.0342	0.0769	0.0247	0.0768	0.0854	0.0342	0.0512	0.1730
(D)	-	0.5525	0.7208	1.0000	-	-	-	-	-	-
(E)	-	0.3352	0.5767	-	-	-	-	-	-	-
(F)	-	0.2327	0.4613	-	-	-	-	-	-	-

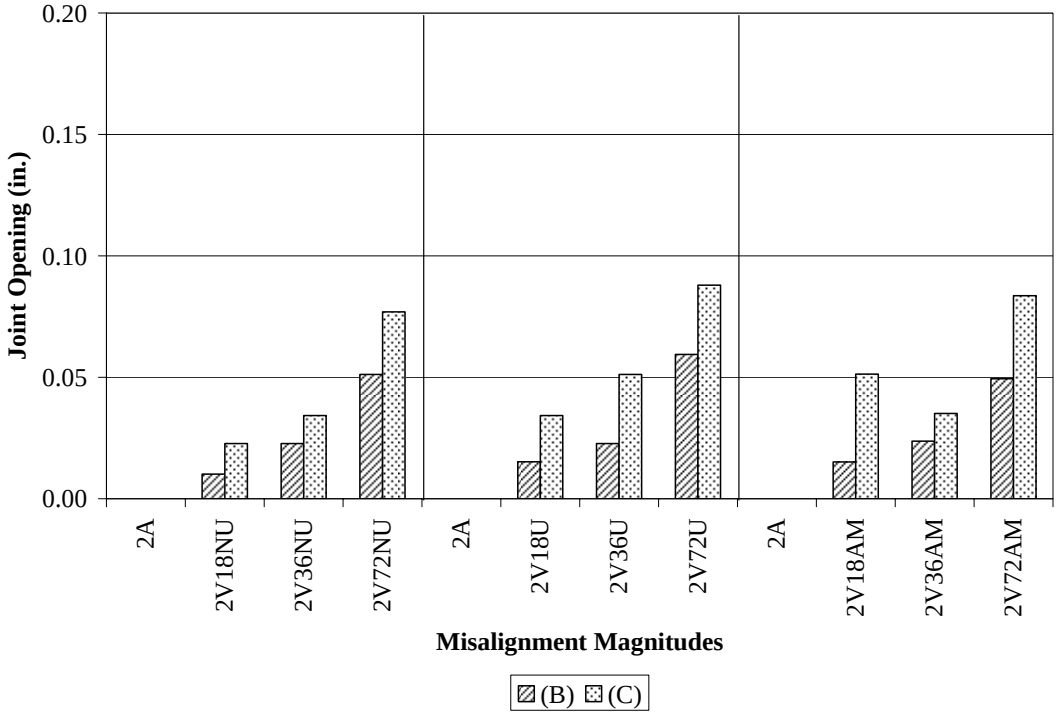

(a) Analysis results for events (B) and (C)

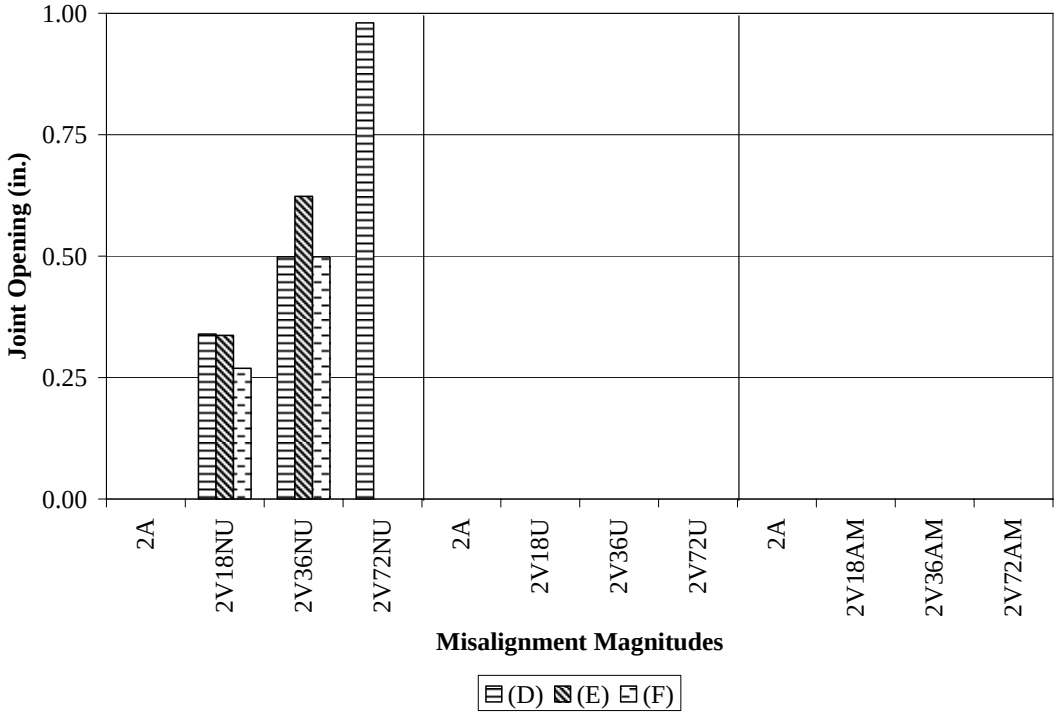

(b) Analysis results for events (D), (E) and (F)

Figure 6.11: Case I analysis summary of Joint Opening Behavior and Limit States of two vertically misaligned dowel bars

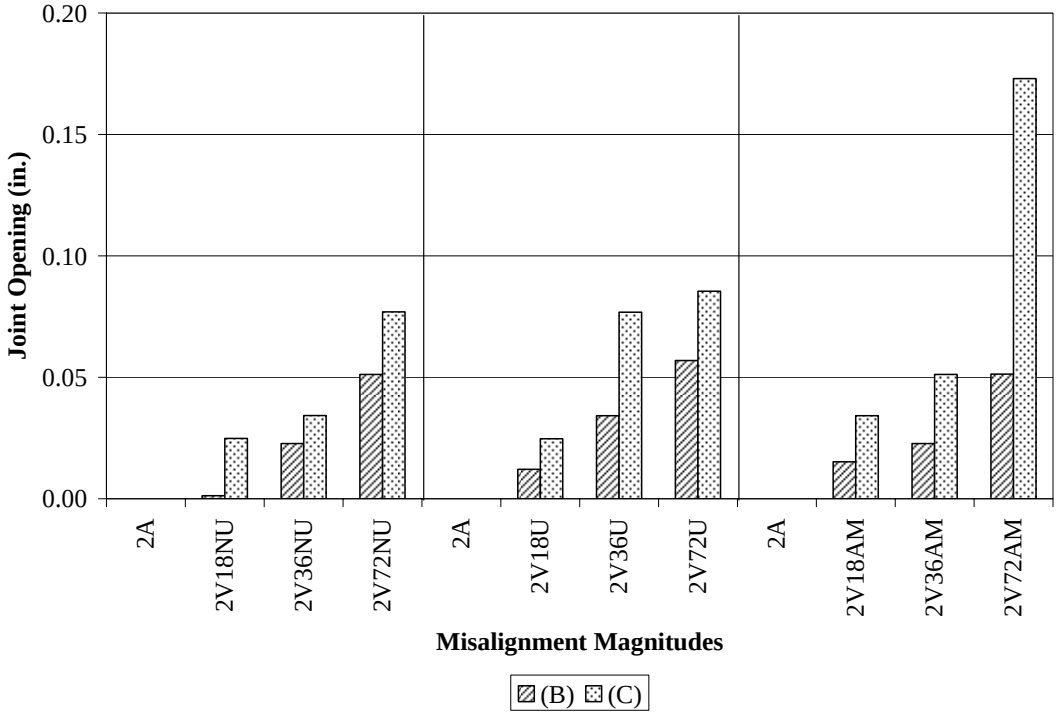

(a) Analysis results for events (B) and (C)

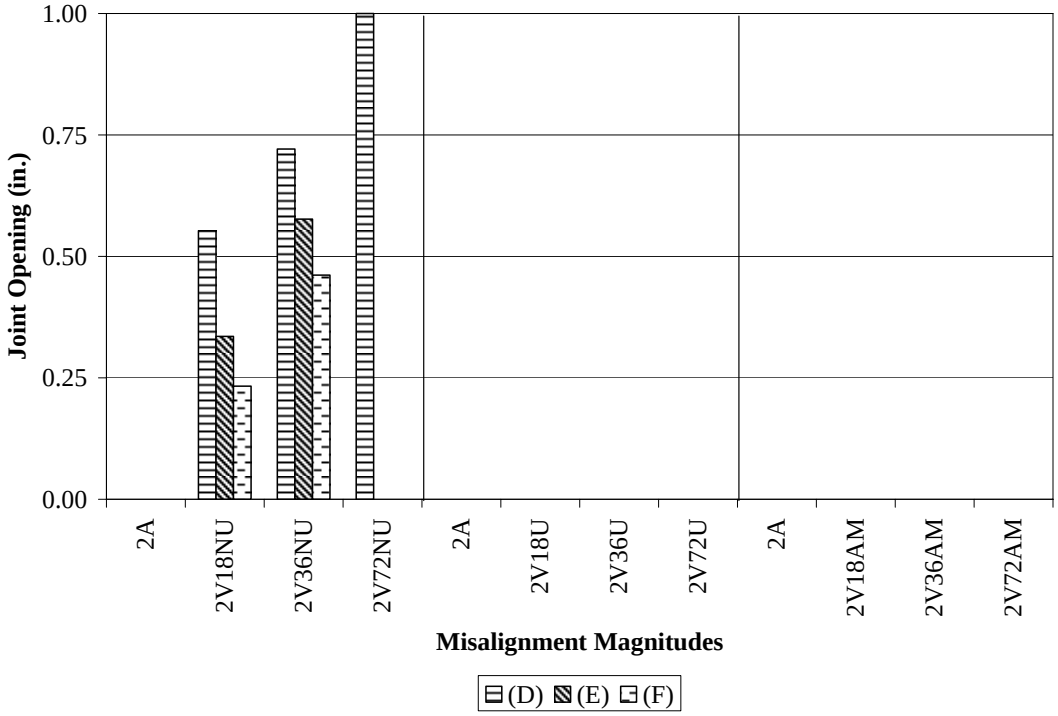

(b) Analysis results for events (D), (E) and (F)

Figure 6.12: Case II analysis summary of Joint Opening Behavior and Limit States of two vertically misaligned dowel bars

Horizontally misaligned dowel bars with case I and II input parameters are shown in figure 6.13 and 6.14. These results are similar to those for models with two vertically misaligned dowels. The results in table 6.6(a-b) and figure 6.11(a-b) and 12(a-b) show that as the dowel misalignment increases from 1/72 radians to 1/18 radians, the events (B) and (C) occur for smaller joint openings. This trend is observed for models with non-uniform, uniform and alternate misaligned dowel bars. Thus events (B and C) are observed for joint openings less than 0.125 in. Events (D), (E) and (F) occur for the models with uniform, non-uniform or alternate misaligned dowel bars. Figures 6.13(b) and 6.14(b) indicate that the type of dowel misalignment, i.e., the uniform, non-uniform, or alternate does not have a significant influence on the occurrence of events (D), (E) and (F) with respect to joint opening. These figures also indicate that the misalignment magnitude has a significant influence on the occurrence of events (D), (E) and (F). as shown in figure 6.13 and 6.14, as the dowel misalignment magnitude increased from 1/72 to 1/18 radians the events (D), E(D) and (F) occur for smaller joint openings. The event or damage limit state D occurs first followed by events (E) and (F). Thus, for horizontal misalignments, compression stress event (D) and significant crushing event (E) occur before significant cracking (F).

Table 6.6(a): Summary of the Damage Limit States and Joint Opening (in.) for Case I with Horizontally Misaligned dowel bars

CaseI: 0.30 and 0.0

	2A	2H18NU	2H36NU	2H72NU	2H18U	2H36U	2H72U	2H18AM	2H36AM	2H72AM
(A)	0.0020	0.0020	0.0020	0.0020	0.0020	0.0020	0.0020	0.0020	0.0020	0.0020
(B)	-	0.0101	0.0227	0.0372	0.0152	0.0227	0.0580	0.0127	0.0227	0.0522
(C)	-	0.0227	0.0342	0.0799	0.0342	0.0416	0.0836	0.0402	0.0512	0.1163
(D)	-	0.2410	0.3844	0.7526	0.3332	-	0.9105	0.2623	0.3969	0.8281
(E)	-	0.2933	0.5190	-	0.5452	0.7860	-	-	0.5430	-
(F)	-	0.2717	0.4998	-	0.4101	0.7860	-	0.2879	0.5430	-

Table 6.6(b): Summary of the Damage Limit States and Joint Opening (in.) for Case II with Horizontally Misaligned dowel bars

CaseII: 0.384 and 0.076

	2A	2H18NU	2H36NU	2H72NU	2H18U	2H36U	2H72U	2H18AM	2H36AM	2H72AM
(A)	0.0020	0.0020	0.0020	0.0020	0.0020	0.0020	0.0020	0.0020	0.0020	0.0020
(B)	-	0.0101	0.0192	0.0372	0.0121	0.0342	0.0542	0.0152	0.0203	0.0522
(C)	-	0.0219	0.0382	0.0799	0.0362	0.0769	0.0799	0.0342	0.0494	0.0779
(D)	-	0.2801	0.4326	0.7815	0.3736	0.3844	0.8680	0.2659	0.3851	0.9189
(E)	-	0.2972	0.5238	-	0.4919	0.6151	-	0.3457	0.5933	-
(F)	-	0.2460	0.6059	-	0.3352	0.7304	-	0.2563	0.5933	-

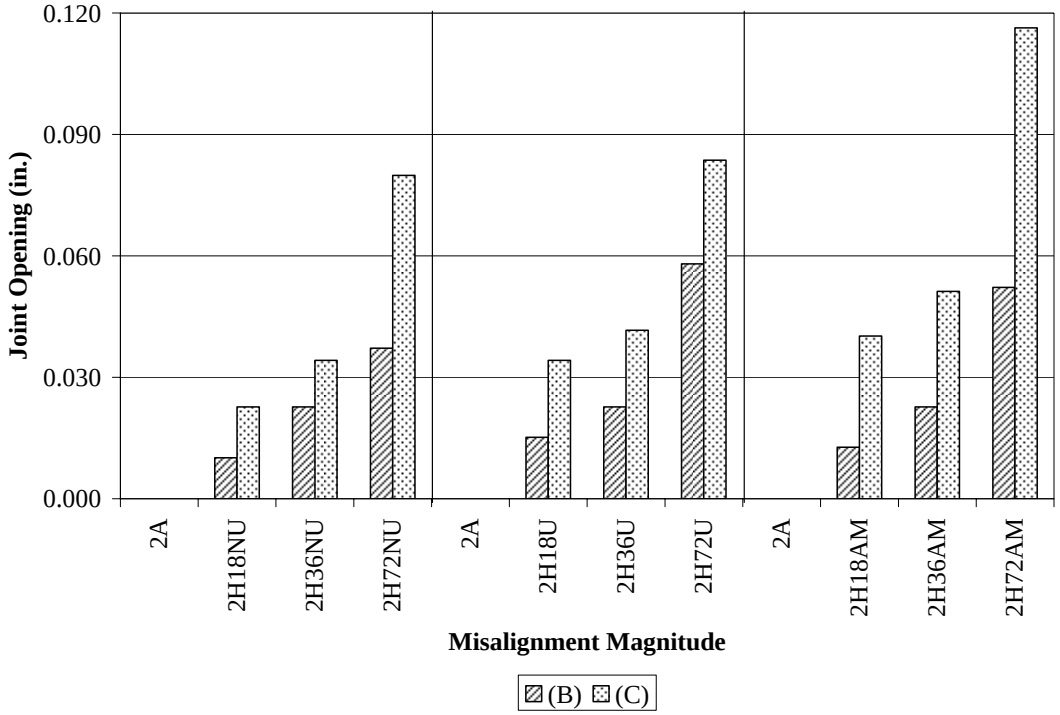

(a) Analysis results for material failure states (B) and (C)

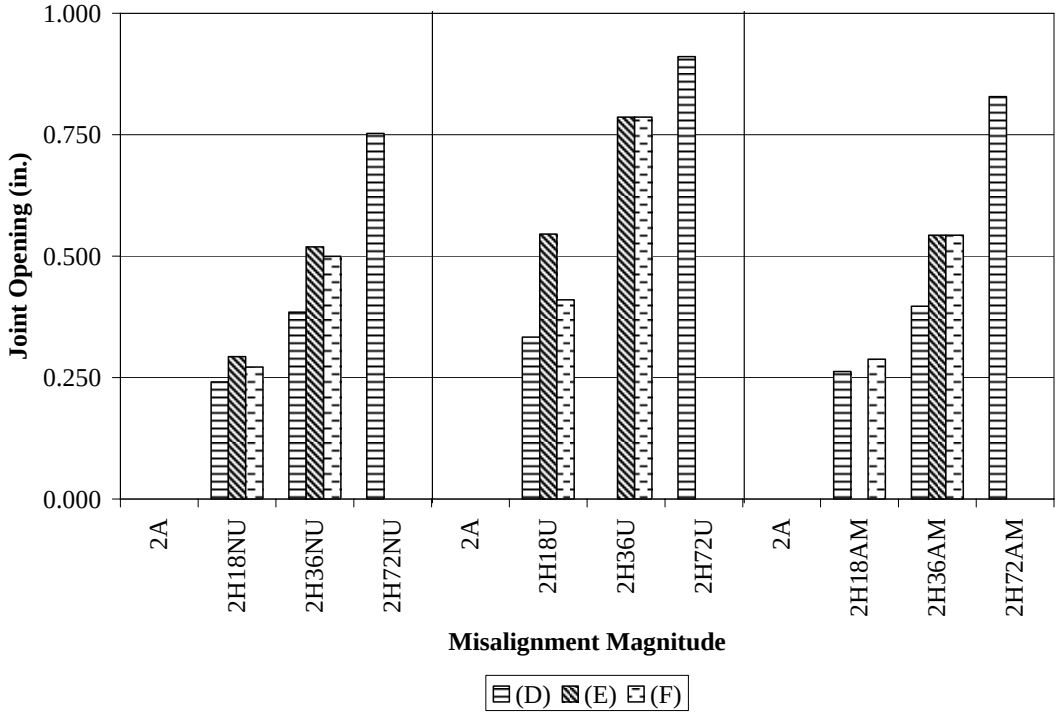

(b) Analysis results for material failure states (D), (E) and (F)

Figure 6.13: Case I analysis summary of Joint Opening Behavior and Limit States of two horizontally misaligned dowel bars

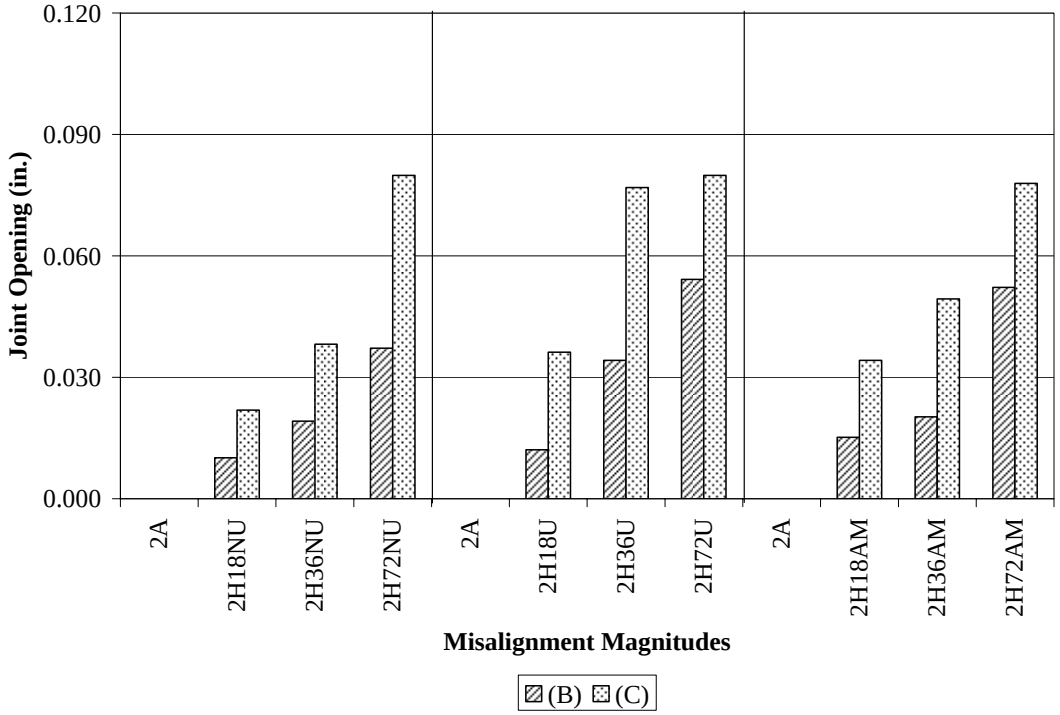

(a) Analysis results for material failure states (B) and (C)

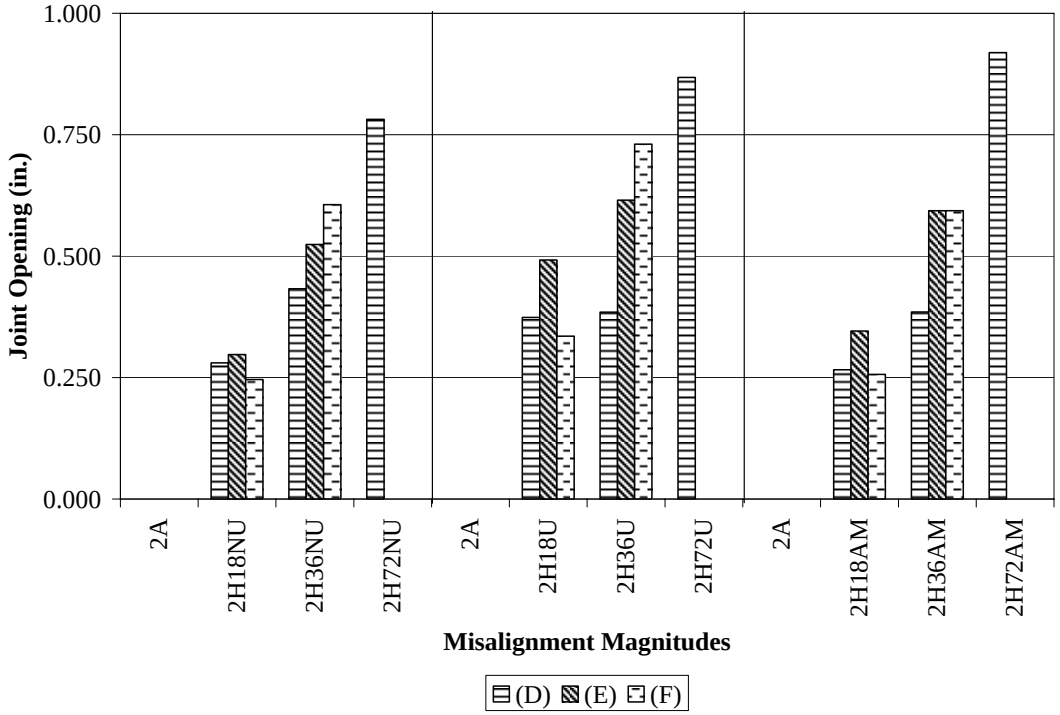

(b) Analysis results for material failure states (D), (E) and (F)

Figure 6.14: Case II analysis summary of Joint Opening Behavior and Limit States of two horizontally misaligned dowel bars

6.5.3 CONCLUDING REMARKS ON THE RESULTS OF THE ANALYTICAL PARAMETRIC STUDIES

Three dimensional finite element models were developed and analyzed to investigate the effects of dowel misalignment magnitude and type on the behavior, 3D stress states and events or damage limit states in jointed pavements. An analytical matrix was developed to conduct the parametric studies. The parameters included were the number of misaligned dowels (1 or 2), the misalignment type (non-uniform, uniform or alternate), and the misalignment magnitude (aligned to 1/18 radians). The analytical results provide significant insight into the behavior, 3D stresses and events or damage limit states. These results indicate that:

(1) For models with one misaligned dowel bar, horizontal misalignment can be more detrimental than vertical misalignment. As the magnitude of misalignment increases, the events occur for smaller joint openings. Events B and C occur for joint openings less than 1/8 in. Event D occurs for joints with horizontally misaligned dowels or vertically misaligned dowel with 1/18 radians magnitude. Events E and F do not occur.

(2) For models with two vertically misaligned dowels, the effects of non –uniform misalignment can be more detrimental than uniform or alternate misalignment. As the misalignment magnitude increases, these events occur for smaller joint openings. Significant tensile cracking (Event F) occurs before compression crushing.

(3) For models with horizontally misaligned dowels, the misalignment orientation (uniform, non-uniform or alternate) does not have a significant influence on the occurrence of events D, E, and F. as the dowel misalignment magnitude increases, these

events occur for smaller joint openings. Compression stresses and crushing occur before significant tensile cracking.

6.6 CONCLUSIONS AND RECOMMENDATIONS

Three dimensional finite element models were developed and analyzed to investigate the effects of dowel misalignment magnitude and type on the behavior, 3D stress states and events or damage limit states in jointed pavements.

The localized material states (stress and strain) and the corresponding events A – F will have a significant influence on the *cyclic material fatigue life* at the distress locations. In the absence of experimental data and models relating the localized stresses and strains to the fatigue life of the pavement, the rational choice would be limit the localized stresses (S_{max} and S_{min}) to the material uniaxial stress capacities (f'_t and f'_c), i.e., to events C and D. These were the recommendations made to the Department of Transportation.

An analytical matrix was developed to conduct the parametric studies. The parameters included were the number of misaligned dowels (1 or 2), the misalignment type (non-uniform, uniform or alternate), and the misalignment magnitude (aligned to 1/18 radians). The analytical results provide significant insight into the behavior, 3D stresses and events or damage limit states. These results indicate that:

(1) The debonding limit state occurs almost instantaneously irrespective of the dowel misalignment type, magnitude, orientation, etc. in the concrete slab.

(2) As the misalignment magnitude (angle of skew) is reduced, the occurrence of a damage limit state is delayed as the joint is opened.

(3) These analytical models, approaches and limit states are recommended for future analytical work on realistic pavement joints with thermal and traffic loads.

(4) As the magnitude of misalignment increases, the events occur for smaller joint openings. Events B and C occur for joint openings less than 1/8 in. The effects of non – uniform misalignment can be more detrimental than uniform or alternate misalignment. Events D, E and F occur at larger joint openings. As the misalignment magnitude increases, these events occur for smaller joint openings.

CHAPTER 7

PRELIMINARY INVESTIGATION OF LOAD EFFECTS COMBINED WITH DOWEL MISALIGNMENTS

7.1 INTRODUCTION

A typical JPCP consists of several components. These include multiple unreinforced concrete slabs connected by dowels that assist in transferring load and. The concrete slab rests on the base layer which distributes the load to the sub-base and the natural sub-grade, illustrated in figure 2.1 chapter 2. A preliminary investigation on the load effects combined with dowel misalignments is presented in this chapter.

The objective of this study was to understand and capture the physical behavior of typically misaligned dowel bars in a dowel jointed concrete pavement slab subjected to joint opening and truck loading. This chapter presents the assumptions and limitations of the three dimensional finite element models that are developed as a part of this study. This is followed by the development of the bond model and the boundary conditions that were used to simulate an as constructed pavement slab. Finally, this chapter presents the various typical dowel misalignment cases that were analyzed, the behavior observed in the analytical models and the results obtained from the analyses.

7.2 ASSUMPTIONS AND LIMITATIONS OF THE FINITE ELEMENT MODEL

Simple assumptions were made to model the realistic pavement slab to limit the size and computational capability of the three dimensional finite element analyses. Finite element models of three dowel bars with typical misalignment magnitudes and orientations were developed assuming that in the wheel path only three dowel bars are influenced by the

axle loads. The dowel – concrete bond interaction model developed in the earlier task of this research was used.

Like in the earlier finite element models, the pavement slab was only subjected to joint opening and not thermal cycling such as joint opening and closing. To facilitate joint opening due to thermal expansion, the concrete slab and base were not bonded to each other. The coefficient of friction between the concrete slab and the base layer was assumed zero as no calibrated laboratory or field investigation was available. Secondly, the finite element model developed in this study focuses on the effects of localized stress formation surrounding the misaligned dowel bar. The influence of fatigue loading was not considered in the finite element analyses. The wheel loads were static monotonically increasing from zero to full load and includes a dynamic impact (magnification) factor of two (Chopra, 2000). Instead of the complete truck, loading under a set of dual wheels of a tandem axle was considered.

7.3 DEVELOPMENT OF THE FINITE ELEMENT MODEL

To model the concrete slab, steel dowel bar, base and sub-base layers, three dimensional (3D) first order reduced integration continuum elements (C3D8R - Bricks) were used. These elements are versatile in modeling simple linear analysis and also complex nonlinear analyses involving material nonlinearity, plasticity and large deformations. To simulate the interaction between the layers of the pavement cross-section, constraint and contact interactions in ABAQUS (2004) are used and presented in the following sections. Compared to the finite element developed in this initial study, the ILLISLAB model (Tabatabaie et. al. 1978) uses elastic homogeneous medium thick plates and elastic

material properties. It considered beam elements with limited degrees of freedom to model the dowel-concrete interaction bond. Similarly, comparing the finite element model developed in this study, the EverFE (Davids et al, 1998) software uses a twenty noded quadratic hexahedral elements to discretize the slabs and its underlying layers. Compared to using complete 3D continuum elements for both the dowel bar and concrete, the EverFE software uses an embedded flexural finite elements.

To model the complex triaxial stress states in the concrete surrounding the dowel bar, the concrete slab mesh was made up of smaller size brick elements and gradual increase in size away from the dowel bar. The base and sub-base layers are extended 12 in. on each side of the concrete slab to reduce effects of side boundary conditions on the slab response. The wheel loads were applied using discrete rigid elements (R3D4). The sub-grade is modeled as a Winkler foundation consisting of a series of springs to ground. These elements are a simple way of including the stiffness effects of a support without actually having to model the details of the support.

7.3.1 DIMENSIONS OF THE ANALYTICAL MODEL

A standard MDOT specified pavement cross section was considered in the finite element analyses, as shown in figure 7.1 (a). The slab dimensions for the single dowel bar and three dowel bar finite element models are shown in figures 7.1(b) and (c).

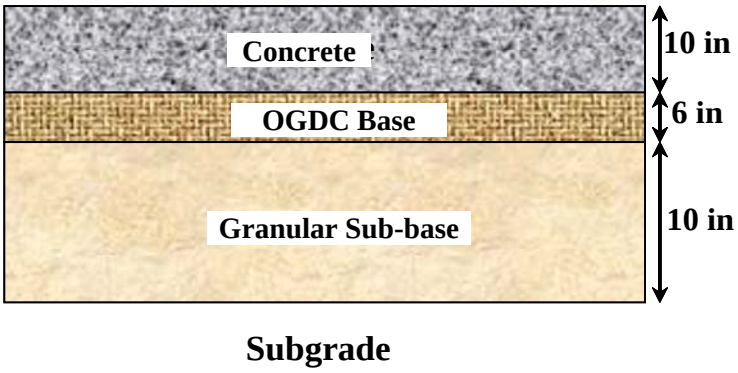

(a) Typical pavement cross section

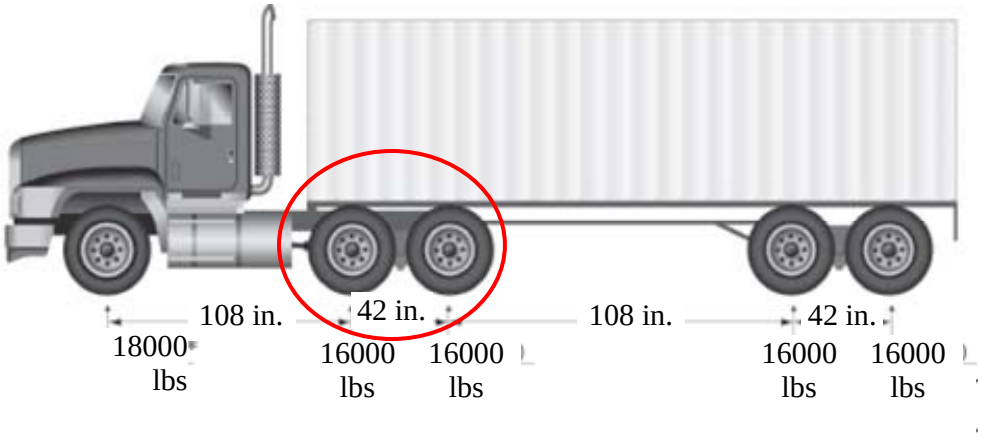

(b) Typical truck loading

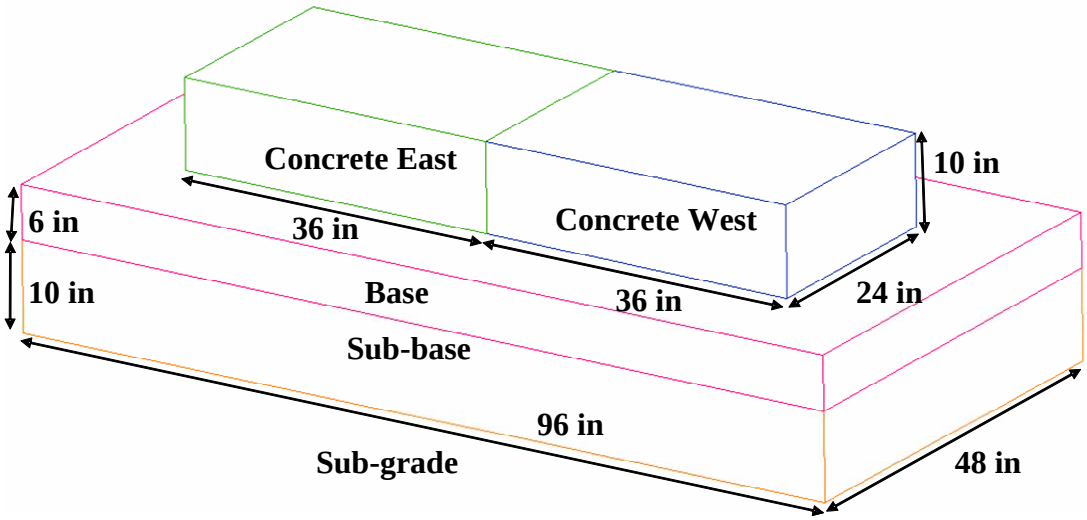

(c) Dimensions for a single dowel bar model

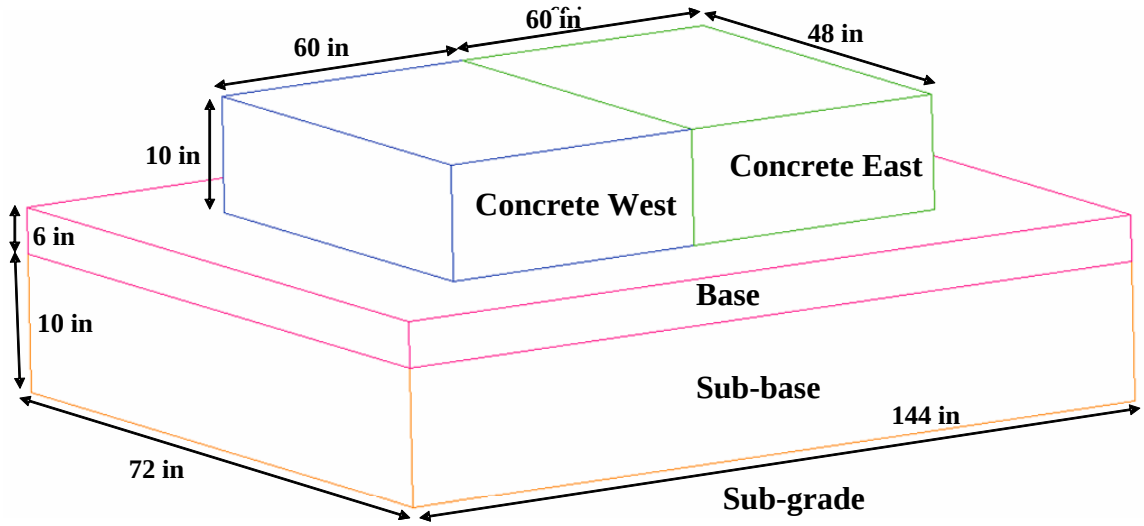

(d) Dimensions for three dowel bar model

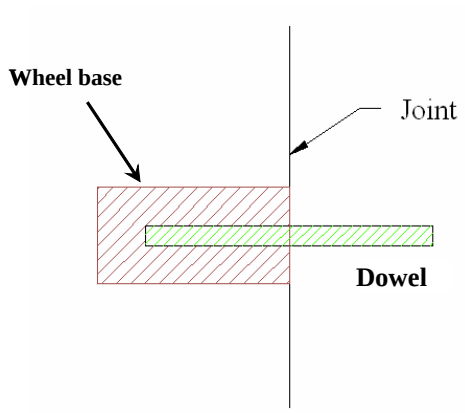

(e) Plan view of the location of wheel base for single dowel model

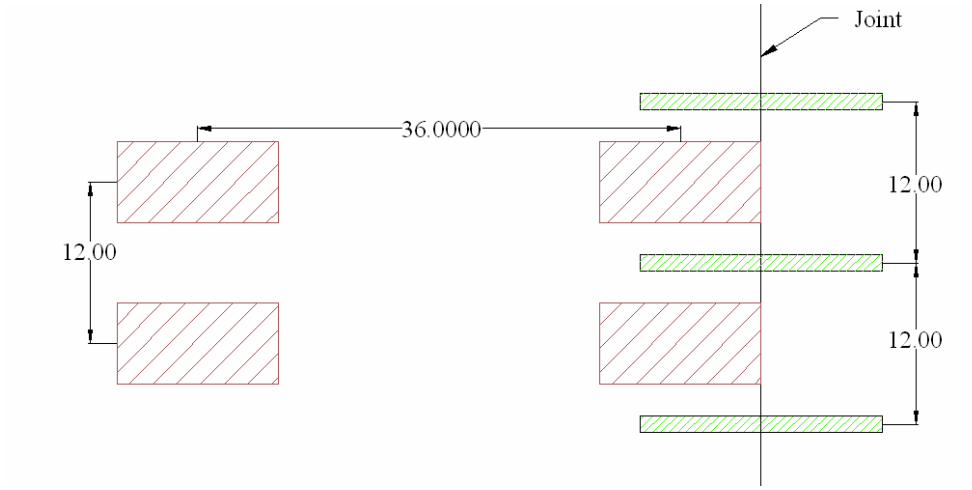

(f) Plan view of the position of wheel base of dual wheel tandem axle

Figure 7.1: Dimensions and location of various parts of the pavement slab and wheel base in the finite element model

Single dowel bar model:

The first model consisted of a single dowel bar with skew misalignment magnitudes ranging from 0 to 1/18 radians (½ in. over 9 in. length). The finite element model was made up of two concrete slabs 36 in. x 24 in. x 10 in. connected at the transverse joint using a single steel dowel bar 18 in. long and 1.25 in. diameter. The dowel bar is placed at mid-height and embedded 9 in. on both sides of the concrete slab. The concrete slab is supported on a base layer 96 in. x 48 in. x 6 in. and a sub-base layer of 96 in. x 48 in. x 10 in. The sub-grade is modeled using the Winkler foundation with spring stiffness of 150 psi/in.

A monotonically static load up to 16000 lbs was applied on the concrete slab, directly on top of the dowel bar on one side of the joint, as shown in figure 7.1 (c). This assumed high load was applied to understand the effects of misalignment after loading under a single dowel bar. The applied load is four times the actual wheel load of 4000 lbs. The load from one line of wheels of the dual wheel tandem gives 8000 lbs multiplied by an assumed dynamic impact factor of two.

Three dowel bar model:

The second model consisted of three dowel bars with typical skew misalignment magnitudes ranging from 0 to 1/36 radians (¼ in. over 9 in. length). The FE model is made up of two concrete slabs 60 in. x 48 in. x 10 in. connected at the transverse joint using a three steel dowel bars 18 in. long and 1.25 in. diameter. The dowel bars are spaced 12 in. on center at mid-height and embedded 9 in. on both sides of the concrete slab. The concrete slab is supported on a base layer 144 in. x 72 in. x 6 in. and a sub-base

layer of 144 in. x 72 in. x 10 in. The sub-grade is modeled using the Winkler foundation with spring stiffness of 150 psi/in. A monotonically static load of 8000 lbs on each of the wheels, as shown in figure 7.1 (d), is applied on one side of the concrete slab at the joint face. Again a dynamic magnification factor of two was assumed and multiplied to each 4000 lb. wheel load.

Table 7.1 presents the various cases that were considered in this preliminary investigation. In this table, the nomenclature used to identify a case study consists of the number of dowel bars (1 or 3), the misalignment type (Aligned, Vertical or Horizontal), the misalignment magnitude (18 represents 1/18 radians) and the misalignment orientation (NU or AM), where non uniform misalignment orientation represents all dowel bars are misaligned in opposite direction and alternate misalignment represents the only the center dowel bar having a misalignment. For example, specimen 3V72NU in Table 7.1 has all three dowel bars with non-uniform vertical misalignment of +1/72, -1/72 and +1/72 radians, i.e., 1/8 in. misalignment measured over 9 in. length of dowel.

The range of misalignment magnitudes from 0, 1/72 and 1/36 radians was chosen to minimize the number of finite element models. Also, only two types of misalignment orientations were considered, i.e., the non-uniform (NU) – worst case scenario and alternate (center misaligned - AM) misaligned dowel bars.

Table 7.1: Misalignment cases considered for single and three dowel bar loaded slabs

ID	Number of dowels	Misalignment type	Misalignment Magnitude (rad.)	Misalignment Magnitude (in.)
1A	1 dowel	Aligned	0	None
1V72		Vertical	$1/72$	$1/8$ in over 9 in.
1V36			$1/36$	$1/4$ in over 9 in
1V18			$1/18$	$1/2$ in over 9 in
1H72		Horizontal	$1/72$	$1/8$ in over 9 in.
1H36			$1/36$	$1/4$ in over 9 in
1H18			$1/18$	$1/2$ in over 9 in
3A	3 dowels	Aligned	0	None
3V72NU		Vertical	$+1/72; -1/72; +1/72$	$1/8$ in. over 9 in.
3V36NU			$+1/36; -1/36; +1/36$	$1/4$ in over 9 in
3V72AM			$0; -1/72; 0$	$1/8$ in. over 9 in.
3V36AM			$0; -1/36; 0$	$1/4$ in over 9 in
3H72NU		Horizontal	$+1/72; -1/72; +1/72$	$1/8$ in. over 9 in.
3H36NU			$+1/36; -1/36; +1/36$	$1/4$ in over 9 in
3H72AM			$0; -1/72; 0$	$1/8$ in. over 9 in.
3H36AM			$0; -1/36; 0$	$1/4$ in over 9 in

7.3.2 MATERIAL MODEL INPUT PARAMETERS

The concrete slabs were modeled using the concrete damaged plasticity model developed by Lubliner et al (1989), modified by Lee and Fenves (1998) and implemented in ABAQUS. Details of the various input parameters and calibration of the concrete model have already been presented in chapter 5. The steel dowel bar was modeled using an isotropic elastic multiaxial material model. The elastic modulus E_s for the models was based on results of standard ASTM (A370-97a) uniaxial tension tests on coupons

extracted from the steel dowel bars. The yield and ultimate stresses were not required because the dowel bar remained elastic throughout the analysis. The base and sub-base layers were modeled using the isotropic elastic multiaxial material model. The modulus of elasticity, poissons ratio and density used for the material model were obtained from Shoukry (2003). Furthermore, Table 7.2 presents some of the material input parameters that were used for the concrete slab, steel dowel bar, base, sub-base and sub-grade layers.

7.3.3 INTERACTION MODELS

The dowel concrete bond interaction model developed in the previous task of this research study was used. The spring force vs. pullout displacement behavior for the single dowel – concrete slab model was calibrated using an idealized curve derived from the 1A experimental data, shown in figure 7.1(a). For the three dowels – concrete slab model, the spring force vs. pullout behavior was calibrated using the experimental data from the three aligned dowel bars test specimen, as shown in figure 7.2(b).

Table 7.2: Material input parameters for the single and three dowel bar finite element models

Concrete Data		
Uniaxial Compressive Strength (f'_c)	=	3500 psi
Modulus of Elasticity ($0.7\ f'_c$)	=	3,372,000 psi
Tensile Strength (f'_t)	=	236 psi
Poisons ratio	=	0.18
Density	=	0.0868 lbs/in^3

Steel Data		
Type	=	Billet Steel
Modulus of Easticity	=	29,000 ksi
Poissons ratio	=	0.3
Density	=	0.282 lbs/in^3

Base Data		
Type	=	Open Graded Drainage Course
Modulus of Easticity	=	30,000 psi
Poissons ratio	=	0.3
Density	=	0.0758 lbs/in^3

Sub-base Data		
Type	=	Grannular Sub-base (sand)
Modulus of Easticity	=	15,000 psi
Poissons ratio	=	0.3
Density	=	0.0758 lbs/in^3

Subgrade Data		
Subgrade stiffness	=	150 psi/in
Modulus of elasticity	=	4000 psi
Poissons ratio	=	0.4
Density	=	0.0736 lbs/in^3

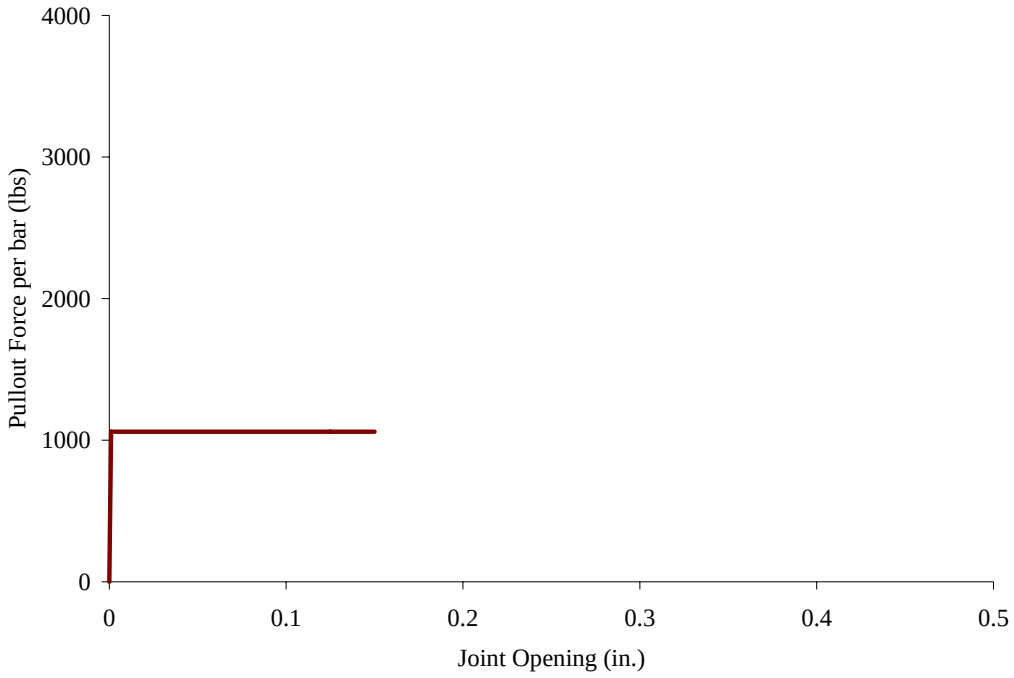

(a) Spring Force – Joint Opening for single dowel bar model

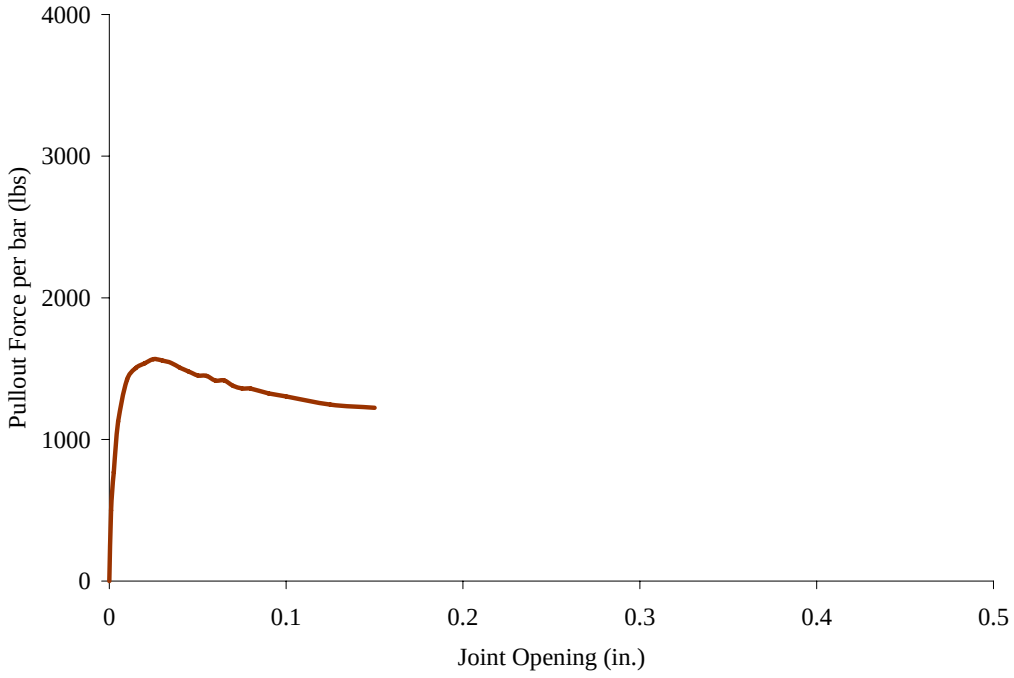

(b) Spring Force – Joint Opening for three dowel bar model

Figure 7.2: Spring Force vs. Joint Opening behavior used in the finite element models

Contact constraint equations were used between the various layers of the pavement cross-section. The OGDC layer is considered as an unbonded base, i.e., there is no friction between the concrete slab and the base layer. This constraint condition helps in modeling the OGDC base layer as a shear flexible layer that can carry normal loads (axle loads) but does not have any shear resistance thereby allowing it to simulate joint opening behavior due to thermal loads. The OGDC base layer and the granular sub-base layer are tied such that deformations in the base and sub-base layer are equal. The subgrade is modeled as an elastic Winkler foundation, i.e., a bed of elastic springs. figure 7.3 presents the various contact conditions used in the tangential and normal directions between the concrete, base, sub-base and sub-grade layers for both the single and three misaligned dowel bars finite element models.

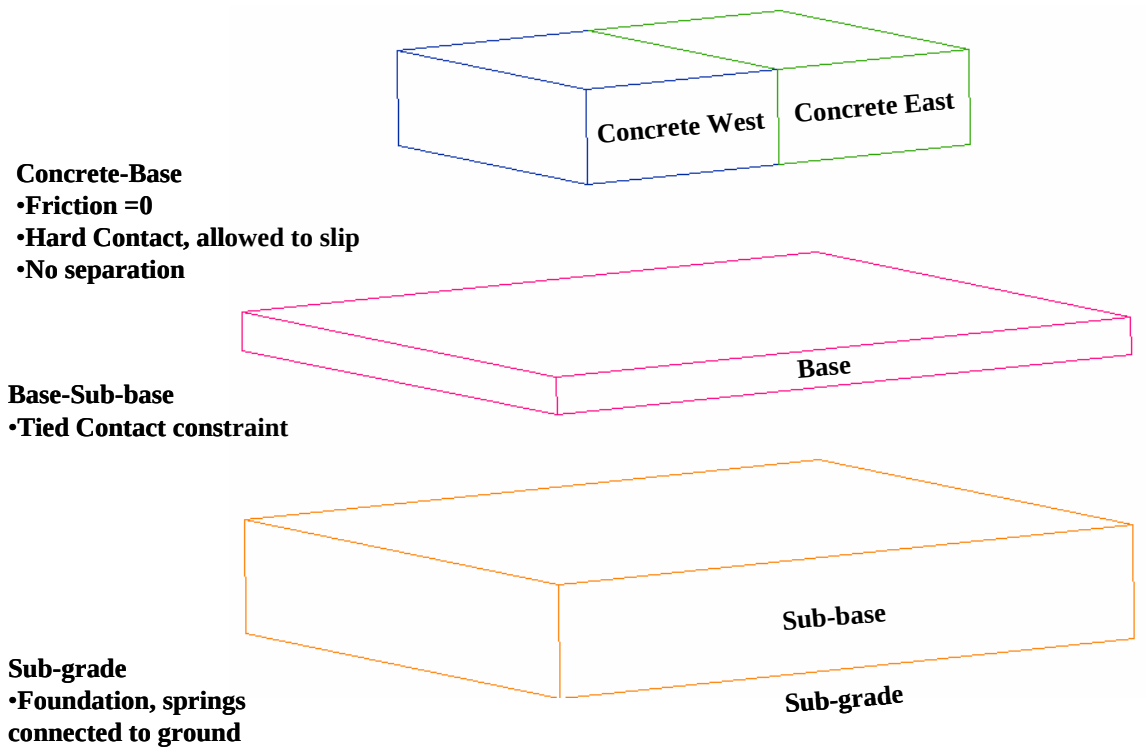

Figure 7.3: Typical constraint conditions used for the finite element model

7.3.4 LOADING AND BOUNDARY CONDITIONS

The first step of application of boundary conditions, only the gravity load is applied to allow for all the constraint conditions to take effect. The boundary and loading conditions are applied such that the model is restrained from any rigid body motion. The concrete slabs are then pulled apart to simulate a maximum joint opening of 1/8 in. due to thermal expansion of the pavement slab. This approximate joint opening was determined using the equation by Darter and Barenberg (1977),

$$\Delta L = C\ L\left(\alpha_t\ \Delta T + \varepsilon\right)$$

where, ΔL = joint opening caused by temperature change and drying shrinkage of concrete.

α_t = coefficient of thermal expansion of concrete (5 to 7 x 10^{-6} /^{o}F)

ε = drying shrinkage coefficient of concrete (0.5 to 2.5 x 10^{-4})

L = joint spacing or slab length = 15 ft.

ΔT = temperature range, i.e., temperature at placement minus lowest mean monthly temperature

C = adjustment factor due to slab-subbase friction, 0.8 for granular subbase.

Finally, the wheel loads are applied close to the face of the joint on one side of the pavement slab. The sequence of boundary and loading conditions is shown in figure 7.4.

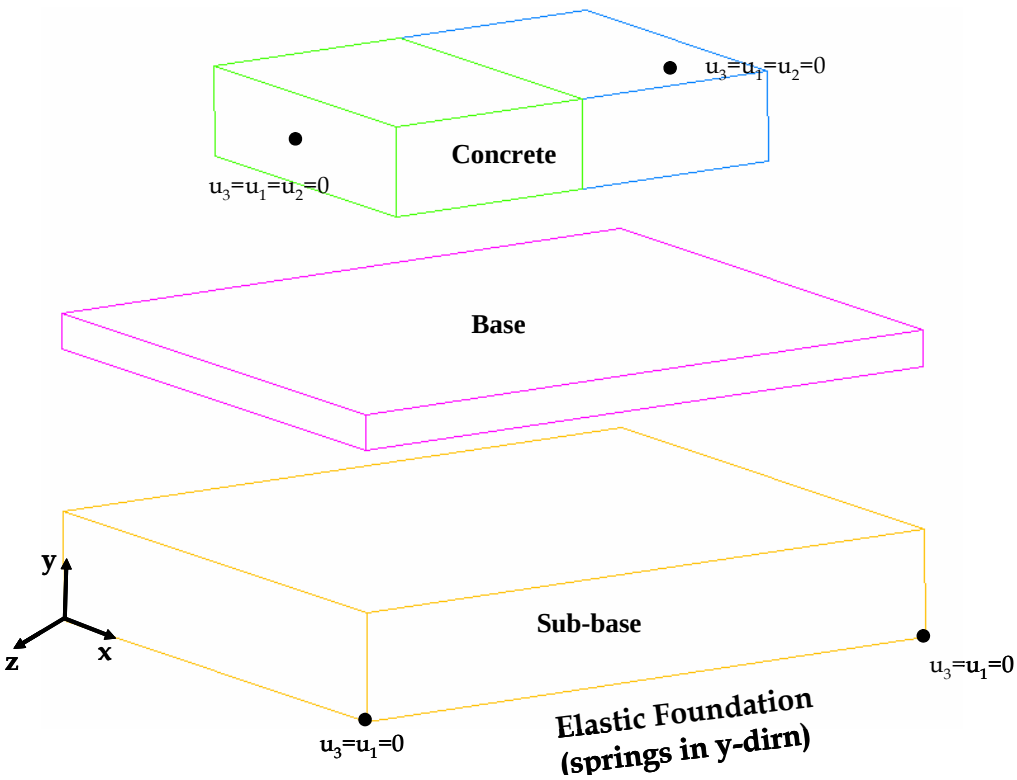

(a) Boundary Conditions for Step I of analysis (Gravity Loading)

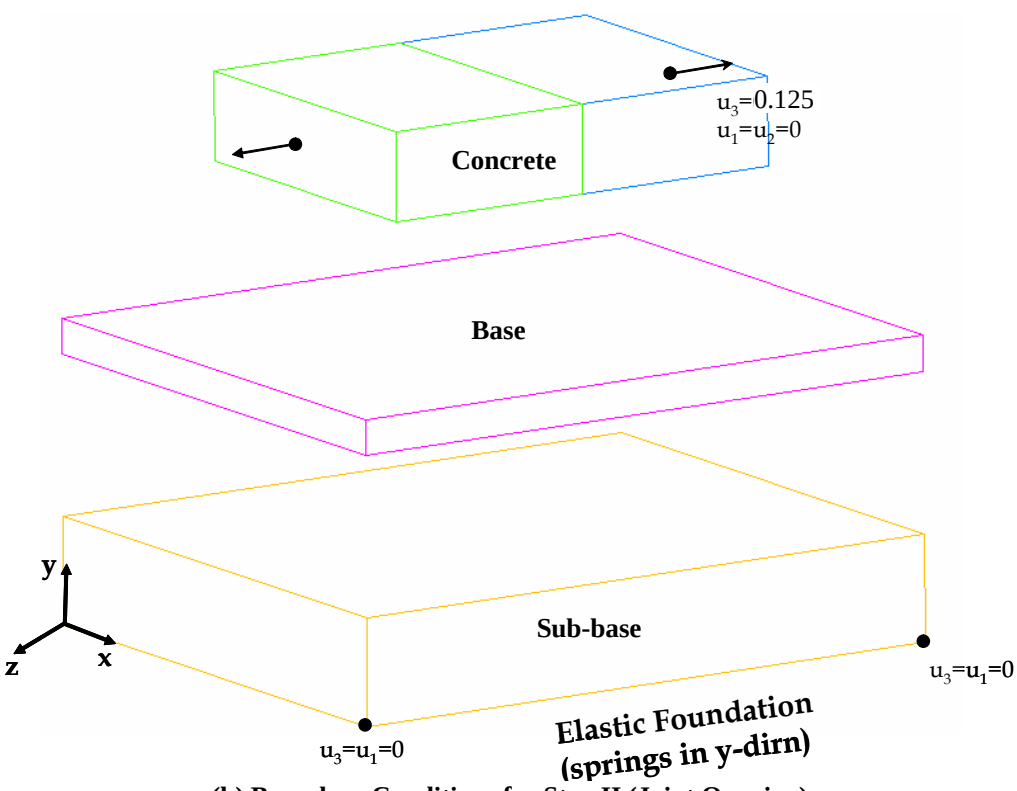

(b) Boundary Conditions for Step II (Joint Opening)

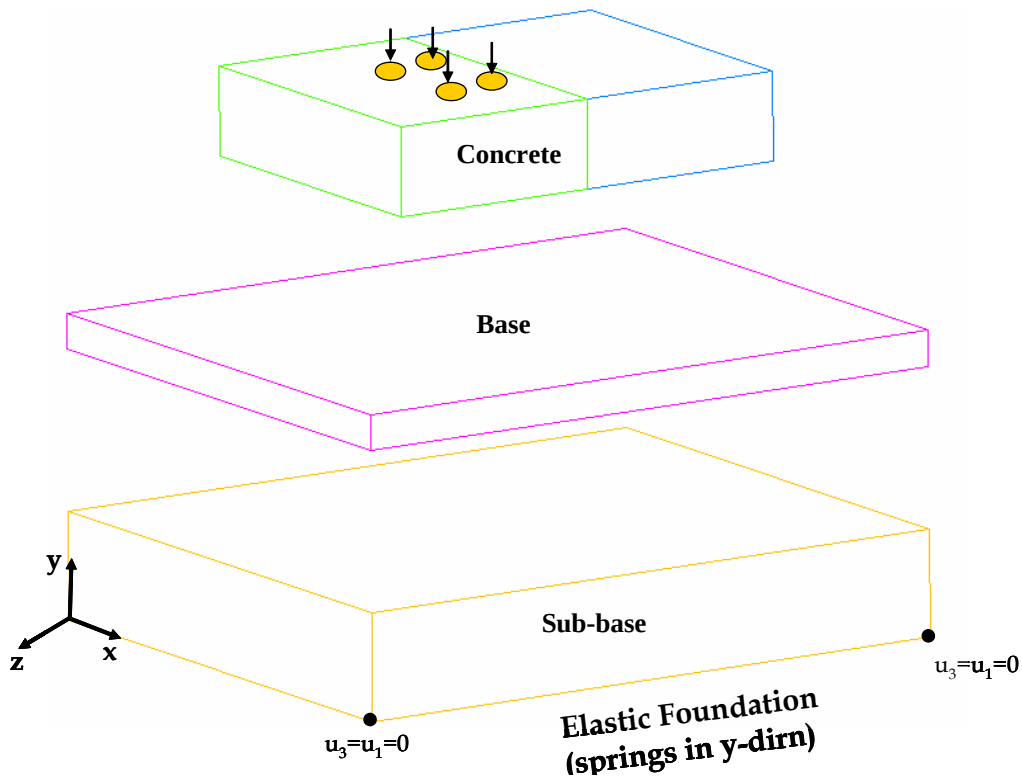

(c) Boundary Conditions for Step III (wheel loading)

Figure 7.4: Typical Boundary and Loading conditions on the pavement system

7.4 RESULTS AND DISCUSSION

The results obtained from the analytical models are summarized in this section. As observed in the FE models of the laboratory specimens, high stress concentration zones are formed in the concrete with joint opening. With the application of wheel loads on the concrete slab, the stress concentration zone in the concrete due to misalignment changes to localized bearing stresses in the concrete.

In the following sections, the results obtained from the finite element analysis of typical misaligned single and multiple dowel bars combined with loading are presented. In the results, the concrete slab where the load is applied is called the “loaded slab” (west side slab) and the opposite side is called the “unloaded side” (east side slab), as shown in Figure 7.5.

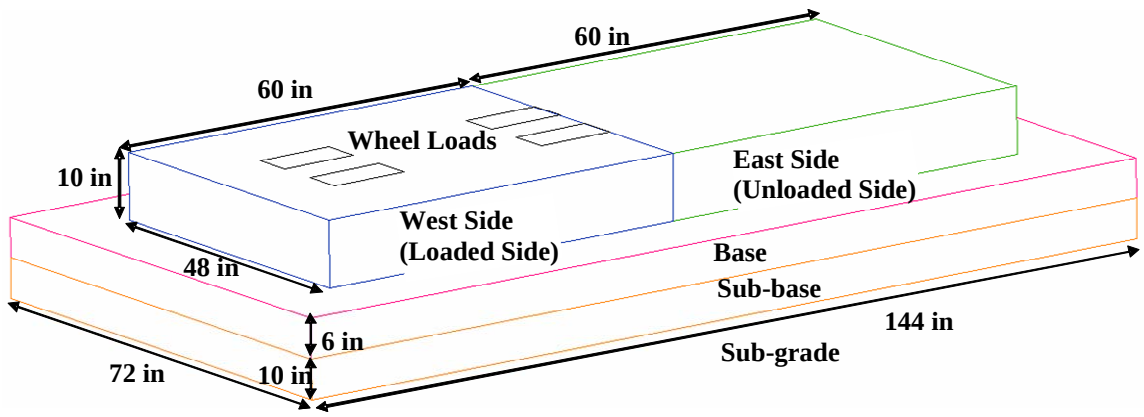

Figure 7.5: Loaded and unloaded sides of the concrete slab

Also, results with the label "before loading" are obtained after joint opening at location. The results labeled "after loading" are after the specified loading has been applied, shown in Figure 7.6 and 7.7.

7.4.1 SINGLE DOWEL BAR MODEL

This model was developed to understand the influence of a wheel load combined with the effects of a misaligned dowel bar and joint opening on the concrete surrounding the dowel bars. The change in stress localization from a stress concentration to a bearing stress is easily understood from the results of this model.

Figure 7.6 shows the minimum compressive stress zones in the concrete slab after joint opening and load application for a 1V72 finite element model. After a joint opening of 1/8 in., shown in Figure 7.6 (a), the stresses on the west and east side of the concrete slab are 1126.0 psi and 550.6 psi, respectively. The load is applied on the west side of the concrete slab and the stresses obtained after load application are 2314.0 psi and 1310.0 psi, respectively, shown in Figure 7.6 (b). Figure 7.7 shows the minimum compressive stress zones in the concrete slab in the 1H72 finite element model. Due to the misaligned dowel bar stress concentration zones are formed in a horizontal plane after joint opening

as shown in Figure 7.7 (a). These stress concentration zones change location when wheel loads are applied on the concrete slab. The bearing stress zones formed under the wheel load in concrete surrounding the dowel bar are shown in figure 7.7(b). The stresses in the concrete surrounding the dowel bar at a joint opening of 1/8 in. on the west and east side are 965.5 psi and 927.1 psi respectively. After load application the bearing stresses on the west and east side are 2392.0 psi and 1213.0 psi

There is an increase in the tensile and compressive stresses and strains magnitude after load application on both the loaded (west) and unloaded (east) side of the concrete slab. The trend showing an increase in stresses and strains for all the cases of vertically and horizontally misaligned bars is shown in figures 7.8 and 7.9

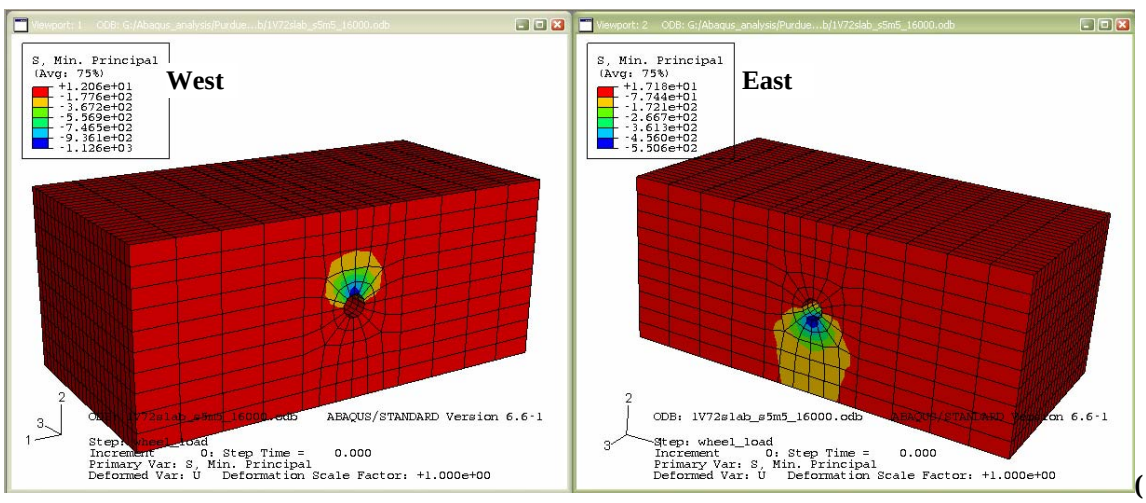

a) Stresses after a joint opening of 1/8 in.

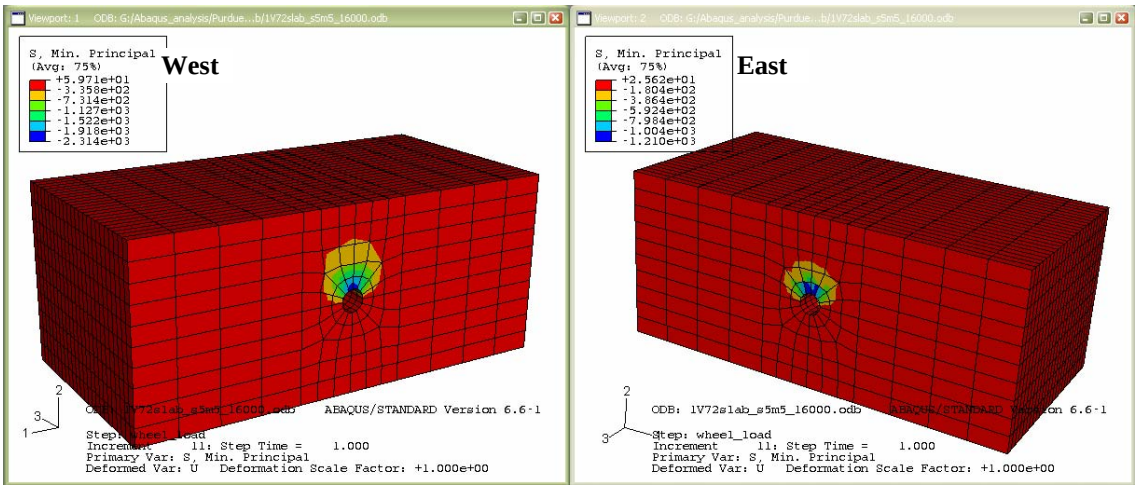

(b) Stresses after application of wheel load

Figure 7.6: Compressive stress zones in the concrete for 1V72 FE model

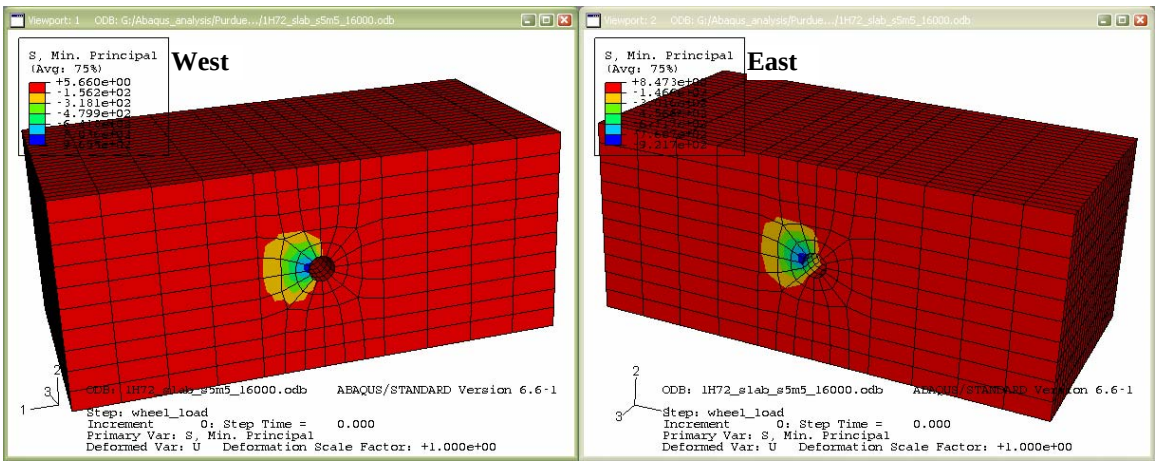

(a) Stresses after a joint opening of 1/8 in.

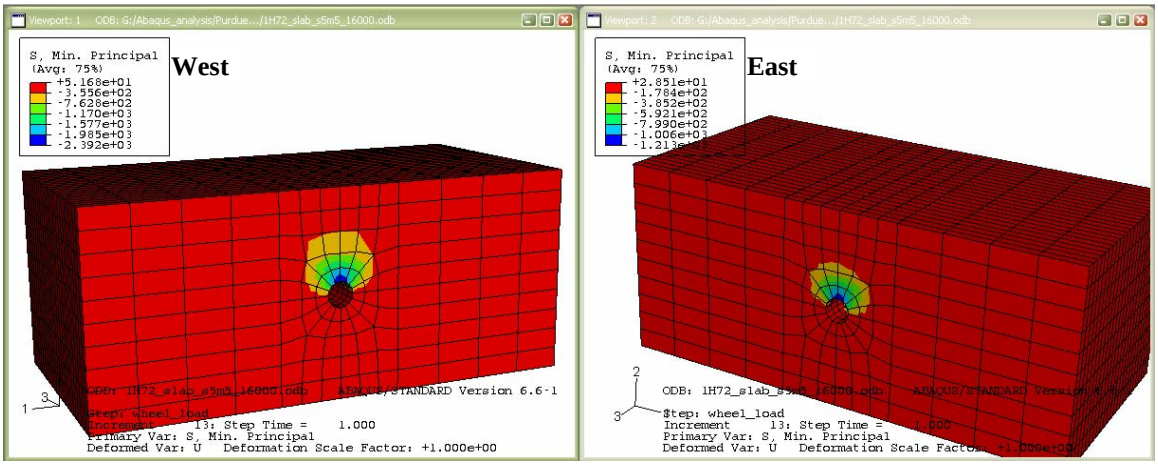

(b) Stresses after application of wheel load

Figure 7.7 Compressive stress zones in the concrete for 1H72 FE model

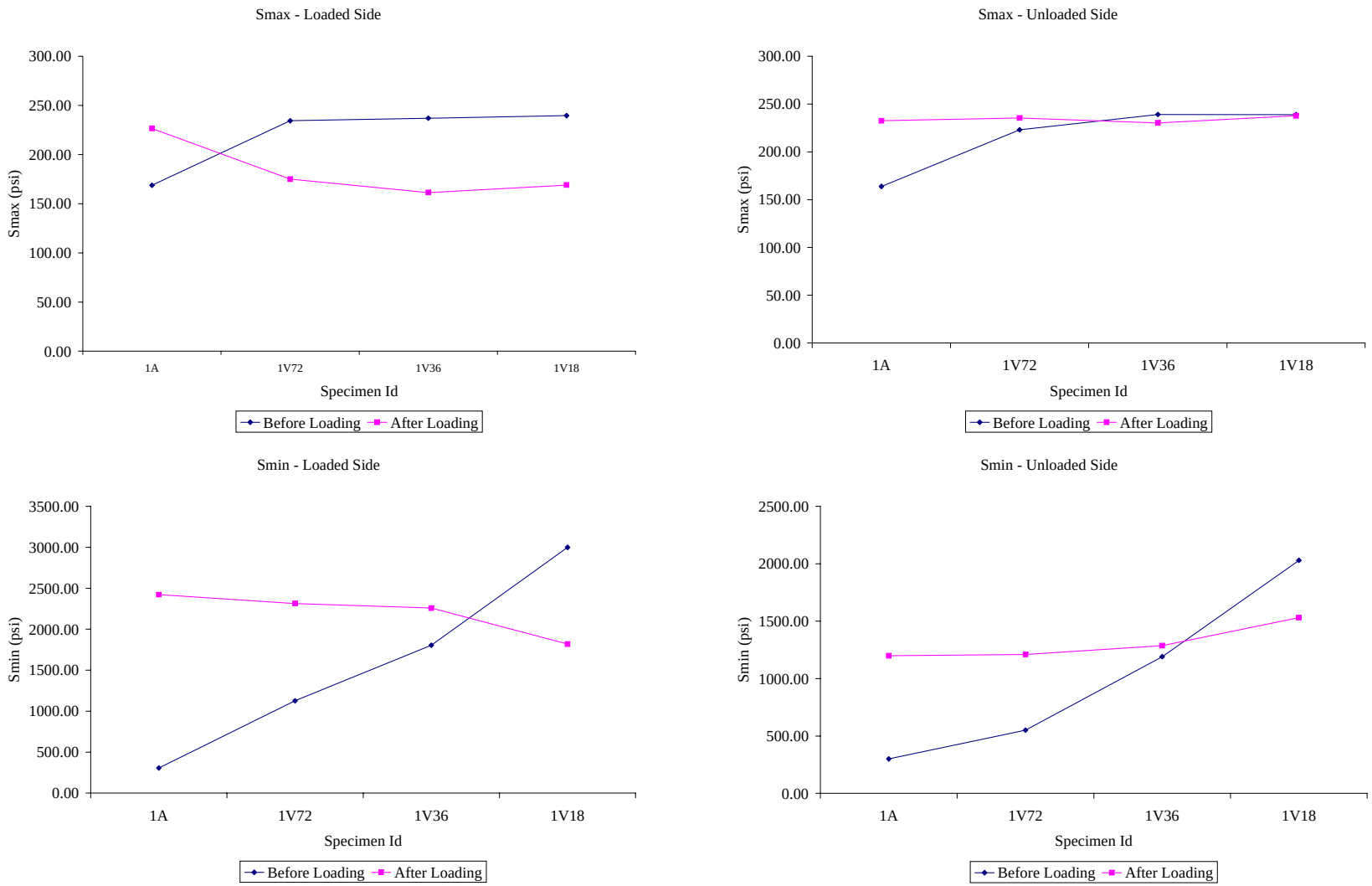

Figure 7.8 Results at location (i) and (ii) for single vertically misaligned dowel bar at 1/8” joint opening

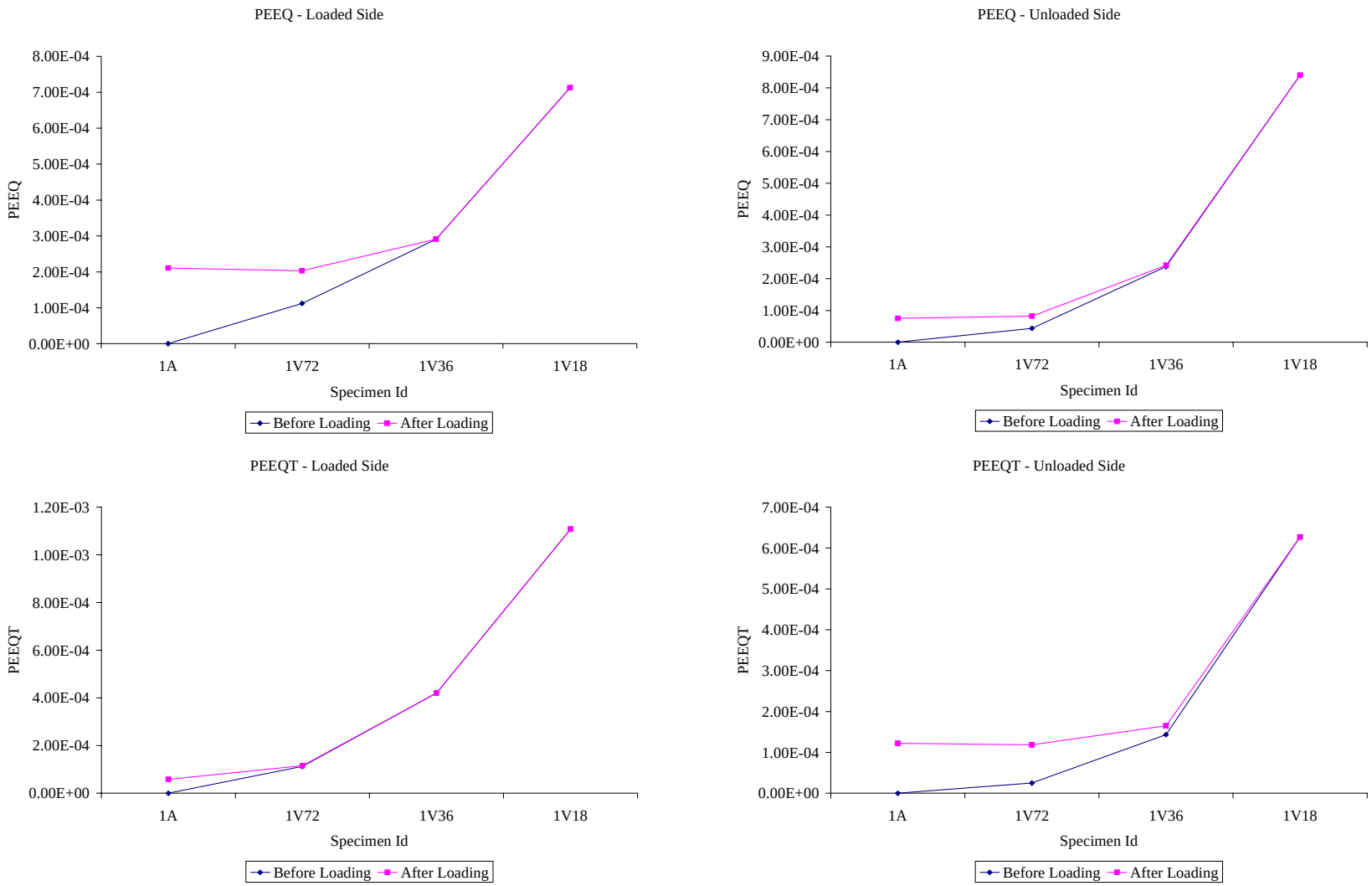

Figure 7.8 (Contd): Results at location (i) and (ii) for single vertically misaligned dowel bar at 1/8” joint opening

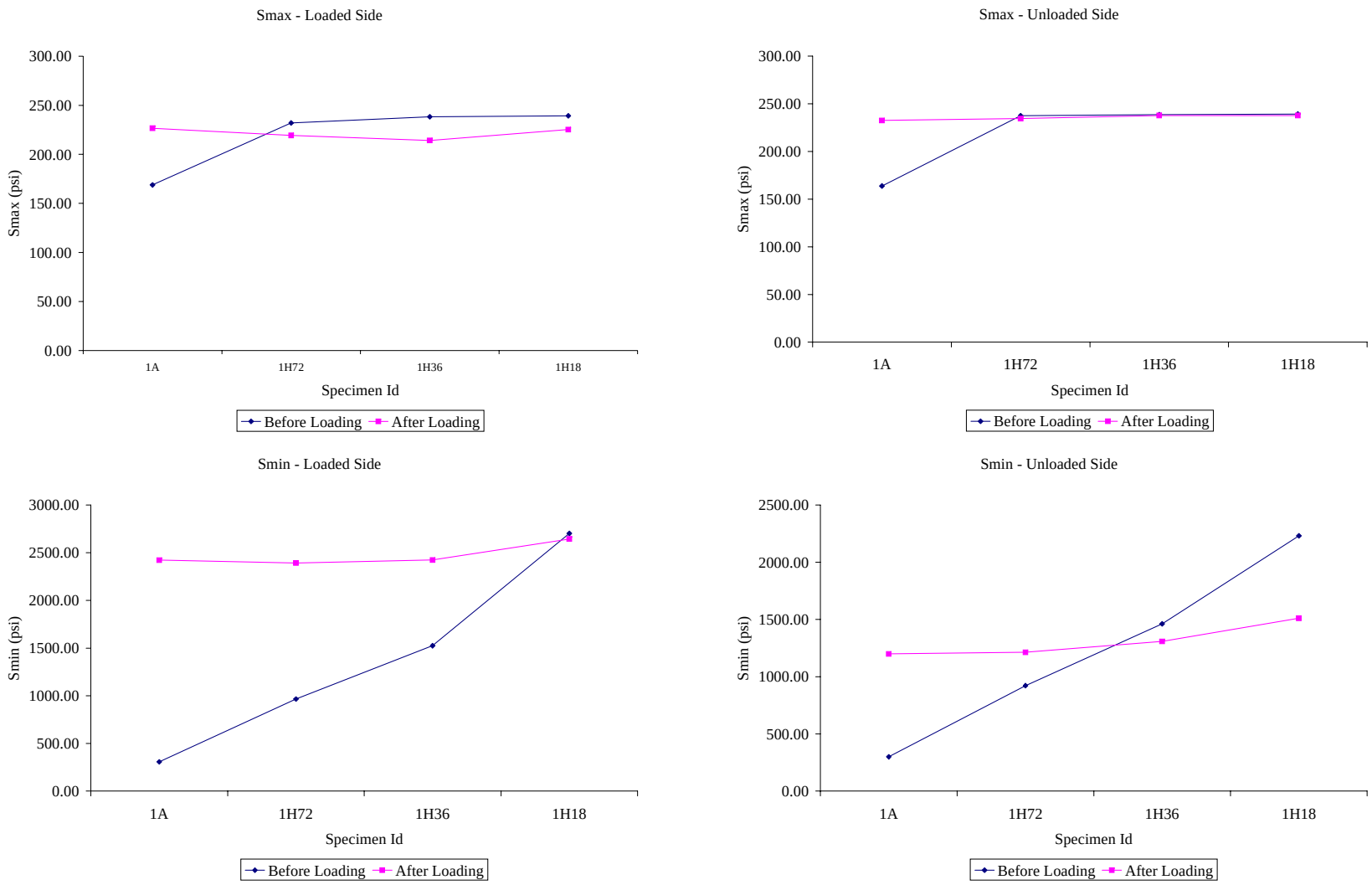

Figure 7.9 Results at location (i) and (ii) for single horizontally misaligned dowel bar at 1/8" joint opening

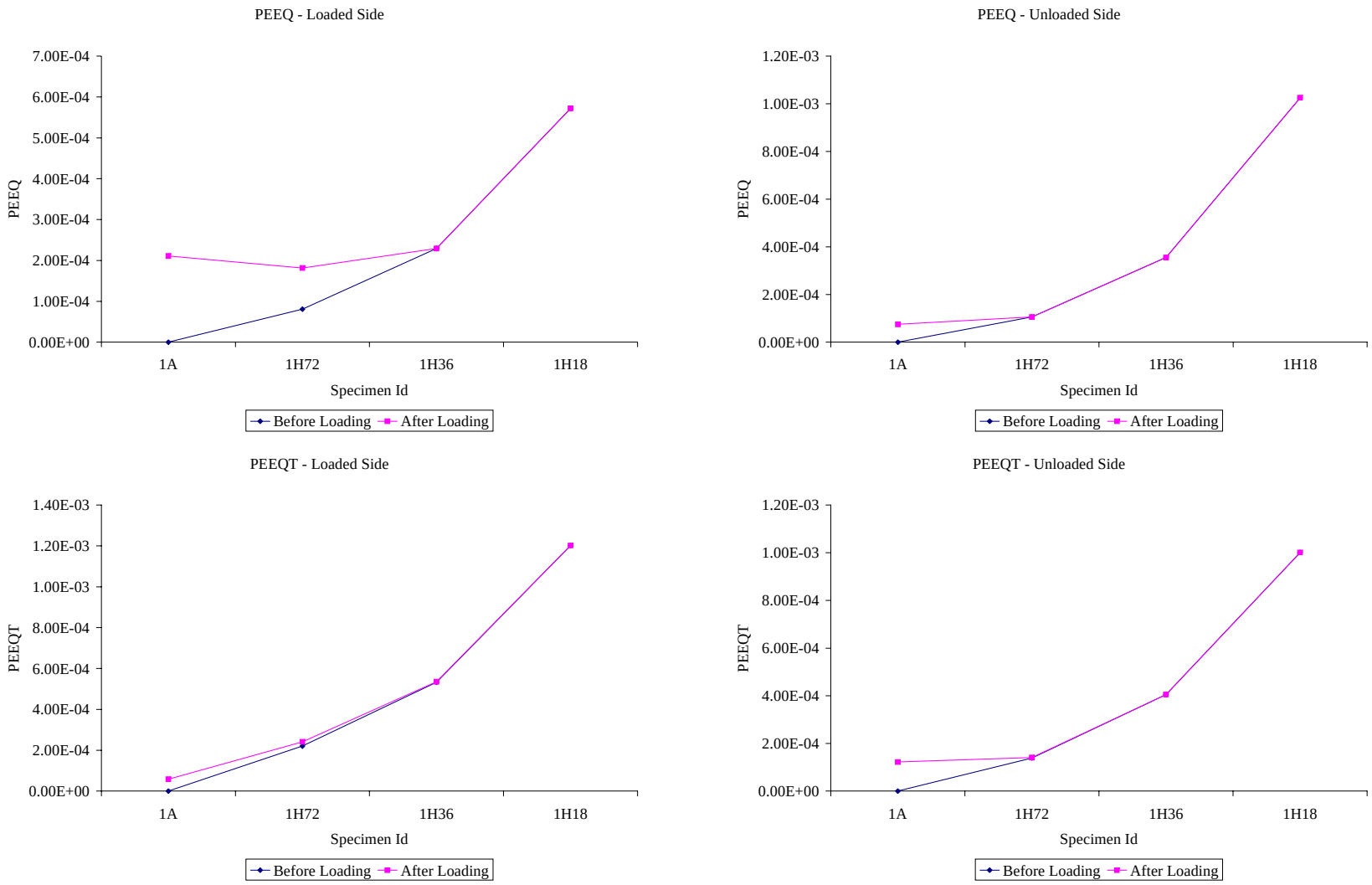

Figure 7.9 (Contd): Results at location (i) and (ii) for single horizontally misaligned dowel bar at 1/8" joint opening

7.4.2 THREE DOWEL BAR MODEL

In the three dowel bar models, the concrete pavements slabs were first pulled apart to 1/8 in and then a set of dual wheels tandem axles applied a load of 8000 lbs each on one side of the slab at the joint face. Complex multiaxial stress and strain zones were captured by the finite element analytical models and have been presented in Appendix D.

Aligned dowel bars

In the case when all the dowel bars are aligned, 3A, as the joint is opened multiaxial stress and strain states are produced in the concrete surrounding the dowel bar. The stress and strain states in this case are well below the inelastic stresses (f'_c and f'_t) and strains (PEEQ and PEEQT). There is a marginal increase in the stress states as the load is applied at the joint face. Overall, the 3A finite element analytical model showed no formation of distresses in the concrete at the joint face.

Non-Uniform orientation of dowel bars

The cases in which all the three dowel bars that were misaligned with vertical (3V36NU and 3V72NU) or horizontal (3H36NU and 3H72NU) misalignment showed the formation of high stress concentration zones in the concrete surrounding the dowel bar. These stress concentration zones formed at a joint opening of 1/8 in. near the face of the joint, as shown in figure 7.10 for 3V36NU and 3H36NU. For example, in the 3H36NU case, with load application, the stress concentration zone around the center dowel bar migrated from the side to the top of the dowel bar as shown in figures 7.10 and 7.11. The results of the 3D finite element model show that the central misaligned dowel bar is loaded more than

the outer misaligned bars. This occurs due to the redistribution of stresses and the location of the wheel loads on the concrete pavement slab. The change in stress intensity in the concrete surround the misaligned dowel bars is shown in figure 7.11 (b). The mechanics of the formation of these bearing stress zones under the misaligned dowel bar are synonymous to the ones observed in the single dowel bar finite element models.

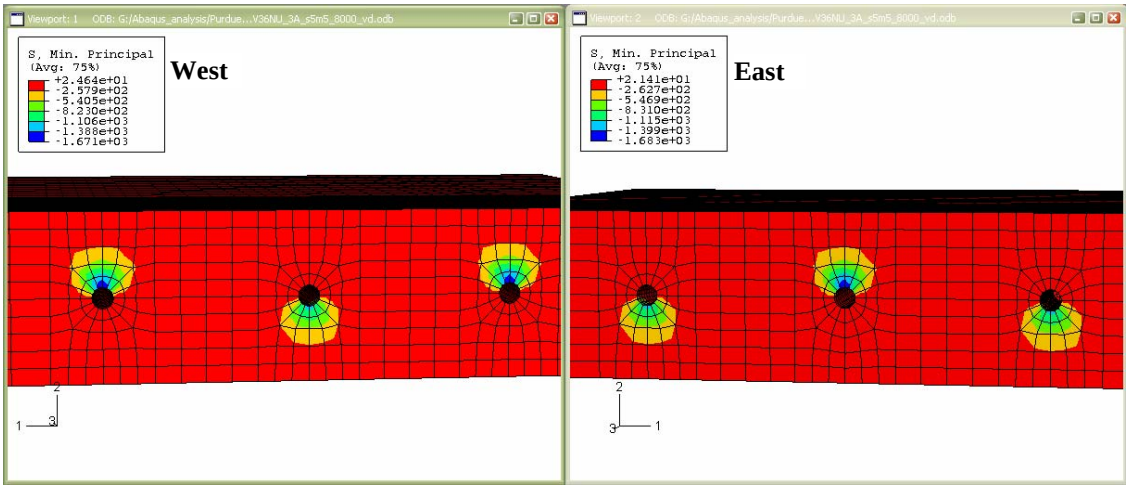

(a) Minimum Compressive Stresses in 3V36NU model

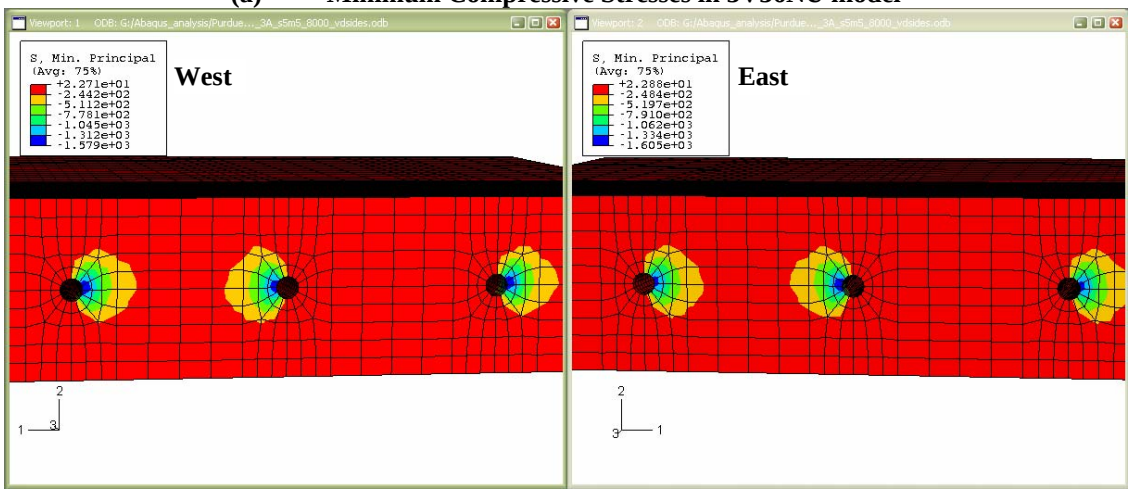

(b) Minimum Compressive Stresses in 3H36NU model

Figure 7.10: Stress concentration zones formed in concrete due to misaligned dowel bars and at joint opening (1/8 in)

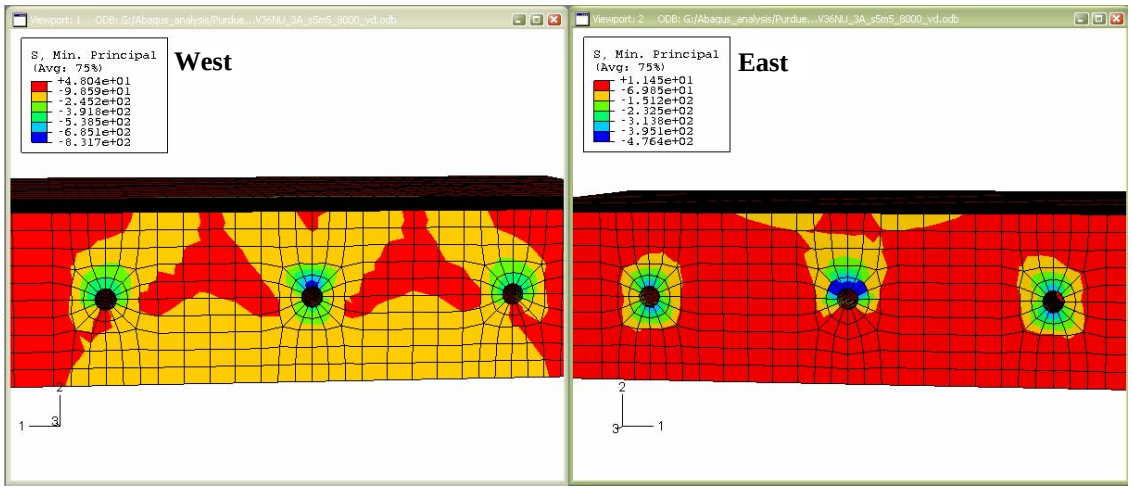

(a) Minimum Compressive Stresses in 3V36NU model

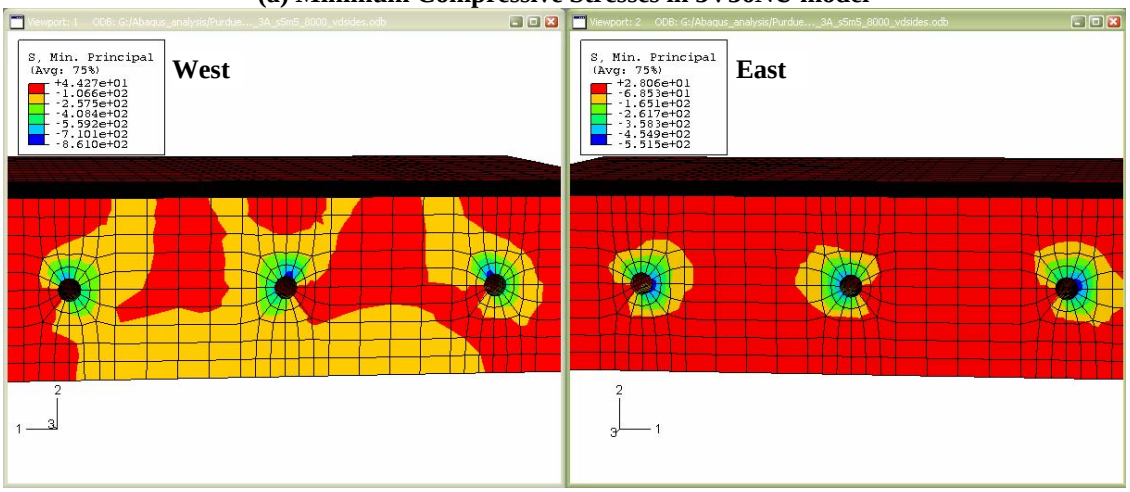

(b) Minimum Compressive Stresses in 3H36NU model

Figure 7.11: Formation of bearing stress zones in the concrete due to load application

Alternate misaligned dowel bars

Similar to the non-uniform orientation of dowel bar cases, the cases with alternate misaligned dowel bars, showed the formation of very high stress concentration zones in the concrete surrounding the dowel bar. In the cases studied only the central dowel was misaligned and the outer dowels were straight. Both the vertically (3V36AM and 3V72AM) and horizontally (3H36AM and 3H72AM) misaligned dowel bar cases were studied and are presented in Appendix D. The stress concentration zones are formed at a joint opening of 1/8 in. near the face of the joint, as shown in figures 7.12 (a) and (b)

corresponding to 3V36AM and 3H36AM analytical models. With the application of wheel loads, stress concentration zones due to misalignment undergo unloading and high bearing stress zones are formed under the location of the wheel loads. Figure 7.13 shows the formation of these bearing stress contours at the end of load application on the pavement slab with 3V36AM and 3H36AM analytical models. The stresses and strains in the 3V72AM and 3H72AM models are lower compared to the results shown in figure 7.12.

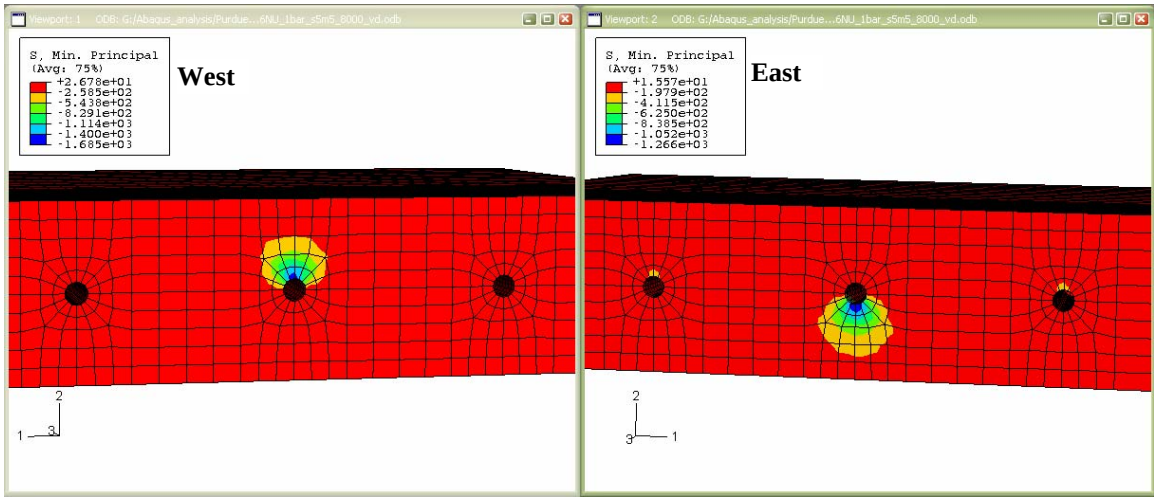

(a) Minimum Compressive Stresses in 3V36AM model

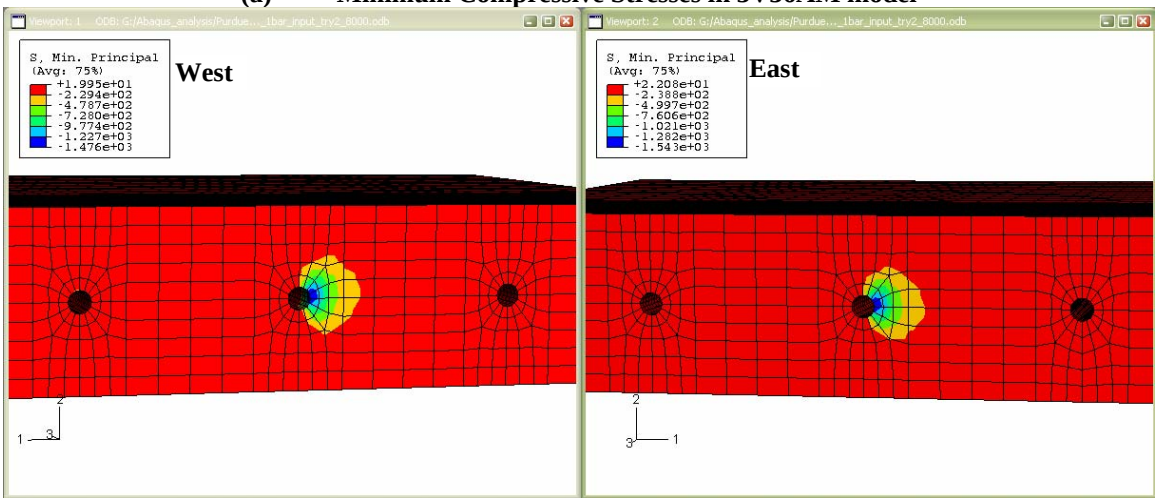

(b) Minimum Compressive Stresses in 3H36AM model

Figure 7.12: Stress concentration zones formed in concrete due to misaligned dowel bars and at joint opening (1/8 in)

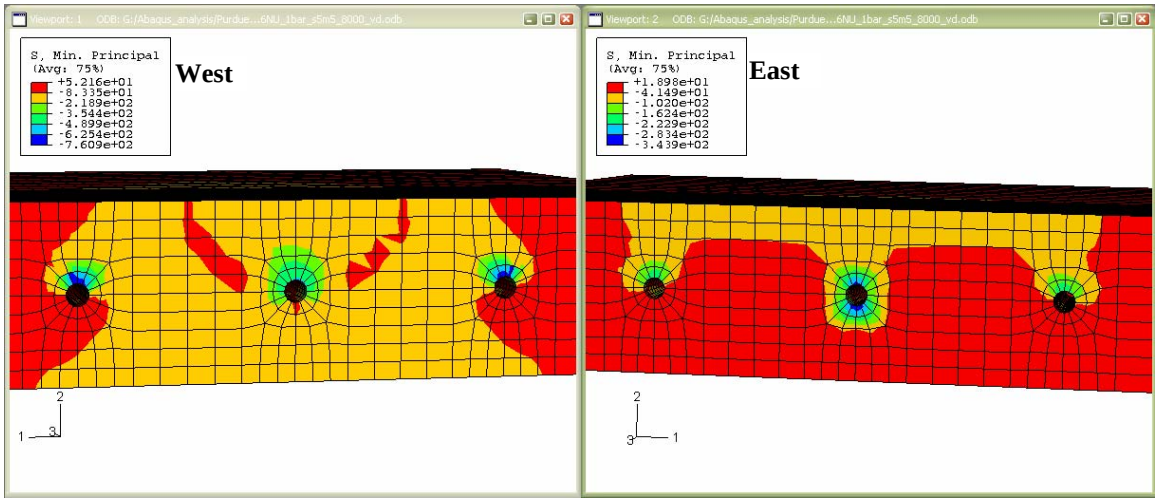

(a) Minimum Compressive Stresses in 3V36AM model

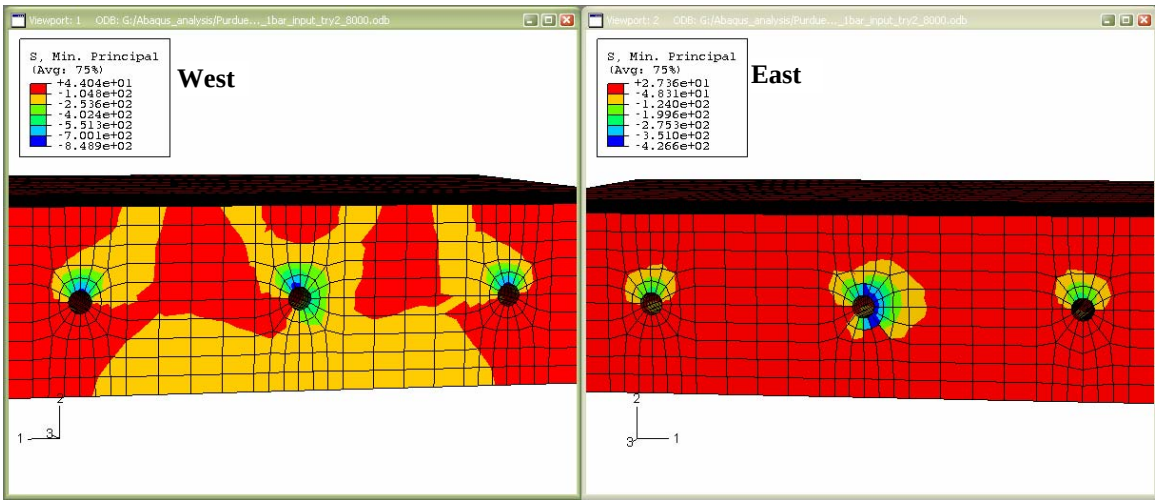

(b) Minimum Compressive Stresses in 3H36AM model

Figure 7.13: Formation of bearing stress zones in the concrete due to load application

Figure 7.14 presents the formation of compressive stresses (S_{min}) in the concrete on the loaded (west) and unloaded (east) sides after joint opening and application of wheel loads. At 1/8 in joint opening before load application, there is an increase in the stress magnitude as more bars are misaligned (from alternate misalignment to non-uniform misalignment) and magnitude of misalignment is increased from 1/72 radians to

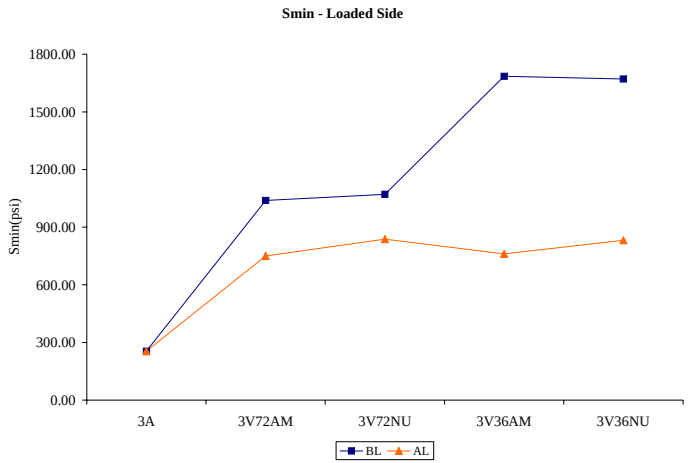

(a) Loaded side Stresses with Vertically Misaligned bars

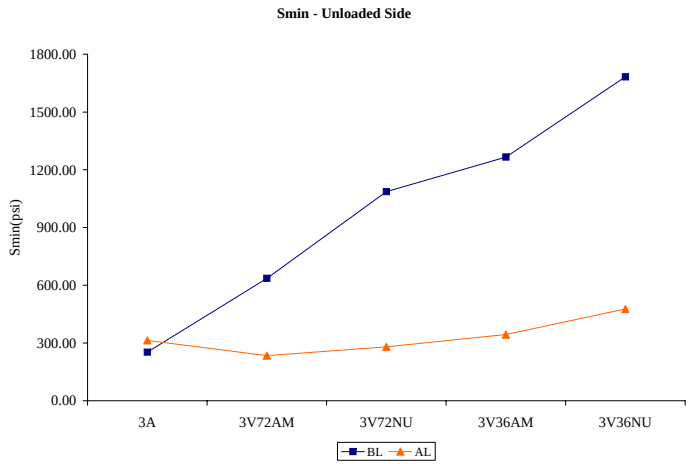

(b) Unloaded side Stresses with Vertically Misaligned bars

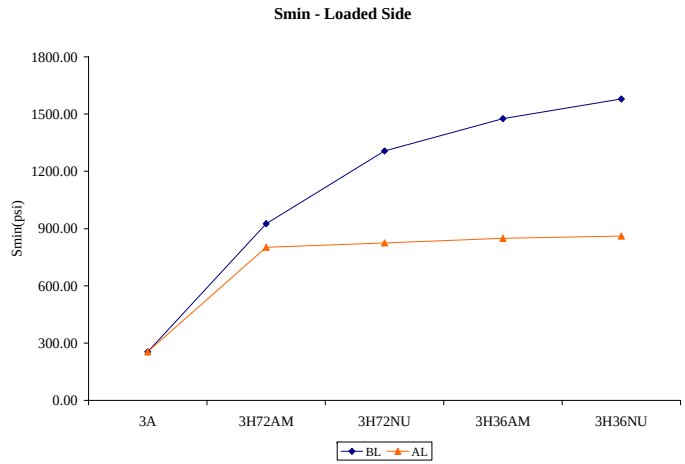

(c) Loaded side Stresses with Horizontally Misaligned bars

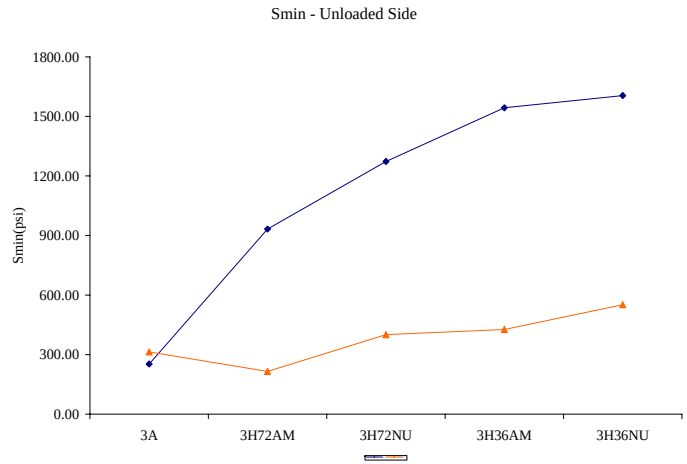

(d) Loaded side Stresses with Horizontally Misaligned bars

Figure 7.14: Compressive stresses in the three dowel bar FE models

1/36 radians. A similar trend in bearing stresses is observed in the concrete surrounding the dowel bars after load application. The magnitude of S_{max}, PEEQ and PEEQT after joint opening and loading are not a cause of concern because of small joint opening and load redistribution.

7.5 CONCLUDING REMARKS

The results from the analyses included the multiaxial stresses and strains in the concrete elements. These results indicated that:

- The joint opening of 0.125 in. produced stress concentration zones in joints with misaligned dowels. These zones were similar to those predicted by the finite element models with joint openings only (section 8.3 and 8.4).
- A joint opening of 0.125 in., does not produce any significant distress for the misalignment magnitudes and type considered in this portion of the study.
- Applying the wheel loading changes the stress states and the stress concentration zones (for the horizontal misalignment) finite element models.
- The inelastic strains (compression and tension) induced in the concrete by the wheel loading increase much faster after the dowel misalignment exceeds 1/36 radians.
- The pavement specimens with three dowel bars with different types and orientations of misalignment with magnitude less than or equal to 1/36 radians do not undergo significant inelastic straining in compression (crushing) or tension (cracking) for total wheel loads equal to 16000 lbs.

CHAPTER 8

SUMMARY, CONCLUSIONS, RECOMMENDATIONS AND FUTURE RESEARCH

8.1 INTRODUCTION

This chapter presents summary and conclusions of the experimental investigations, the analytical modeling, parametric studies and of the combined effects of misalignment and wheel loading.

8.2 SUMMARY AND CONCLUSIONS BASED ON EXPERIMENTAL INVESTIGATIONS

A comprehensive experimental investigation was conducted on laboratory-scale pavement specimens with aligned or misaligned dowel bars at contraction joints. The parameters included in the experimental investigations were the dowel misalignment type, magnitude, and uniformity. The experimental test matrix consisted of 54 laboratory scaled slab specimens with limited repetitions.

Pavement joint opening occurs due to thermal movements induced by changes in ambient conditions. It is a cyclic, time-varying phenomenon that depends completely on the weather (ambient) conditions. The joint in the slab specimens were created using a 1/8 in. aluminum separator plate to eliminate effects of aggregate interlock. The slab specimens in the experimental investigation were cast in steel molds to eliminate effects due to base friction and isolate distresses caused due to misaligned dowel bars. Also, no axle wheel loads were considered during the experimental investigation. The effects of

base friction and axle loads on the pavement slabs should be considered for future research.

The experimental results included the pullout force per dowel-joint opening behavior of the pavement specimens and the observed structural distresses. The experimental results indicated that:

- The pullout force per dowel-joint opening behavior of all specimens consisted of two regions: (1) the initial fully bonded region, and (2) the post-slip debonded region. Debonding or initial slip occurs typically when the pullout force per dowel exceeds 1124 -1574 lbs. This corresponds to average bond shear stress (τ_b) equal to 30.0 - 43.0 psi.
- Dowel misalignment has a small influence on the initial debond shear stress (τ_b), but it has significant influence on the post-slip pullout force per dowel-joint opening behavior.
- For all misalignment types (horizontal, vertical, or combined), the pullout force per dowel bar increases with increase in misalignment magnitude (1/36 to 1/9 radians.) and non-uniformity.
- Structural distresses in the form of concrete spalling and cracking were observed for specimens with larger dowel misalignments (greater than 1/18 radians) and non-uniformity. The severity of the structural distress increased further with the number of misaligned dowel bars at the joint.
- Specimens with horizontal (H) or combined (C) misalignments and large (greater than 1/18 radians), non-uniform dowel misalignments experienced significant structural distress in the form of spalling and transverse cracking of the slab specimens.

- Specimen with vertical (V) misalignments with large (greater than 1/18 radians), non-uniform dowel misalignments experienced structural distress in the form of spalling and uplift of the slab specimens.

The experimental results and observations provide valuable information regarding the joint opening behavior of pavement specimens with various dowel misalignment types, magnitudes, and uniformity. They provide limited information regarding the overall interaction between the dowel and the surrounding concrete. They do not provide comprehensive knowledge of the mechanics of dowel-concrete interaction. Hence, analytical investigations based on the experimental results were performed to better understand the basic dowel-concrete interaction mechanics.

The experimental investigation focused on overall pullout force per dowel-joint opening behavior on laboratory scaled concrete pavement specimens. The localized multiaxial stresses, strains and the distresses observed in the test specimens were not measured during the experimental investigation as sensors required to measure the localized stresses and strains were not embedded in the specimens. Additionally, non-destructive techniques were not used to monitor the formation of distresses within the concrete specimens at the dowel-concrete interfaces. These are some of the limitations of the experimental approach used in this research, and should be addressed by future research.

8.3 SUMMARY AND CONCLUSIONS BASED ON ANALYTICAL INVESTIGATIONS

The 3D finite element models were developed to further investigate the behavior of the pavement specimens with misaligned dowel bars. The dowel-concrete longitudinal bond model was calibrated using the experimental results for the pavement specimens with aligned dowel bars. The transverse interaction between the dowel bar and the concrete was modeled using surface-to-surface contact elements. Two cases were considered for the coefficient of friction between the dowel bar and the concrete in contact. Case I used idealized values and case II used experimentally measured values for the friction coefficient. The concrete material was modeled using a damaged plasticity model with multiaxial plasticity behavior in compression and damaged elasticity behavior in tension. The concrete material properties required to completely define this material model were based on idealized (case I) and measured (case II) values. The steel material was modeled using a multiaxial elasticity model.

The results from the 3D finite element analyses indicated that:

- The analytically predicted dowel pullout force-joint opening behavior compared favorably with the experimental measurements.
- The analytical and experimental comparisons are reasonable for all pavement specimens with different numbers, magnitudes and orientation of dowel misalignment.
- The analytical models and the analysis approach can be used to expand the experimental behavior database and conduct parametric studies.

- The analytical results indicate the formation of significant stress concentration zones in the concrete at the joint face around the misaligned dowel bars.

The comparisons focused on the overall pullout force per dowel-joint opening behavior predicted by the models and measured experimentally. The localized multiaxial stresses and strains computed by the models at the sites of stress concentration could not be verified because the corresponding measurements were not performed during the experiments. Additionally, non-destructive techniques were not used to monitor the formation of distresses within the concrete specimens at the dowel-concrete interfaces.

The analytical results (3D stresses and strains) from the finite element analyses were used to identify significant events or damage limit states occurring in the concrete material at the dowel-pavement interface. The events / damage limit states are indicated on the analytically predicted pullout force-joint opening behavior plots from event (A – F). The localized multiaxial stresses and strains and events (A – F) predicted by the numerical models could not be validated experimentally as the distresses caused were highly localized and occurred deep inside the concrete pavement specimens. The events (A – F) do not imply or suggest that they occur at the same joint opening as in real pavement specimens but it is logically assumed that these distresses and events (A – F) will occur eventually in the experimental or real pavement specimens. The relative occurrence of these events for pavement specimens with different misaligned dowel bars is probably more important than their absolute joint opening values.

8.4 SUMMARY AND CONCLUSIONS OF PARAMETRIC STUDIES

The 3D finite element models that were developed and verified using experimental results, were used to conduct analytical parametric studies. The parameters considered were the number of dowel bars (one or two), dowel misalignment magnitude (0, 1/72, 1/36 and 1/18 radians), the dowel misalignment type (vertical and horizontal) and the dowel misalignment orientation (uniform, non-uniform or alternate). The analytical matrix consisted of seven specimens with one dowel bar and nineteen specimens with two dowel bars. The results from the parametric studies indicated that:

- For models with one misaligned dowel bar, horizontal misalignment can be more detrimental than vertical misalignment.
- For models with two vertically misaligned dowels, the effects of non –uniform misalignment can be more detrimental than uniform or alternate misalignment.
- For models with horizontally misaligned dowels, the misalignment orientation (uniform, non-uniform or alternate) does not have a significant influence on the occurrence of events / material damage limit states as the dowel misalignment magnitude increases, these events occur for smaller joint openings.

8.5 SUMMARY AND CONCULSIONS BASED ON THE STUDIES FOR MISALIGNED DOWELS COMBINED WITH WHEEL LOADING

The analytical models were modified slightly to investigate the effects of combined wheel loading and joint opening on the behavior of pavement specimen models. This was a preliminary investigation that attempted to evaluate the effects of wheel loading on the

behavior of joints with misaligned dowel bars. The models and the analysis results could not be verified due to the lack of experimental data and results. The findings of this portion of the study must be considered carefully and verified experimentally before any action.

The 3D finite element models were developed for pavement specimens with transverse joints. The pavements were supported by a base, sub-base and sub-grade layers with assumed idealized material properties. Seven pavement specimens were analyzed with transverse joints with one misaligned dowel bar. The dowel bar misalignment orientations was either vertical or horizontal, with misalignment magnitudes ranging from 0 to 1/18 radians. Nine pavement specimens were analyzed with joints with three misaligned dowel bars. The misalignment orientations were either vertical or horizontal, with non-uniform or alternate misalignment and misalignment magnitudes ranging from 0 to 1/36 radians.

The pavement specimen models were analyzed by subjecting them to a joint opening equal to 0.125 in. which simulated a change in temperature. After joint opening, the specimen models were subjected to monotonically increasing wheel loading at the joint face. The total value of wheel loading was equal to 16000 lbs, which includes the dynamic magnification factor and is conservative (four times the wheel load of 4000 lbs).

The results from the analyses included the multiaxial stresses and strains in the concrete elements. These results indicated that:

- The joint opening of 0.125 in. produced stress concentration zones in joints with misaligned dowels. These zones were similar to those predicted by the finite element models with joint openings only (section 8.3 and 8.4).

- A joint opening of 0.125 in., does not produce any significant distress for the misalignment magnitudes and type considered in this portion of the study.
- Applying the wheel loading changes the stress states and the stress concentration zones (for the horizontal misalignment) finite element models.
- The inelastic strains (compression and tension) induced in the concrete by the wheel loading increase much faster after the dowel misalignment exceeds 1/36 radians.
- The pavement specimens with three dowel bars with different types and orientations of misalignment with magnitude less than or equal to 1/36 radians do not undergo significant inelastic straining in compression (crushing) or tension (cracking) for total wheel loads equal to 16000 lbs.

8.6 RECOMMENDATIONS AND FUTURE RESEARCH

The recommendation on misalignment magnitude is based on the limitations and assumptions associated with the experimental investigation and analytical approach. The localized material states (stress and strain) and the corresponding events (A – F) will have a significant influence on the *cyclic material fatigue life* at the distress locations. In the absence of experimental data and models relating the localized stresses and strains to the fatigue life of the pavement, the rational choice would be limit the localized stresses (S_{max} and S_{min}) to the material uniaxial stress capacities (f'_t and f'_c), i.e., to events C and D. A misalignment tolerance range of 1/72 - 1/36 radians skew angle or 1/8 – 1/4 in. per half length of the dowel bar is recommended for construction to the Department of Transportation.

In order to develop an analytical model, experimental investigations on slab specimens with misaligned dowel bars subjected to thermal effects such as expansion and contraction of the joint is needed. Furthermore, experimental investigations can focus on laboratory scaled concrete slab specimens, to study the effects of typical misaligned dowel bars, subjected to thermal effects combined with axle loads.

The analytical models in the future studies can be developed to capture effects due to temperature gradients along the slab thickness thereby addressing issues related to curling combined with misaligned dowel bars. It is hypothesized that fatigue loading causes dowel looseness that affects the load transfer efficienty of the joint leading to joint failure. As future goals, analytical models should be developed to capture and study behavior of complex multiaxial stress states caused due to misaligned dowels, dowel looseness, environmental changes combined with axle loads.

APPENDIX A

DETAILS OF EXPERIMENTAL SETUP

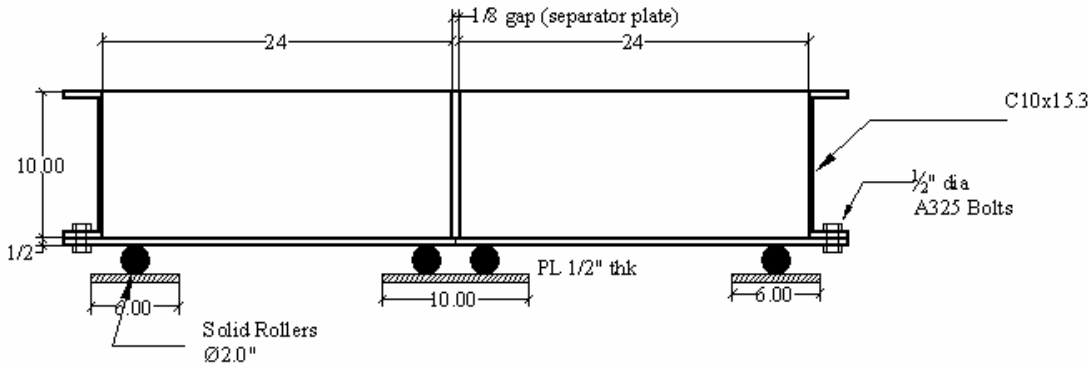

Figure A-1. Cross section of the small mold for pullout test

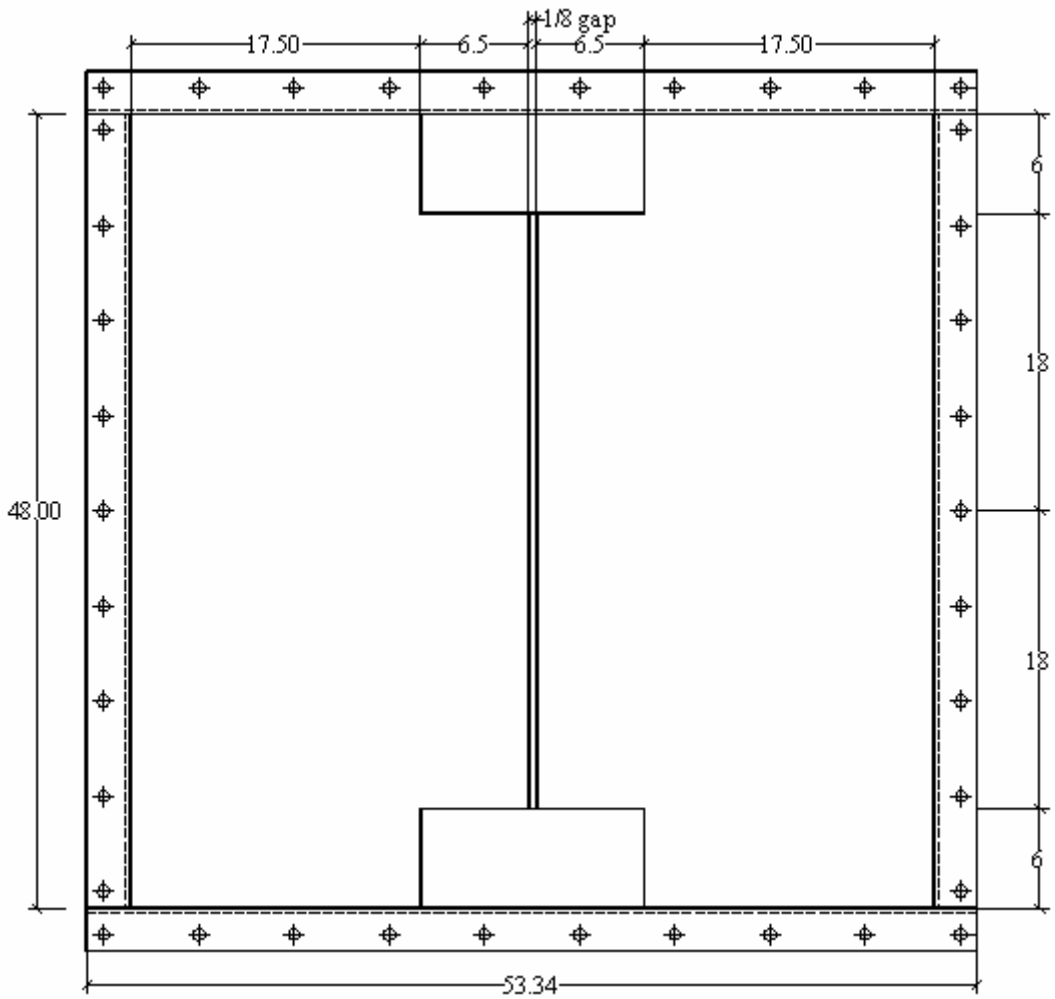

Figure A-2. Plan of the small mold with outside dimensions

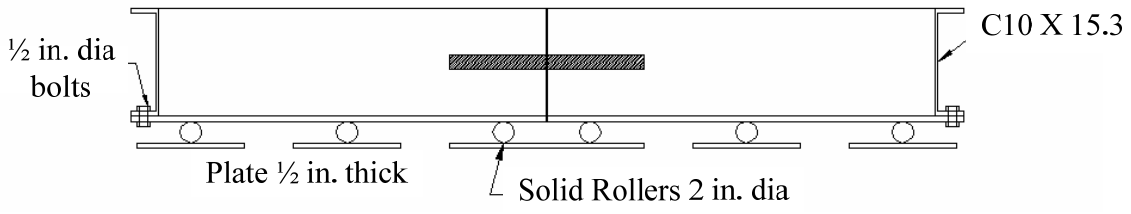

Figure A-3. Typical sectional view of the big mold

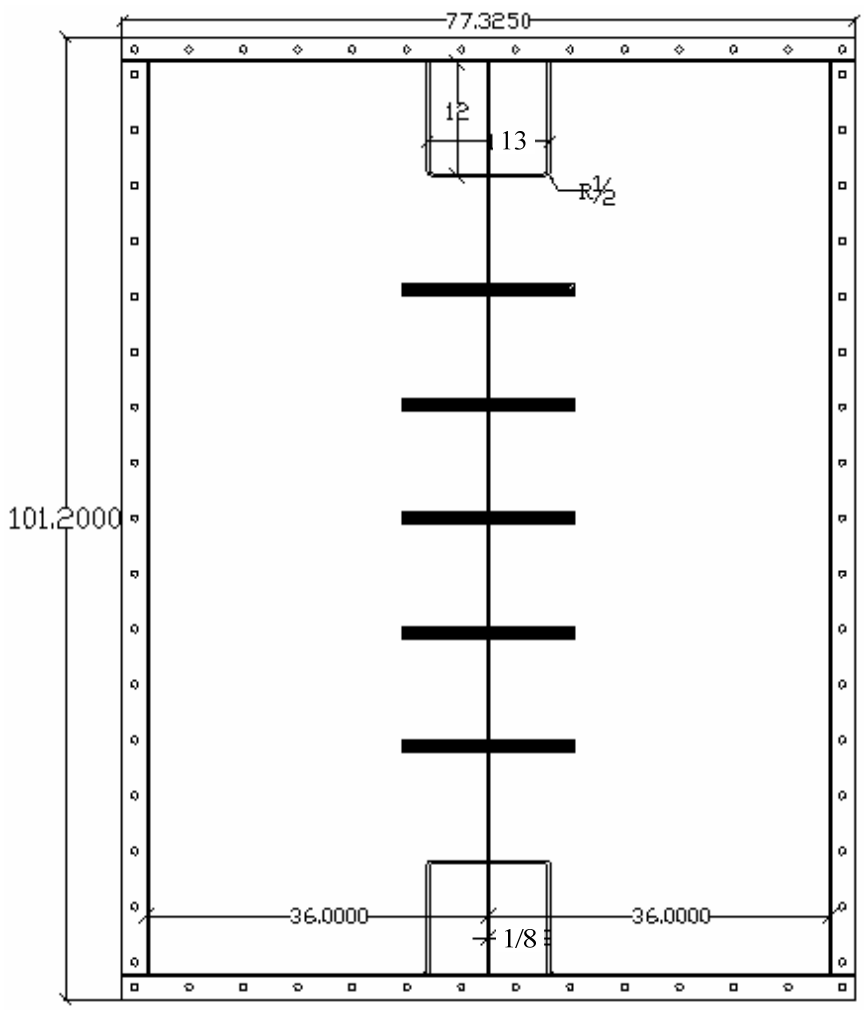

Figure A-4. Typical plan view of mold with 5 dowel bars

Table A-1. Mix Design Specifications

Specification: 2003 Standard Specifications
Grade of Concrete: P1
Intended Use of Concrete: Pavement Form

Material	Class	Specific Gravity	Absorption %
Cement	I/IA	3.13	
Fine Aggregate	2NS	2.61	1.47
Coarse Aggregate	6AA	2.66	1.50

Cement content	: 564 lb/yd^3	B/Bo	: 0.72
Air Content	(design): 6.5 % (specified): 6.5 %	Specification Tolerance	: 1.5 %
R.W.C	: 1.15	Theoretical Yield	: 100.00%
Fly Ash Content, lb/yd^3	: 0		

Weight of Coarse Aggregate (Dry/Loose) lb/ft^3	Aggregate and Water Proportions Quantities, lb/yd^3 of concrete		
	Fine Aggregate (Oven Dry)	Coarse Aggregate (Oven Dry)	Total Water
88	1330	1711	288
89	1313	1730	287
90	1297	1750	286
91	1280	1769	286
92	1264	1788	285
93	1247	1808	284
94	1231	1827	283
95	1214	1847	282
96	1198	1866	281
97	1181	1886	280
98	1164	1905	279

Typical Unit Weight (dry, loose) of coarse aggregate as described above is 93 lb/ft^3

Table A-2: Concrete Specimen strength at 7 days

Slab Dimensions	Number of Dowels	ID	Misalignment	Magnitude	Concrete Properties (7 days)		
				(in rad.)	f'_c *(psi)*	f'_t *(psi)*	f'_b *(psi)*
2 slabs each - 1220 x 610 x 250 mm (48 x 24 x 10 in.)	1	1A	Aligned	0	2544	540	346
		1V9	Vertical	1/9	2544	540	346
		1V12		1/12	3880	390	458
		1V18		1/18	2544	540	346
		1V36		1/36	3328	240	491
		1H9	Horizontal	1/9	4142	440	438
		1H12		1/12	3880	390	458
		1H18		1/18	4142	440	438
		1H36		1/36	3328	240	491
		1C9	Combined	1/9	3764	358	551
		1C12		1/12	3396	251	698
		1C18		1/18	3530	355	-
		1C36		1/36	3673	383	636

Table A-2 (Cont'd): Concrete Specimen strength at 7 days

Slab Dimensions	Number of Dowels	ID	Misalignment	Magnitude	Concrete Properties (7 days)		
				(in rad.)	f'_c *(psi)*	f'_t *(psi)*	f'_b *(psi)*
2 slabs each - 48 x 24 x 10 in.	2 (Uniform)	2A	Aligned	0	3396.0	251.0	698.0
		2V9U	Vertical	+1/9 ;+1/9	5545.0	367.0	572.0
		2V18U		+1/18;+1/18	3654.0	217.0	534.0
		2V36U		+1/36;+1/36	3673.0	383.0	636.0
		2H9U	Horizontal	+1/9;+1/9	5545.0	367.0	572.0
		2H18U		+1/18;+1/18	3654.0	217.0	534.0
		2H36U		+1/36;+1/36	3673.0	383.0	636.0
		2C9U	Combined	+1/9;+1/9	5545.0	367.0	572.0
		2C18U		+1/18;+1/18	3654.0	217.0	534.0
2 slabs each - 48 x 24 x 10 in.	2 (Non - Uniform)	2V9NU	Vertical	+1/9;-1/9	4227	317.0	400.0
		2V12NU		+1/12;-1/12	5540	474.0	636.0
		2V18NU		+1/18;-1/18	4931	280.0	632.0
		2V36NU		+1/36;-1/36	4931	290.0	632.0
		2H9NU	Horizontal	+1/9;-1/9	4227	317.0	400.0
		2H12NU		+1/12;-1/12	5540	474.0	636.0
		2H18NU		+1/18;-1/18	4931	280.0	632.0
		2H36NU		+1/36;-1/36	4931	290.0	632.0
		2C9NU	Combined	+1/9;-1/9	4227	317.0	400.0
		2C12NU		+1/12;-1/12	5540	474.0	636.0
		2C18NU		+1/18;-1/18	4931	280.0	632.0
		2C36NU		+1/36;-1/36	4931	290.0	632.0
	2 (One Bar Misaligned)	2V12AM	Vertical	+1/12;0	3919	336.0	481.0
		2V18AM		+1/18;0	3520	245.0	378.0
		2H12AM	Horizontal	+1/12;0	3919	336.0	481.0
		2H18AM		+ 1/18;0	3520	245.0	378.0
		2C12AM	Combined	+ 1/12;0	3919	336.0	481.0
		2C18AM		+ 1/18;0	3520	245.0	378.0

Table A-2 (Cont'd): Concrete Specimen strength at 7 days

Slab Dimensions	Number of Dowels	ID	Misalignment	Magnitude	Concrete Properties (7 days)		
				(in rad.)	f'_c *(psi)*	f'_t *(psi)*	f'_b *(psi)*
2 slabs each - 96 x 36 x 10 in.	3 (Aligned)	3A	None	0; 0; 0	3326.6	354.02	540
	3 (Non - Uniform)	3V18NU	Vertical	+1/18;-1/18;+1/18	4931.0	290.0	632.0
		3H18NU	Horizontal	+1/18;-1/18;+1/18	3919.0	336.0	481.0
		3C18NU	Combined	+1/18;-1/18;+1/18	3520.0	245.0	378.0

Table A-2 (Cont'd): Concrete Specimen strength at 7 days

Slab Dimensions	Number of Dowels	ID	Misalignment	Magnitude	Concrete Properties (7 days)		
				(in rad.)	f'_c *(psi)*	f'_t *(psi)*	f'_b *(psi)*
2 slabs each 2440 x 915 x 250 mm (96 x 36 x 10 in.)	5 (Aligned)	5A	Aligned	0; 0; 0; 0; 0			
	5 (Non -Uniform)	5V18NU	Vertical	+ 1/18; - 1/18; + 1/18; - 1/18; + 1/18	4822	363	491
		5H18NU	Horizontal	+ 1/18; - 1/18; + 1/18; - 1/18; + 1/18	3654	217	534
		5C18NU	Combined	+ 1/18; - 1/18; + 1/18; - 1/18; + 1/18	3396	251	698
	5 (Alternate Misaligned)	5V18AM	Vertical	+ 1/18; 0; - 1/18; 0; +1/18	3530	355	-
		5V36AM		+ 1/36; 0; - 1/36; 0; +1/36	3673	636	383
		5H18AM	Horizontal	+ 1/18; 0; - 1/18; 0; +1/18	3880	390	458
		5H36AM		+ 1/36; 0; - 1/36; 0; +1/36			
		5C18AM	Combined	+ 1/18; 0; - 1/18; 0; +1/18	4238	244	540
		5C36AM		+ 1/36; 0; - 1/36; 0; +1/36	3859.5	269.2	623.4

Table A-3. Description of Linear Variable Differential Transducer

Model	LD610-15
Excitation Voltage	± 15 V@ 18 mA maximum
Output	± 10 V DC
Stroke	± 15 mm
Total Stroke	30 mm (1.18 in.)

Table A-4. Description of the Hydraulics (Actuators RC 156 and RC 256)

Name	Capacity (ton)	Stroke (in.)	Cylinder Effective Area ($in.^2$)	Weight (lbs)
Actuator RC 156	15	6	3.14	15
Actuator RC 256	25	6	5.16	22

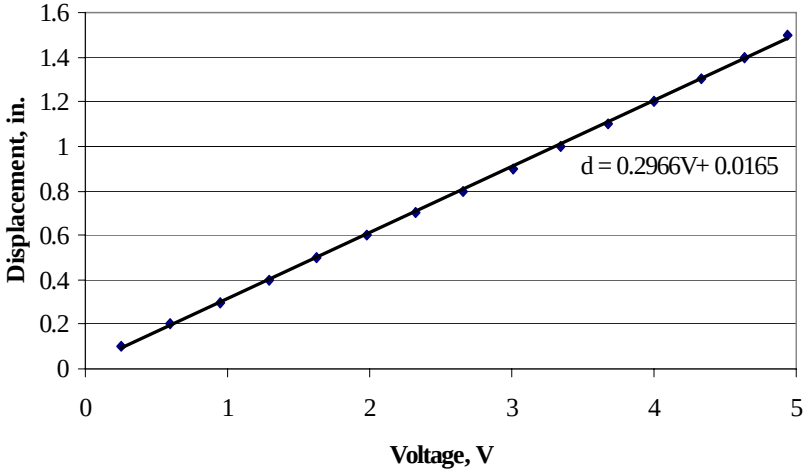

Figure A-5. Calibration of 1.5 in. slider-1

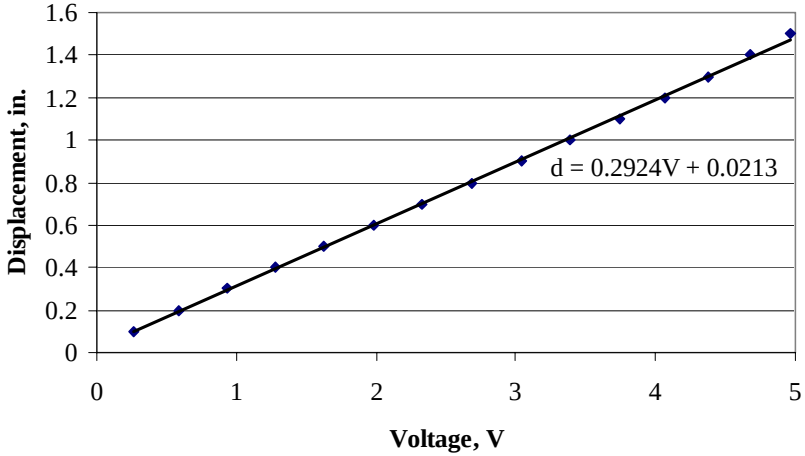

Figure A-6. Calibration of 1.5 in. slider-2

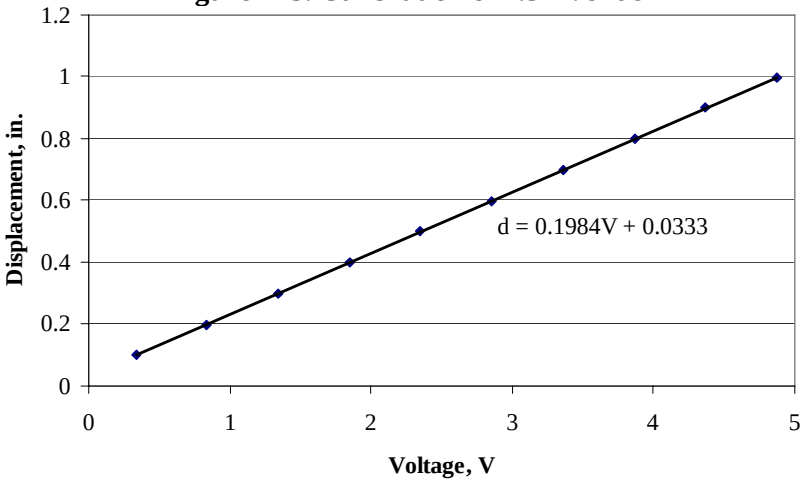

Figure A-7. Calibration of 1.0 in. slider-1

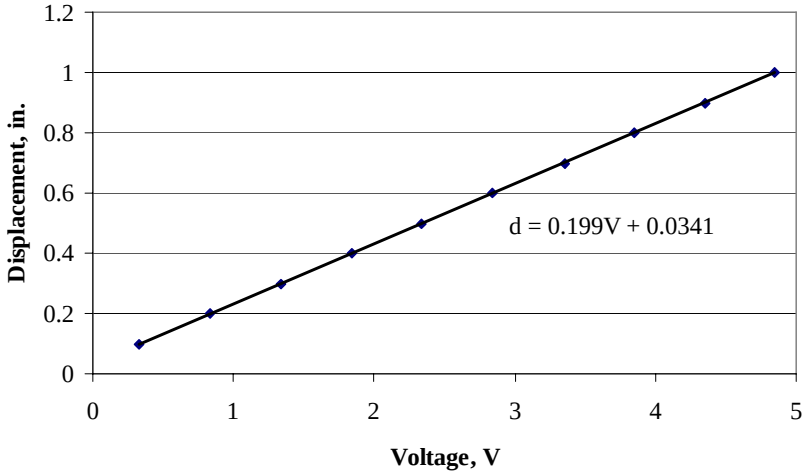

Figure A-8. Calibration of 1.0 in. slider-2

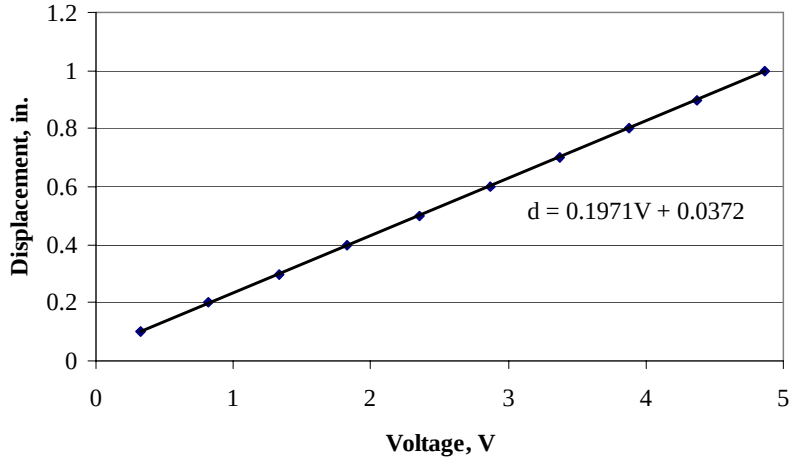

Figure A-9. Calibration of 1.0 in. slider-3

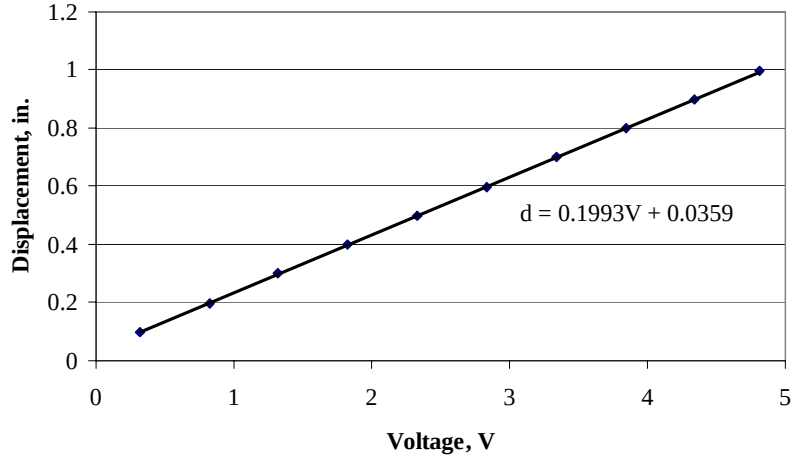

Figure A-10. Calibration of 1.0 in. slider-4

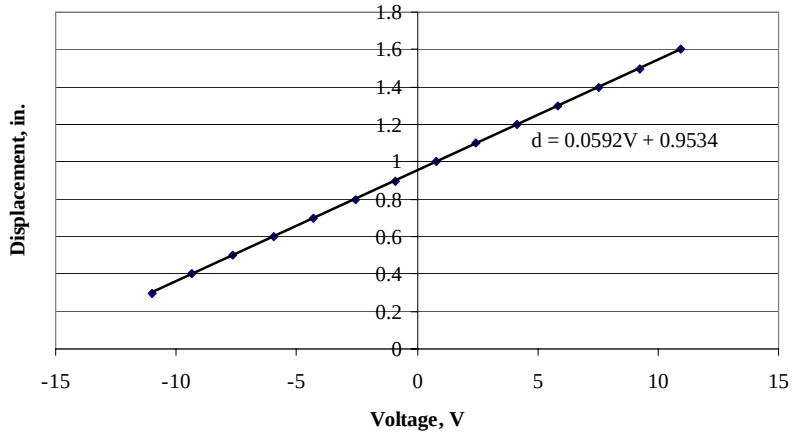

Figure A-11. Calibration of LVDT-1

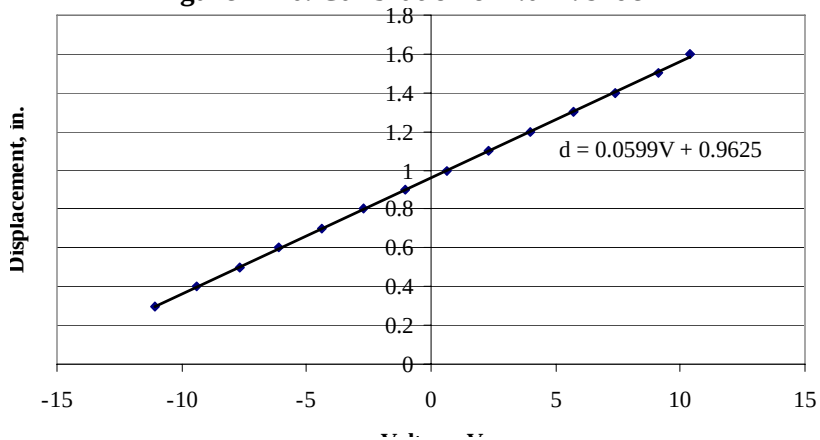

Figure A-12. Calibration of LVDT-2

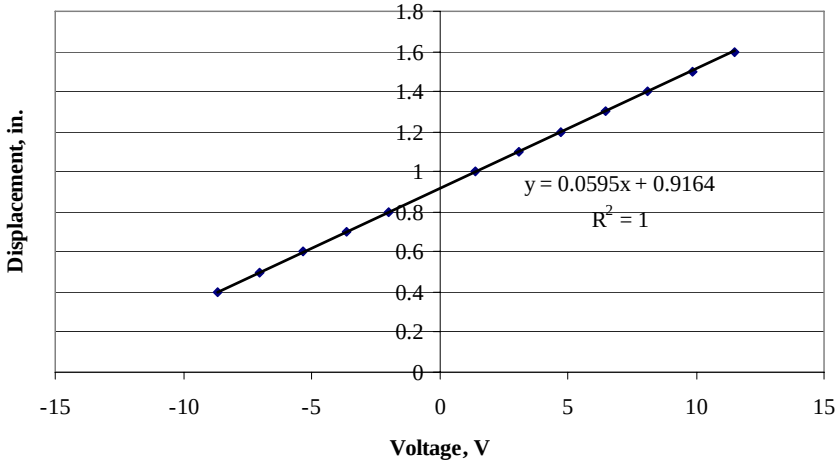

Figure A-13. Calibration of LVDT-3

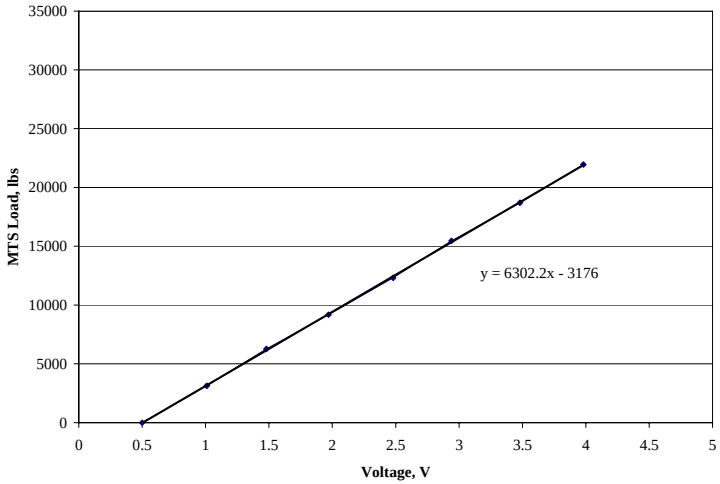

Figure A-14. Calibration of RC156 Actuator 1

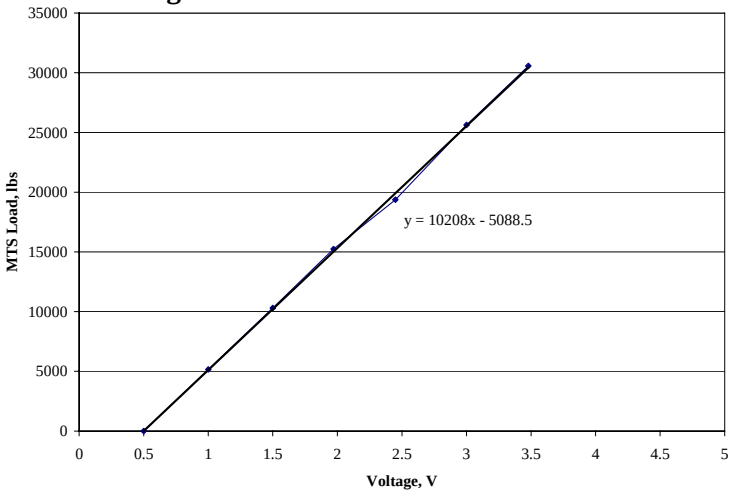

Figure A-15. Calibration of RC256 Actuator 1

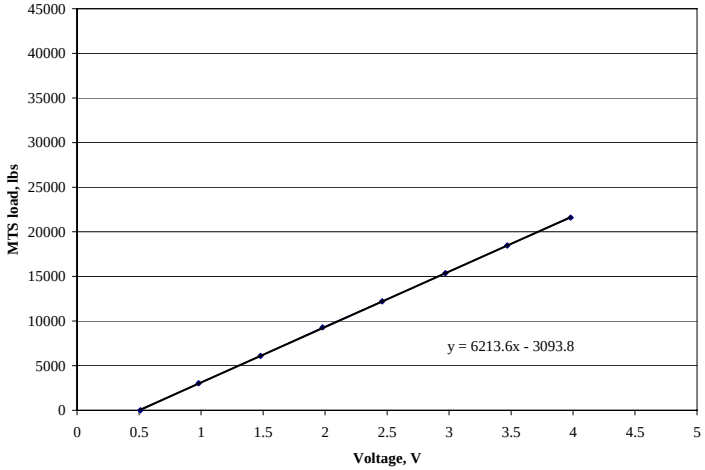

Figure A-16. Calibration of RC156 Actuator 2

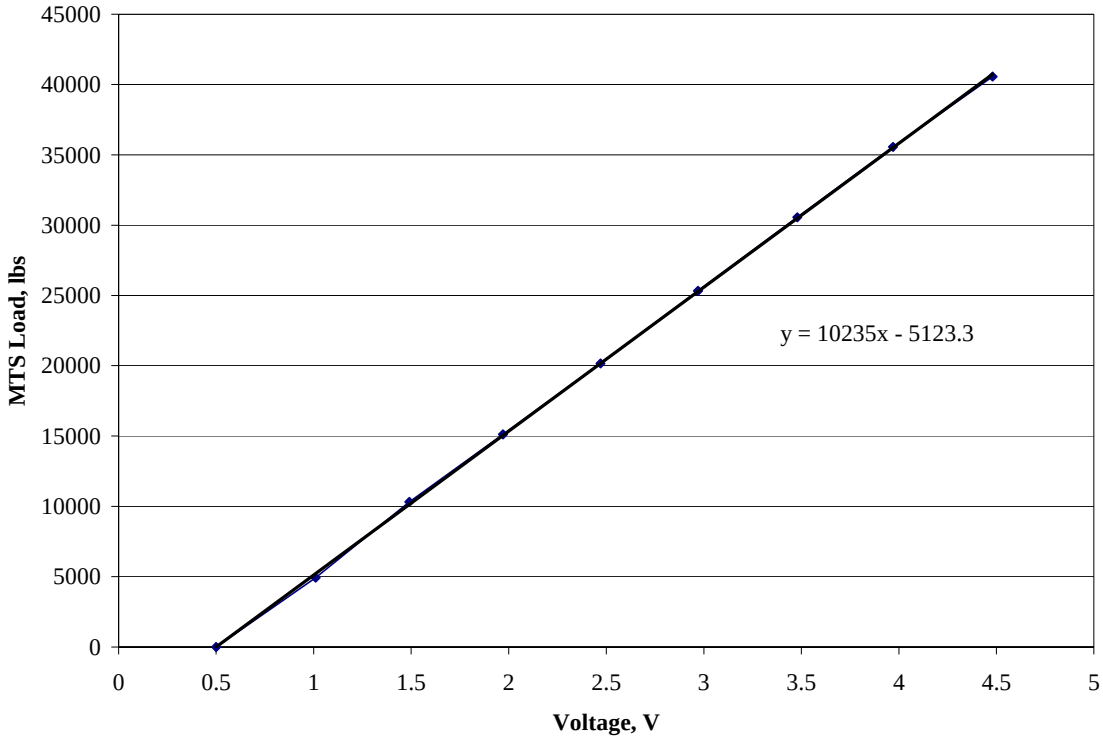

Figure A-17. Calibration of RC256 Actuator 2

Data Acquisition System

The data from the different instrumentation was collected at the rate of 6 scans per second, using a data acquisition system. The data acquisition system is capable of handling all the different instruments – sliders, LVDTs, and pressure transducers. The data flow is illustrated in Figure A-18.

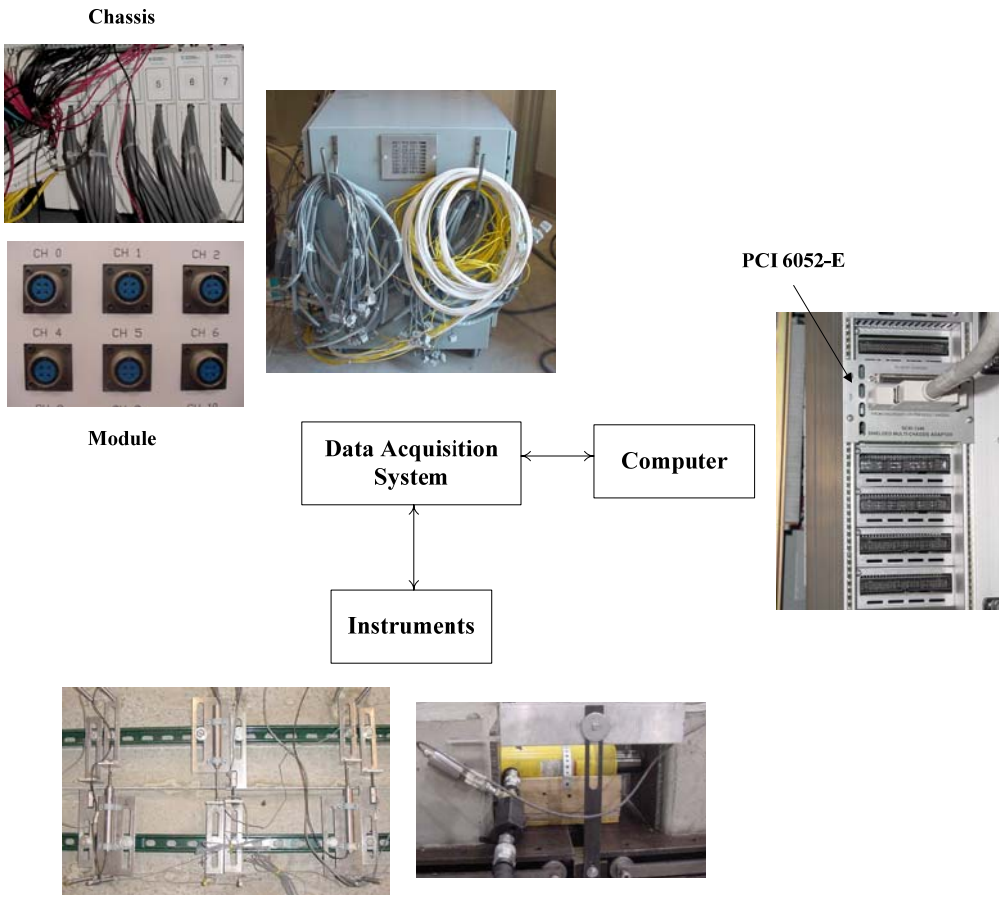

Figure A-18. Data Flow

The data acquisition system is designed to hold the chassis and provide access and power to each channel on the chassis. The chassis is the main unit which consists of all the channels of the data acquisition system. The chassis model is a SCXI-1001. The chassis consists of a series of modules connected together to form a unit. A module consists of a series of channels which are used for certain instrument types. For instance, module 1 consists of the first 32 channels and modules 2-7 all consist of eight strain gage channels. The modules are cards (SCXI-1102B or SCXI-1520) which can be individually removed from the chassis. Module 1 is a NI DAQ card termed SCXI-1102B and is the only module used in the pullout tests. Out of the 32 channels, channels 0-15 are three-wire connections, 16-25 are thermocouple connections, and channels 26-31 are four-wire

connections. The three wire connections accommodate the sliders and the pressure transducers (Channels 0-15) while the four wire connections (Channels 26-31) accommodate the LVDTs. External power supplies are linked to the data acquisition system to provide the necessary excitation voltages for the different instruments.

The calibration files corresponding to the different instrumentation are fed into the computer. The instruments are connected to the different channels on the data acquisition system using connectors and wires. As shown in Figure A-18, the connection between the computer and the data acquisition system is established using a cable and the Analog-Digital card PCI 6052-E present in the computer. Measurement and automation explorer (MAX) is a DAQ program set up by National Instruments and is responsible for the configuring the computer to read the DAQ. This data is then converted to the corresponding measurement units by the software interface (Little General Version 6.1) using the calibration files mentioned earlier. Little General run off the configuration of MAX.

APPENDIX B
MISALIGNMENT CHECK - SURVEYING SUMMARY

Table B-1. Misalignment Check Summary – One Dowel Tests

Type	Misalign-ment, in.	Misalignment through surveying, in.		Actual Misalignment, in.		Absolute Error, in.		Error, in.	
		West	East	West	East	West	East	West Side	East Side
Straight	0	5.074	5.028	5.00	5.00	0.074	0.028	>1/16 and <1/8	<1/16
		5.012	5.083	5.00	5.00	0.012	0.083	<1/16	>1/16 and <1/8
		5.028	5.022	5.00	5.00	0.028	0.022	<1/16	<1/16
V	0.25	5.168	4.804	5.25	4.75	0.082	0.054	>1/16 and <1/8	<1/16
	0.5	5.520	4.443	5.50	4.50	0.020	0.057	<1/16	<1/16
	0.75	5.816	4.312	5.75	4.25	0.066	0.062	>1/16 and <1/8	<1/16
	1	5.922	4.099	6.00	4.00	0.078	0.099	>1/16 and <1/8	>1/16 and <1/8
	2	7.046	3.062	7.00	3.00	0.046	0.062	<1/16	<1/16
H	0.25	4.983	5.105	5.00	5.00	0.017	0.105	<1/16	>1/16 and <1/8
	0.5	5.069	5.095	5.00	5.00	0.069	0.095	>1/16 and <1/8	>1/16 and <1/8
	0.75	5.100	5.082	5.00	5.00	0.100	0.082	>1/16 and <1/8	>1/16 and <1/8
	1	4.926	5.122	5.00	5.00	0.074	0.122	>1/16 and <1/8	>1/16 and <1/8
	2	4.979	4.974	5.00	5.00	0.021	0.026	<1/16	<1/16
C	0.25	5.333	4.780	5.25	4.75	0.083	0.030	>1/16 and <1/8	<1/16
	0.5	5.593	4.549	5.50	4.50	0.093	0.049	>1/16 and <1/8	<1/16
	0.75	5.821	4.237	5.75	4.25	0.071	0.013	>1/16 and <1/8	<1/16
	1	6.044	3.981	6.00	4.00	0.044	0.019	<1/16	<1/16

Table B-2. Misalignment Check Summary – Two Dowel Tests (North Dowel)

Type	Misalign-ment, in.	Misalignment through surveying, in.		Actual Misalignment, in.		Absolute Error, in.		Error, in.	
		West	East	West	East	West	East	West	East
Straight	0	5.042	5.068	5.000	5.000	0.042	0.068	<1/16	>1/16 and <1/8
V	0.25	5.300	4.825	5.500	4.500	0.200	0.325	>1/16 and <1/8	>1/16 and <1/8
	0.5	5.599	4.580	5.500	4.500	0.099	0.080	>1/16 and <1/8	>1/16 and <1/8
	0.75	5.779	4.244	5.750	4.25	0.029	0.006	<1/16	<1/16
	1	6.027	4.042	6	4	0.027	0.042	<1/16	<1/16
	0.5_U	5.586	4.554	5.500	4.500	0.086	0.054	>1/16 and <1/8	<1/16
	1_U	6.070	4.217	6.0	4.0	0.070	0.217	>1/16 and <1/8	>1/16 and <1/8
H	0.25	5.080	4.972	5	5	0.080	0.028	>1/16 and <1/8	<1/16
	0.5	5.069	5.065	5.000	5.000	0.069	0.065	>1/16 and <1/8	>1/16 and <1/8
	0.75	5.045	5.049	5	5	0.045	0.049	<1/16	<1/16
	1	5.049	5.036	5	5	0.049	0.036	<1/16	<1/16
	0.5_U	5.030	5.037	5.000	5.000	0.030	0.037	<1/16	<1/16
	1_U	4.959	5.049	5.0	5.0	0.041	0.049	<1/16	<1/16
C	0.25	5.308	4.808	5.500	4.500	0.192	0.308	>1/16 and <1/8	>1/16 and <1/8
	0.5	5.567	4.552	5.500	4.500	0.067	0.052	>1/16 and <1/8	<1/16
	0.75	5.797	4.261	5.750	4.250	0.047	0.011	<1/16	<1/16
	1	6.057	3.959	6.0	4.0	0.057	0.041	<1/16	<1/16
	0.5_U	5.576	4.583	5.500	4.500	0.076	0.083	>1/16 and <1/8	>1/16 and <1/8
	1_U	5.930	4.066	6.0	4.0	0.070	0.066	>1/16 and <1/8	>1/16 and <1/8
V	0,0.5	5.115	5.055	5.000	5.000	0.115	0.055	>1/16 and <1/8	<1/16
	0,0.75	5.069	5.064	5.000	5.000	0.069	0.064	>1/16 and <1/8	>1/16 and <1/8
H	0,0.5	5.070	5.050	5	5	0.070	0.050	>1/16 and <1/8	<1/16
	0,0.75	5.021	5.063	5.000	5.000	0.021	0.063	<1/16	>1/16 and <1/8
C	0,0.5	4.997	5.043	5.000	5.000	0.003	0.043	<1/16	<1/16
	0,0.75	5.047	5.057	5.000	5.000	0.047	0.057	<1/16	<1/16

Table B-3. Misalignment Check Summary – Two Dowel Tests (South Dowel)

Type	Misalign-ment, in.	Misalignment through surveying, in.		Actual Misalignment, in.		Absolute Error, in.		Error, in.	
		West	East	West	East	West	East	West	East
Straight	0	5.057	5.076	5.000	5.000	0.057	0.076	<1/16	>1/16 and <1/8
V	0.25	4.766	5.291	4.500	5.500	0.266	0.209	>1/16 and <1/8	>1/16 and <1/8
	0.5	4.430	5.547	4.500	5.500	0.070	0.047	>1/16 and <1/8	<1/16
	0.75	4.298	5.783	4.250	5.750	0.048	0.033	<1/16	<1/16
	1	4.074	6.066	4	6	0.074	0.066	>1/16 and <1/8	>1/16 and <1/8
	0.5_U	5.591	4.558	4.500	5.500	1.091	0.942	>1/16 and <1/8	>1/16 and <1/8
	1_U	6.078	4.208	6.0	4.0	0.078	0.208	>1/16 and <1/8	>1/16 and <1/8
H	0.25	5.031	4.903	5	5	0.031	0.097	<1/16	>1/16 and <1/8
	0.5	5.087	5.023	5.000	5.000	0.087	0.023	>1/16 and <1/8	<1/16
	0.75	5.095	5.025	5	5	0.095	0.025	>1/16 and <1/8	<1/16
	1	5.044	5.077	5	5	0.044	0.077	<1/16	>1/16 and <1/8
	0.5_U	5.084	5.111	4.500	5.500	0.584	0.389	>1/16 and <1/8	>1/16 and <1/8
	1_U	4.960	5.057	5.0	5.0	0.040	0.057	<1/16	<1/16
C	0.25	4.801	5.308	4.5	5.5	0.301	0.192	>1/16 and <1/8	>1/16 and <1/8
	0.5	4.600	5.534	4.500	5.500	0.100	0.034	>1/16 and <1/8	<1/16
	0.75	4.295	5.737	4.250	5.750	0.045	0.013	<1/16	<1/16
	1	4.030	5.964	4.0	6.0	0.030	0.036	<1/16	<1/16
	0.5_U	5.619	4.588	4.500	5.500	1.119	0.912	>1/16 and <1/8	>1/16 and <1/8
	1_U	5.961	3.999	6.0	4.0	0.039	0.001	<1/16	<1/16
V	0,0.5	4.581	5.548	4.500	5.500	0.081	0.048	>1/16 and <1/8	<1/16
	0,0.75	4.305	5.837	4.250	5.750	0.055	0.087	<1/16	>1/16 and <1/8
H	0,0.5	5.025	5.009	5	5	0.025	0.009	<1/16	<1/16
	0,0.75	4.935	4.959	5.000	5.000	0.065	0.041	>1/16 and <1/8	<1/16
C	0,0.5	4.589	5.472	4.500	5.500	0.089	0.028	>1/16 and <1/8	<1/16
	0,0.75	4.293	5.797	4.250	5.750	0.043	0.047	<1/16	<1/16

Table B-4. Misalignment Check Summary – Three and Five Dowel Tests

Type	Dowels Misaligned	Misalign-ment, in.	Misalignment through surveying, in.		Actual Misalignment, in.		Absolute Error, in.		Error, in.	
			West	East	West	East	West	East	West	East
3C	All	0.5	5.491	4.575	5.5	4.5	0.009	0.075	<1/16	>1/16 and <1/8
			4.589	5.489	4.5	5.5	0.089	0.011	>1/16 and <1/8	<1/16
			5.509	4.585	5.5	4.5	0.009	0.085	<1/16	>1/16 and <1/8
3H	All		4.988	5.075	5	5	0.012	0.075	<1/16	>1/16 and <1/8
			5.056	5.063	5	5	0.056	0.063	<1/16	>1/16 and <1/8
			4.993	5.082	5	5	0.007	0.082	<1/16	>1/16 and <1/8
3V	All		5.591	4.577	5.5	4.5	0.091	0.077	>1/16 and <1/8	>1/16 and <1/8
			4.575	5.490	4.5	5.5	0.075	0.010	>1/16 and <1/8	<1/16
			5.559	4.569	5.5	4.5	0.059	0.069	<1/16	>1/16 and <1/8
5C	Outer & Center	0.5	5.391	4.596	5.5	4.5	0.109	0.096	>1/16 and <1/8	>1/16 and <1/8
		0	4.898	5.025	5	5	0.102	0.025	>1/16 and <1/8	<1/16
		0.5	4.416	5.574	4.5	5.5	0.084	0.074	>1/16 and <1/8	>1/16 and <1/8
		0	4.976	5.059	5	5	0.024	0.059	<1/16	<1/16
		0.5	5.393	4.568	5.5	4.5	0.107	0.068	>1/16 and <1/8	>1/16 and <1/8
5H	Outer & Center	0.5	5.079	-	5	-	0.079	-	>1/16 and <1/8	-
		0	5.045	-	5	-	0.045	-	<1/16	-
		0.5	4.926	-	5	-	0.074	-	>1/16 and <1/8	-
		0	5.106	-	5	-	0.106	-	>1/16 and <1/8	-
		0.5	4.959	-	5	-	0.041	-	<1/16	-
5H	All	0.5	5.153	5.033	5.000	5.000	0.153	0.033	>1/16 and <1/8	<1/16
		0.5	5.020	5.042	5.000	5.000	0.020	0.042	<1/16	<1/16
		0.5	4.949	5.110	5.000	5.000	0.051	0.110	<1/16	>1/16 and <1/8
		0.5	5.009	5.105	5.000	5.000	0.009	0.105	<1/16	>1/16 and <1/8
		0.5	5.047	5.106	5.000	5.000	0.047	0.106	<1/16	>1/16 and <1/8
5V	Outer & Center	0.5	5.447	4.596	5.5	4.5	0.053	0.096	<1/16	>1/16 and <1/8
		0	5.038	4.993	5	5	0.038	0.007	<1/16	<1/16
		0.5	4.549	5.465	4.5	5.5	0.049	0.035	<1/16	<1/16
		0	4.930	5.018	5	5	0.070	0.018	>1/16 and <1/8	<1/16
		0.5	5.561	4.503	5.5	4.5	0.061	0.003	<1/16	<1/16

Table B-5. Horizontal Misalignment Summary – One Dowel Tests

Type	Misalign-ment, in.	Distance through surveying, in.		Actual Distance, in.		Absolute Error, in.		Error, in.	
		West	East	West	East	West	East	West	East
H	0.25	0.270	0.244	0.250	0.250	0.020	0.006	<1/16	<1/16
	0.5	0.527	0.517	0.500	0.500	0.027	0.017	<1/16	<1/16
	0.75	0.778	0.783	0.750	0.750	0.028	0.033	<1/16	<1/16
	1	1.133	1.031	1.000	1.000	0.133	0.031	>1/16 and <1/8	<1/16
	2	2.083	2.032	2.000	2.000	0.083	0.032	>1/16 and <1/8	<1/16
C	0.25	0.252	0.316	0.250	0.250	0.002	0.066	<1/16	>1/16 and <1/8
	0.5	0.448	0.475	0.500	0.500	0.052	0.025	<1/16	<1/16
	0.75_old	0.839	0.739	0.750	0.750	0.089	0.011	>1/16 and <1/8	<1/16
	0.75	0.752	0.778	0.750	0.750	0.002	0.028	<1/16	<1/16
	1	0.955	1.041	1.000	1.000	0.045	0.041	<1/16	<1/16

Table B-6. Horizontal Misalignment Summary – Two Dowel Tests (North Dowel)

Type	Misalign-Ment, in.	Distance through surveying, in.		Actual Distance, in.		Absolute Error, in.		Error, in.	
		West	East	West	East	West	East	West	East
H	0.25	0.287	0.345	0.25	0.25	0.037	0.095	<1/16	>1/16 and <1/8
	0.5	0.520	0.500	0.500	0.500	0.020	0.000	<1/16	<1/16
	0.75	0.786	0.803	0.750	0.750	0.036	0.053	<1/16	<1/16
	1	0.998	0.976	1.000	1.000	0.002	0.024	<1/16	<1/16
	0.5_U	0.513	0.514	0.5	0.5	0.013	0.014	<1/16	<1/16
	1_U	1.093	1.031	1.000	1.000	0.093	0.031	>1/16 and <1/8	<1/16
C	0.25	0.276	0.276	0.250	0.250	0.026	0.026	<1/16	<1/16
	0.5	0.551	0.525	0.5	0.5	0.051	0.025	<1/16	<1/16
	0.75	0.754	0.763	0.750	0.750	0.004	0.013	<1/16	<1/16
	1	1.097	1.092	1.000	1.000	0.097	0.092	>1/16 and <1/8	>1/16 and <1/8
	0.5_U	0.552	0.479	0.5	0.5	0.052	0.021	<1/16	<1/16
	1_U	1.010	1.047	1.000	1.000	0.010	0.047	<1/16	<1/16

Table B-7. Horizontal Misalignment Summary – Two Dowel Tests (South Dowel)

Type	Misalign-ment, in.	Distance through surveying, in.		Actual Distance, in.		Absolute Error, in.		Error, in.	
		West	East	West	East	West	East	West	East
H	0.25	0.344	0.342	0.25	0.25	0.094	0.092	>1/16 and <1/8	>1/16 and <1/8
	0.5	0.486	0.505	0.500	0.500	0.014	0.005	<1/16	<1/16
	0.75	0.786	0.798	0.750	0.750	0.036	0.048	<1/16	<1/16
	1	0.983	0.961	1.000	1.000	0.017	0.039	<1/16	<1/16
	0.5_U	0.514	0.541	0.5	0.5	0.014	0.041	<1/16	<1/16
	1_U	1.021	1.021	1.000	1.000	0.021	0.021	<1/16	<1/16
C	0.25	0.259	0.277	0.250	0.250	0.009	0.027	<1/16	<1/16
	0.5	0.511	0.437	0.5	0.5	0.011	0.063	<1/16	>1/16 and <1/8
	0.75	0.762	0.736	0.750	0.750	0.012	0.014	<1/16	<1/16
	1	0.958	0.980	1.000	1.000	0.042	0.020	<1/16	<1/16
	0.5_U	0.513	0.514	0.5	0.5	0.013	0.014	<1/16	<1/16
	1_U	1.014	1.012	1.000	1.000	0.014	0.012	<1/16	<1/16
H	0.5	0.513	0.458	0.5	0.5	0.013	0.042	<1/16	<1/16
	0.75	0.693	0.762	0.750	0.750	0.057	0.012	<1/16	<1/16
C	0.5	0.473	0.477	0.5	0.5	0.027	0.023	<1/16	<1/16
	0.75	0.750	0.731	0.750	0.750	0.000	0.019	<1/16	<1/16

Table B-8. Horizontal Misalignment Summary – Three and Five Dowel Tests

Type	Dowels Misaligned	Misalign-ment, in.	Distance through surveying, in.		Actual Distance, in.		Absolute Error, in.		Error, in.	
			West	East	West	East	West	East	West	East
3C	All	0.5	0.517	0.526	0.5	0.5	0.017	0.026	<1/16	<1/16
		0.5	0.510	0.512	0.5	0.5	0.010	0.012	<1/16	<1/16
		0.5	0.515	0.416	0.5	0.5	0.015	0.084	<1/16	>1/16 and <1/8
3H	All	0.5	0.503	0.549	0.5	0.5	0.003	0.049	<1/16	<1/16
		0.5	0.501	0.510	0.5	0.5	0.001	0.010	<1/16	<1/16
		0.5	0.502	0.500	0.5	0.5	0.002	0.000	<1/16	<1/16
5C	Outer & Center	0.5	0.399	0.531	0.5	0.5	0.101	0.031	>1/16 and <1/8	<1/16
		0.5	-	-	-	-	-	-	-	-
		0.5	0.495	0.538	0.5	0.5	0.005	0.038	<1/16	<1/16
		0.5	-	-	-	-	-	-	-	-
		0.5	0.509	0.545	0.5	0.5	0.009	0.045	<1/16	<1/16
5H	All	0.5	0.513	0.482	0.5	0.5	0.013	0.018	<1/16	<1/16
		0.5	0.500	0.482	0.5	0.5	0.000	0.018	<1/16	<1/16
		0.5	0.499	0.540	0.5	0.5	0.001	0.040	<1/16	<1/16
		0.5	0.457	0.474	0.5	0.5	0.043	0.026	<1/16	<1/16
		0.5	0.515	0.514	0.5	0.5	0.015	0.014	<1/16	<1/16
5H	Outer & Center	0.5	0.473		0.5		0.027		<1/16	<1/16
		0.5	-	-	-	-	-	-	-	-
		0.5	0.489		0.5		0.011	0	<1/16	<1/16
		0.5	-	-	-	-	-	-	-	-
		0.5	0.507		0.5		0.007		<1/16	<1/16

APPENDIX C

RESULTS OF 3D FINITE ELEMENT MODELS

Results of 1A Finite element model

The dowel-concrete friction coefficients and material properties used in the analysis are shown in table C1. A comparison of the pullout force per bar (lbs.) vs. the joint opening (in.) is shown in figure C1. A summary of the various material failure / damage limit states is presented in Table C2.

Table C-1: Dowel-Concrete Friction Coefficients; Material Properties used and limit states obtained from the analysis.

	μ_g	μ_w	f'_c (psi)	f'_t (psi)
Case I	0.0	0.30	3500.0	236.64
Case II	0.074	0.384	2544.0	540.0

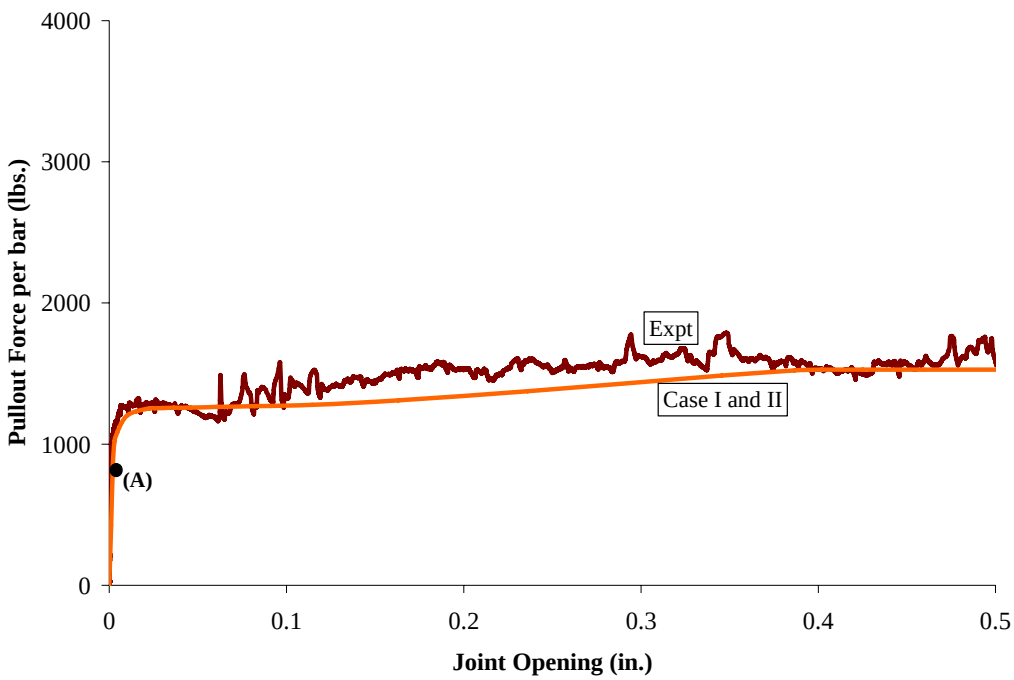

Figure C-1: Comparison of the FEM model with the experimental data for 1A specimen

Table C-2: Summary of Material Failure / Damage Limit States from the analysis

Material Damage / Limit States	Joint Opening (in.)		Pullout Load (lbs)	
	(I)	(II)	(I)	(II)
(A)	0.003	0.003	1020.0	1020.0
(B)	-	-	-	-
(C)	-	-	-	-
(D)	-	-	-	-
(E)	-	-	-	-
(F)	-	-	-	-

Results of 1V18 Finite Element Model

The dowel-concrete friction coefficients and material properties used in the analysis are shown in table C3. A comparison of the pullout force per bar (lbs.) vs. the joint opening (in.) is shown in figure C2. A summary of the various material failure / damage limit states is presented in table C4.

Table C-3: Dowel-Concrete Friction Coefficients; Material Properties used and limit states obtained from the analysis.

	μ_g	μ_w	f'_c (psi)	f'_t (psi)
Case I	0.0	0.30	3500.0	236.64
Case II	0.074	0.384	2544.0	540.0

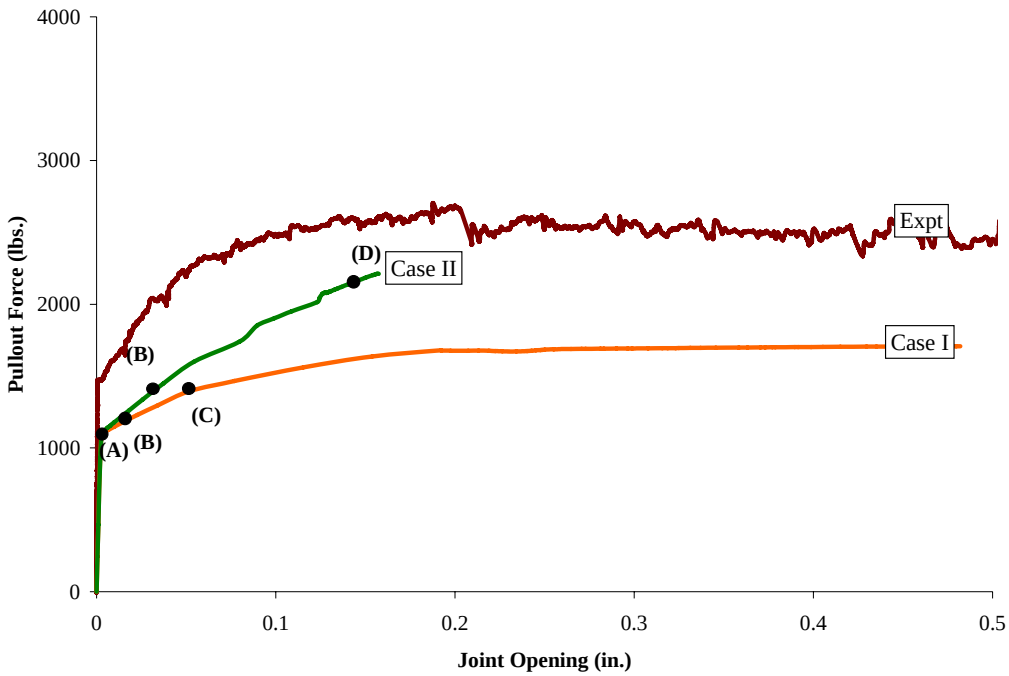

Figure C-2: Comparison of the FEM model with the experimental data for 1V18 specimen

Table C-4: Summary of Material Failure / Damage Limit States from the analysis

Material Damage / Limit States	Joint Opening (in.)		Pullout Load (lbs)	
	(I)	(II)	(I)	(II)
(A)	0.003	0.003	1100.0	1100.0
(B)	0.015	0.038	1180.0	1450
(C)	0.115	-	1560.0	-
(D)	-	0.148	-	2170
(E)	-	-	-	-
(F)	-	-	-	-

Results of 1V36 Finite Element Model

The dowel-concrete friction coefficients and material properties used in the analysis are shown in table C5. A comparison of the pullout force per bar (lbs.) vs. the joint opening (in.) is shown in figure C3. A summary of the various material failure / damage limit states is presented in table C6.

Table C-5: Dowel-Concrete Friction Coefficients; Material Properties used and limit states obtained from the analysis.

	μ_g	μ_w	f'_c (psi)	f'_t (psi)
Case I	0.0	0.30	3500.0	236.64
Case II	0.074	0.384	3328.0	240.0

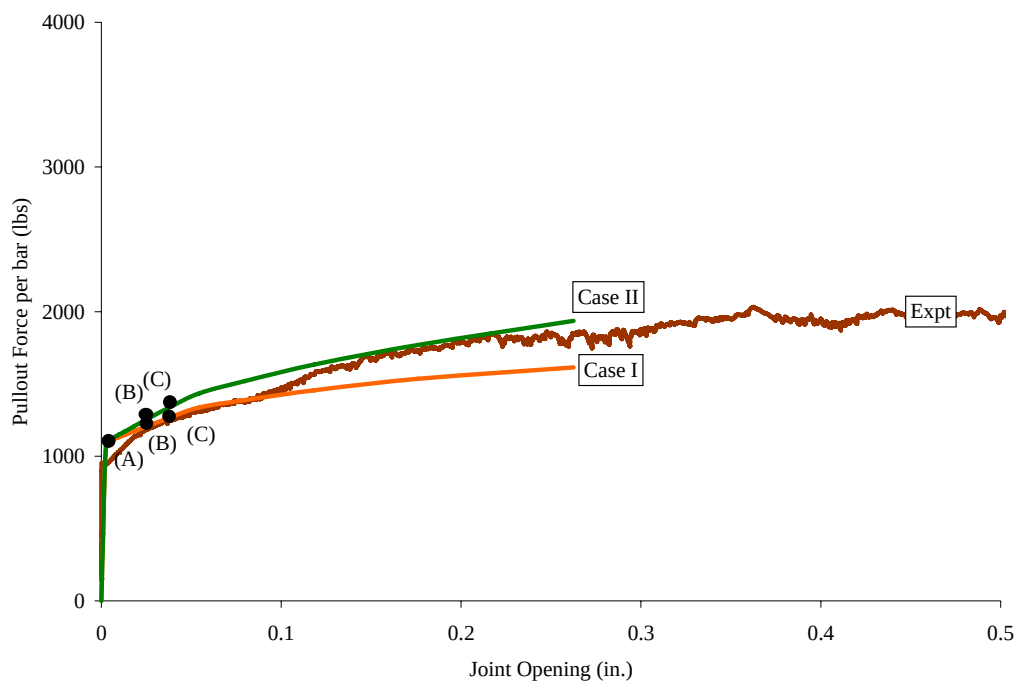

Figure C-3: Comparison of the FEM model with the experimental data for 1V36 specimen

Table C-6: Summary of Material Failure / Damage Limit States from the analysis

Material Damage / Limit States	Joint Opening (in.)		Pullout Load (lbs)	
	(I)	(II)	(I)	(II)
(A)	0.003	0.003	1100.0	1100.0
(B)	0.026	0.026	1210.0	1260.0
(C)	0.037	0.037	1260.0	1330.0
(D)	-	-	-	-
(E)	-	-	-	-
(F)	-	-	-	-

Results of 1V72 Finite Element Model

The dowel-concrete friction coefficients and material properties used in the analysis are shown in table C7. A comparison of the pullout force per bar (lbs.) vs. the joint opening (in.) is shown in figure C4. A summary of the various material failure / damage limit states is presented in table C8.

Table C-7: Dowel-Concrete Friction Coefficients; Material Properties used and limit states obtained from the analysis.

	μ_g	μ_w	f'_c (psi)	f'_t (psi)
Case I	0.0	0.30	3500.0	236.64
Case II	0.074	0.384	3500.0	236.64

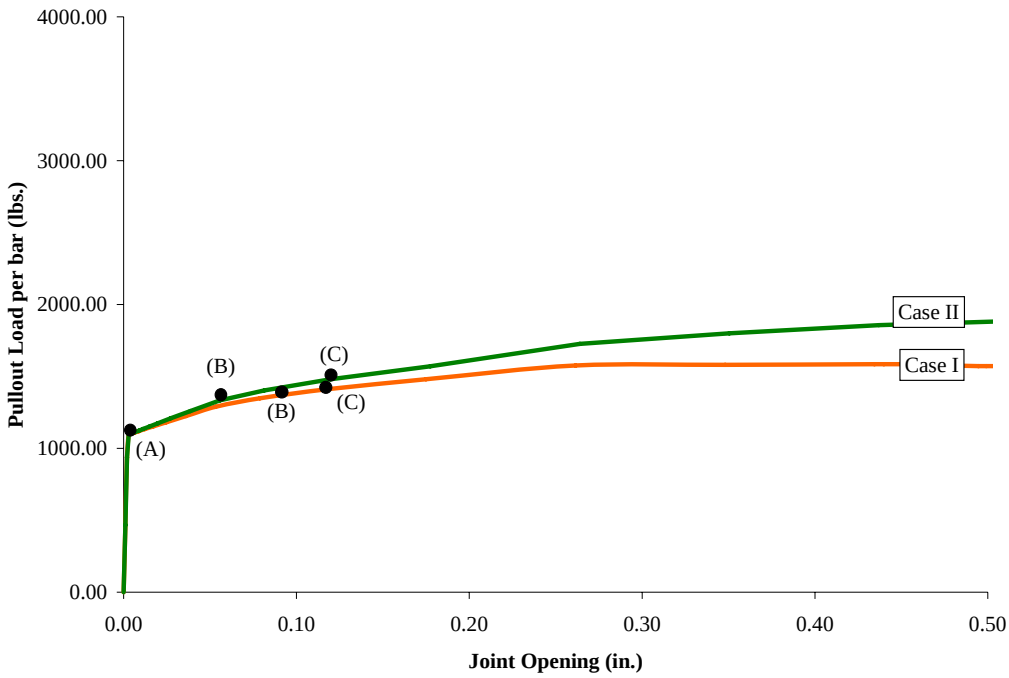

Figure C-4: Comparison of the FEM model with the experimental data for 1V72 specimen

Table C-8: Summary of Material Failure / Damage Limit States from the analysis

Material Damage / Limit States	Joint Opening (in.)		Pullout Load (lbs)	
	(I)	(II)	(I)	(II)
(A)	0.003	0.003	1100.0	1100.0
(B)	0.079	0.056	1350.0	1130.0
(C)	0.117	0.119	1410.0	1570.0
(D)	-	-	-	-
(E)	-	-	-	-
(F)	-	-	-	-

Results of 1H18 Finite Element Model

The dowel-concrete friction coefficients and material properties used in the analysis are shown in table C9. A comparison of the pullout force per bar (lbs.) vs. the joint opening (in.) is shown in figure C5. A summary of the various material failure / damage limit states is presented in table C10.

Table C-9: Dowel-Concrete Friction Coefficients; Material Properties used and limit states obtained from the analysis.

	μ_g	μ_w	f'_c (psi)	f'_t (psi)
Case I	0.0	0.30	3500.0	236.64
Case II	0.074	0.384	4142.0	440.0

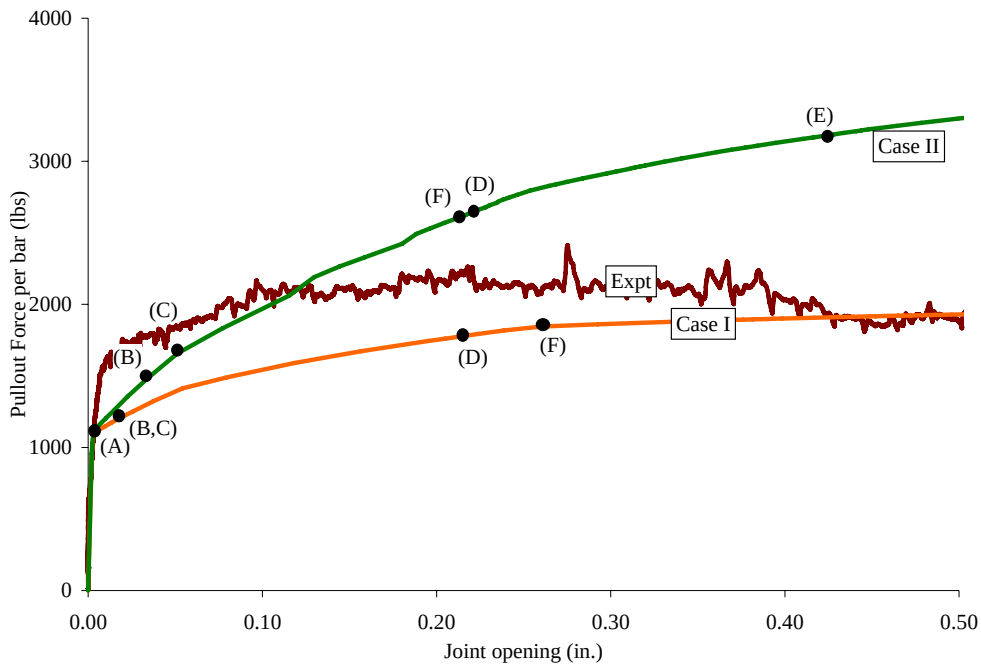

Figure C-5: Comparison of the FEM model with the experimental data for 1H18 specimen

Table C-10: Summary of Material Failure / Damage Limit States from the analysis

Material Damage / Limit States	Joint Opening (in.)		Pullout Load (lbs)	
	(I)	(II)	(I)	(II)
(A)	0.003	0.003	1100.0	1120.0
(B)	0.018	0.034	1200.0	1480.0
(C)	0.018	0.051	1200.0	1660.0
(D)	0.214	0.228	1780.0	2680.0
(E)	0.535	0.425	1940.0	3180.0
(F)	0.260	0.217	1840.0	2620.0

Results of 1H36 Finite Element Model

The dowel-concrete friction coefficients and material properties used in the analysis are shown in table C11. A comparison of the pullout force per bar (lbs.) vs. the joint opening (in.) is shown in figure C6. A summary of the various material failure / damage limit states is presented in table C12.

Table C-11: Dowel-Concrete Friction Coefficients; Material Properties used and limit states obtained from the analysis.

	μ_g	μ_w	f'_c (psi)	f'_t (psi)
Case I	0.0	0.30	3500.0	236.64
Case II	0.074	0.384	3328.0	248.0

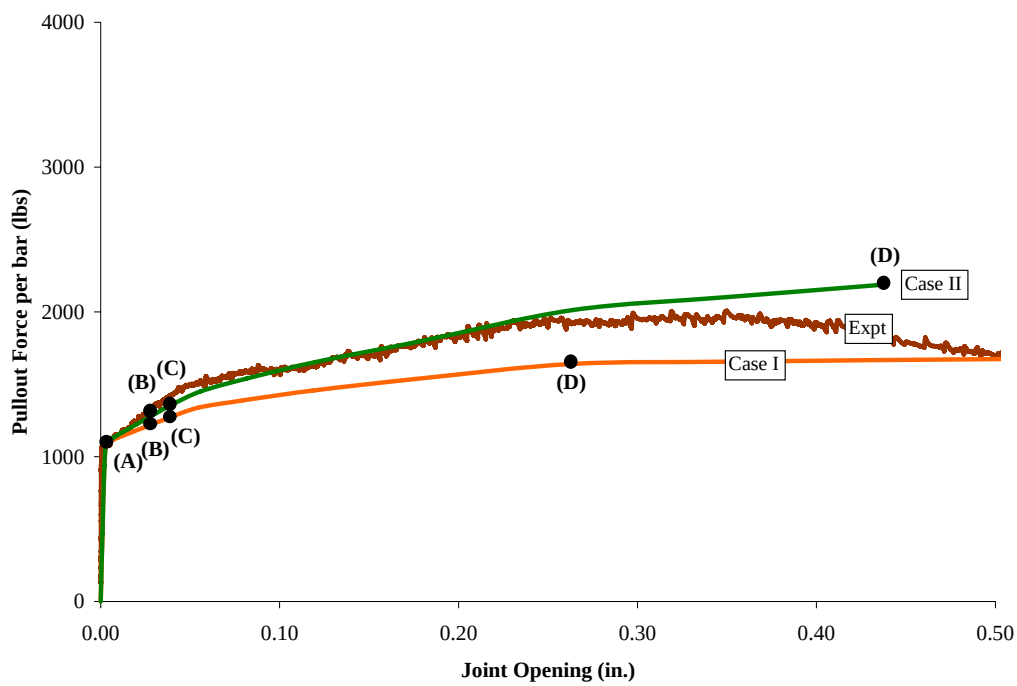

Figure C-6: Comparison of the FEM model with the experimental data for 1H36 specimen

Table C-12: Summary of Material Failure / Damage Limit States from the analysis

Material Damage / Limit States	Joint Opening (in.)		Pullout Load (lbs)	
	(I)	(II)	(I)	(II)
(A)	0.003	0.003	1100.0	1100.0
(B)	0.026	0.027	1210.0	1270.0
(C)	0.037	0.0387	1260.0	1350.0
(D)	0.349	0.4370	1660.0	2190.0
(E)	-	-	-	-
(F)	-	-	-	-

Results of 1H72 Finite Element Model

The dowel-concrete friction coefficients and material properties used in the analysis are shown in table C13. A comparison of the pullout force per bar (lbs.) vs. the joint opening (in.) is shown in figure C7. A summary of the various material failure / damage limit states is presented in table C14.

Table C-13: Dowel-Concrete Friction Coefficients; Material Properties used and limit states obtained from the analysis.

	μ_g	μ_w	f'_c (psi)	f'_t (psi)
Case I	0.0	0.30	3500.0	236.64
Case II	0.074	0.384	3500.0	236.64

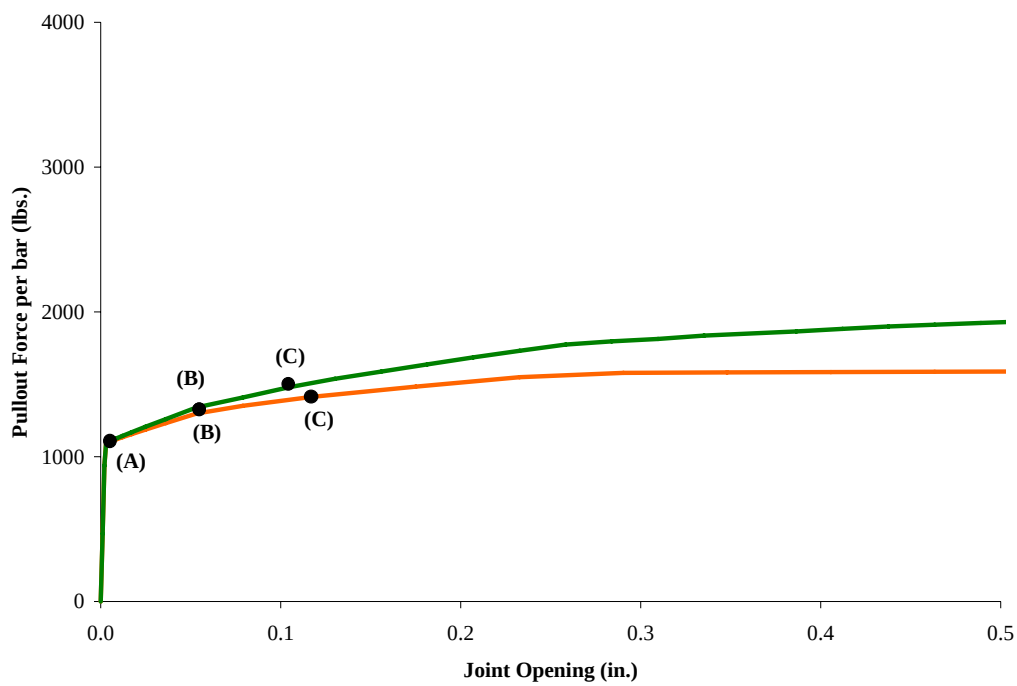

Figure C-7: Comparison of the FEM model with the experimental data for 1H72 specimen

Table C-14: Summary of Material Failure / Damage Limit States from the analysis

Material Damage / Limit States	Joint Opening (in.)		Pullout Load (lbs)	
	(I)	(II)	(I)	(II)
(A)	0.003	0.003	1100.0	1100.0
(B)	0.053	0.053	1300.0	1340.0
(C)	0.117	0.104	1410.0	1480.0
(D)	0.809	0.801	1600.0	2050.0
(E)	-	-	-	-
(F)	-	-	-	-

Results of 1C18 Finite Element Model

The dowel-concrete friction coefficients and material properties used in the analysis are shown in table C15. A comparison of the pullout force per bar (lbs.) vs. the joint opening (in.) is shown in figure C8. A summary of the various material failure / damage limit states is presented in table C16.

Table C-15: Dowel-Concrete Friction Coefficients; Material Properties used and limit states obtained from the analysis.

	μ_g	μ_w	f'_c (psi)	f'_t (psi)
Case I	0.0	0.30	3500.0	236.64
Case II	0.074	0.384	3530.0	355.0

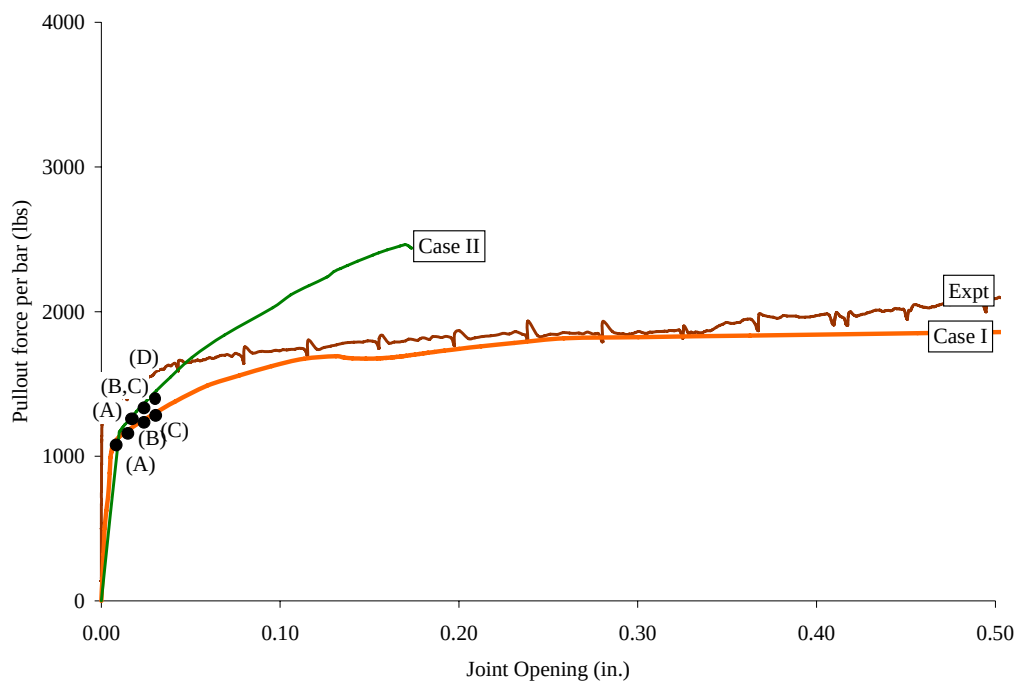

Figure C-8: Comparison of the FEM model with the experimental data for 1C18 specimen

Table C-16: Summary of Material Failure / Damage Limit States from the analysis

Material Damage / Limit States	Joint Opening (in.)		Pullout Load (lbs)	
	(I)	(II)	(I)	(II)
(A)	0.003	0.003	720.0	750.0
(B)	0.012	0.014	1160.0	1240.0
(C)	0.016	0.014	1190.0	1240.0
(D)	-	0.116	-	2180.0
(E)	-	0.126	-	2240.0
(F)	-	-	-	-

Results of 1C36 Finite Element Model

The dowel-concrete friction coefficients and material properties used in the analysis are shown in table C17. A comparison of the pullout force per bar (lbs.) vs. the joint opening (in.) is shown in figure C9. A summary of the various material failure / damage limit states is presented in table C18.

Table C-17: Dowel-Concrete Friction Coefficients; Material Properties used and limit states obtained from the analysis.

	μ_g	μ_w	f'_c (psi)	f'_t (psi)
Case I	0.0	0.30	3500.0	236.64
Case II	0.074	0.384	3328.0	240.0

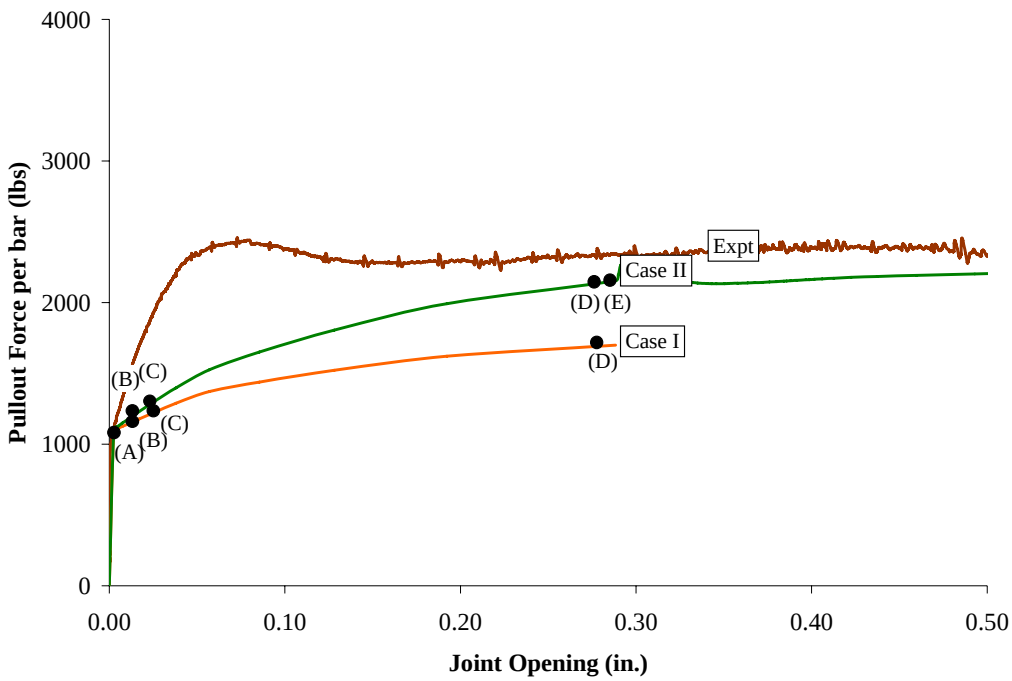

Figure C-9: Comparison of the FEM model with the experimental data for 1C36 specimen

Table C-18: Summary of Material Failure / Damage Limit States from the analysis

Material Damage / Limit States	Joint Opening (in.)		Pullout Load (lbs)	
	(I)	(II)	(I)	(II)
(A)	0.003	0.003	1100.0	1100.0
(B)	0.025	0.025	1220.0	1300.0
(C)	0.038	0.038	1290.0	1400.0
(D)	0.288	0.288	1700.0	2150.0
(E)	-	0.300	-	2220.0
(F)	-	-	-	-

Results of 2A Finite element model

The dowel-concrete friction coefficients and material properties used in the analysis are shown in table C19. A comparison of the pullout force per bar (lbs.) vs. the joint opening (in.) is shown in figure C10. A summary of the various material failure / damage limit states is presented in table C20.

Table C-19: Dowel-Concrete Friction Coefficients; Material Properties used and limit states obtained from the analysis.

	μ_g	μ_w	f'_c (psi)	f'_t (psi)
Case I	0.0	0.30	3500.0	236.64
Case II	0.074	0.384	3400.0	251.0

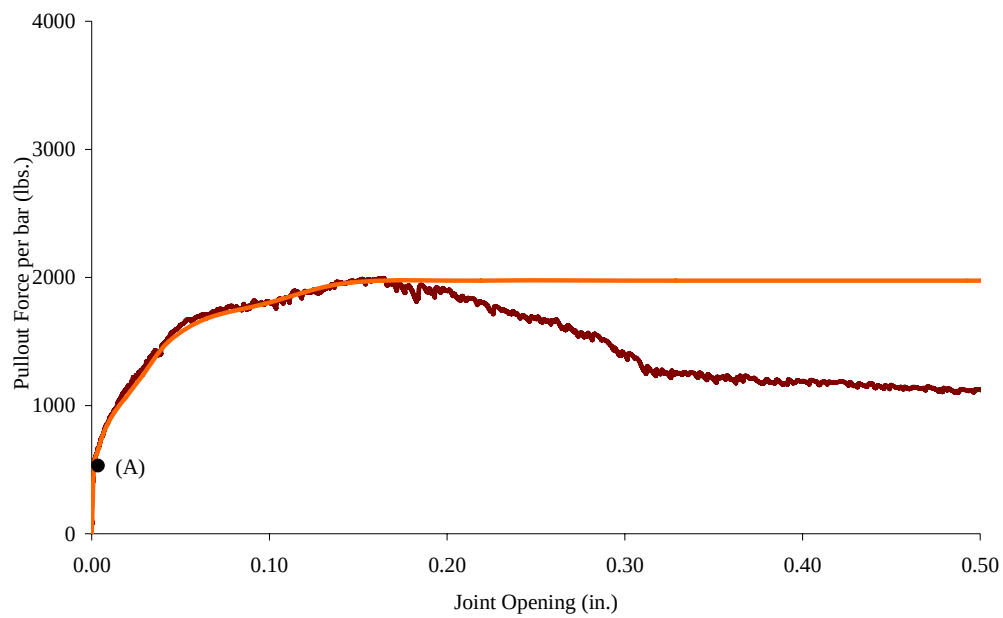

Figure C-10: Comparison of the FEM model with the experimental data for 2A specimen

Table C-20: Summary of Material Failure / Damage Limit States from the analysis

Material Damage / Limit States	Joint Opening (in.)		Pullout Load (lbs)	
	(I)	(II)	(I)	(II)
(A)	0.002	0.002	501.0	501.0
(B)	-	-	-	-
(C)	-	-	-	-
(D)	-	-	-	-
(E)	-	-	-	-
(F)	-	-	-	-

Results of 2V18NU Finite Element Model

The dowel-concrete friction coefficients and material properties used in the analysis are shown in table C21. A comparison of the pullout force per bar (lbs.) vs. the joint opening (in.) is shown in figure C11. A summary of the various material failure / damage limit states is presented in table C22.

Table C-21: Dowel-Concrete Friction Coefficients; Material Properties used and limit states obtained from the analysis.

	μ_g	μ_w	f'_c (psi)	f'_t (psi)
Case I	0.0	0.30	3500.0	236.64
Case II	0.074	0.384	4931.0	280.0

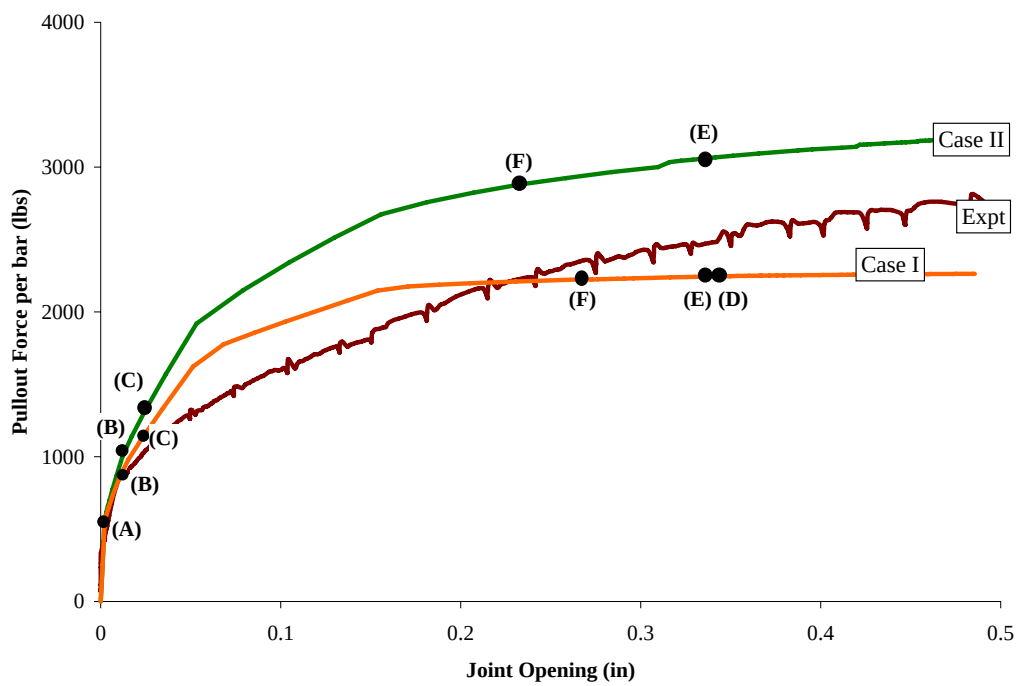

Figure C-11: Comparison of the FEM model with the experimental data for 2V18NU specimen

Table C-22: Summary of Material Failure / Damage Limit States from the analysis

Material Damage / Limit States	Joint Opening (in.)		Pullout Load (lbs)	
	(I)	(II)	(I)	(II)
(A)	0.002	0.002	513.00	525.92
(B)	0.010	0.021	846.00	1002.53
(C)	0.023	0.025	112.82	1321.06
(D)	0.339	0.552	2244.78	3247.22
(E)	0.337	0.335	2244.09	3059.84
(F)	0.269	0.233	2225.76	2880.03

Results of 2V18U Finite Element Model

The dowel-concrete friction coefficients and material properties used in the analysis are shown in table C23. A comparison of the pullout force per bar (lbs.) vs. the joint opening (in.) is shown in figure C12. A summary of the various material failure / damage limit states is presented in table C24.

Table C-23: Dowel-Concrete Friction Coefficients; Material Properties used and limit states obtained from the analysis.

	μ_g	μ_w	f'_c (psi)	f'_t (psi)
Case I	0.0	0.30	3500.0	236.64
Case II	0.074	0.384	3654.0	217.0

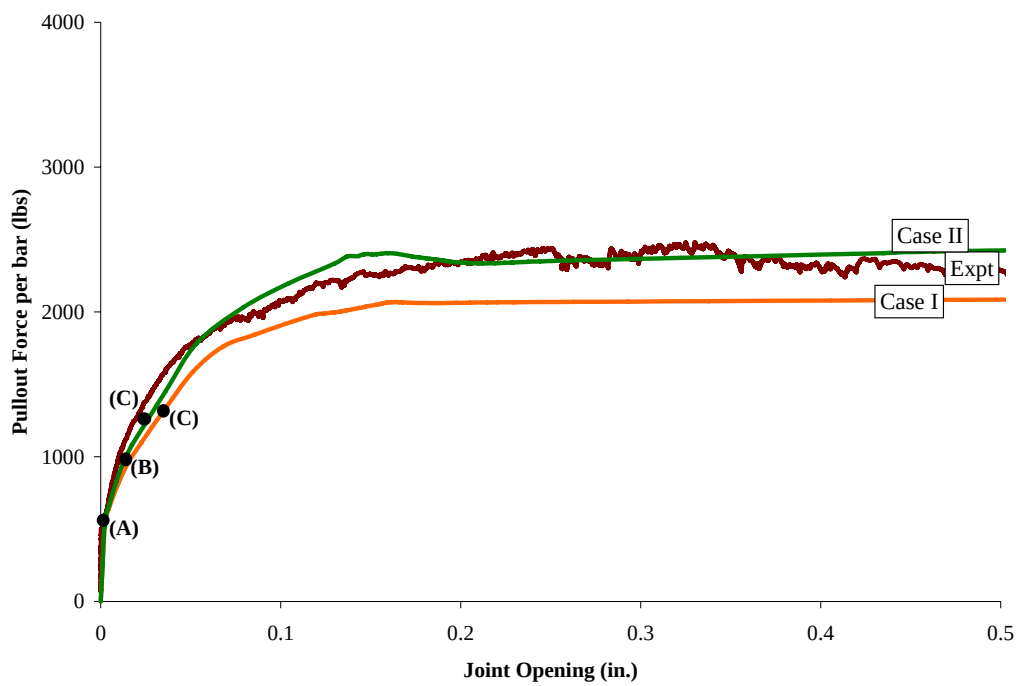

Figure C-12: Comparison of the FEM model with the experimental data for 2V18U specimen

Table C-24: Summary of Material Failure / Damage Limit States from the analysis

Material Damage / Limit States	Joint Opening (in.)		Pullout Load (lbs)	
	(I)	(II)	(I)	(II)
(A)	0.002	0.002	509.00	513.57
(B)	0.015	0.012	957.78	947.95
(C)	0.034	0.025	1302.88	1229.25
(D)	-	-	-	-
(E)	-	-	-	-
(F)	-	-	-	-

Results of 2V18AM Finite Element Model

The dowel-concrete friction coefficients and material properties used in the analysis are shown in table C25. A comparison of the pullout force per bar (lbs.) vs. the joint opening (in.) is shown in figure C13. A summary of the various material failure / damage limit states is presented in table C26.

Table C-25: Dowel-Concrete Friction Coefficients; Material Properties used and limit states obtained from the analysis.

	μ_g	μ_w	f'_c (psi)	f'_t (psi)
Case I	0.0	0.30	3500.0	236.64
Case II	0.074	0.384	3520.0	245.0

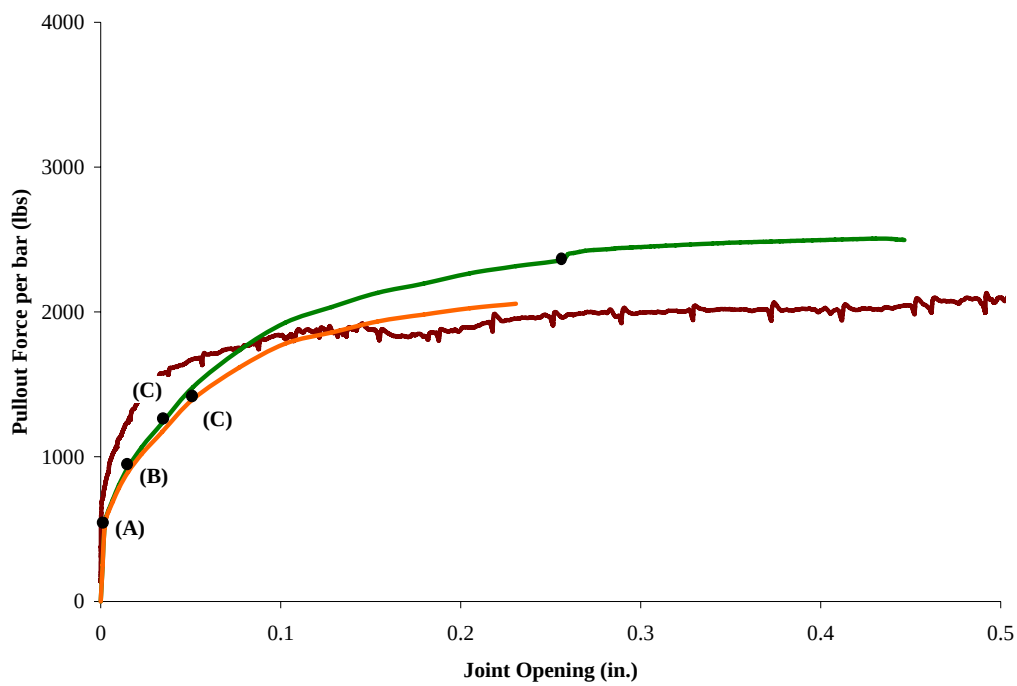

Figure C-13: Comparison of the FEM model with the experimental data for 2V18AM specimen

Table C-26: Summary of Material Failure / Damage Limit States from the analysis

Material Damage / Limit States	Joint Opening (in.)		Pullout Load (lbs)	
	(I)	(II)	(I)	(II)
(A)	0.002	0.002	505.34	507.34
(B)	0.015	0.015	893.57	925.84
(C)	0.051	0.034	1397.25	1232.84
(D)	-	-	-	-
(E)	-	-	-	-
(F)	-	-	-	-

Results of 2V36NU Finite Element Model

The dowel-concrete friction coefficients and material properties used in the analysis are shown in table C27. A comparison of the pullout force per bar (lbs.) vs. the joint opening (in.) is shown in figure C14. A summary of the various material failure / damage limit states is presented in table C28.

Table C-27: Dowel-Concrete Friction Coefficients; Material Properties used and limit states obtained from the analysis.

	μ_g	μ_w	f'_c (psi)	f'_t (psi)
Case I	0.0	0.30	3500.0	236.64
Case II	0.074	0.384	4931.0	280.0

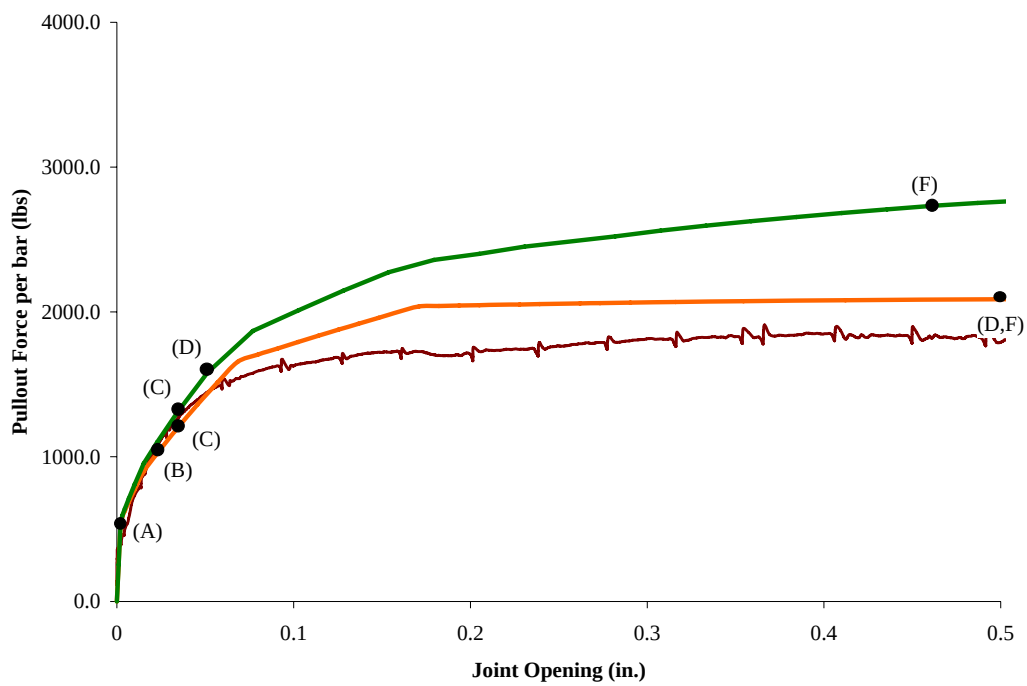

Figure C-14: Comparison of the FEM model with the experimental data for 2V36NU specimen

Table C-28: Summary of Material Failure / Damage Limit States from the analysis

Material Damage / Limit States	Joint Opening (in.)		Pullout Load (lbs)	
	(I)	(II)	(I)	(II)
(A)	0.002	0.002	504.5	512.48
(B)	0.023	0.023	1021.91	1100.62
(C)	0.034	0.034	1195.91	1306.52
(D)	0.498	0.721	2087.94	2875.67
(E)	0.623	0.577	2093.81	2808.90
(F)	0.498	0.461	2087.94	2733.14

Results of 2V36U Finite Element Model

The dowel-concrete friction coefficients and material properties used in the analysis are shown in table C29. A comparison of the pullout force per bar (lbs.) vs. the joint opening (in.) is shown in figure C15. A summary of the various material failure / damage limit states is presented in table C30.

Table C-29: Dowel-Concrete Friction Coefficients; Material Properties used and limit states obtained from the analysis.

	μ_g	μ_w	f'_c (psi)	f'_t (psi)
Case I	0.0	0.30	3500.0	236.64
Case II	0.074	0.384	3673.0	383.0

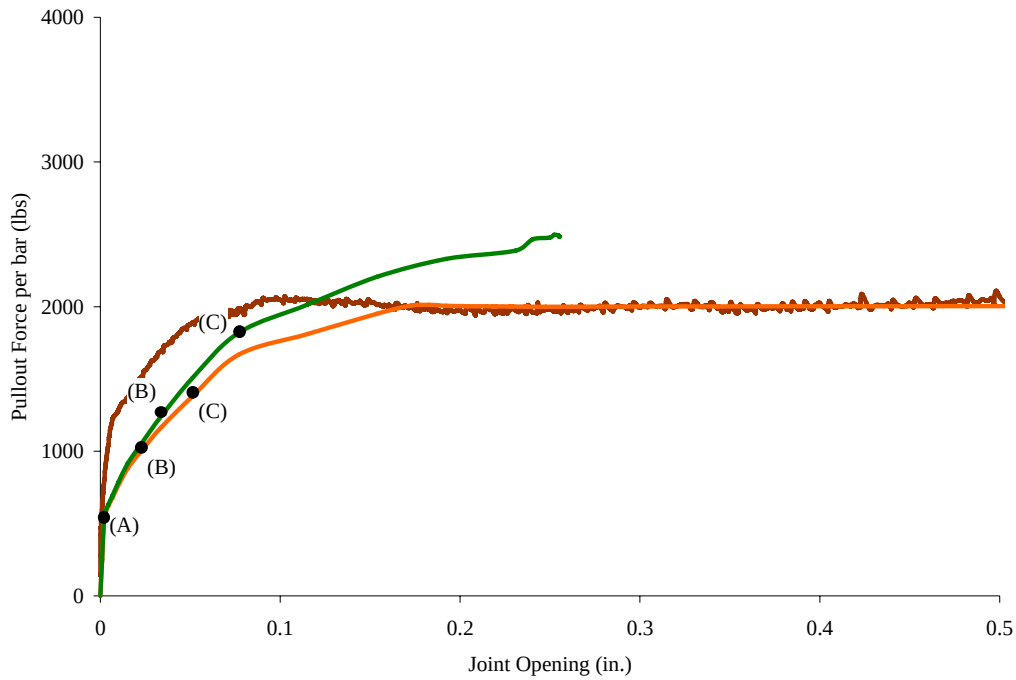

Figure C-15: Comparison of the FEM model with the experimental data for 2V36U specimen

Table C-30: Summary of Material Failure / Damage Limit States from the analysis

Material Damage / Limit States	Joint Opening (in.)		Pullout Load (lbs)	
	(I)	(II)	(I)	(II)
(A)	0.002	0.002	503.21	506.46
(B)	0.027	0.034	1003.51	1247.02
(C)	0.051	0.077	1379.87	1819.15
(D)	-	-	-	-
(E)	-	-	-	-
(F)	-	-	-	-

Results of 2V36AM Finite Element Model

The dowel-concrete friction coefficients and material properties used in the analysis are shown in table C31. A comparison of the pullout force per bar (lbs.) vs. the joint opening (in.) is shown in figure C16. A summary of the various material failure / damage limit states is presented in table C32.

Table C-31: Dowel-Concrete Friction Coefficients; Material Properties used and limit states obtained from the analysis.

	μ_g	μ_w	f'_c (psi)	f'_t (psi)
Case I	0.0	0.30	3500.0	236.64
Case II	0.074	0.384	3500.0	236.0

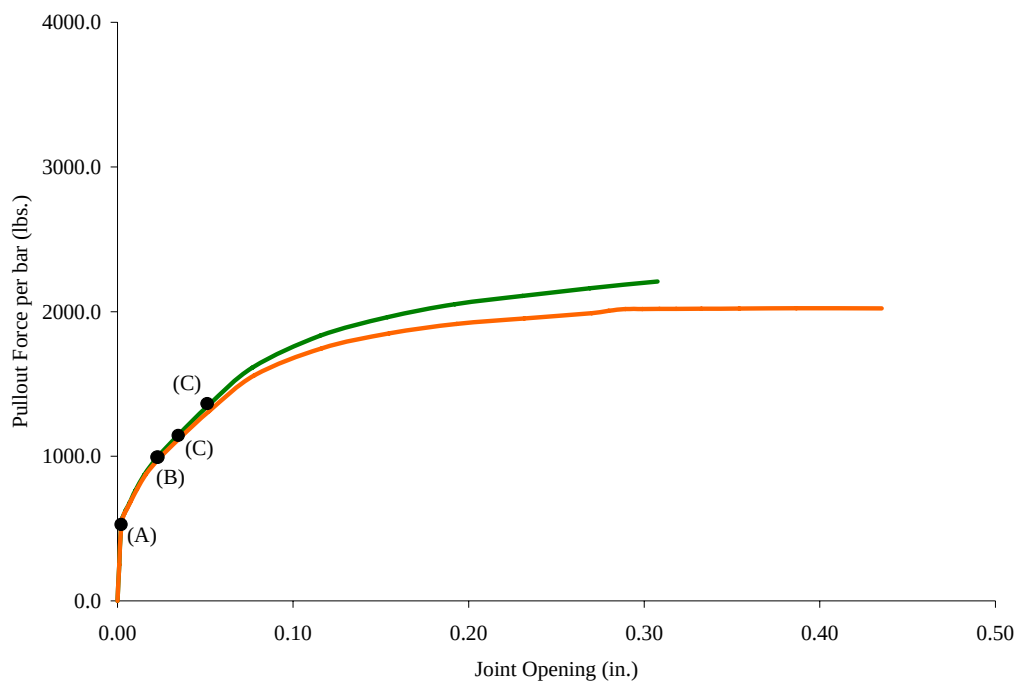

Figure C-16: Comparison of the FEM model with the experimental data for 2V36AM specimen

Table C-32: Summary of Material Failure / Damage Limit States from the analysis

Material Damage / Limit States	Joint Opening (in.)		Pullout Load (lbs)	
	(I)	(II)	(I)	(II)
(A)	0.002	0.002	501.33	502.58
(B)	0.024	0.023	984.51	993.41
(C)	0.035	0.051	1122.04	1345.74
(D)	-	-	-	-
(E)	-	-	-	-
(F)	-	-	-	-

Results of 2V72NU Finite Element Model

The dowel-concrete friction coefficients and material properties used in the analysis are shown in table C33. A comparison of the pullout force per bar (lbs.) vs. the joint opening (in.) is shown in figure C17. A summary of the various material failure / damage limit states is presented in table C34.

Table C-33: Dowel-Concrete Friction Coefficients; Material Properties used and limit states obtained from the analysis.

	μ_g	μ_w	f'_c (psi)	f'_t (psi)
Case I	0.0	0.30	3500.0	236.64
Case II	0.074	0.384	3500.0	236.64

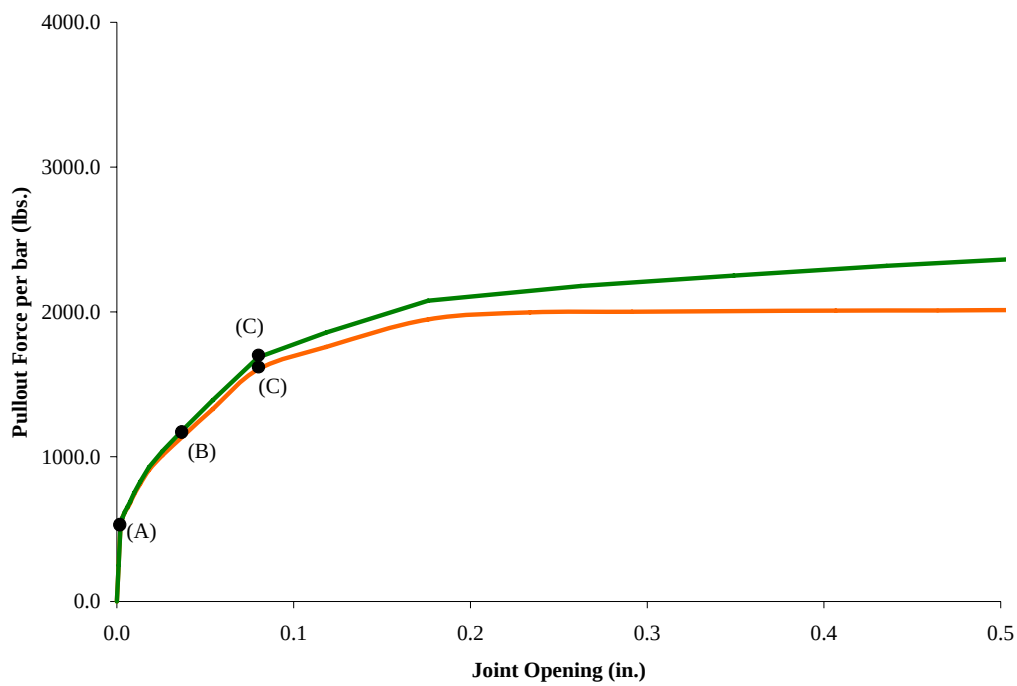

Figure C-17: Comparison of the FEM model with the experimental data for 2V72NU specimen

Table C-34: Summary of Material Failure / Damage Limit States from the analysis

Material Damage / Limit States	Joint Opening (in.)		Pullout Load (lbs)	
	(I)	(II)	(I)	(II)
(A)	0.002	0.002	500.53	501.86
(B)	0.051	0.051	1329.31	1391.04
(C)	0.077	0.077	1603.38	1686.42
(D)	-	-	-	-
(E)	-	-	-	-
(F)	-	-	-	-

Results of 2V72U Finite Element Model

The dowel-concrete friction coefficients and material properties used in the analysis are shown in table C35. A comparison of the pullout force per bar (lbs.) vs. the joint opening (in.) is shown in figure C18. A summary of the various material failure / damage limit states is presented in table C36.

Table C-35: Dowel-Concrete Friction Coefficients; Material Properties used and limit states obtained from the analysis.

	μ_g	μ_w	f'_c (psi)	f'_t (psi)
Case I	0.0	0.30	3500.0	236.64
Case II	0.074	0.384	3500.0	236.64

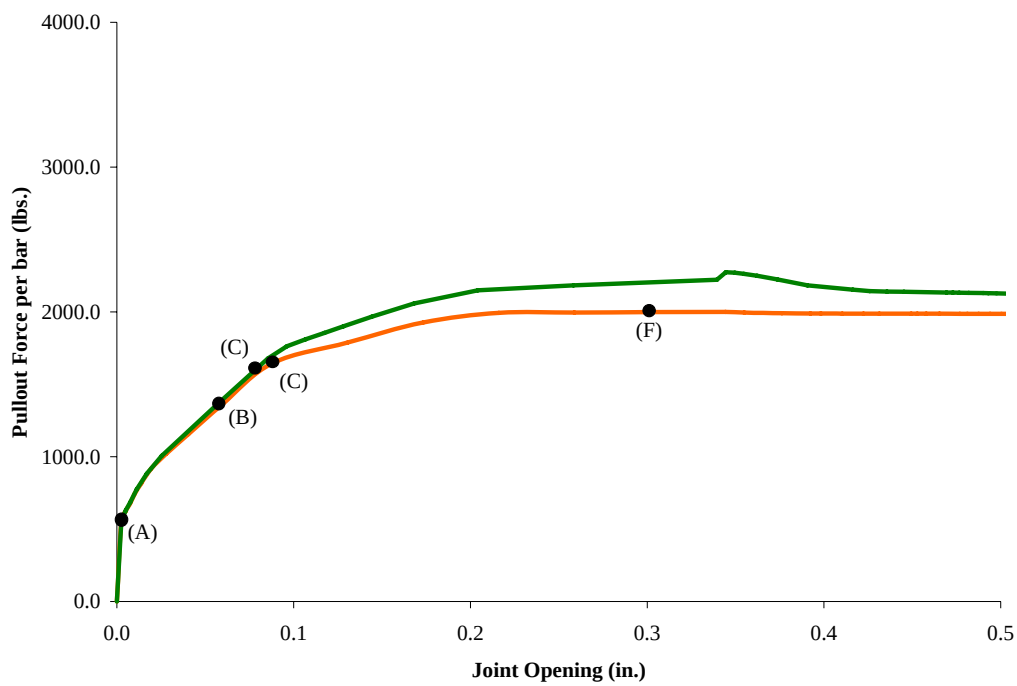

Figure C-18: Comparison of the FEM model with the experimental data for 2V72U specimen

Table C-36: Summary of Material Failure / Damage Limit States from the analysis

Material Damage / Limit States	Joint Opening (in.)		Pullout Load (lbs)	
	(I)	(II)	(I)	(II)
(A)	0.0025	0.002	555.53	557.14
(B)	0.059	0.057	1359.27	1363.32
(C)	0.088	0.085	1645.48	1678.98
(D)	-	-	-	-
(E)	-	-	-	-
(F)	-	-	-	-

Results of 2V72AM Finite Element Model

The dowel-concrete friction coefficients and material properties used in the analysis are shown in table C37. A comparison of the pullout force per bar (lbs.) vs. the joint opening (in.) is shown in figure C19. A summary of the various material failure / damage limit states is presented in table C38.

Table C-37: Dowel-Concrete Friction Coefficients; Material Properties used and limit states obtained from the analysis.

	μ_g	μ_w	f'_c (psi)	f'_t (psi)
Case I	0.0	0.30	3500.0	236.64
Case II	0.074	0.384	3500.0	236.64

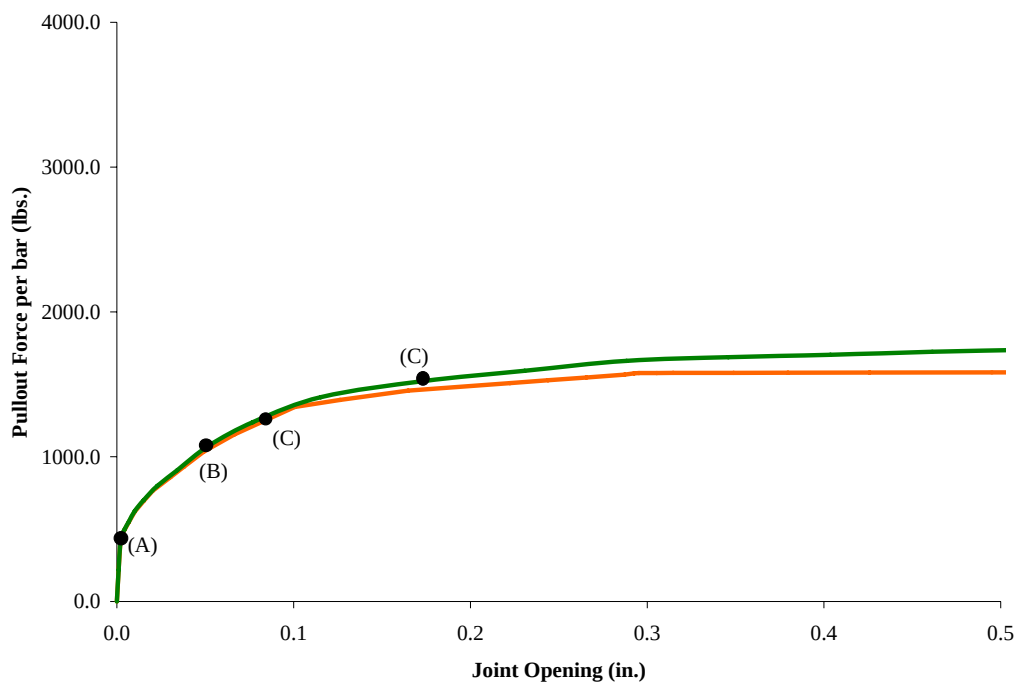

Figure C-19: Comparison of the FEM model with the experimental data for 2V72AM specimen

Table C-38: Summary of Material Failure / Damage Limit States from the analysis

Material Damage / Limit States	Joint Opening (in.)		Pullout Load (lbs)	
	(I)	(II)	(I)	(II)
(A)	0.002	0.002	412.75	413.56
(B)	0.049	0.051	1035.97	1070.28
(C)	0.083	0.173	1248.65	1522.05
(D)	-	-	-	-
(E)	-	-	-	-
(F)	-	-	-	-

Results of 2H18NU Finite Element Model

The dowel-concrete friction coefficients and material properties used in the analysis are shown in table C39. A comparison of the pullout force per bar (lbs.) vs. the joint opening (in.) is shown in figure C20. A summary of the various material failure / damage limit states is presented in table C40.

Table C-39: Dowel-Concrete Friction Coefficients; Material Properties used and limit states obtained from the analysis.

	μ_g	μ_w	f'_c (psi)	f'_t (psi)
Case I	0.0	0.30	3500.0	236.64
Case II	0.074	0.384	4931.0	280.0

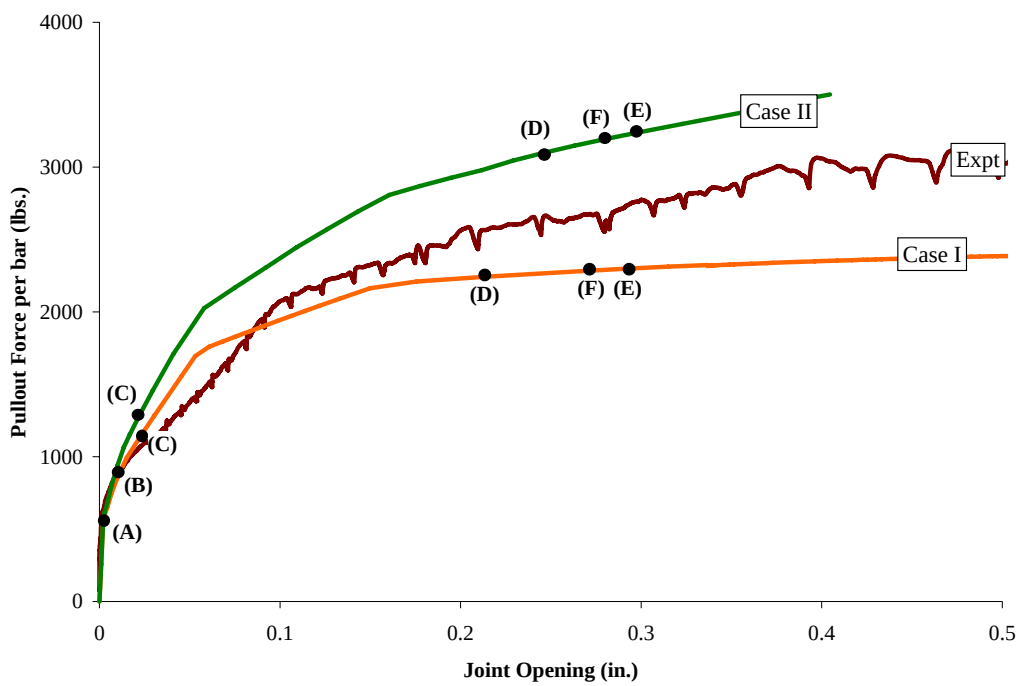

Figure C-20: Comparison of the FEM model with the experimental data for 2H18NU specimen

Table C-40: Summary of Material Failure / Damage Limit States from the analysis

Material Damage / Limit States	Joint Opening (in.)		Pullout Load (lbs)	
	(I)	(II)	(I)	(II)
(A)	0.002	0.002	516.12	529.74
(B)	0.010	0.010	859.91	943.06
(C)	0.023	0.022	1141.23	1279.29
(D)	0.214	0.280	2243.57	3139.88
(E)	0.293	0.297	2299.83	3236.9
(F)	0.272	0.246	2285.39	3098.24

Results of 2H18U Finite Element Model

The dowel-concrete friction coefficients and material properties used in the analysis are shown in table C41. A comparison of the pullout force per bar (lbs.) vs. the joint opening (in.) is shown in figure C21. A summary of the various material failure / damage limit states is presented in table C42.

Table C-41: Dowel-Concrete Friction Coefficients; Material Properties used and limit states obtained from the analysis.

	μ_g	μ_w	f'_c (psi)	f'_t (psi)
Case I	0.0	0.30	3500.0	236.64
Case II	0.074	0.384	3654.0	217.0

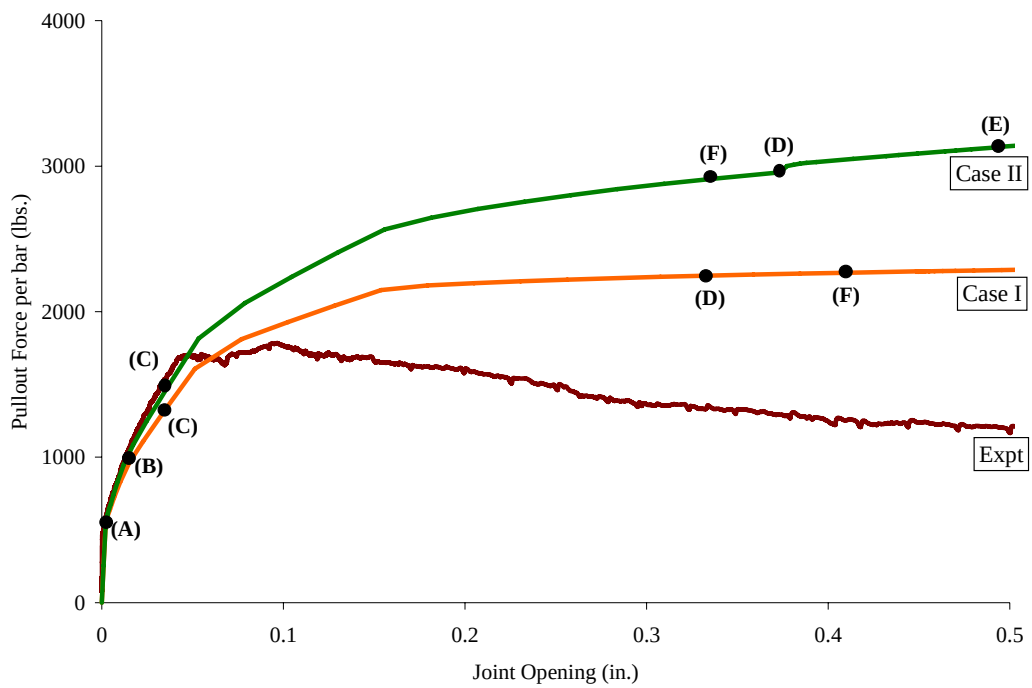

Figure C-21: Comparison of the FEM model with the experimental data for 2H18U specimen

Table C-42: Summary of Material Failure / Damage Limit States from the analysis

Material Damage / Limit States	Joint Opening (in.)		Pullout Load (lbs)	
	(I)	(II)	(I)	(II)
(A)	0.002	0.002	509.56	514.81
(B)	0.016	0.012	963.53	949.91
(C)	0.034	0.0362	1314.26	1481.65
(D)	0.333	0.374	2247.57	2957.96
(E)	0.5452	0.492	2297.17	3128.53
(F)	0.4101	0.335	2267.68	2912.34

Results of 2H18AM Finite Element Model

The dowel-concrete friction coefficients and material properties used in the analysis are shown in table C43. A comparison of the pullout force per bar (lbs.) vs. the joint opening (in.) is shown in figure C22. A summary of the various material failure / damage limit states is presented in table C44.

Table C-43: Dowel-Concrete Friction Coefficients; Material Properties used and limit states obtained from the analysis.

	μ_g	μ_w	f'_c (psi)	f'_t (psi)
Case I	0.0	0.30	3500.0	236.64
Case II	0.074	0.384	3520.0	245.0

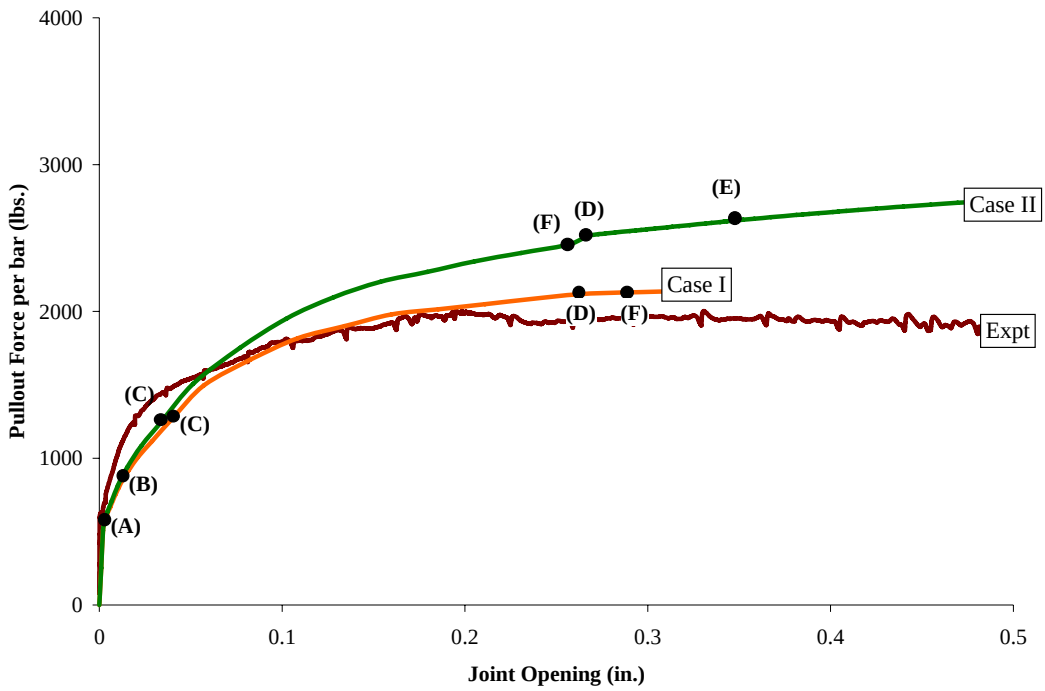

Figure C-22: Comparison of the FEM model with the experimental data for 2H18AM specimen

Table C-44: Summary of Material Failure / Damage Limit States from the analysis

Material Damage / Limit States	Joint Opening (in.)		Pullout Load (lbs)	
	(I)	(II)	(I)	(II)
(A)	0.002	0.002	505.61	508.25
(B)	0.013	0.015	852.68	937.34
(C)	0.040	0.034	1272.77	1251.89
(D)	0.262	0.266	2116.95	2507.60
(E)	-	0.348	-	2619.57
(F)	0.288	0.256	2129.46	2454.00

Results of 2H36NU Finite Element Model

The dowel-concrete friction coefficients and material properties used in the analysis are shown in table C45. A comparison of the pullout force per bar (lbs.) vs. the joint opening (in.) is shown in figure C23. A summary of the various material failure / damage limit states is presented in table C46.

Table C-45: Dowel-Concrete Friction Coefficients; Material Properties used and limit states obtained from the analysis.

	μ_g	μ_w	f'_c (psi)	f'_t (psi)
Case I	0.0	0.30	3500.0	236.64
Case II	0.074	0.384	4941.0	280.0

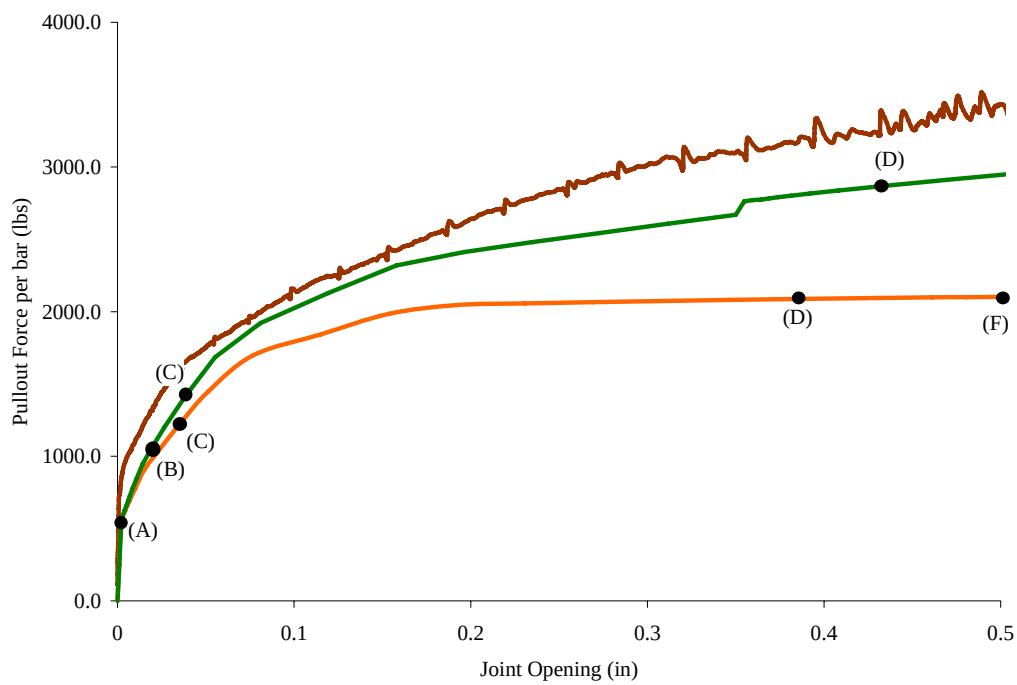

Figure C-23: Comparison of the FEM model with the experimental data for 2H36NU specimen

Table C-46: Summary of Material Failure / Damage Limit States from the analysis

Material Damage / Limit States	Joint Opening (in.)		Pullout Load (lbs)	
	(I)	(II)	(I)	(II)
(A)	0.002	0.002	504.46	509.93
(B)	0.023	0.019	1031.14	1053.07
(C)	0.034	0.038	1206.82	1410.53
(D)	0.384	0.432	2087.58	2867.48
(E)	0.519	0.524	2105.33	2972.23
(F)	0.499	0.606	2102.89	3057.04

Results of 2H36U Finite Element Model

The dowel-concrete friction coefficients and material properties used in the analysis are shown in table C47. A comparison of the pullout force per bar (lbs.) vs. the joint opening (in.) is shown in figure C24. A summary of the various material failure / damage limit states is presented in table C48.

Table C-47: Dowel-Concrete Friction Coefficients; Material Properties used and limit states obtained from the analysis.

	μ_g	μ_w	f'_c (psi)	f'_t (psi)
Case I	0.0	0.30	3500.0	236.64
Case II	0.074	0.384	3673.0	383.0

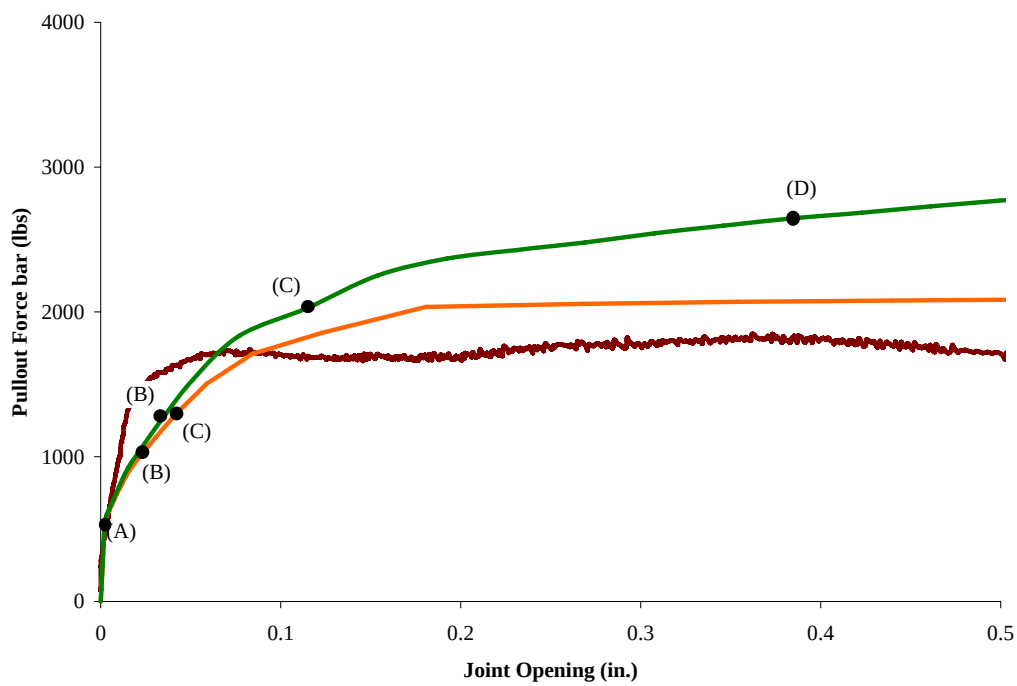

Figure C-24: Comparison of the FEM model with the experimental data for 2H36U specimen

Table C-48: Summary of Material Failure / Damage Limit States from the analysis

Material Damage / Limit States	Joint Opening (in.)		Pullout Load (lbs)	
	(I)	(II)	(I)	(II)
(A)	0.002	0.002	503.57	507.53
(B)	0.023	0.034	1014.38	1260.96
(C)	0.042	0.115	1294.47	2030.29
(D)	0.5265	0.384	2086.17	2646.19
(E)	0.7860	0.6151	2098.56	2871.68
(F)	0.7860	0.7304	2098.56	2941.00

Results of 2H36AM Finite Element Model

The dowel-concrete friction coefficients and material properties used in the analysis are shown in table C49. A comparison of the pullout force per bar (lbs.) vs. the joint opening (in.) is shown in figure C25. A summary of the various material failure / damage limit states is presented in table C50.

Table C-49: Dowel-Concrete Friction Coefficients; Material Properties used and limit states obtained from the analysis.

	μ_g	μ_w	f'_c (psi)	f'_t (psi)
Case I	0.0	0.30	3500.0	236.64
Case II	0.074	0.384	3500.0	236.64

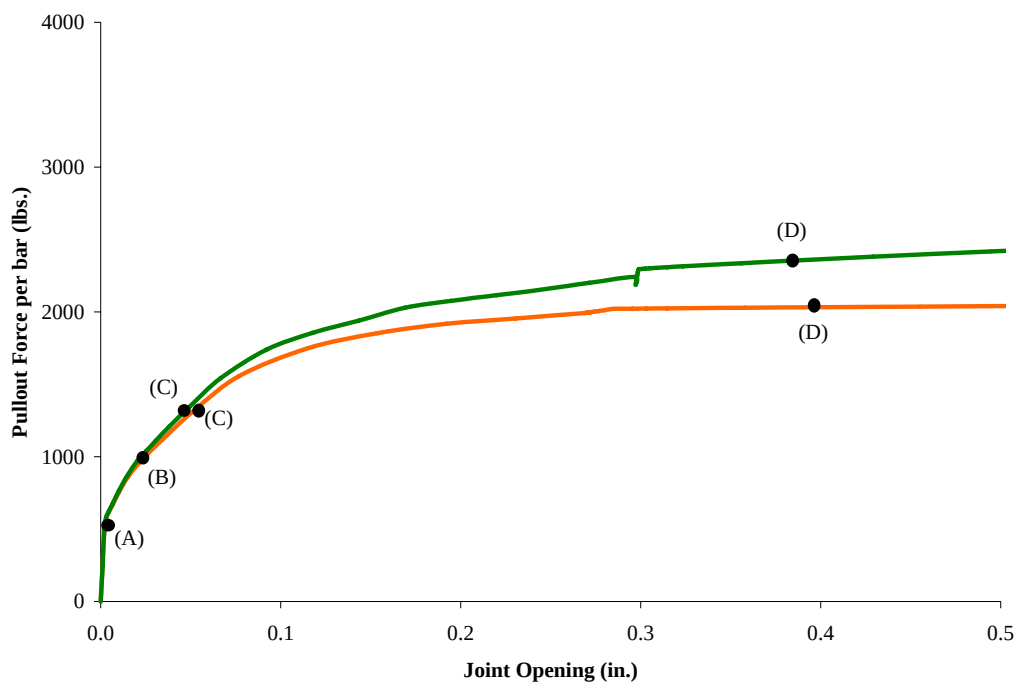

Figure C-25: Comparison of the FEM model with the experimental data for 2H36AM specimen

Table C-50: Summary of Material Failure / Damage Limit States from the analysis

Material Damage / Limit States	Joint Opening (in.)		Pullout Load (lbs)	
	(I)	(II)	(I)	(II)
(A)	0.002	0.002	501.83	503.88
(B)	0.023	0.020	977.21	969.89
(C)	0.051	0.049	1313.20	1344.32
(D)	0.397	0.385	2032.31	2355.03
(E)	0.54	0.593	2042.36	2467.74
(F)	0.54	0.593	2042.36	2467.74

Results of 2H72NU Finite Element Model

The dowel-concrete friction coefficients and material properties used in the analysis are shown in table C51. A comparison of the pullout force per bar (lbs.) vs. the joint opening (in.) is shown in figure C26. A summary of the various material failure / damage limit states is presented in table C52.

Table C-51: Dowel-Concrete Friction Coefficients; Material Properties used and limit states obtained from the analysis.

	μ_g	μ_w	f'_c (psi)	f'_t (psi)
Case I	0.0	0.30	3500.0	236.64
Case II	0.074	0.384	3500.0	236.64

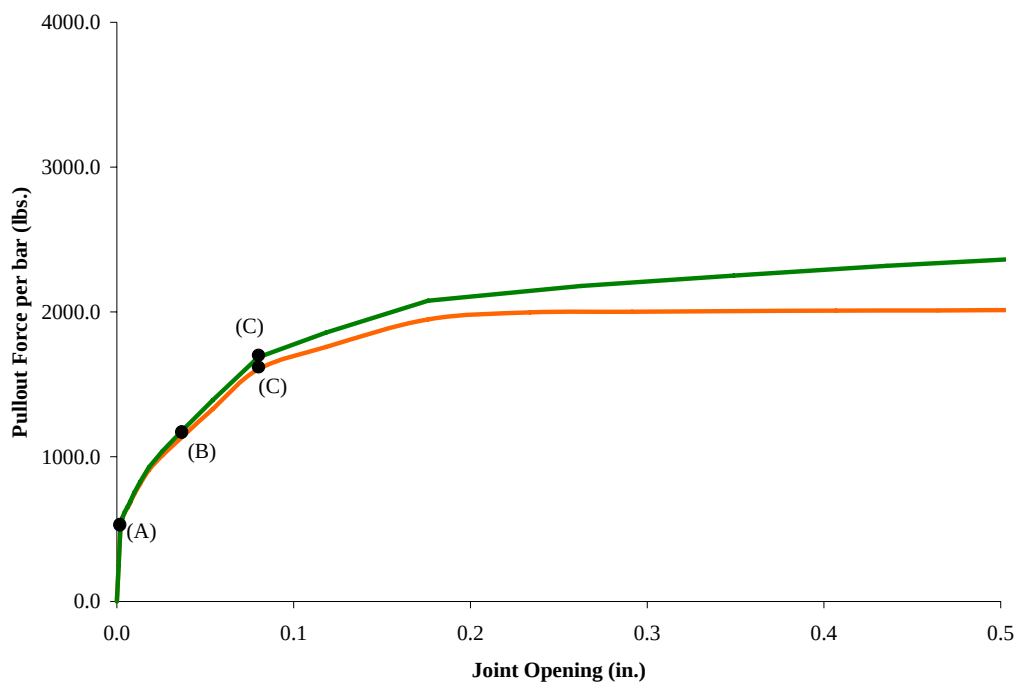

Figure C-26: Comparison of the FEM model with the experimental data for 2H72NU specimen

Table C-52: Summary of Material Failure / Damage Limit States from the analysis

Material Damage / Limit States	Joint Opening (in.)		Pullout Load (lbs)	
	(I)	(II)	(I)	(II)
(A)	0.002	0.002	500.23	501.86
(B)	0.037	0.037	1139.24	1183.07
(C)	0.078	0.079	1603.38	1686.42
(D)	0.752	0.782	2018.69	2496.33
(E)	-	-	-	-
(F)	-	-	-	-

Results of 2H72U Finite Element Model

The dowel-concrete friction coefficients and material properties used in the analysis are shown in table C53. A comparison of the pullout force per bar (lbs.) vs. the joint opening (in.) is shown in figure C27. A summary of the various material failure / damage limit states is presented in table C54.

Table C-53: Dowel-Concrete Friction Coefficients; Material Properties used and limit states obtained from the analysis.

	μ_g	μ_w	f'_c (psi)	f'_t (psi)
Case I	0.0	0.30	3500.0	236.64
Case II	0.074	0.384	3500.0	236.64

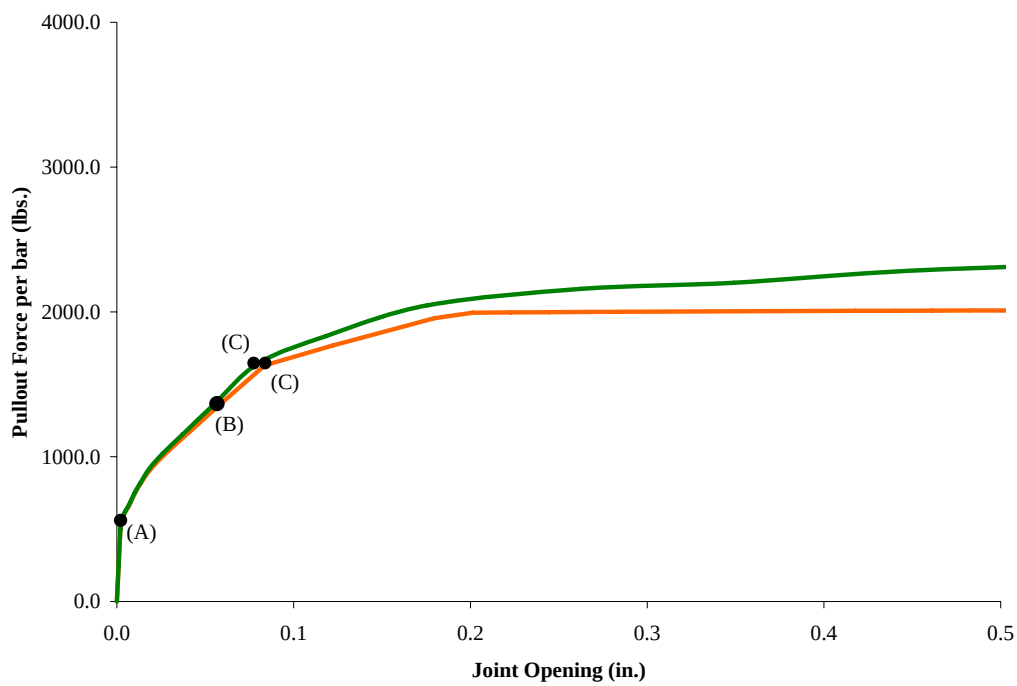

Figure C-27: Comparison of the FEM model with the experimental data for 2H72U specimen

Table C-54: Summary of Material Failure / Damage Limit States from the analysis

Material Damage / Limit States	Joint Opening (in.)		Pullout Load (lbs)	
	(I)	(II)	(I)	(II)
(A)	0.002	0.002	498.99	500.14
(B)	0.058	0.054	1357.57	1353.23
(C)	0.084	0.079	1631.36	1644.15
(D)	0.910	0.868	2018.16	2467.27
(E)	-	-	-	-
(F)	-	-	-	-

Results of 2H72AM Finite Element Model

The dowel-concrete friction coefficients and material properties used in the analysis are shown in table C55. A comparison of the pullout force per bar (lbs.) vs. the joint opening (in.) is shown in figure C28. A summary of the various material failure / damage limit states is presented in table C56.

Table C-55: Dowel-Concrete Friction Coefficients; Material Properties used and limit states obtained from the analysis.

	μ_g	μ_w	f'_c (psi)	f'_t (psi)
Case I	0.0	0.30	3500.0	236.64
Case II	0.074	0.384	3500.0	236.64

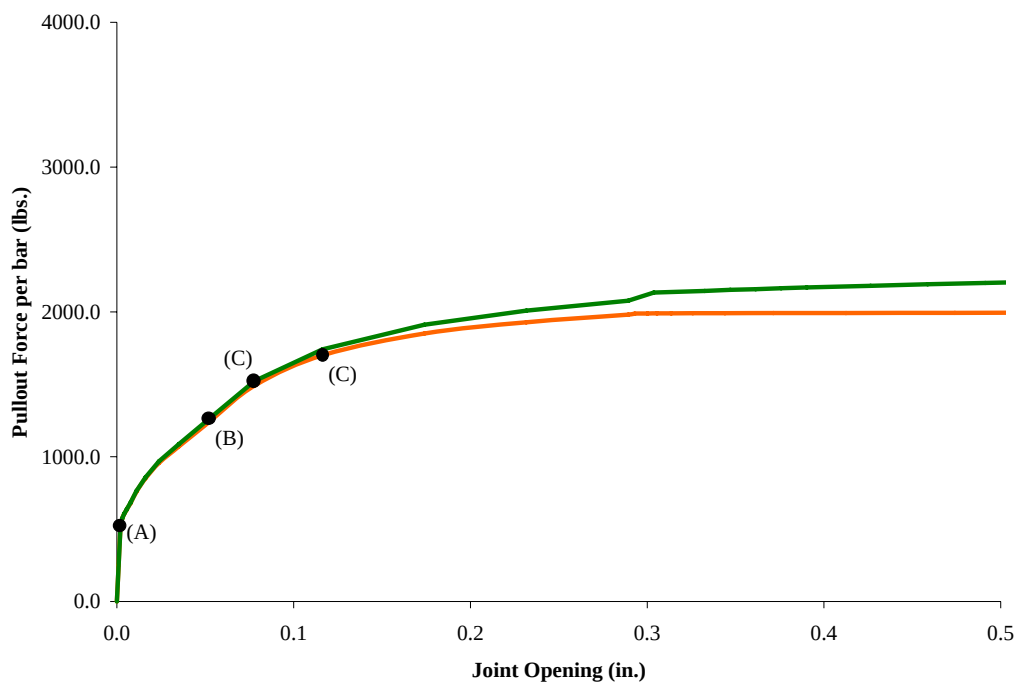

Figure C-28: Comparison of the FEM model with the experimental data for 2H72AM specimen

Table C-56: Summary of Material Failure / Damage Limit States from the analysis

Material Damage / Limit States	Joint Opening (in.)		Pullout Load (lbs)	
	(I)	(II)	(I)	(II)
(A)	0.002	0.002	500.41	501.34
(B)	0.052	0.052	1240.74	1263.06
(C)	0.116	0.078	1700.82	1522.59
(D)	0.828	0.918	1998.47	2296.83
(E)	-	-	-	-
(F)	-	-	-	-

Results of 2C18NU Finite Element Model

The dowel-concrete friction coefficients and material properties used in the analysis are shown in table C57. A comparison of the pullout force per bar (lbs.) vs. the joint opening (in.) is shown in figure C29. A summary of the various material failure / damage limit states is presented in table C58.

Table C-57: Dowel-Concrete Friction Coefficients; Material Properties used and limit states obtained from the analysis.

	μ_g	μ_w	f'_c (psi)	f'_t (psi)
Case I	0.0	0.30	3500.0	236.64
Case II	0.074	0.384	4930.0	280.0

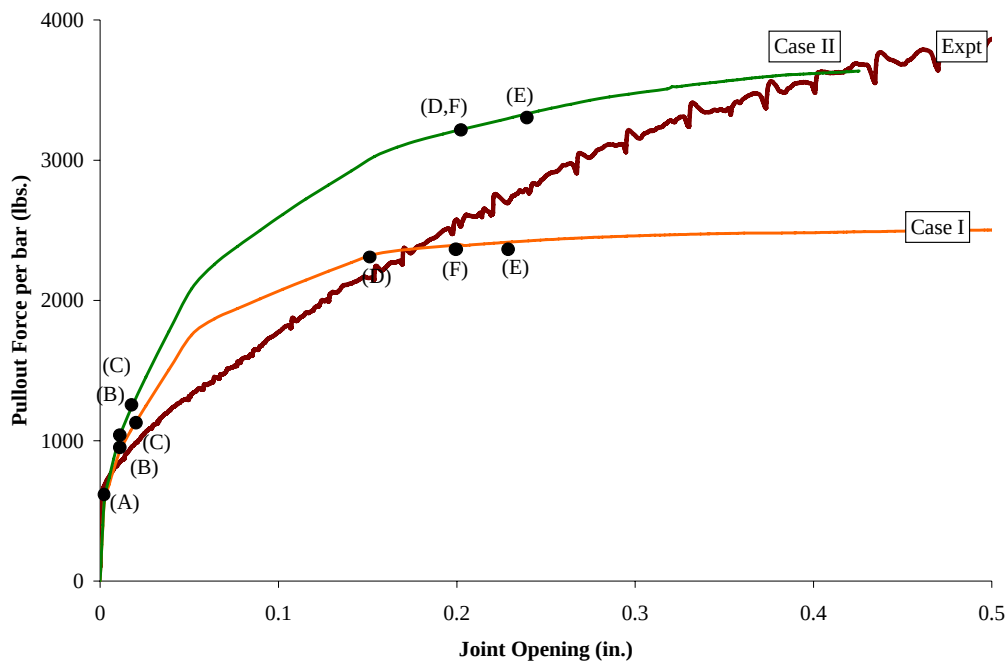

Figure C-29: Comparison of the FEM model with the experimental data for 2C18NU specimen

Table C-58: Summary of Material Failure / Damage Limit States from the analysis

Material Damage / Limit States	Joint Opening (in.)		Pullout Load (lbs)	
	(I)	(II)	(I)	(II)
(A)	0.0038	0.0038	625.0	650.0
(B)	0.014	0.014	935.0	1025.0
(C)	0.017	0.017	1070.0	1225.0
(D)	0.154	0.205	2330.0	3225.0
(E)	0.231	0.239	2415.0	3330.0
(F)	0.202	0.205	2395.0	3225.0

Results of 2C18U Finite Element Model

The dowel-concrete friction coefficients and material properties used in the analysis are shown in table C59. A comparison of the pullout force per bar (lbs.) vs. the joint opening (in.) is shown in figure C30. A summary of the various material failure / damage limit states is presented in table C60.

Table C-59: Dowel-Concrete Friction Coefficients; Material Properties used and limit states obtained from the analysis.

	μ_g	μ_w	f'_c (psi)	f'_t (psi)
Case I	0.0	0.30	3500.0	236.64
Case II	0.074	0.384	3654.0	217.0

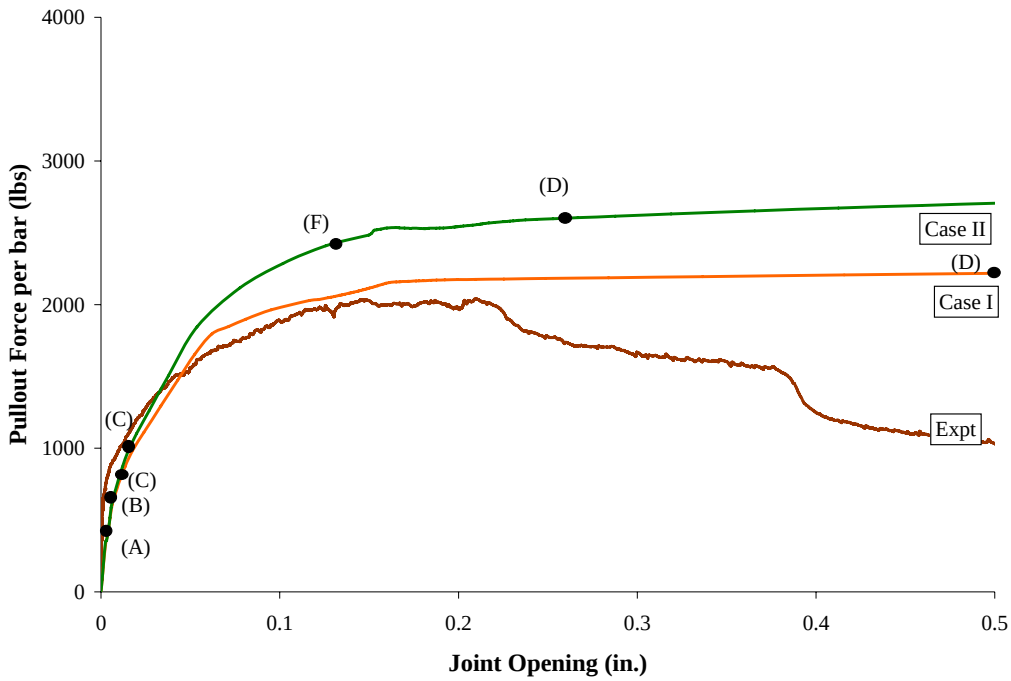

Figure C-30: Comparison of the FEM model with the experimental data for 2C18U specimen

Table C-60: Summary of Material Failure / Damage Limit States from the analysis

Material Damage / Limit States	Joint Opening (in.)		Pullout Load (lbs)	
	(I)	(II)	(I)	(II)
(A)	0.0025	0.003	460.0	460.
(B)	0.0038	0.0098	530.65	735.0
(C)	0.0075	0.015	615.0	980.0
(D)	0.534	0.253	1125.0	1165.0
(E)	-	0.126	-	2410.0
(F)	-	-	-	-

Results of 2C18AM Finite Element Model

The dowel-concrete friction coefficients and material properties used in the analysis are shown in table C61. A comparison of the pullout force per bar (lbs.) vs. the joint opening (in.) is shown in figure C31. A summary of the various material failure / damage limit states is presented in table C62.

Table C-61: Dowel-Concrete Friction Coefficients; Material Properties used and limit states obtained from the analysis.

	μ_g	μ_w	f'_c (psi)	f'_t (psi)
Case I	0.0	0.30	3500.0	236.64
Case II	0.074	0.384	3520.0	245.00

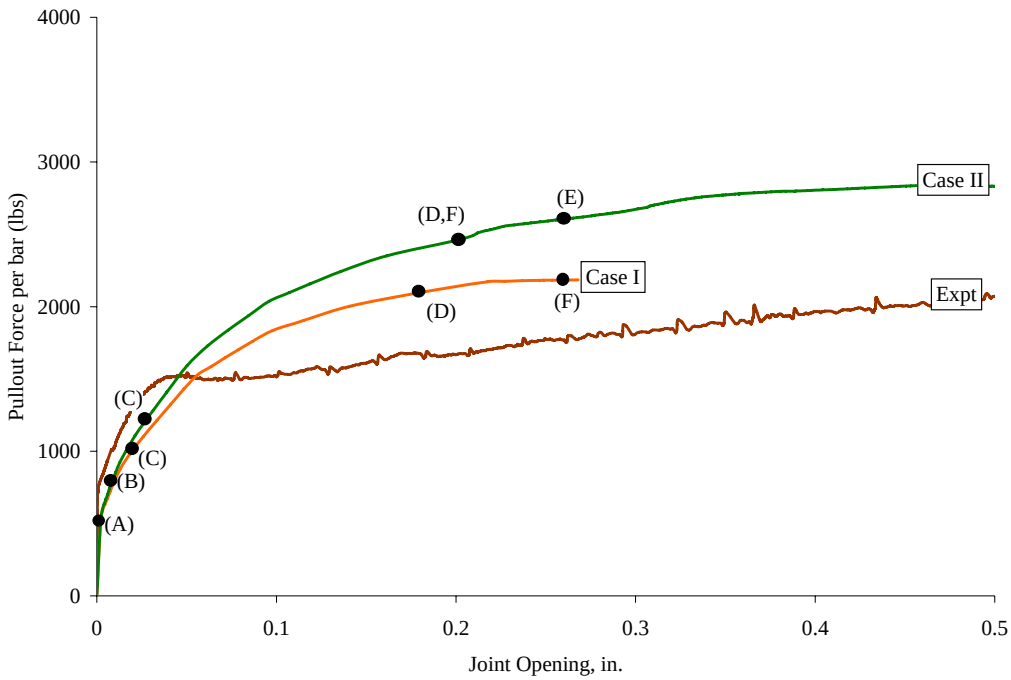

Figure C-31: Comparison of the FEM model with the experimental data for 2C18AM specimen

Table C-62: Summary of Material Failure / Damage Limit States from the analysis

Material Damage / Limit States	Joint Opening (in.)		Pullout Load (lbs)	
	(I)	(II)	(I)	(II)
(A)	0.003	0.003	585.0	585.0
(B)	0.0097	0.009	794.0	805.0
(C)	0.018	0.026	980.0	1195.0
(D)	0.179	0.200	2095.0	2455.0
(E)	-	0.259	-	2605.0
(F)	0.227	0.200	2175.0	2455.0

Results of 2C36NU Finite Element Model

The dowel-concrete friction coefficients and material properties used in the analysis are shown in table C63. A comparison of the pullout force per bar (lbs.) vs. the joint opening (in.) is shown in figure C32. A summary of the various material failure / damage limit states is presented in table C64.

Table C-63: Dowel-Concrete Friction Coefficients; Material Properties used and limit states obtained from the analysis.

	μ_g	μ_w	f'_c (psi)	f'_t (psi)
Case I	0.0	0.30	3500.0	236.64
Case II	0.074	0.384	4931.0	290.00

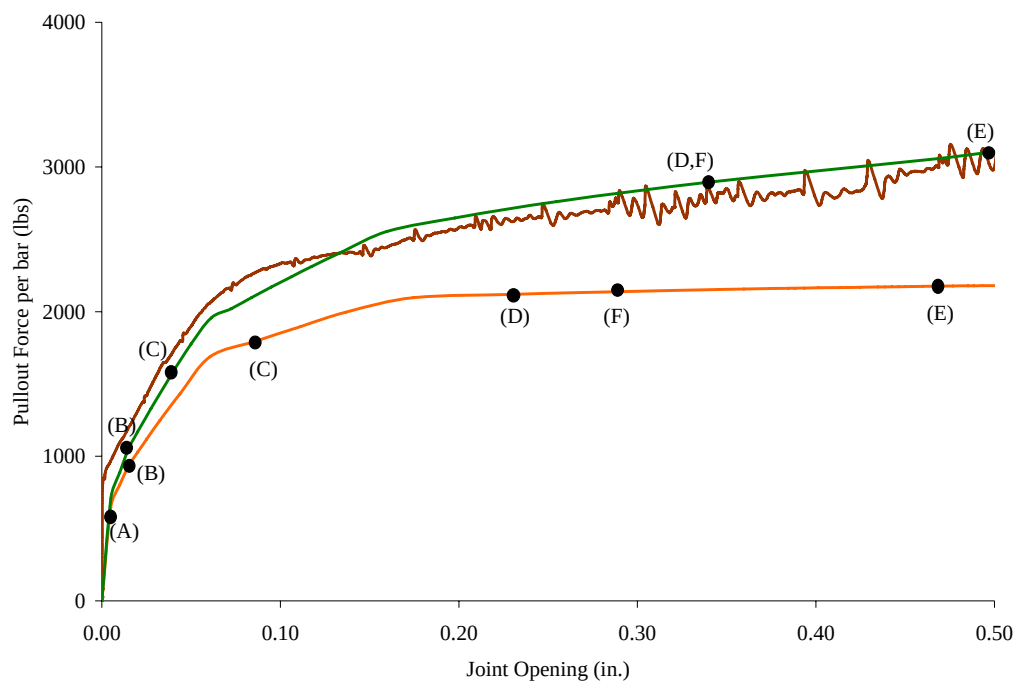

Figure C-32: Comparison of the FEM model with the experimental data for 2C36NU specimen

Table C-64: Summary of Material Failure / Damage Limit States from the analysis

Material Damage / Limit States	Joint Opening (in.)		Pullout Load (lbs)	
	(I)	(II)	(I)	(II)
(A)	0.003	0.003	550.0	575.0
(B)	0.015	0.015	935.0	1055.0
(C)	0.086	0.038	1795.0	1560.0
(D)	0.231	0.340	2120.0	2695.0
(E)	0.288	0.50	2140.0	3105.0
(F)	0.468	0.340	2175.0	2895.0

Results of 3A Finite element model

The dowel-concrete friction coefficients and material properties used in the analysis are shown in table C65. A comparison of the pullout force per bar (lbs.) vs. the joint opening (in.) is shown in figure C33. A summary of the various material failure / damage limit states is presented in table C66.

Table C-65: Dowel-Concrete Friction Coefficients; Material Properties used and limit states obtained from the analysis.

	μ_g	μ_w	f'_c (psi)	f'_t (psi)
Case I	0.0	0.30	3500.0	236.64
Case II	0.074	0.384	3326.0	354.00

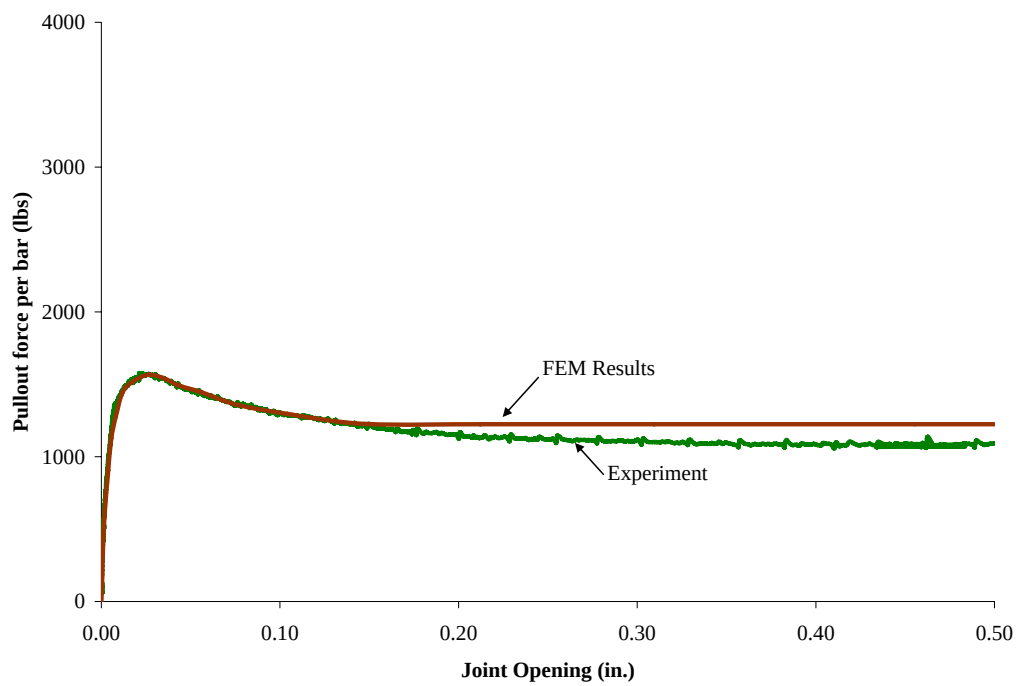

Figure C-33: Comparison of the FEM model with the experimental data for 3A specimen

Table C-66: Summary of Material Failure / Damage Limit States from the analysis

Material Damage / Limit States	Joint Opening (in.)		Pullout Load (lbs)	
	(I)	(II)	(I)	(II)
(A)	0.002	0.002	625.0	630.0
(B)	-	-	-	-
(C)	-	-	-	-
(D)	-	-	-	-
(E)	-	-	-	-
(F)	-	-	-	-

Results of 3V18NU Finite element model

The dowel-concrete friction coefficients and material properties used in the analysis are shown in table C67. A comparison of the pullout force per bar (lbs.) vs. the joint opening (in.) is shown in figure C34. A summary of the various material failure / damage limit states is presented in table C68.

Table C-67: Dowel-Concrete Friction Coefficients; Material Properties used and limit states obtained from the analysis.

	μ_g	μ_w	f'_c (psi)	f'_t (psi)
Case I	0.0	0.30	3500.0	236.64
Case II	0.074	0.384	4931.0	290.0

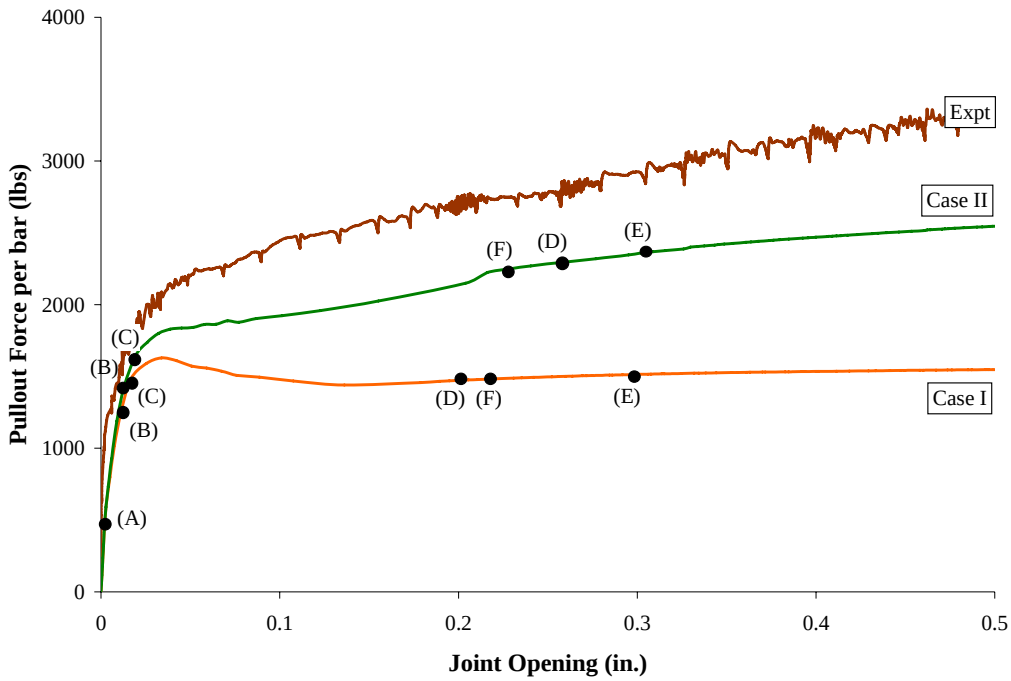

Figure C-34: Comparison of the FEM model with the experimental data for 3V18NU specimen

Table C-68: Summary of Material Failure / Damage Limit States from the analysis

Material Damage / Limit States	Joint Opening (in.)		Pullout Load (lbs)	
	(I)	(II)	(I)	(II)
(A)	0.003	0.003	600.0	620.0
(B)	0.011	0.0131	1260.0	1430.0
(C)	0.017	0.0195	1490.0	1650.0
(D)	0.200	0.259	1470.0	2300.0
(E)	0.297	0.309	1510.0	2370.0
(F)	0.219	0.228	1480.0	2250.0

Results of 3H18NU Finite element model

The dowel-concrete friction coefficients and material properties used in the analysis are shown in table C69. A comparison of the pullout force per bar (lbs.) vs. the joint opening (in.) is shown in figure C35. A summary of the various material failure / damage limit states is presented in table C70.

Table C-69: Dowel-Concrete Friction Coefficients; Material Properties used and limit states obtained from the analysis.

	μ_g	μ_w	f'_c (psi)	f'_t (psi)
Case I	0.0	0.30	3500.0	236.64
Case II	0.074	0.384	3919.0	336.0

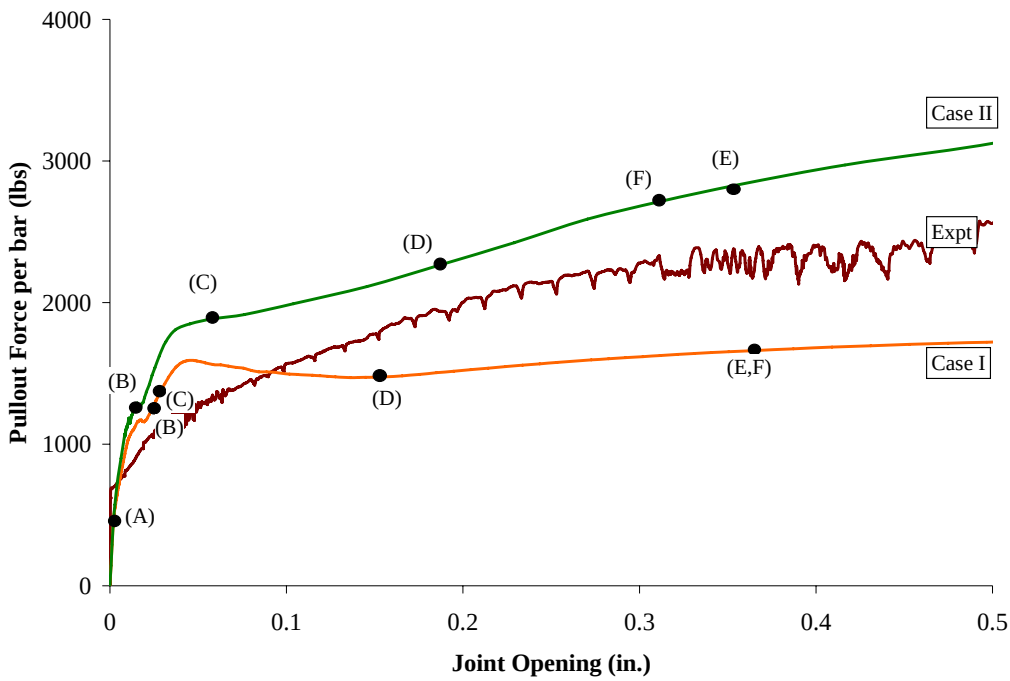

Figure C-35: Comparison of the FEM model with the experimental data for 3H18NU specimen

Table C-70: Summary of Material Failure / Damage Limit States from the analysis

Material Damage / Limit States	Joint Opening (in.)		Pullout Load (lbs)	
	(I)	(II)	(I)	(II)
(A)	0.003	0.003	557.0	610.0
(B)	0.026	0.0141	1310.0	1250.0
(C)	0.0277	0.0577	1350.0	1880.0
(D)	0.149	0.187	1470.0	2270.0
(E)	0.365	0.354	1660.0	2830.0
(F)	0.365	0.312	1660.0	2720.0

Results of 3C18NU Finite element model

The dowel-concrete friction coefficients and material properties used in the analysis are shown in table C71. A comparison of the pullout force per bar (lbs.) vs. the joint opening (in.) is shown in figure C36. A summary of the various material failure / damage limit states is presented in table C72.

Table C-71: Dowel-Concrete Friction Coefficients; Material Properties used and limit states obtained from the analysis.

	μ_g	μ_w	f'_c (psi)	f'_t (psi)
Case I	0.0	0.30	3500.0	236.64
Case II	0.074	0.384	3520.0	245.0

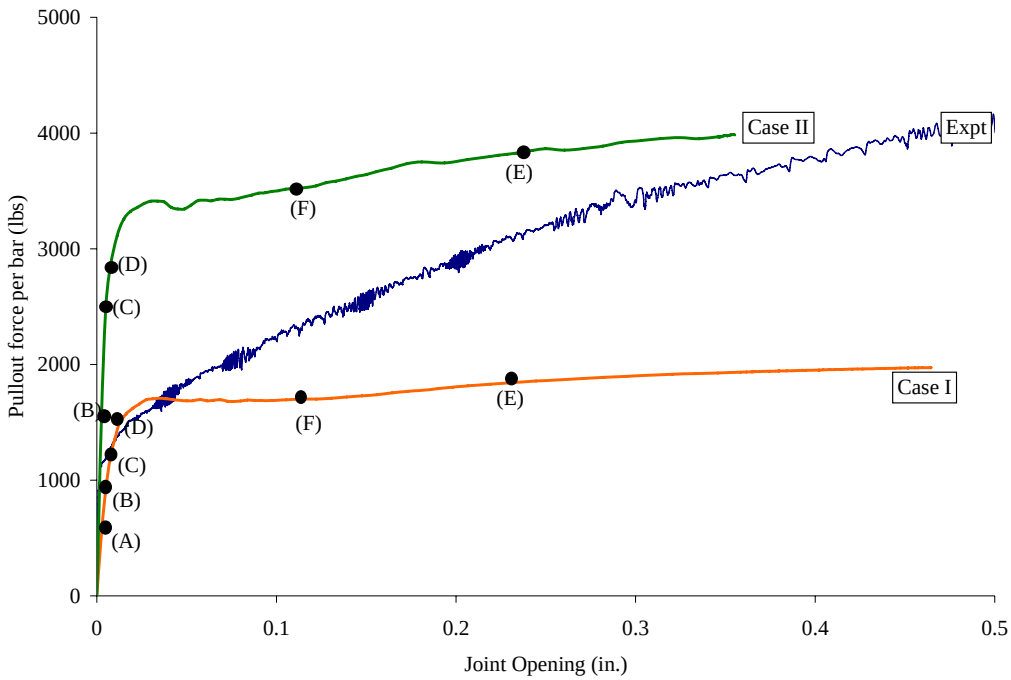

Figure C-36: Comparison of the FEM model with the experimental data for 3C18NU specimen

Table C-72: Summary of Material Failure / Damage Limit States from the analysis

Material Damage / Limit States	Joint Opening (in.)		Pullout Load (lbs)	
	(I)	(II)	(I)	(II)
(A)	0.025	0.025	540.0	1540.0
(B)	0.005	0.005	921.0	2500.0
(C)	0.075	0.075	1200.0	2850.0
(D)	0.01	0.013	1360.0	3110.0
(E)	0.232	0.238	1840.0	3840.0
(F)	0.198	0.110	1800.0	3520.0

Results of 5A Finite element model

The dowel-concrete friction coefficients and material properties used in the analysis are shown in table C73. A comparison of the pullout force per bar (lbs.) vs. the joint opening (in.) is shown in figure C37. A summary of the various material failure / damage limit states is presented in table C74.

Table C-73: Dowel-Concrete Friction Coefficients; Material Properties used and limit states obtained from the analysis.

	μ_g	μ_w	f'_c (psi)	f'_t (psi)
Case I	0.0	0.30	3500.0	236.64
Case II	0.074	0.384	3151.0	413.0

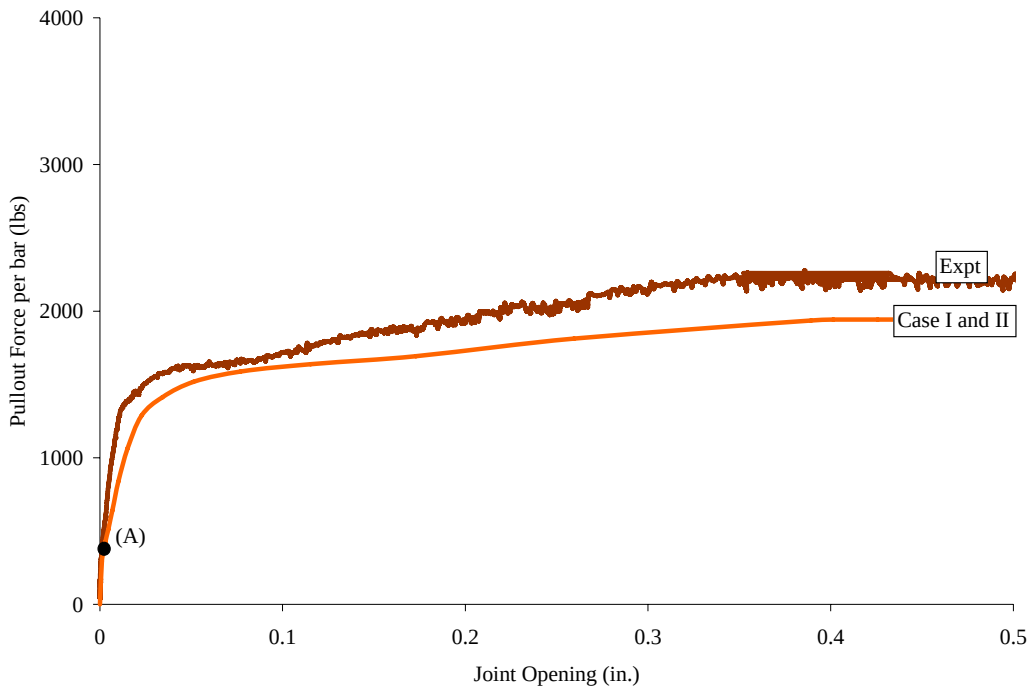

Figure C-37: Comparison of the FEM model with the experimental data for 5A specimen

Table C-74: Summary of Material Failure / Damage Limit States from the analysis

Material Damage / Limit States	Joint Opening (in.)		Pullout Load (lbs)	
	(I)	(II)	(I)	(II)
(A)	0.002	0.002	510.0	510.0
(B)	-	-	-	-
(C)	-	-	-	-
(D)	-	-	-	-
(E)	-	-	-	-
(F)	-	-	-	-

Results of 5V18NU Finite Element Model

The dowel-concrete friction coefficients and material properties used in the analysis are shown in table C75. A comparison of the pullout force per bar (lbs.) vs. the joint opening (in.) is shown in figure 38. A summary of the various material failure / damage limit states is presented in table C76.

Table C-75: Dowel-Concrete Friction Coefficients; Material Properties used and limit states obtained from the analysis.

	μ_g	μ_w	f'_c (psi)	f'_t (psi)
Case I	0.0	0.30	3500.0	236.64
Case II	0.074	0.384	4931.0	363.0

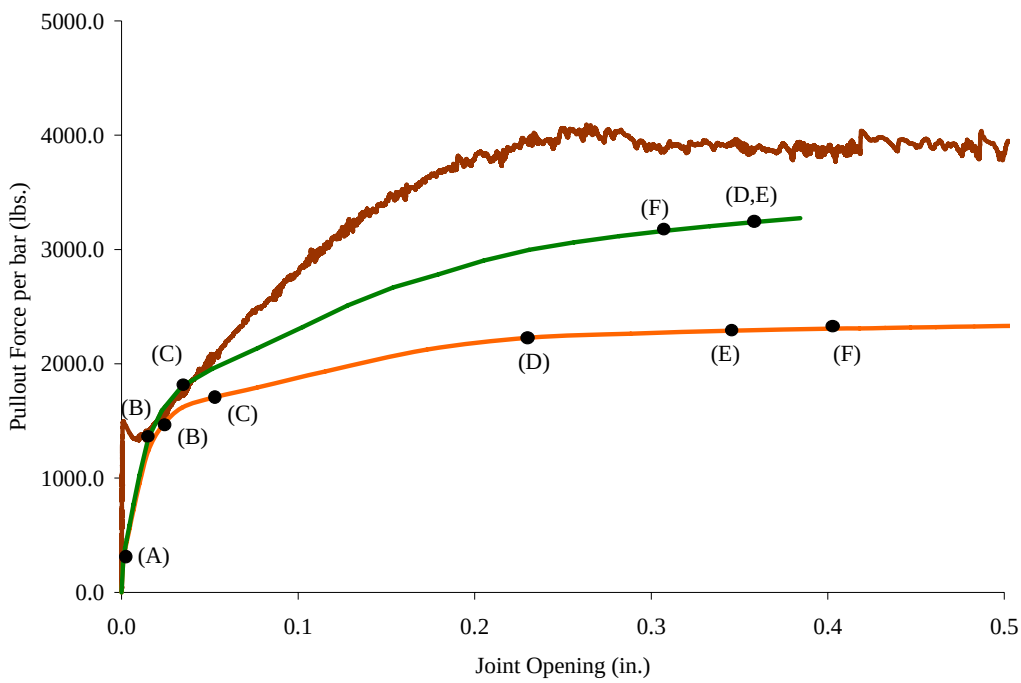

Figure C-38: Comparison of the FEM model with the experimental data for 5V18NU specimen

Table C-76: Summary of Material Failure / Damage Limit States from the analysis

Material Damage / Limit States	Joint Opening (in.)		Pullout Load (lbs)	
	(I)	(II)	(I)	(II)
(A)	0.002	0.002	379.54	388.34
(B)	0.022	0.015	1451.97	1353.50
(C)	0.051	0.034	1701.96	1802.57
(D)	0.230	0.358	2227.88	3239.90
(E)	0.346	0.358	2289.98	3239.90
(F)	0.404	0.307	2307.90	3163.28

Results of 5V18AM Finite Element Model

The dowel-concrete friction coefficients and material properties used in the analysis are shown in table C77. A comparison of the pullout force per bar (lbs.) vs. the joint opening (in.) is shown in figure C39. A summary of the various material failure / damage limit states is presented in table C78.

Table C-77: Dowel-Concrete Friction Coefficients; Material Properties used and limit states obtained from the analysis.

	μ_g	μ_w	f'_c (psi)	f'_t (psi)
Case I	0.0	0.30	3500.0	236.64
Case II	0.074	0.384	3530.0	355.0

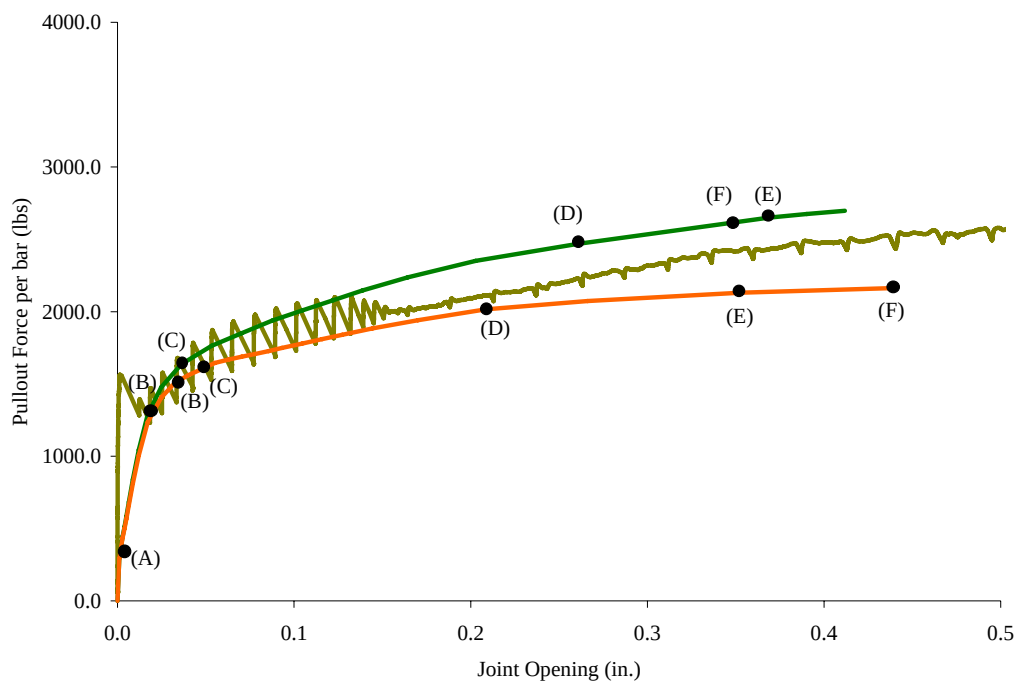

Figure C-39: Comparison of the FEM model with the experimental data for 5V18AM specimen

Table C-78: Summary of Material Failure / Damage Limit States from the analysis

Material Damage / Limit States	Joint Opening (in.)		Pullout Load (lbs)	
	(I)	(II)	(I)	(II)
(A)	0.002	0.002	374.0	378.0
(B)	0.032	0.017	1510.0	1290.0
(C)	0.047	0.036	1600.0	1640.0
(D)	0.208	0.260	2020.0	2470.0
(E)	0.352	0.368	2130.0	2610.0
(F)	0.439	0.347	2160.0	2650.0

Results of 5V36AM Finite Element Model

The dowel-concrete friction coefficients and material properties used in the analysis are shown in table C79. A comparison of the pullout force per bar (lbs.) vs. the joint opening (in.) is shown in figure C40. A summary of the various material failure / damage limit states is presented in table C80.

Table C-79: Dowel-Concrete Friction Coefficients; Material Properties used and limit states obtained from the analysis.

	μ_g	μ_w	f'_c (psi)	f'_t (psi)
Case I	0.0	0.30	3500.0	236.64
Case II	0.074	0.384	3530.0	355.0

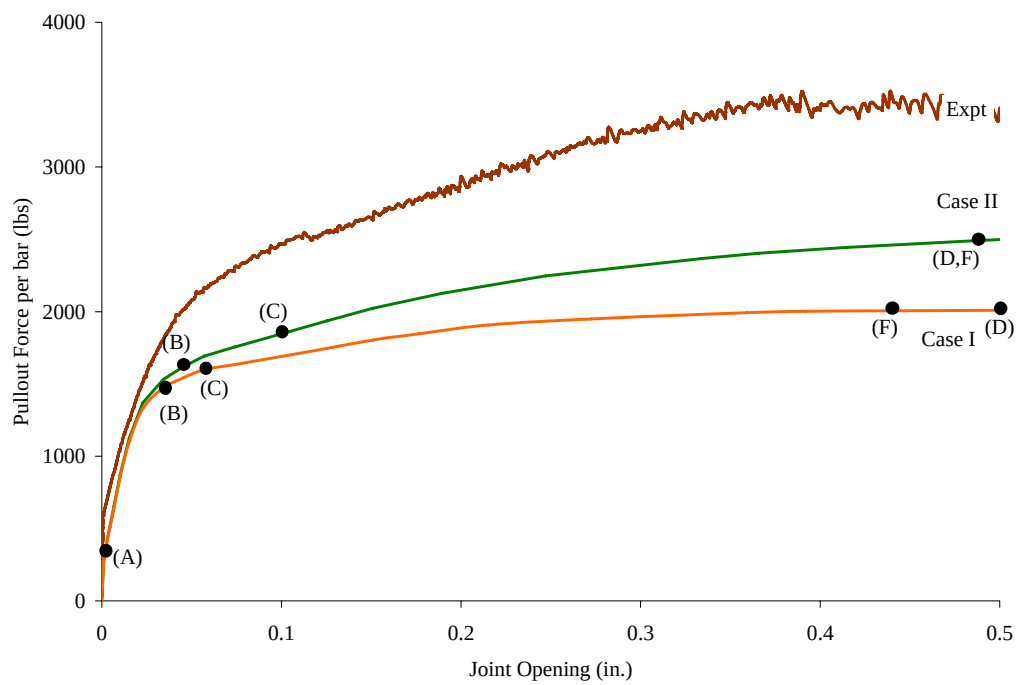

Figure C-40: Comparison of the FEM model with the experimental data for 5V36AM specimen

Table C-80: Summary of Material Failure / Damage Limit States from the analysis

Material Damage / Limit States	Joint Opening (in.)		Pullout Load (lbs)	
	(I)	(II)	(I)	(II)
(A)	0.003	0.003	419.68	424.46
(B)	0.034	0.045	1472.3	1620.3
(C)	0.056	0.099	1598.3	1845.7
(D)	0.513	0.487	2009.3	2491.64
(E)	-	-	-	-
(F)	0.440	0.487	2005.8	2491.64

Results of 5H18NU Finite Element Model

The dowel-concrete friction coefficients and material properties used in the analysis are shown in table C81. A comparison of the pullout force per bar (lbs.) vs. the joint opening (in.) is shown in figure C41. A summary of the various material failure / damage limit states is presented in table C82.

Table C-81: Dowel-Concrete Friction Coefficients; Material Properties used and limit states obtained from the analysis.

	μ_g	μ_w	f'_c (psi)	f'_t (psi)
Case I	0.0	0.30	3500.0	236.64
Case II	0.074	0.384	3654.0	217.0

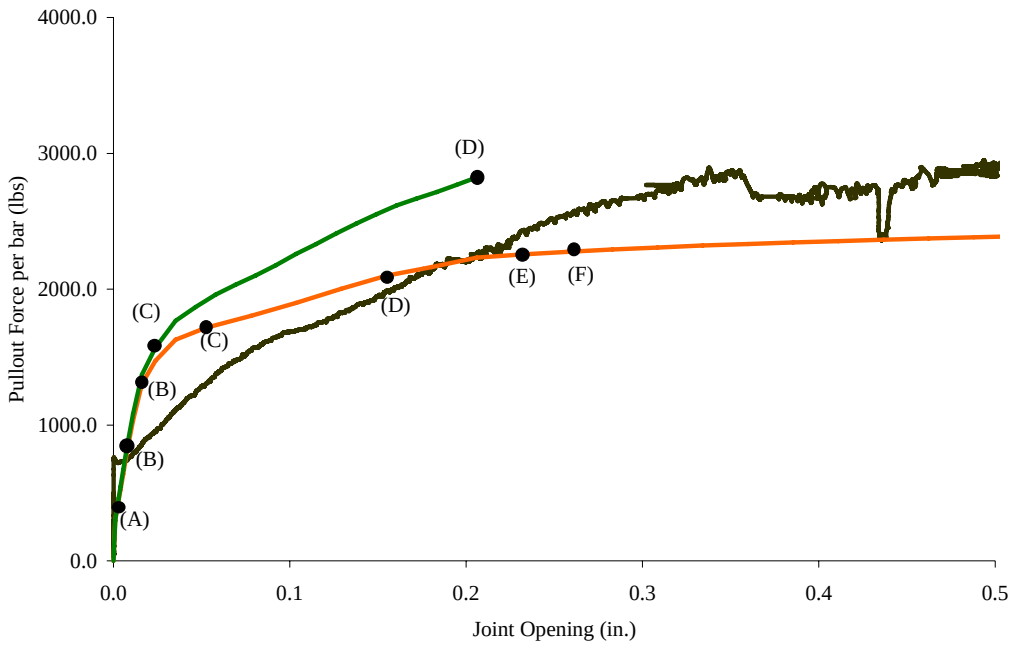

Figure C-41: Comparison of the FEM model with the experimental data for 5H18NU specimen

Table C-82: Summary of Material Failure / Damage Limit States from the analysis

Material Damage / Limit States	Joint Opening (in.)		Pullout Load (lbs)	
	(I)	(II)	(I)	(II)
(A)	0.002	0.002	380.52	386.0
(B)	0.016	0.0077	1302.90	843.0
(C)	0.052	0.023	1715.65	1570.0
(D)	0.155	0.206	2099.70	2820.0
(E)	0.232	-	2256.34	-
(F)	0.257	-	2275.36	-

Results of 5H18AM Finite Element Model

The dowel-concrete friction coefficients and material properties used in the analysis are shown in table C83. A comparison of the pullout force per bar (lbs.) vs. the joint opening (in.) is shown in figure C42. A summary of the various material failure / damage limit states is presented in table C84.

Table C-83: Dowel-Concrete Friction Coefficients; Material Properties used and limit states obtained from the analysis.

	μ_g	μ_w	f'_c (psi)	f'_t (psi)
Case I	0.0	0.30	3500.0	236.64
Case II	0.074	0.384	3880.0	390.0

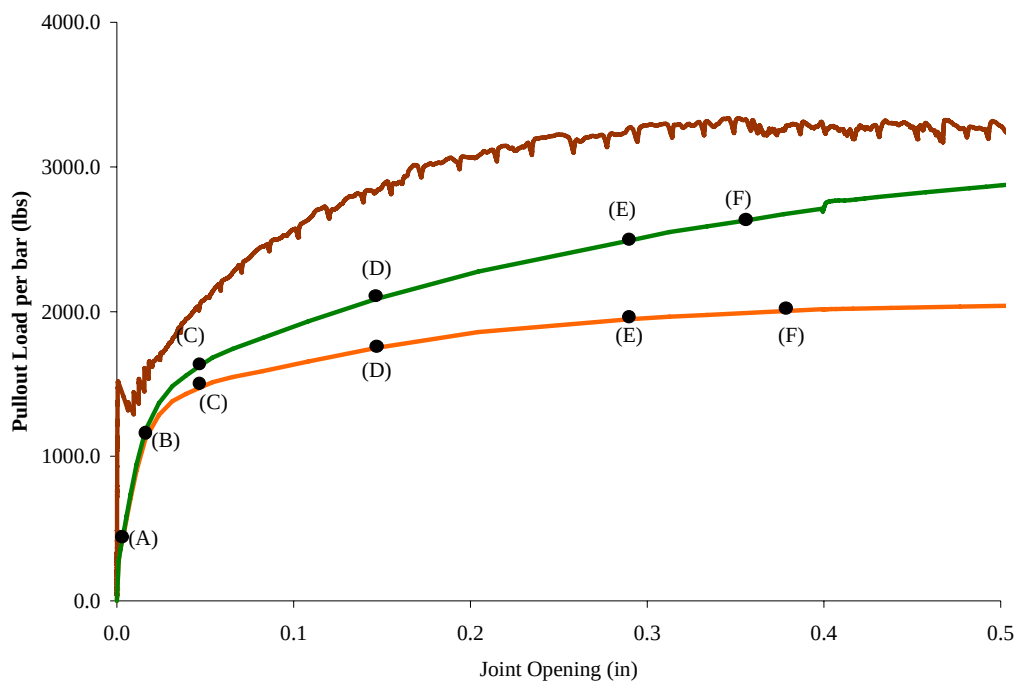

Figure C-42: Comparison of the FEM model with the experimental data for 5H18AM specimen

Table C-84: Summary of Material Failure / Damage Limit States from the analysis

Material Damage / Limit States	Joint Opening (in.)		Pullout Load (lbs)	
	(I)	(II)	(I)	(II)
(A)	0.002	0.002	352.0	357.0
(B)	0.016	0.016	1120.0	1180.0
(C)	0.046	0.046	1470.0	1620.0
(D)	0.146	0.147	1750.0	2090.0
(E)	0.290	0.290	1950.0	2490.0
(F)	0.377	0.355	2000.0	2630.0

Results of 5H36AM Finite Element Model

The dowel-concrete friction coefficients and material properties used in the analysis are shown in table C85. A comparison of the pullout force per bar (lbs.) vs. the joint opening (in.) is shown in figure C43. A summary of the various material failure / damage limit states is presented in table C86.

Table C-85: Dowel-Concrete Friction Coefficients; Material Properties used and limit states obtained from the analysis.

	μ_g	μ_w	f'_c (psi)	f'_t (psi)
Case I	0.0	0.30	3500.0	236.64
Case II	0.074	0.384	3500.0	240.0

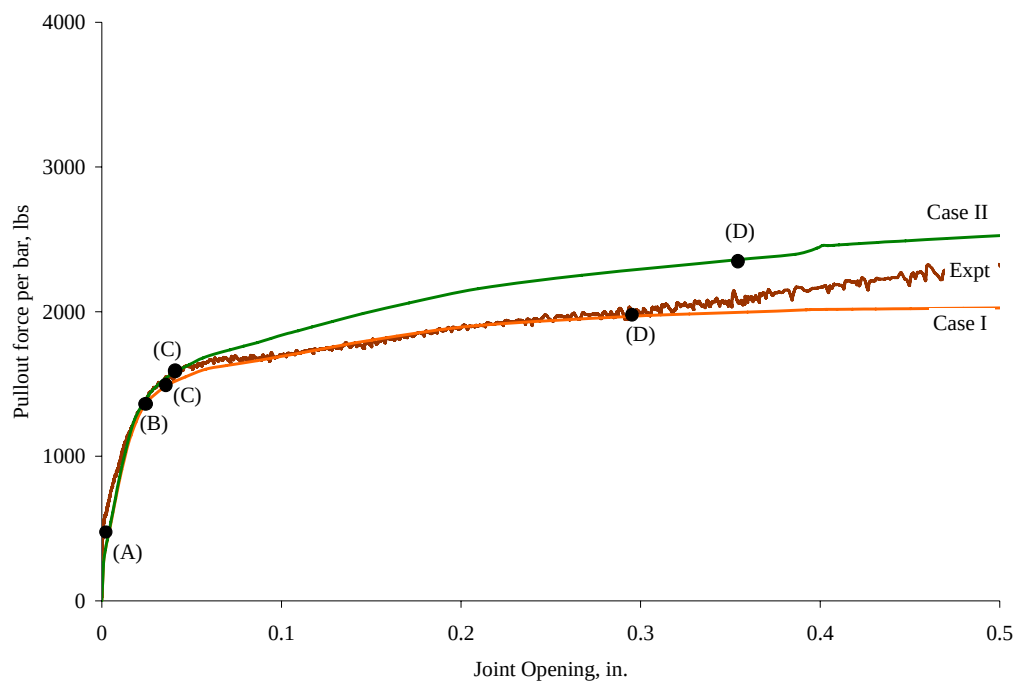

Figure C-43: Comparison of the FEM model with the experimental data for 5H36AM specimen

Table C-86: Summary of Material Failure / Damage Limit States from the analysis

Material Damage / Limit States	Joint Opening (in.)		Pullout Load (lbs)	
	(I)	(II)	(I)	(II)
(A)	0.003	0.003	418.44	422.26
(B)	0.024	0.018	1352.4	1252.1
(C)	0.035	0.041	1480.4	1585.0
(D)	0.295	0.353	1967.8	2358.4
(E)	-	-	-	-
(F)	-	-	-	-

Results of 5C18NU Finite Element Model

The dowel-concrete friction coefficients and material properties used in the analysis are shown in table C87. A comparison of the pullout force per bar (lbs.) vs. the joint opening (in.) is shown in figure C44. A summary of the various material failure / damage limit states is presented in table C88.

Table C-87: Dowel-Concrete Friction Coefficients; Material Properties used and limit states obtained from the analysis.

	μ_g	μ_w	f'_c (psi)	f'_t (psi)
Case I	0.0	0.30	3500.0	236.64
Case II	0.074	0.384	3396.0	251.0

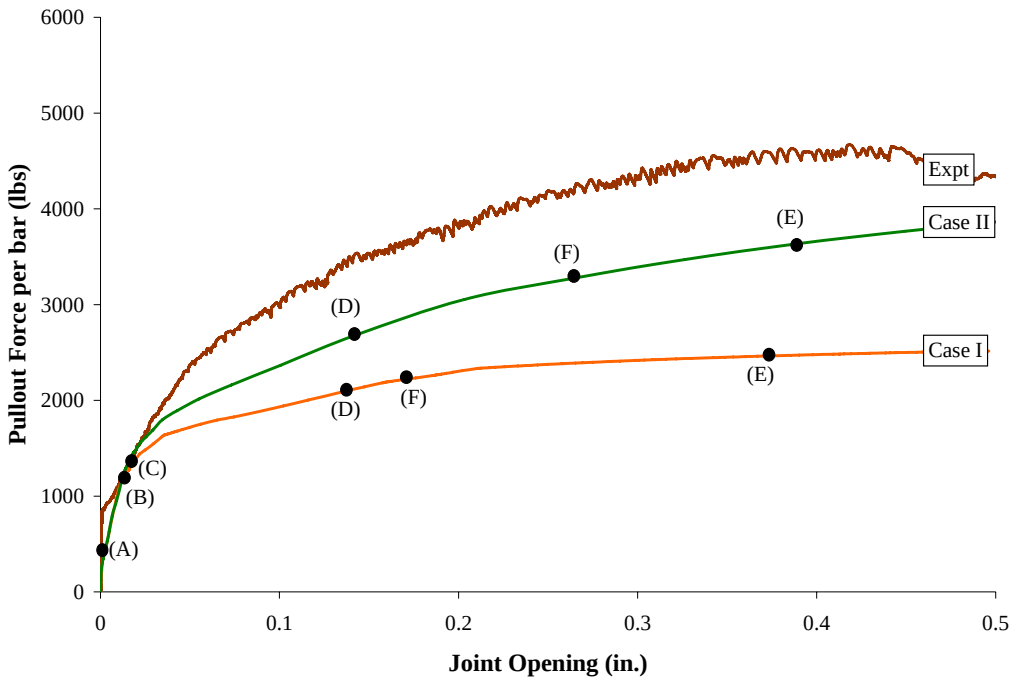

Figure C-44: Comparison of the FEM model with the experimental data for 5C18NU specimen

Table C-88: Summary of Material Failure / Damage Limit States from the analysis

Material Damage / Limit States	Joint Opening (in.)		Pullout Load (lbs)	
	(I)	(II)	(I)	(II)
(A)	0.002	0.002	383.0	385.0
(B)	0.0152	0.012	1340.0	1140.0
(C)	0.0158	0.013	1360.0	1240.0
(D)	0.137	0.142	2100.0	2670.0
(E)	0.373	0.388	2460.0	3630.0
(F)	0.170	0.265	2230.0	3280.0

Results of 5C18AM Finite Element Model

The dowel-concrete friction coefficients and material properties used in the analysis are shown in table C89. A comparison of the pullout force per bar (lbs.) vs. the joint opening (in.) is shown in figure C45. A summary of the various material failure / damage limit states is presented in table C90.

Table C-89: Dowel-Concrete Friction Coefficients; Material Properties used and limit states obtained from the analysis.

	μ_g	μ_w	f'_c (psi)	f'_t (psi)
Case I	0.0	0.30	3500.0	236.64
Case II	0.074	0.384		

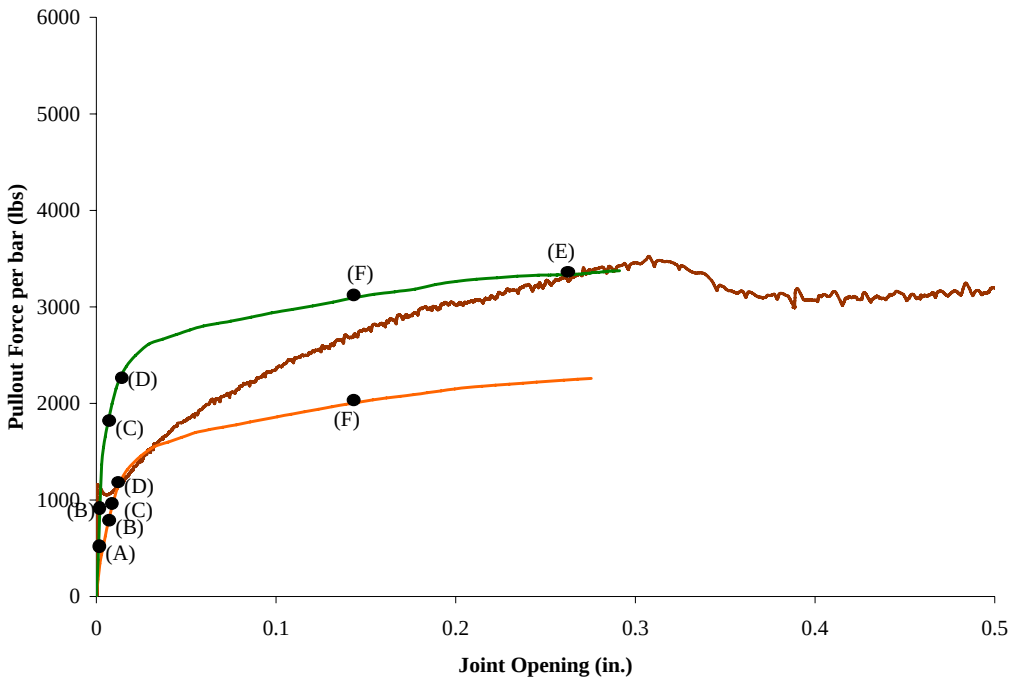

Figure C-45: Comparison of the FEM model with the experimental data for 5C18AM specimen

Table C-90: Summary of Material Failure / Damage Limit States from the analysis

Material Damage / Limit States	Joint Opening (in.)		Pullout Load (lbs)	
	(I)	(II)	(I)	(II)
(A)	0.003	0.003	439.0	1360.0
(B)	0.004	0.004	531.0	1550.0
(C)	0.006	0.006	759.0	1810.0
(D)	0.012	0.013	1140.0	2270.0
(E)	-	0.254	-	3330.0
(F)	0.154	0.143	2040.0	3090.0

Results of 5C36AM Finite Element Model

The dowel-concrete friction coefficients and material properties used in the analysis are shown in table C91. A comparison of the pullout force per bar (lbs.) vs. the joint opening (in.) is shown in figure C46. A summary of the various material failure / damage limit states is presented in table C92.

Table C-91: Dowel-Concrete Friction Coefficients; Material Properties used and limit states obtained from the analysis.

	μ_g	μ_w	f'_c (psi)	f'_t (psi)
Case I	0.0	0.30	3500.0	236.64
Case II	0.074	0.384	3860.0	269.0

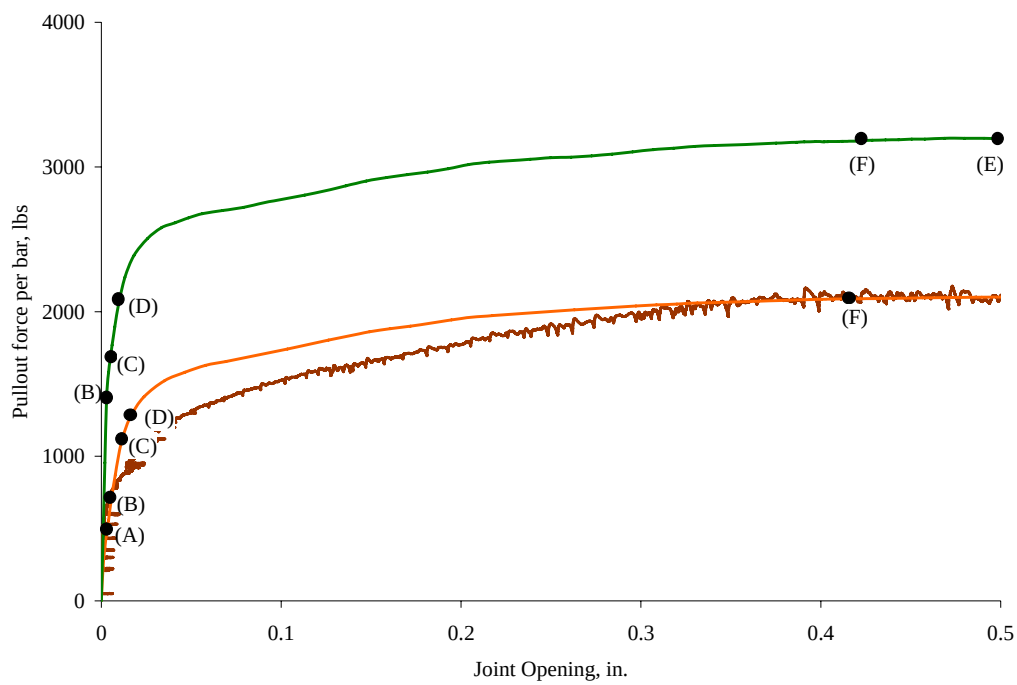

Figure C-46: Comparison of the FEM model with the experimental data for 5C36AM specimen

Table C-92: Summary of Material Failure / Damage Limit States from the analysis

Material Damage / Limit States	Joint Opening (in.)		Pullout Load (lbs)	
	(I)	(II)	(I)	(II)
(A)	0.003	0.003	465.0	500.0
(B)	0.005	0.006	693.0	1770.0
(C)	0.011	0.009	1100.0	2060.0
(D)	0.016	0.018	1270.0	2390.0
(E)	-	0.50	-	3200.0
(F)	0.412	0.429	2090.0	3180.0

APPENDIX D

RESULTS OF THREE DOWEL BARS WITH TYPICAL MISALIGNMENT COMBINED WITH LOADING EFFECTS

BEHAVIOR OF 3A FINITE ELEMENT MODEL

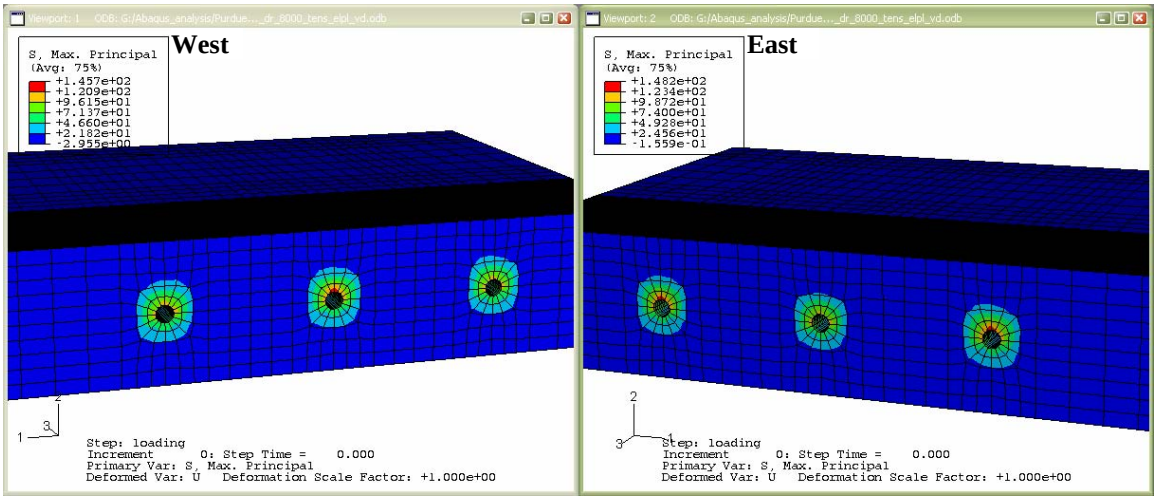

(a) Maximum Tensile Stresses at joint opening of 1/8 in.

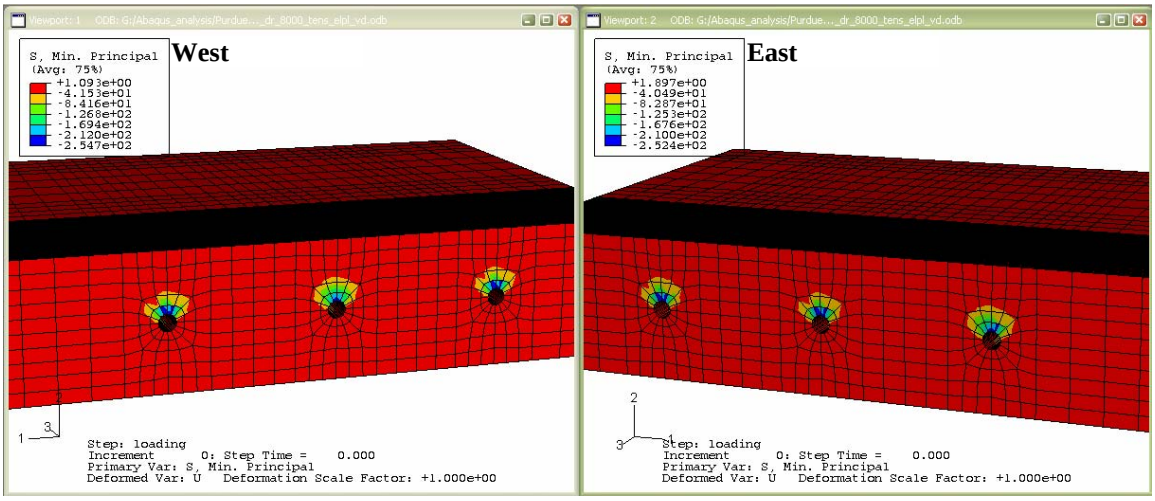

(b) Maximum Compressive Stresses at joint opening of 1/8 in.

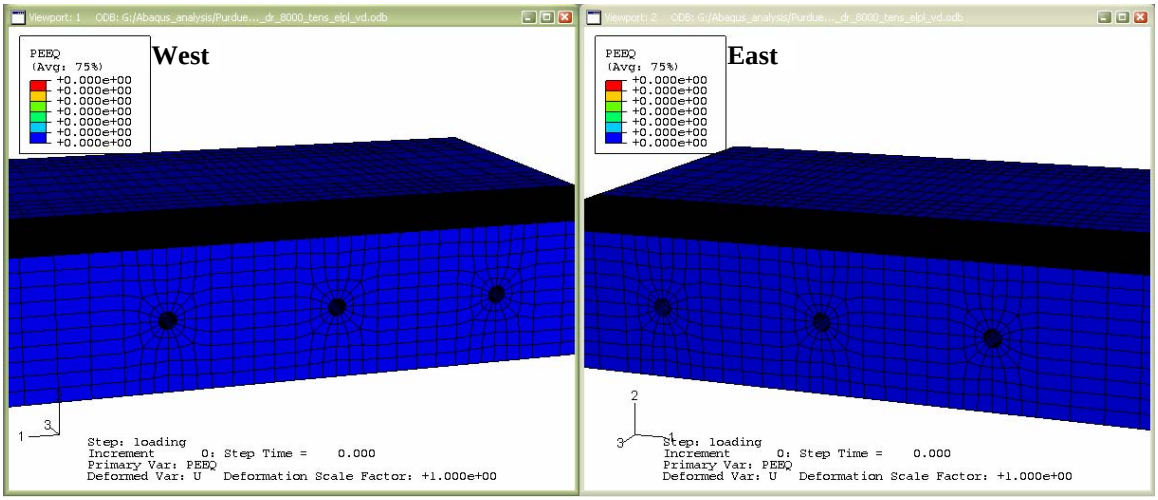

(c) Maximum Compressive Strains at joint opening of 1/8 in.

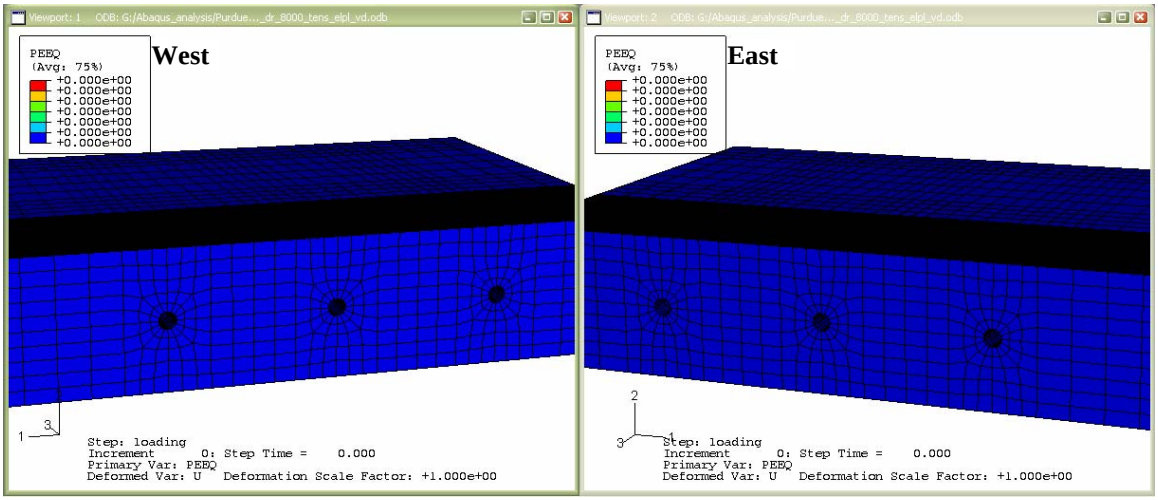

(d) Maximum Tensile Strains at joint opening of 1/8 in.

Figure D-1: Stress and Strains for 3A slab model at joint opening of 1/8 in.

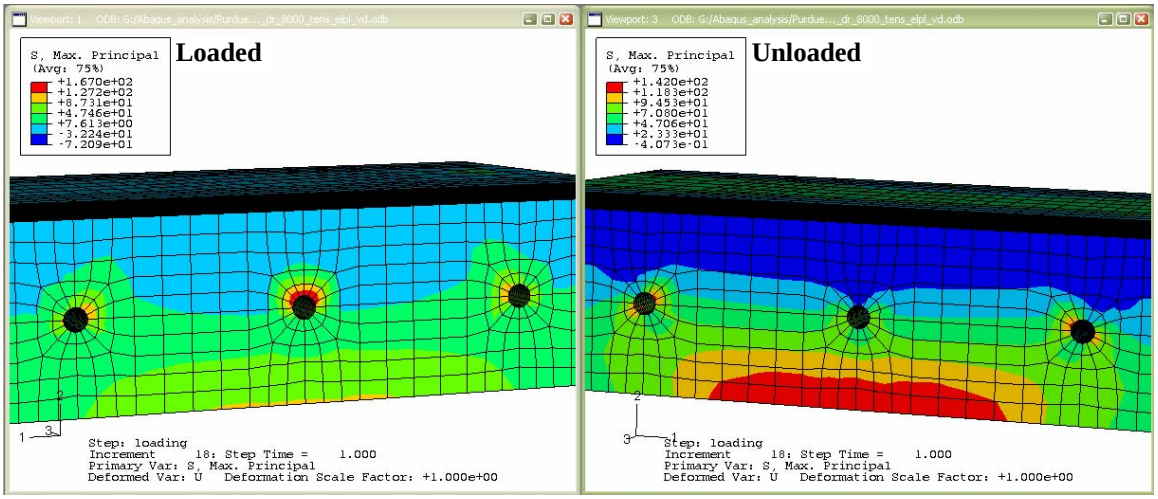

(a) Maximum Tensile Stresses at end of load application

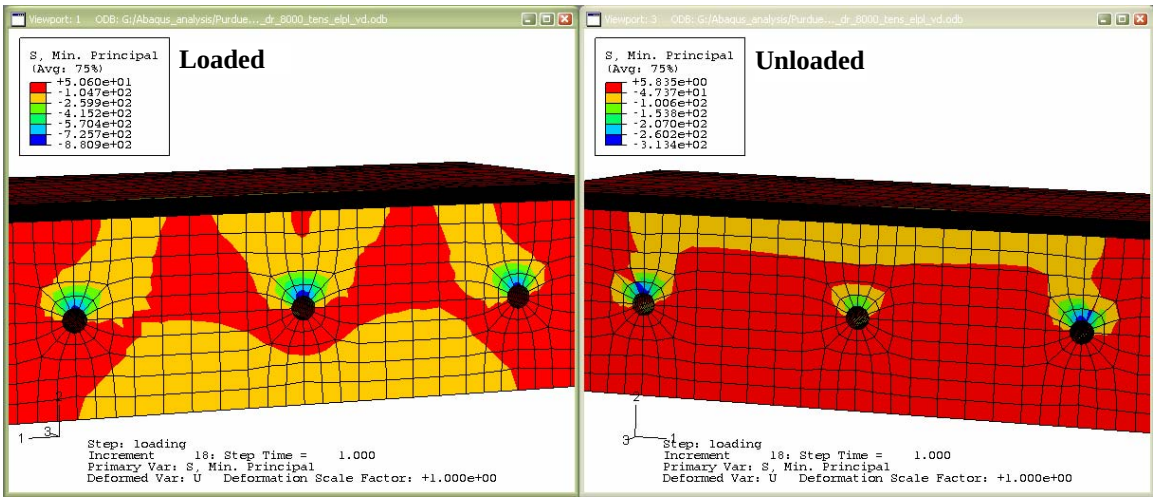

(b) Maximum Compressive Stresses at end of load application

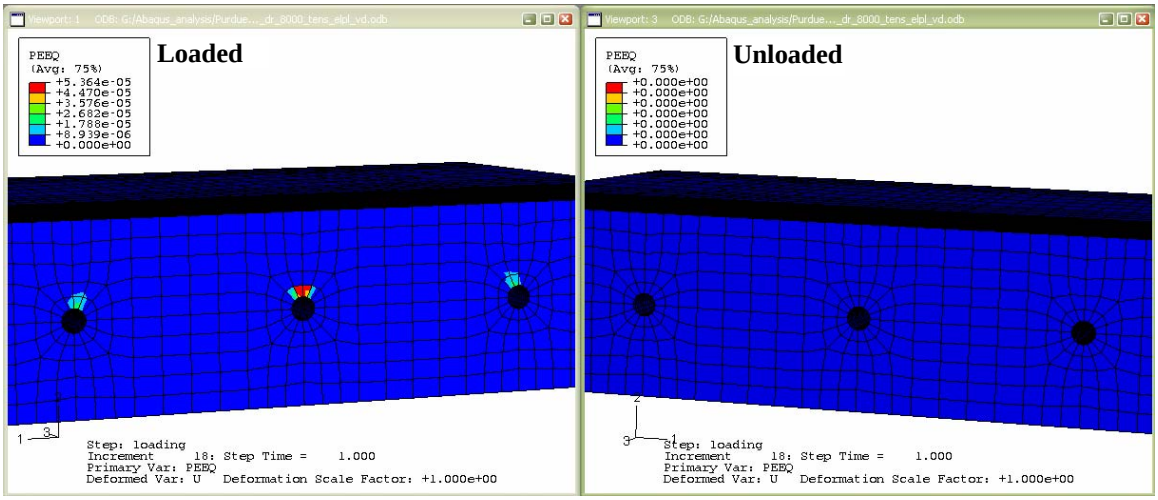

(c) Inelastic Compressive Strains at end of load application

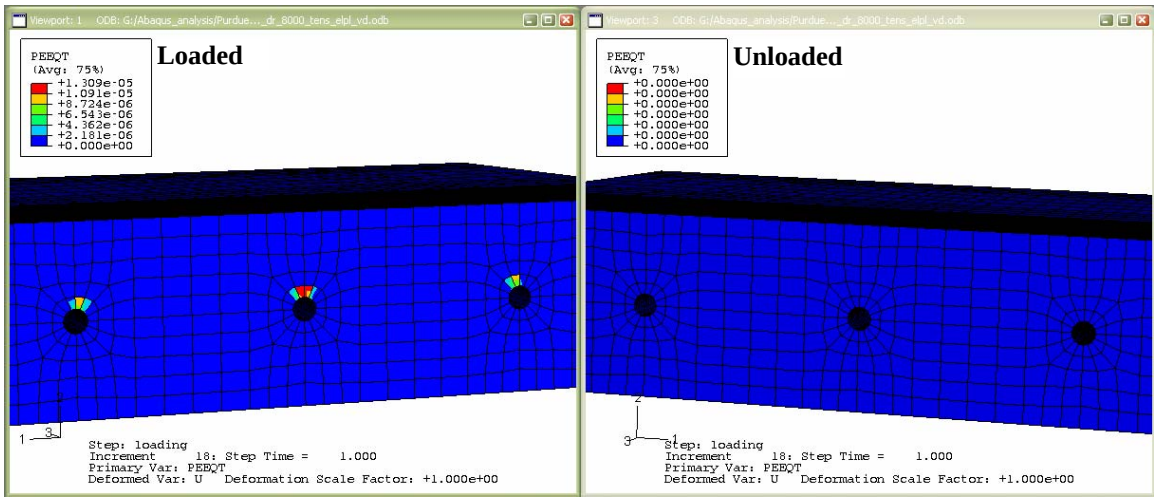

(d) Inelastic Tensile Strains at end of load application

Figure D-2: Stresses and Strains for 3A model after load application

BEHAVIOR OF 3V36NU FINITE ELEMENT MODEL

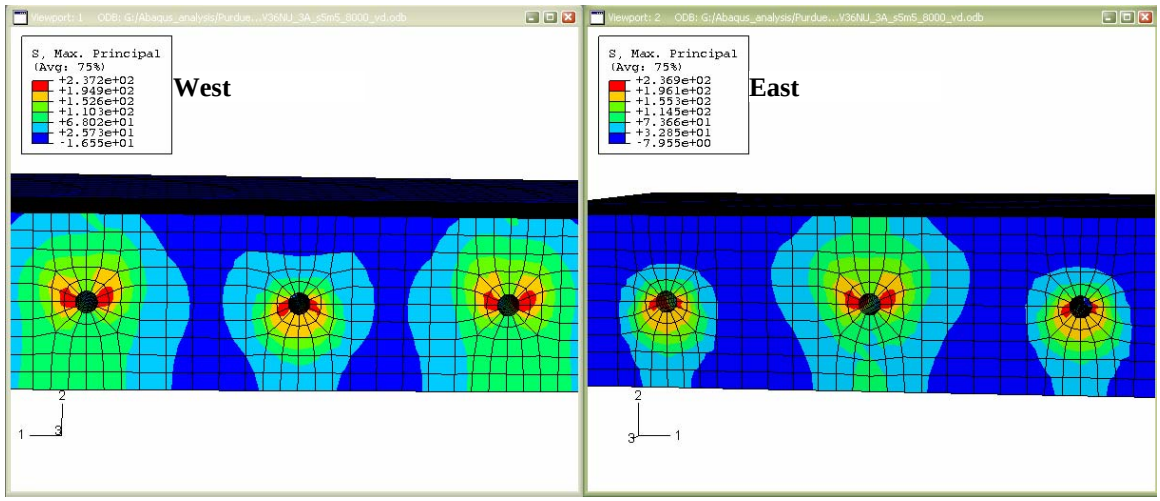

(a) Maximum Tensile Stresses at joint opening of 1/8 in.

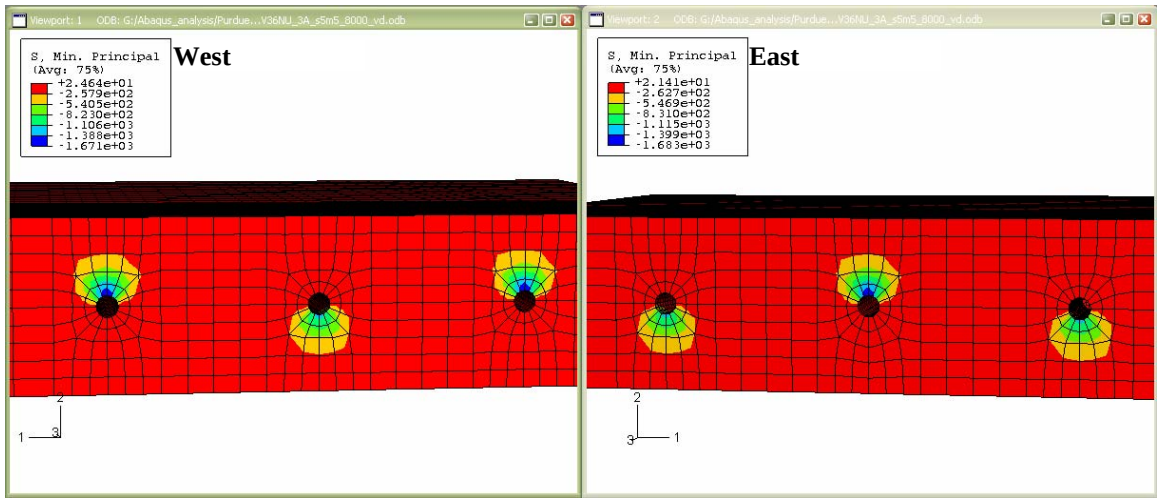

(b) Maximum Compressive Stresses at joint opening of 1/8 in.

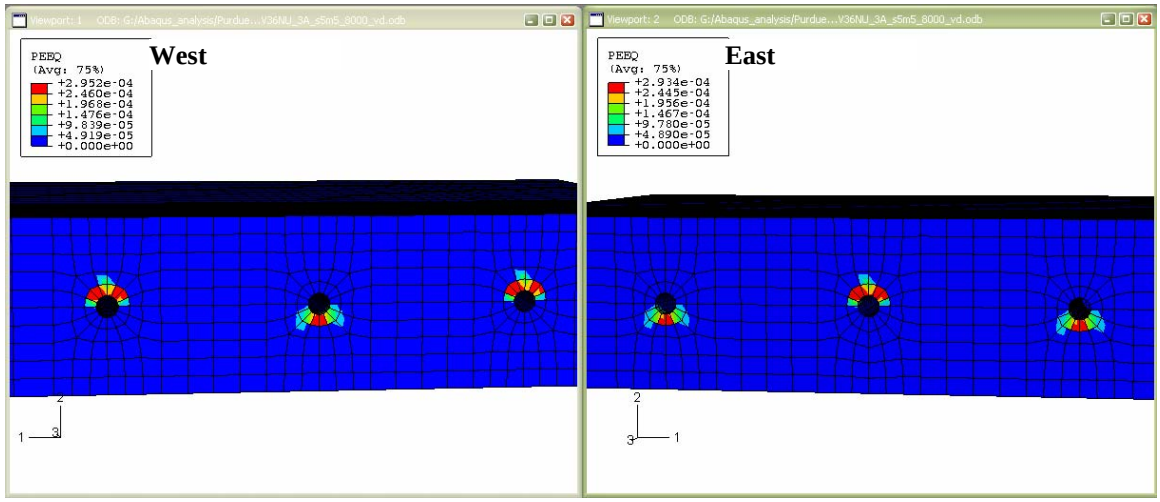

(c) Maximum Compressive Strains at joint opening of 1/8 in.

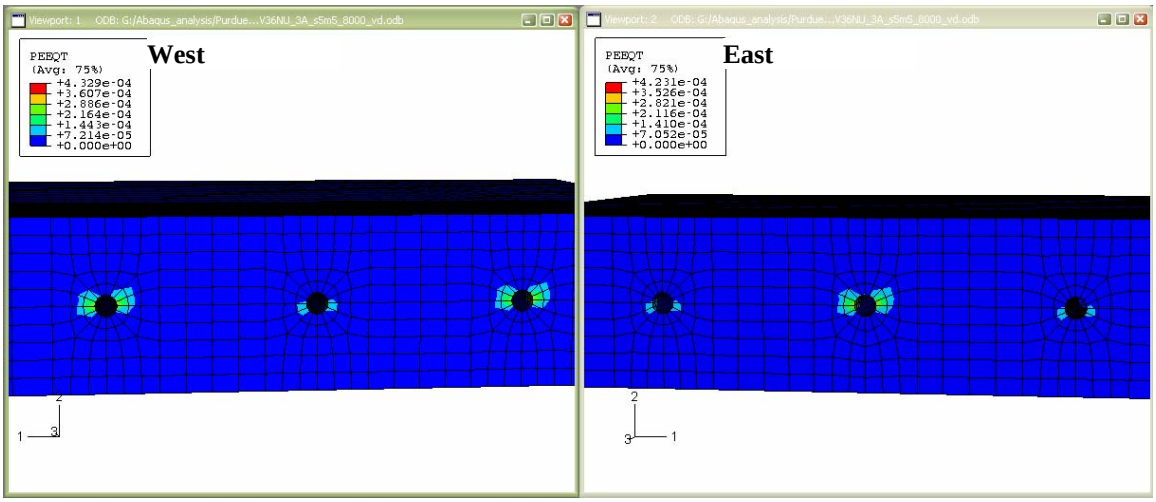

(d) Maximum Tensile Strains at joint opening of 1/8 in.

Figure D-3: Stress and Strains for 3V36NU slab model at joint opening of 1/8 in.

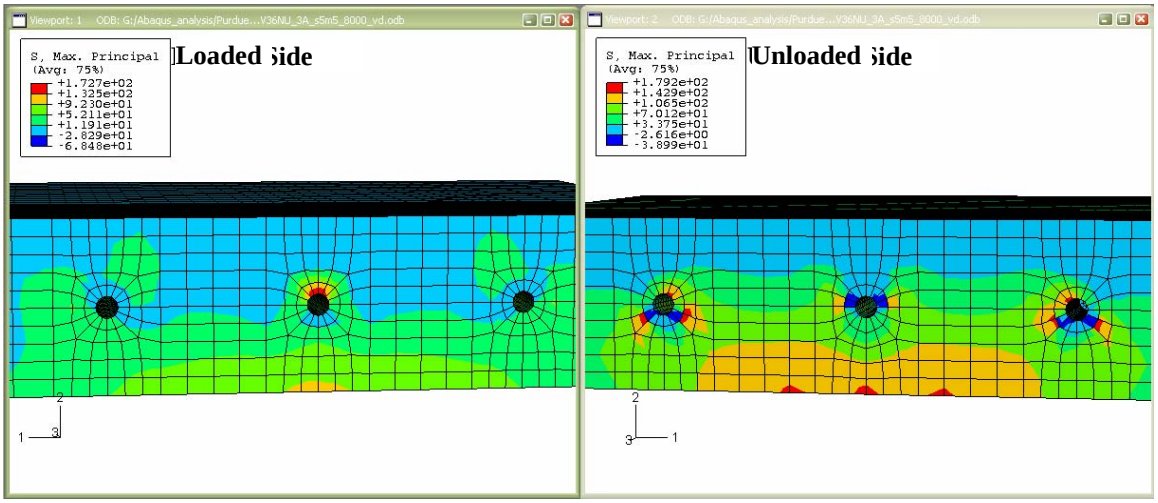

(a) Maximum Tensile Stresses at end of load application

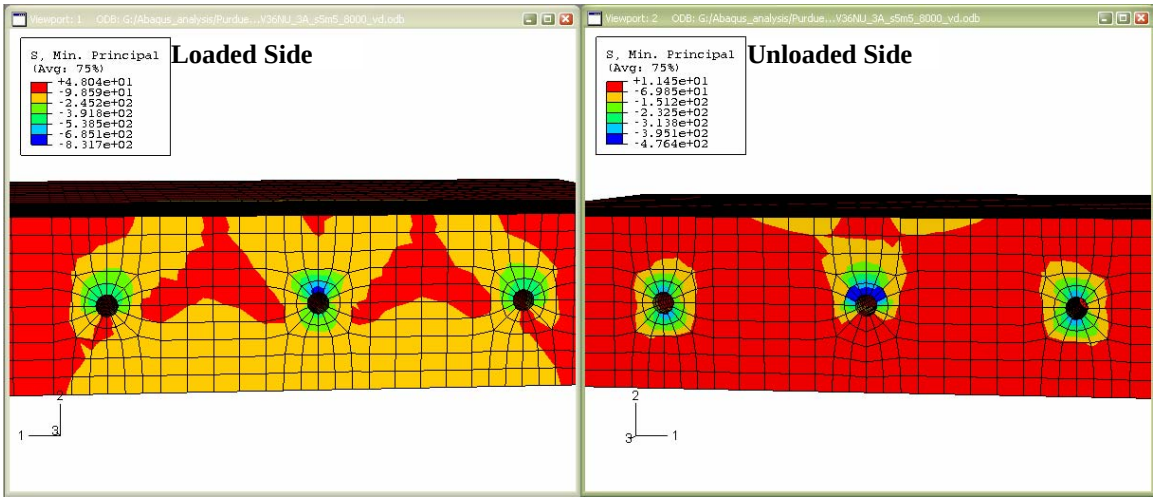

(b) Maximum Compressive Stresses at end of load application